



HAL
open science

Continuum vs. dislocation dynamics modelling of thin films

Filip Siska

► **To cite this version:**

Filip Siska. Continuum vs. dislocation dynamics modelling of thin films. Mechanics [physics.med-ph]. École Nationale Supérieure des Mines de Paris, 2007. English. NNT : 2007ENMP1481 . tel-00204422

HAL Id: tel-00204422

<https://pastel.hal.science/tel-00204422>

Submitted on 14 Jan 2008

HAL is a multi-disciplinary open access archive for the deposit and dissemination of scientific research documents, whether they are published or not. The documents may come from teaching and research institutions in France or abroad, or from public or private research centers.

L'archive ouverte pluridisciplinaire **HAL**, est destinée au dépôt et à la diffusion de documents scientifiques de niveau recherche, publiés ou non, émanant des établissements d'enseignement et de recherche français ou étrangers, des laboratoires publics ou privés.



Collège Doctoral

N° attribué par la bibliothèque

/--/--/--/--/--/--/--/--/--/

THESE

Pour obtenir le grade de
Docteur de l'Ecole Nationale Supérieure des Mines de Paris
Spécialité Sciences et Génie des Matériaux

Présentée et soutenue publiquement par

Filip ŠIŠKA

Le 26 novembre 2007

Continuum vs. dislocation dynamics modelling of thin films

*Directeurs de thèse : Samuel FOREST
Peter GUMBSCH*

Jury

M. D. RAABE	Rapporteur	Max Planck Institute–Düsseldorf, Germany
M. E. Van der GIESSEN	Rapporteur	University of Groningen, Netherlands
M. M. FIVEL	Examinateur	INP–Grenoble, France
M. S. FOREST	Examinateur	Ecole des Mines de Paris, France
M. P. GUMBSCH	Examinateur	University of Karlsruhe, Germany
M. R. SEDLÁČEK	Examinateur	Technical University of München, Germany
M. O. THOMAS	Examinateur	UPC–Marseille, France
M. D. WEYGAND	Examinateur	University of Karlsruhe, Germany

Centre des Matériaux P.M. FOURT de l'Ecole des Mines de Paris

Acknowledgements

First of all, I would like to express many thanks to my advisor **Mr. Samuel FOREST** for giving me the opportunity to work on this thesis and participate in the SizeDepEn project. He provided me very valuable ideas, advices and guiding during the whole thesis. I would like to also thank for his personal support and spirit. Also his indestructible enthusiasm and positive mood brought big inspiration and favour for my work. Thank You very much again.

Further I would like to thank to my other advisors **Mr. Daniel WEYGAND** and **Mr. Peter GUMBSCH** for their help, advices and guiding during my studies at University of Karlsruhe.

I would like to thank to **Mr. Dierk RAABE** and **Mr. Erik Van der GIESSEN** for accepting to write a report on this work and also to **Mr. Marc FIVEL**, **Mr. Radan SEDLÁČEK** and **Mr. Olivier THOMAS** for accepting to participate in the jury.

I would like to also say thanks to all staffs and students in Paris and Karlsruhe for helping me to manage life abroad.

Last but not least I would like to express thanks to my family and all close friends for support and help during whole my studies.

Thanks again to all, this thesis would never be finished without your help and support.

Contents

1	Introduction – crystal plasticity, thin films and size effects	1
1.1	Crystal plasticity and finite element simulations of polycrystals	1
1.2	Thin film structures and their investigation	4
1.2.1	Thin films production	5
1.2.2	Copper thin films	8
1.2.3	Thin film investigation methods	9
1.3	Size effects in thin film structures	11
1.4	SizeDepEn network	15
1.5	Objectives and methods	16
1.6	Outline of the thesis	18
	Motivation	1
2	Finite element simulations of elastic properties of copper thin films	21
2.1	Introduction	21
2.1.1	Objectives	21
2.1.2	Notation	21
2.1.3	Theory of cubic elasticity	23
2.1.4	Transformation of tensors	24
2.2	Determination of simulation parameters	25
2.2.1	Film representation and grain morphology	25
2.2.2	Mesh density	26

CONTENTS

2.2.3	Representative volume element	27
2.3	Tensile test for a single crystal	30
2.3.1	Orientation {111}	31
2.3.2	Orientation {001}	33
2.4	Tensile test of polycrystalline films	34
2.4.1	Texture {001}: mean value per grain	35
2.4.2	Texture {111}: mean values per grain	36
2.4.3	Heterogeneities inside the grains	38
2.5	Conclusions	43
3	Finite element simulations of the plasticity of copper thin films	47
3.1	Crystal plasticity theory	47
3.1.1	Setting of parameters	49
3.2	Plastic deformation of single crystal	52
3.2.1	Tensile loading of the {001} oriented single crystal	52
3.2.2	Tensile loading of the {111} oriented single crystal	56
3.2.3	Biaxial loading of the {001} oriented single crystal	58
3.2.4	Biaxial loading of the {111} oriented single crystal	60
3.3	Plastic deformation of polycrystalline aggregates	61
3.3.1	Parameters of simulation	62
3.3.2	Global stress–strain curves	63
3.3.3	Stress–strain heterogeneities	66
3.4	Conclusions	68
4	Mechanical behaviour of copper thin films under cyclic loading	71
4.1	Parameters of simulations	71
4.1.1	Representative volume element, mesh size effect and boundary conditions	71
4.1.2	Crystallographic texture and material behaviour	75
4.2	Strain heterogeneities in cyclically deformed thin films	76

CONTENTS

4.2.1	Overall cyclic hardening	76
4.2.2	Levels of heterogeneity and statistical analysis	81
4.3	Plasticity induced roughness	95
4.3.1	Definition of roughness parameters	95
4.3.2	Results	96
4.4	Conclusion	104
5	Comparison of the simulations with experimental data	107
5.1	Introduction – experiments on thin films	107
5.2	Simulations of aggregates with suitable grain orientations	110
5.3	Comparison of macroscopic behaviour	111
5.4	Comparison of local strain and displacement evolution	116
5.5	Comparison of the influence of the different grain morphology	120
5.6	Conclusion	127
6	Discrete dislocation dynamics simulations of polycrystalline aggregates	129
6.1	Introduction	129
6.1.1	DDD theory	129
6.1.2	Presentation of the polycrystalline simulations	133
6.2	Results	141
6.2.1	Macroscopic behaviour of aggregates	141
6.2.2	Summary of macroscopic behaviour	150
6.2.3	Stress/strain heterogeneities - evolution of plasticity	153
6.3	Conclusions	164
7	Comparison of the crystal plasticity and DDD simulations	165
7.1	Continuum crystal plasticity simulations	165
7.2	DDD simulations	168
7.3	Results	169
7.4	Conclusions	176

CONTENTS

8	Conclusions and prospects	177
8.1	Conclusions	177
8.2	Prospects	180
	Bibliography	183

Chapter 1

Introduction – crystal plasticity, thin films and size effects

1.1 Crystal plasticity and finite element simulations of polycrystals

The crystal plasticity theory has brought a new insight and possibility of description of material behaviour. The classical theories like von Mises plasticity do not take into account the properties like crystal lattice type, orientation in the space and number of slip systems and their interactions. These properties are not important when we deal with the structures where the grain size and behaviour of individual grain can be neglected. This approach is no longer sufficient, as soon as the scale of the investigated structures becomes smaller and smaller and the individual grain behaviour becomes more and more significant. The crystal plasticity theory was presented by (Mandel [1973], Teodosiu and Sidoroff [1976a], Teodosiu and Sidoroff [1976b], Asaro [1983a], Asaro [1983b]). This theory can take into account the properties of crystal lattice and interactions of slip systems, therefore, it can reasonably describe the mechanical behaviour of crystals. However most of the real structures are polycrystalline aggregates and this fact rises the problem of mutual interactions between the individual crystals. The first theory for polycrystals was proposed by Taylor (Taylor [1938]). Its theory assumes that all grains are subjected to the same macroscopic strain. However this assumption causes the violation of the stress equilibrium on the grain boundaries. The

opposite theories assume the homogeneity in stresses. Such a theory was given by Sachs (Sachs [1928]). Since these models have strong assumptions, models with weaker ones were created. These models can be called relax-constraints Taylor type models or modified Sachs models (Kocks and H. [1982], Raphanel and van Houtte [1985], Mao [1998]). The other approach is represented by self-consistent models (Berveiller and Zaoui [1978], Molinari and Canova [1987]). These models treat the problem of the individual grain embedded by a matrix with average properties of a polycrystalline aggregate. They satisfy the compatibility of stresses and strains, but they are not able to provide more detailed description of grain interactions and stress and strain heterogeneities. Such a more detailed description can be provided combining the crystal plasticity theory with finite element methods. The finite element method divides the investigated structure into small volume elements and the material behaviour is treated locally according to constitutive models under local loading conditions. The finite element method is used in three types of approaches.

First approach uses the homogenized models, which are prescribed at each integration point like Taylor model. The properties at integration points are computed by averaging of the stress tensor or stiffness matrix for all crystals in the aggregate (Kalidindi et al. [1992], Beaudoin et al. [1993]). The self-consistent models can be included also in this category (Lebensohn et al. [2004]). The techniques using this approach are simple for implementation into finite element codes therefore they can be used in industrial applications. But they are not able to describe the realistic strain inhomogeneities inside the grains.

Second type of approach is based on the prescription of single crystal behaviour into each element which represents one grain. This method is used for the computation of macroscopic behaviour of polycrystalline aggregates (Beaudoin et al. [1995], Sarma and Dawson [1996], Bachu and Kalidindi [1998], Raabe et al. [2002]). However this method is not able to describe the deformation inside the grains.

Third category of simulations involve the computations with grains which consist of larger number of elements. These simulations can provide the full description of the stress/strain heterogeneities inside the grains and mutual grains interactions. This kind of simulations necessitate high computational effort. The first simulations were made in

2D for simplified hexagonal grain shapes (Harren et al. [1988], Harren and Asaro [1989], Becker [1991]). The 3D computations were performed for different grain shapes. The first simulations were made for the simplified rhombic dodecahedral grains (Mika and Dawson [1998], Mika and Dawson [1999], Zhao et al. [2007]). The irregular grain shape is mostly created by the Voronoï construction (Barbe et al. [2001a], Barbe et al. [2001b], Diard et al. [2005]). Some experimental procedures which has been developed in the present days, allow to obtain the full 3D image of a grain structure. These real 3D images were then used in creation of real 3D grain shaped meshes and simulations of such aggregates were performed by (Buchheit et al. [2005], Musienko et al. [2007]). This type of simulations provides the realistic picture of the grain interaction, evolution of stresses and strains inside the grains or evolution of dislocation densities according to the used constitutive model.

Together with the finite element method, the crystal plasticity based models become very useful for applications which deal with structures with highly pronounced crystallographic texture. One of these areas is metal sheet forming. The metal sheets are produced by rolling, therefore, they have an organized texture in the direction of the rolling. Such a strong texture then influences the forming process of the sheets. The typical experiment where the influence of texture can be observed is deep cup drawing. Because of the strong texture, the sheet creates the wavy shape edge during this process. The modeling and simulations of these phenomena are presented in (Raabe and Roters [2004], Raabe et al. [2005], Duchene and Habraken [2005], Palumbo and Tricarico [2007], Tikhovskiy et al. [2007], Walde and Riedel [2007]). The other application in which the texture plays major role is the deformation of metal coatings. This problem is also closely connected to the topic of the present work because coatings are thin layers. This coating is very often deformed together with the metal sheet and this forming can cause the stress and strain concentrations and roughening of the surface of this coating. These processes can cause the decohesion of the coating or crack initiation and propagation in the coating and the sheet consequently. These processes may limit the protective function of such layers. Some experimental measurements and finite element simulations of stress/strain evolutions in the metal coating have been made (Lazik et al. [1995], Maeda et al. [1996], Parisot et al. [2001],

Parisot et al. [2004]). The coating surface roughening is mostly caused by the mismatch in grain crystallographic orientations since the roughness parameters correlate with the grain size (Wilson and Lee [2001]). Therefore the continuum crystal plasticity is well-suited theory for the investigation of the plasticity induced roughness. The results of the investigation of plasticity induced roughness are presented in the following works (Becker [1998], Mahmudi and Mehdizadeh [1998], Wittridge and Knutsen [1999], Oh et al. [2002], Raabe et al. [2003], Sachtleber et al. [2004], Kim et al. [2005]).

1.2 Thin film structures and their investigation

Thin film structures play an important role in the recent technologies. The typical example is electronics industry where the thin metallic layers create the essence of microelectronics devices like microprocessors. In the last years the interest has been focused on MEMS (microelectronics–mechanical systems). These MEMS are devices of nano to micro scales which can perform electrical or mechanical tasks. They are widely used as sensors for measuring of forces or acceleration. Typical present use is in automotive industry for sensors in airbags activation. They can be used as manipulators like nano or micro grippers, or as actuators like nano or micro engines or drives. These applications are also very often used in biotechnologies. Three examples of MEMS are shown in figure 1.1(a),(b),(c) (MiNDSLab [2007]). Case (a) shows the comb–drive which can be used for manipulation, case (b) corresponds to probes for neural spike detection and case (c) is an on–chip toroidal inductor. The dimensions of these MEMS devices vary from tens of nanometers to tenth of millimeters. The behaviour of the material on these length–scales is very different from that observed in bulk structures, therefore, the microstructural phenomena and processes become very important and drive the material properties. Therefore it was necessary to start investigating properties and behaviour of these thin film structures. The investigation is performed on experimental and theoretical levels due to the fact that thin film structures are subjected to wide range of conditions during their service life. The thin films are very often subjected to mechanical loading, therefore, it is necessary to know the behaviour of such structures under the wide range of mechanical loading conditions. For instance

1.2. THIN FILM STRUCTURES AND THEIR INVESTIGATION

long-time mechanical loading could lead to fatigue damage of these films which proceeds again differently from the bulk structures. The influence of the temperature plays also an important role. The increased temperature can cause structural changes or induce the plastic deformation and creep.

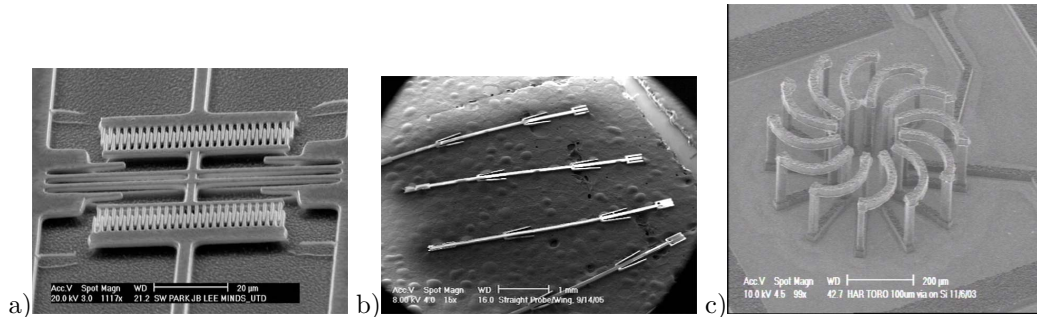


Figure 1.1: Examples of MEMS a) comb-drive, b) probes for neural spike detection, c) on-chip toroidal inductor (MiNDSLab [2007]).

1.2.1 Thin films production

The thin films are mostly deposited on substrates. The way of deposition influences the film properties. Main deposition techniques are:

- *Sputtering*: This method is based on the principle of shooting off the atoms from the source by neutral gas atoms. These released atoms then impact on the target layer and build the film. The basic design of this method is shown in figure 1.2. The advantages of this method are the low temperature of the target substrate and also the impacting atoms are able to cover a substrate with higher roughness or more complex shape. Therefore this method is widely used in microelectronic industry for creation of interconnecting lines.
- *Physical Vapor deposition*: Basic principle of this method is the evaporation of the material from the source layer and its consequent condensation on the target layer. The most used way of evaporation of the source material is its heating by electron

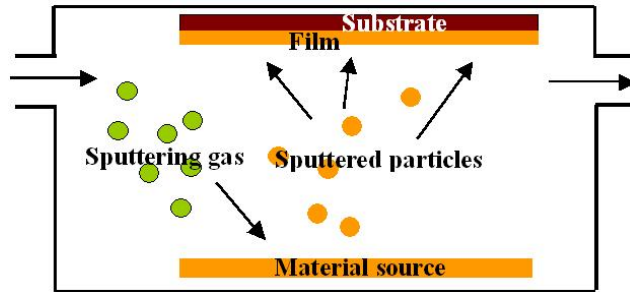


Figure 1.2: The basic scheme of the sputter deposition of thin films

beam. Such a method is called Electron Beam Physical Vapor Deposition (EBPVD). The scheme of the deposition process is demonstrated in figure 1.3. The advantage of this method is that the deposition rate can be tuned from few nanometers per minute up to micrometer per minute. This high deposition rates are useful in industrial applications. Another important advantage is the high efficiency of source material using. The disadvantage is that the material impacts the target substrate only from one direction which may produce irregular layers especially if the substrate is very rough. This is solved by the rotation of the target with respect to the impacting atoms however the target with complex geometry cannot be covered by film with this method.

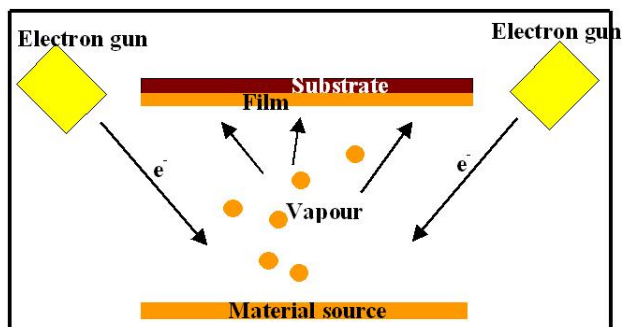


Figure 1.3: The basic scheme of the Electron Beam Physical Vapor Deposition of thin films

- *Chemical Vapor deposition:* This kind of deposition is based on the chemical reactions in which the source material chemically reacts with carrying gas. This compound then dissolves on the target substrate and creates the film made of pure material and some residual product of this reaction (Cho and Park [1997]). The advantage of this method is good covering of target substrate and also the possibility of the very high deposition rate. The disadvantage is that this process takes place at high temperatures and some corrosive product can be created in the presence of several reactants. These reactants can also be trapped as impurities inside the deposited film. This method is widely used for the production of films made of molybdenum, tantalum, titanium and tungsten.
- *Electroplating:* This method is based on the electrolytic process in which two electrodes are immersed in the electrolytic solution. The target substrate creates the negative electrode (cathode) and the source material creates the positive electrode (anode). The solution can also consist of the source material ions. When the direct current starts to flow through the system, the positive ions of the material are released from the anode and move towards the cathode. These ions then attach the cathode and create the continuous layer. The image of electroplating process is shown in figure 1.4. This method is simple but the target substrate must be conductible and resistive against the electrolytic solution.

Taking into account the scientific investigation of the metallic thin films there are two main types of substrates. Hard substrates are made of silicon and its oxides and soft substrates are made of polyimide. The silicon substrate is used for the thermomechanical tests because silicon can sustain high temperatures (Vinci et al. [1995], Keller et al. [1999], Baker et al. [2001], Weiss et al. [2001], Baker et al. [2003]). Also the silicon substrate is the most preferred material in microelectronic devices. The polyimide substrate is used for the mechanical testing like tensile tests or cyclic tests. The advantage of this substrate is such that its behaviour remains elastic up to 3% of applied deformation which is very useful for investigation of plasticity of thin films (Hommel and Kraft [2001], Schwaiger et al. [2003]). There are also experimental measurements with free-standing films (Huang and Spaepen

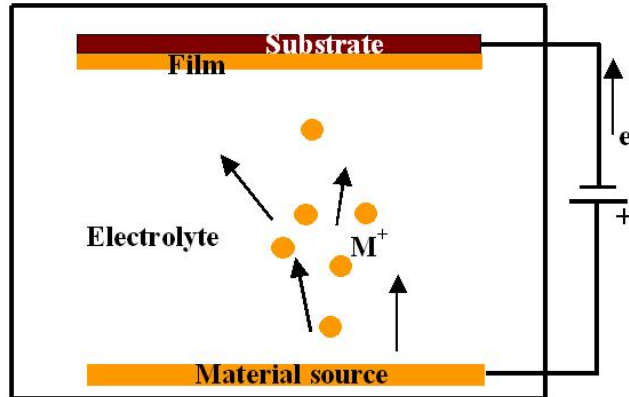


Figure 1.4: The basic scheme of the Electroplating deposition of thin films

[2000]). The most used materials for the films are aluminum, copper and silver (Huang and Spaepen [2000], Kobrinsky et al. [2001], Schwaiger and Kraft [2003]). This corresponds also to the materials used in industrial applications.

1.2.2 Copper thin films

Special attention was recently given to copper films because it is supposed that copper will replace aluminum in electronic applications. Copper provides better properties than aluminum. It has smaller coefficient of thermal expansion, higher electrical and thermal conductivity and twice higher melting point. The disadvantage of copper is its higher anisotropy which may lead to stress concentrations. Moreover copper cannot create a stable protective oxide layer on its surface. This fact can increase the amount of damage in such films (Vinci et al. [1995]). The experimental measurements of crystallographic texture with EBSD technique show that the copper thin films have preferable $\{111\}$ oriented grains (Knorr and Tracy [1995], Wendrock et al. [2000], Weihnacht and Bruckner [2002], Mane and Shivashankar [2005], Okolo et al. [2005]). This means that the crystallographic direction $\{111\}$ is parallel to the normal of the film, due to the fact that this organization of atoms has the lowest energy. The other preferable orientation is $\{001\}$ and some amount of grains have random orientations. The volumic amount of individual orientations also depend

1.2. THIN FILM STRUCTURES AND THEIR INVESTIGATION

on the film thickness. With increasing thickness, the amount of $\{111\}$ oriented grains decreases while the amount of $\{001\}$, $\{110\}$ and random grains increases (Perez-Prado and Vlassak [2002]). The texture also depends on temperature. Textural changes occur during the annealing of the films (Baker et al. [2001]). A randomization of texture occurs with increasing temperature and the amount of $\{111\}$ oriented grains decreases. Another significant feature of the films with thickness up to $1\text{--}2\ \mu\text{m}$ is that they have columnar grain structure with only one grain through the thickness and mostly the in-plane grain size is the same as the film thickness. The thicker films about $6\text{--}8\ \mu\text{m}$ have several grains through the thickness because the in-plane grain size is mostly about $1\text{--}2\ \mu\text{m}$ (Perez-Prado and Vlassak [2002], Okolo et al. [2005]). An example of a copper thin film on a silicon oxide substrate is shown in figure 1.5.

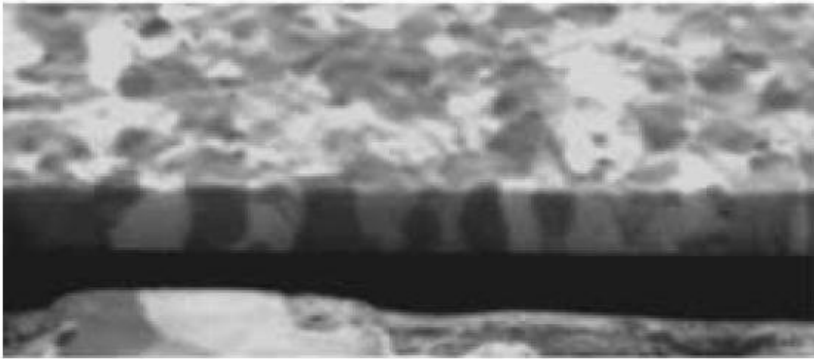


Figure 1.5: The copper thin film on the SiO_2 substrate created by sputtering method (Okolo et al. [2005]).

1.2.3 Thin film investigation methods

Experimental measurements of the mechanical properties like stresses and strains are performed by two main methods:

- *Wafer curvature method*: This method is based on the measurement of the stress in the film by the changes of curvature of the system film/substrate (Gonda et al. [2007],

Janssen [2007]). This method is mostly used for the measurement of stresses during thermal loading (Vinci et al. [1995], Keller et al. [1999], Baker et al. [2001], Weiss et al. [2001], Baker et al. [2003]). Different coefficients of thermal expansion of film and substrate cause different expansion and curving of the system and the biaxial stress can be estimated according to the relation:

$$\sigma = \frac{1}{6} \frac{E_s}{1 - \nu_s} \frac{h_s^2}{h_f} \frac{1}{R}, \quad (1.1)$$

where E_s and ν_s are the Young's modulus and the Poisson's ratio for the substrate, h_s and h_f are the thicknesses of the substrate and the film respectively. The parameter R is the experimentally measured curvature of the substrate wafer. This curvature is generally measured by laser beams. This wafer curvature method is very often used for the measurement of stresses in metallic films deposited on silicon substrates.

- *X-ray diffraction*: These measurements are based on the determination of interplanar spacing of the film crystal lattice. The elastic strain of the film causes the changes in this spacing which can be measured by the diffraction of the incident X-rays. The lattice spacing is estimated by the $\sin^2 \Psi$ method. X-ray diffraction can also be used in estimation of the dislocation density and the evolution of microstrains (Kraft et al. [2000], Hommel and Kraft [2001]). This method will be described in more details in chapter 5.

A powerful tool for the thin film investigation is TEM (Transmission Electron Microscopy). This technique is based on the evaluation of deflected electron beam which passes through the thin film. This method allows to observe the morphological properties of the film as well as their structural changes like grain boundary migration. Transmission electron microscopy is also able to detect the motion of dislocations and the evolution of their structure which helps to understand the processes of thin film plasticity. The observations of crack initiation and propagation then allow to evaluate the processes of damage in thin films.

Another aspect of the research on thin film properties is their theoretical investigation and simulations. The thin film behaviour was investigated within the framework of several different theories. The classical continuum theory with von Mises plasticity was used by (Wikström and Nygård [2002]). The extension of the continuum approach is based on the classical crystal plasticity (Parisot et al. [2001], Houdaigui et al. [2007a], Sai et al. [2006], Yefimov and Van der Giessen [2005], Houdaigui et al. [2007b]). The simulations within the framework of classical continuum crystal plasticity theory are the main part of this work. Further extension of the continuum approach is using the higher order plasticity theories like Cosserat crystal plasticity (Shu and Fleck [1999], Forest et al. [2000], Cheong and Busso [2004], Ma et al. [2006], Borg [2007], Han et al. [2007], Kuroda and Tvergaard [2007]). Dimensions of thin film structures are of the same order of magnitude as microstructural phenomena, therefore, they must be taken into account. These phenomena are mostly based on the dislocation processes which are localized and discrete events. Therefore, discrete theories like discrete dislocation dynamics were developed and used for the description of thin film structures behaviour (Van der Giessen and Needleman [1995], von Blanckenhagen et al. [2001], Weygand et al. [2001], Weygand et al. [2002], von Blanckenhagen et al. [2004], Nicola et al. [2005], Devincre et al. [2006]). One of the most visible and important phenomena of the thin film behaviour is the dependence of their properties on the thin film structure dimensions (grain size, film thickness). These effects are generally called “size effects” and they will be described in more details in the following section.

1.3 Size effects in thin film structures

The size effects are the phenomena which manifest as the dependence of the properties of thin film structures on their dimensions. These effects are observed in the behaviour of small scale structures. The typical mechanical size effect is the increase of yield stress with decreasing dimension of structure. Smaller scale structures can also sustain higher level of stress. These effects are observed in many experiments with thin films which were subjected to different loading conditions like tensile loading or thermomechanical loading.

First theory which deals with the size effects is known also in the bulk structure. It is the dependence of the yield stress on the grain size. This relation is known as the Hall–Petch relation:

$$\sigma = \sigma_0 + kd^{-1/2}, \quad (1.2)$$

where σ_0 is the yield stress for bulk single crystal material, k is a constant and d is the grain size. However the validity of this relation on micron scale and for thin film structures is still controversial. The experiments show that for copper this relation is valid down to $1\mu\text{m}$ size (Spaepen and Yu [2004]) but the experiments for the other metals show the variation of the exponent in the relation between $-1/2$ to -1 and it is not clear which value can be taken as correct.

The models of size effects in thin films are based on the assumption of constrained dislocation motion. The dislocation is supposed to move only in the "channel" through the film. The dislocation must fit into the dimension of the film (see figure 1.6). The simplest estimation of the critical resolved shear stress can be based on this assumption of fitting the dislocation into the film size (Arzt et al. [2001], Choi and Suresh [2002]). The yield stress can be estimated by the relation:

$$\tau = \frac{G_f b}{h_g}, \quad (1.3)$$

where G_f is the shear modulus of the film, h_g is the thickness measured along the glide plane and b is the Burgers vector.

A more sophisticated estimation was developed by (Nix [1989]) and (Freund [1987]). They suppose the creation of interface dislocation segments during the glide. The experimentally observed examples of such segments are shown in figure 1.7.

The resolved shear stress then depends on the film thickness and it can be determined by the relations:

$$\tau_{Nix} = \frac{bG_{eff}}{2\pi(1-\nu_f)} \frac{\sin \phi}{h_f}, \quad (1.4)$$

where

$$G_{eff} = \frac{G_f G_s}{G_f + G_s} \ln \left(\frac{\xi_s h_f}{b} \right), \quad (1.5)$$

1.3. SIZE EFFECTS IN THIN FILM STRUCTURES

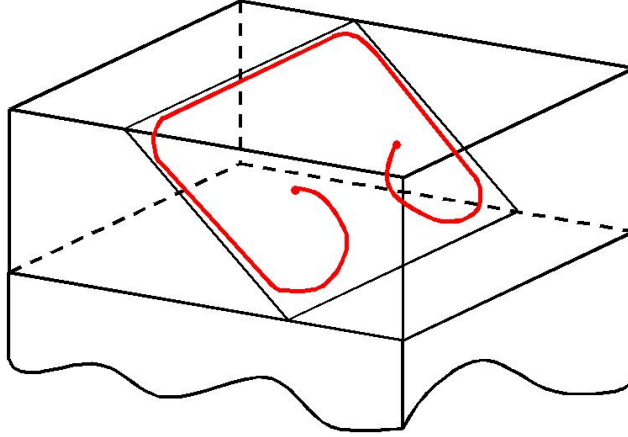


Figure 1.6: Scheme of the constrained dislocation motion in thin film.

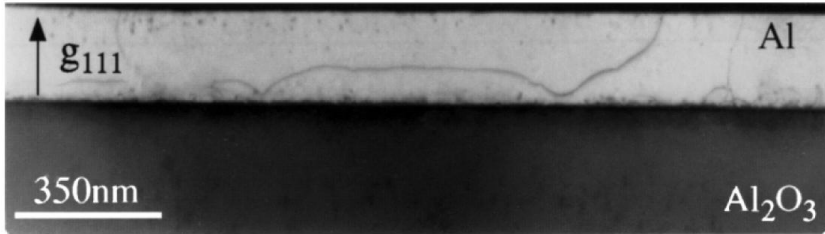


Figure 1.7: Scheme of the constrained dislocation motion in thin film (Arzt et al. [2001]).

ϕ is the angle between the glide plane normal and the film normal, b is the Burgers vector, ν_f is the Poisson ratio of the film, G_f and G_s are the shear moduli of the film and substrate respectively and ξ_s is the numerical constant which defines the cutoff radius of the stress field of the dislocation at the film/substrate interface. This model significantly underestimates the stress levels which are measured experimentally. An extension of the model was proposed by Thompson for polycrystalline films (Thompson [1993]). This model takes into account additional dislocation segments at grain boundaries. The resolved shear stress can then be estimated as:

$$\tau_{Th} = \frac{W}{b} \left(\frac{2}{d} + \frac{\sin \phi}{h_f} \right), \quad (1.6)$$

where

$$W = \frac{G_f b^2}{4\pi(1 - \nu_f)} \ln \left(\frac{d}{b} \right), \quad (1.7)$$

d is the grain size, W is the line energy of the dislocation segments along the grain boundaries and the interface between the film and the substrate and G_f is the film shear modulus. This model cannot explain the levels of yield stress of thin films because it does not take into account the obstacles which can restrain the dislocation motion. These obstacles are mainly the formation of other dislocations. In thin films dislocations are concentrated at the interface between the film and the substrate due to the misfit of crystal lattices. The other obstacles are the geometrically necessary dislocations at grain boundaries which are caused by strain incompatibilities due to grain orientations. Such a model, which takes into account the GND's, was developed to interpret some experimental stress–strain curves for copper thin films on the polyimide substrate up to a certain value of imposed strain (Hommel and Kraft [2001]). The simulations with discrete dislocation dynamics then showed the other possible effects which leads to higher yield stress values and higher hardening rates of thin film structures. One possible explanation is the limited number of dislocation sources in the grains because of their small dimension (von Blanckenhagen et al. [2004]). Then, the plasticity of the films is not driven by the interaction of the dislocations with obstacles but by the activation of these sources. The lack of sources can cause that only few of them are correctly oriented and can be activated. Furthermore the position of these sources inside the grains is very important. Sources which are closer to the grain boundaries or interface need higher stress level for their activation. The critical value of film dimension under which the plasticity is source–controlled and above which the plasticity is driven by the Hall–Petch behaviour was derived by (von Blanckenhagen et al. [2001]). The dominant dimension which determines the behaviour in the thin films is the smaller one from the pair of film thickness h and grain size d . The critical value of this dimension can be estimated as:

$$d_c = \left(\frac{G_f b}{ck} \right)^2 \quad (1.8)$$

where G_f is the film shear modulus, k is the Hall–Petch constant for bulk material, b is the Burgers vector and c is the ratio between the source length and the plasticity controlled film dimension.

1.4 SizeDepEn network

This thesis was realized as a part of the SizeDepEn network – “Engineering mechanics based on size–dependent materials properties” (www.sizedepen.de). This project belongs to Marie–Curie training networks which are the European projects aimed at the training of new scientists in the environment of international cooperation. This network consists of 6 groups from 5 European countries:

- Institut für Zuverlässigkeit von Bauteilen und Systemen, Universität Karlsruhe, Germany
- Intitute for Materials and Processes, University of Edinburgh, United Kingdom
- Centre des Matériaux de l’École des Mines de Paris, ARMINES, France
- Department of Applied Physics, Micromechanics of Materials Group, Rijksuniversiteit Groningen, The Netherlands
- Fraunhofer Institut für Werkstoffmechanik, Fraunhofer-Gesellschaft, Freiburg, Germany
- Department of General Physics, Eötvös University Budapest, Hungary

The research topics of this project are focused on the description of size–dependent material properties. These properties are treated on several length–scales (micro, meso, macro) within the framework of several different theories. The micro scale is represented by the molecular dynamics simulations of the dislocation motion in the confined volumes and the interactions of the single dislocation with obstacles and grain boundaries. The results of the molecular dynamics simulations are then implemented via the constitutive laws into the discrete dislocation dynamics simulations at the mesoscale. This investigation is pursued

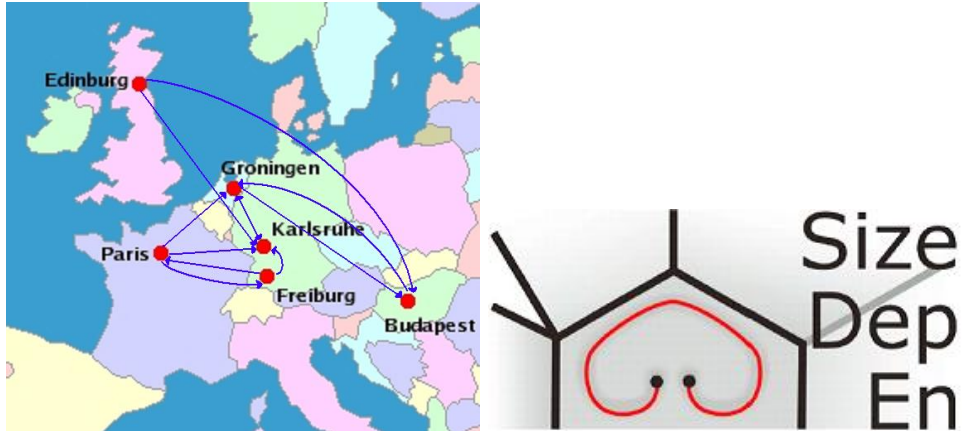


Figure 1.8: The scheme of the collaboration and mutual contacts within the SizeDepEn network and the logo of SizeDepEn.

at IZBS in Karlsruhe. The application of discrete dislocation dynamics in the problematic of fracture is investigated at the University of Groningen. The further step up in the scale is the description of collective behaviour of many dislocations. The methods of statistical mechanics are used for this description. The theory of multiple-slip in crystals based on this statistical description of collective behaviour of dislocation is developed at Eötvös University Budapest and University of Edinburgh. The macroscopic approach using the continuum crystal plasticity is applied in the investigation of the behaviour of the thin metallic films. These results are compared with DDD simulations of multicrystals. This work is done by École des Mines de Paris in cooperation with IZBS at University of Karlsruhe. The work and results which are described in this thesis represent this part of the project.

1.5 Objectives and methods

The main goal of this thesis is to investigate the mechanical properties of the thin copper film within the framework of classical continuum crystal plasticity and discrete dislocation dynamics. The objectives are the study of:

- The evolution of the stress/strain heterogeneities caused by the strong elastic

1.5. OBJECTIVES AND METHODS

anisotropy of copper.

- The evolution of the plasticity in the polycrystalline aggregates during tensile loading with different boundary conditions which simulate the behaviour of free-standing films, films on a soft substrate and films on a stiff substrate. The influence of the different crystallographic orientations on the adjacent grains is investigated.
- The Evolution of the hardening of the different crystallographic orientations during the cycling of aggregates.
- The evolution of the plastic strain fields in different crystallographic orientations in the aggregates (free-standing, on a stiff substrate) subjected to different types of cyclic loading.
- The evolution of the global and local plasticity induced roughness of the aggregates (free-standing, on a stiff substrate) subjected to different types of cyclic loading.
- The comparison of the simulations with experimental results. Comparison is undertaken for macroscopic behaviour and evolution of microstrains.
- The evaluation of the influence of the simplified Voronoï shaped grains on the macroscopic behavior and plastic strain distribution.
- The simulations of the 3D multicrystalline aggregates by discrete dislocation dynamics and investigation of the influence of the grain size, film thickness, crystallographic orientation, initial dislocation density and initial source length on the resulting macroscopic behaviour (yield stress, hardening rate) and local distribution of stress.
- The comparison of the stress distribution and levels in aggregates obtained by the DDD and classical and possibly generalized continuum crystal plasticity simulations.

The crystal plasticity simulations are performed by finite element method with the Z-set (Zebulon) code (www.nwnumerics.com). The DDD simulations are done by the finite element code developed at IZBS, University of Karlsruhe. The investigation of the properties is based on a statistical approach. This approach consists in collecting and averaging

the results from different realizations of polycrystalline aggregates. The advantage is the computations with rather small aggregates (Kanit et al. [2003]).

This thesis contains new advances, only partially presented in literature:

- The simulations of tensile test of the copper thin film on the polyimide substrate using the crystal plasticity model.
- The simulations of the cyclic loading of the copper thin films with evaluation of its mechanical behaviour and evolution of given quantities (hardening, plastic strain, plasticity induced surface roughness) for high number of cycles.
- 3D discrete dislocation dynamics of the multicrystalline aggregates.
- Comparison of the stress distributions in 3D continuum crystal plasticity and discrete dislocation simulations.

1.6 Outline of the thesis

The whole work is divided into 8 chapters. The first chapter is devoted to introduction and short summary of the research in the area of the crystal plasticity and finite element method, simulations of polycrystals, thin film structures and its investigation and the size effects, which occurs in thin films. Chapter 2 is focused on the estimation of the elastic properties of the copper thin films by FE simulations. The simulations are performed by the finite element method which necessitates to set up some basic parameters, like mesh density and representative volume element size, to be able to obtain reliable results. Copper is known for its strong anisotropy in elastic behaviour and it is necessary to investigate its influence on the evolution of stresses and strains in thin films because the stress level then directly influences the plasticity of copper thin films. Since the main crystallographic orientations in copper thin films are $\{111\}$ and $\{001\}$, the elastic behaviour of single crystal with these orientations is analytically investigated first. Then the distributions of the elastic stress and strain are investigated in the aggregates which is formed by the grains with these orientations. Chapter 3 is focused on the elasto–plastic behaviour of copper thin films.

1.6. OUTLINE OF THE THESIS

The theory of crystal plasticity is explained in this chapter. At first, the plasticity of the $\{111\}$ and $\{001\}$ oriented single crystals is solved analytically and then the elasto-plastic behaviour of copper thin films on a soft polyimide substrate is inspected. The thin films are often subjected to cyclic loading and also some experiments about cyclic and fatigue behaviour were performed in the literature. Therefore the next step is the simulation of the cyclic loading of thin copper films. This is described in chapter 4. The evolution of hardening, distribution of plastic strain and also the surface roughness are investigated in this part. Possible precursors of fatigue damage are also indicated. To verify the ability of this continuum approach, it is necessary to compare the simulation results with experimental data. This is done in the chapter 5. The comparison of the simulations with experimental tensile tests of copper thin films on polyimide substrate is also presented in this chapter. Since the aggregates used in simulations have the grains with Voronoï shapes, simulations with more realistic grains are proposed and compared with previous ones. This comparison can show if the simplified grain shape gives suitable results.

The discrete dislocation simulations are described in the chapter 6. The discrete dislocation dynamics simulations are presented for multicrystalline aggregates to discover the dependence of the yield stress and hardening rate on the grain size, film thickness, initial dislocation density and initial source length. The source activation and dislocation reactions are also observed and compared for different grain orientations.

The comparison of the continuum and DDD approach is compared in the chapter 7. The global stress-strain behaviour as well as the average stress per grain and the distribution of the stress and plastic strain is compared for multicrystalline aggregates computed by the different approaches, namely the continuum and discrete ones.

Chapter 2

Finite element simulations of elastic properties of copper thin films

2.1 Introduction

2.1.1 Objectives

The starting point of the investigation of mechanical properties of thin films is studying their elastic properties. The films behave elastically at the beginning of loading and plasticity starts and develops upon these elastic response. Therefore, it is necessary to investigate such an elastic response in systematic way. This study can be divided into two main parts: analytical and numerical. Analytical computations are used for determination of single crystal properties and numerical simulations are used for investigation of polycrystalline aggregate properties. The results of both approaches are presented in this chapter. The numerical simulations are done by the finite element method. The determination of necessary parameters of such simulations is described also in this chapter.

2.1.2 Notation

The following symbols and their definitions are used in this chapter and thesis:

- Local values at the integration point or analytical results:

2. FINITE ELEMENT SIMULATIONS OF ELASTIC PROPERTIES OF COPPER THIN FILMS

σ_{ij} – component of the stress tensor

ε_{ij} – component of the strain tensor

von Mises stress

$$\sigma_{eq} = \sqrt{\frac{3}{2} \sigma^{dev} : \sigma^{dev}}, \quad (2.1)$$

equivalent strain

$$\varepsilon_{eq} = \sqrt{\frac{2}{3} \varepsilon : \varepsilon}, \quad (2.2)$$

where σ^{dev} is the deviatoric part of stress tensor and ":" is double contraction.

- Average values per grain:

von Mises stress

$$\langle \sigma_{eq} \rangle_g = \frac{1}{V_g} \int_{V_g} \sqrt{\frac{3}{2} \sigma^{dev} : \sigma^{dev}} dV_g, \quad (2.3)$$

equivalent strain

$$\langle \varepsilon_{eq} \rangle_g = \frac{1}{V_g} \int_{V_g} \sqrt{\frac{2}{3} \varepsilon : \varepsilon} dV_g, \quad (2.4)$$

where V_g is the volume of grain g .

- Average values per aggregate:

component of stress tensor

$$\Sigma_{ij} = \frac{1}{V} \int_V \sigma_{ij} dV, \quad (2.5)$$

component of strain tensor

$$E_{ij} = \frac{1}{V} \int_V \varepsilon_{ij} dV, \quad (2.6)$$

von Mises stress

$$\Sigma_{eq} = \frac{1}{V} \int_V \sqrt{\frac{3}{2} \sigma^{dev} : \sigma^{dev}} dV, \quad (2.7)$$

2.1. INTRODUCTION

equivalent strain

$$E_{eq} = \frac{1}{V} \int_V \sqrt{\frac{2}{3} \varepsilon : \varepsilon} dV, \quad (2.8)$$

where V is the total volume of the aggregate.

These quantities are different from the von Mises stress of the mean stresses and equivalent of the mean strain which are defined as:

$$\Sigma_{eq}^m = \sqrt{\frac{3}{2} \Sigma^{dev} : \Sigma^{dev}}, \quad (2.9)$$

$$E_{eq}^m = \sqrt{\frac{2}{3} E : E}. \quad (2.10)$$

These quantities are not used in this work.

2.1.3 Theory of cubic elasticity

Only the elastic behaviour is considered in this part and the theory of cubic elasticity is used. Cubic elasticity is described by the tensor of cubic elasticity and relation between the stresses and strains is described by Hooke's law:

$$\sigma_{ij} = C_{ijkl} \varepsilon_{kl}, \quad \varepsilon_{ij} = S_{ijkl} \sigma_{kl}, \quad (2.11)$$

which can be rewritten as:

$$\begin{pmatrix} \varepsilon_{11} \\ \varepsilon_{22} \\ \varepsilon_{33} \\ 2\varepsilon_{12} \\ 2\varepsilon_{23} \\ 2\varepsilon_{31} \end{pmatrix} = \begin{pmatrix} S_{11} & S_{12} & S_{12} & 0 & 0 & 0 \\ S_{12} & S_{11} & S_{12} & 0 & 0 & 0 \\ S_{12} & S_{12} & S_{11} & 0 & 0 & 0 \\ 0 & 0 & 0 & S_{44} & 0 & 0 \\ 0 & 0 & 0 & 0 & S_{44} & 0 \\ 0 & 0 & 0 & 0 & 0 & S_{44} \end{pmatrix} \begin{pmatrix} \sigma_{11} \\ \sigma_{22} \\ \sigma_{33} \\ \sigma_{12} \\ \sigma_{23} \\ \sigma_{31} \end{pmatrix}, \quad (2.12)$$

where S_{ij} are the cubic elastic compliances. This form of matrix is valid in the coordinate frame of the crystal. Usually the crystallographic orientation of grains in aggregate is different according to the direction of loading, therefore, it is necessary to express the values of stresses and strains in the laboratory or the crystal coordinate system.

2.1.4 Transformation of tensors

The transformation between the two coordinates systems can be done using the three Euler angles ϕ_1, Φ, ϕ_2 is shown in figure 2.1.

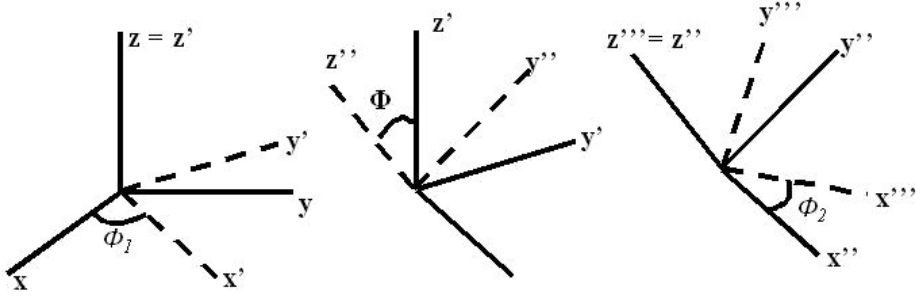


Figure 2.1: Definition of Euler angles

The components of tensors are transformed according the relation:

$$x'_{ij} = T_{ik}T_{jl}x_{kl}, \quad (2.13)$$

Transformation matrix from the laboratory coordinate system to the crystal one can be expressed in the following form:

$$T = \begin{pmatrix} \cos \phi_1 \cos \phi_2 - \cos \Phi \sin \phi_1 \sin \phi_2 & \sin \phi_1 \cos \phi_2 + \cos \Phi \sin \phi_2 \cos \phi_1 & \sin \Phi \sin \phi_2 \\ -(\cos \phi_1 \sin \phi_2 + \cos \Phi \cos \phi_2 \sin \phi_1) & \cos \phi_1 \cos \phi_2 \cos \Phi - \sin \phi_2 \sin \phi_1 & \sin \Phi \cos \phi_2 \\ \sin \phi_1 \sin \Phi & -\cos \phi_1 \sin \Phi & \cos \Phi \end{pmatrix} \quad (2.14)$$

and the inverse transformation is given by its transpose.

2.2 Determination of simulation parameters

The starting point of the simulations is the setting of their parameters. The representation of the film and grain morphology is described in this chapter as well as the determination of the suitable mesh density.

2.2.1 Film representation and grain morphology

The real film is represented by a polycrystalline aggregate in the computations. This aggregate mimics some properties of the real films but some simplifications are introduced. The real films have usually only one grain through the thickness and the grain boundaries are almost perpendicular to the film plane (Bhattacharyya et al. [2001], Parisot et al. [2001], Perez-Prado and Vlassak [2002], Weihnacht and Bruckner [2002], Okolo et al. [2005]). The grain size distribution is log-normal and the real films consist of combination of small and large grains (Weygand et al. [1998]). Most of the grains have size about the thickness of film. The films are produced for our simulations by the Voronoï tessellation method in 2D with an exclusion distance (Barbe et al. [2001a]). This method leads to grains with more or less the same size so there is no large variation of the in-plane grain size contrary to the real case. This is the first simplification. The 3D structures are created from the 2D by the extension of the 2D map of the grains along the third perpendicular direction. This method creates aggregates with one grain through the thickness and the grain boundaries are strictly perpendicular to the film plane which is the second simplification. The process of the creation of the film is shown in figure 2.2(a). The third simplification is the absence of the twin structures observed in the real films. All these factors can influence the results and should be taken into account in future more realistic simulations. The real films in the experiments are deposited on the substrate or they are free-standing. These two cases are simulated in this section by two types of boundary conditions. The tensile test of the film

is simulated by the imposing displacement U_2 on one side of the film, while the opposite side is fixed in the direction of tension – direction 2. The lateral faces of aggregate are free. Two extreme conditions are applied on the bottom side of the aggregate:

- *free surface*: There are no constraints applied on this surface which corresponds to a free-standing film.
- *fixed surface*: The surface is not allowed to move in the direction perpendicular to the plane of the film: $U_3 = 0$. This corresponds to the case of a non-deformable substrate.

The boundary conditions are shown in the figure 2.2(b). Crystallographic texture is taken from the experimental observations (Hommel and Kraft [2001]). There are two main crystallographic orientations in the copper thin films: $\{111\}$ and $\{001\}$. This means that the normals to these planes are perpendicular to the plane of the film. These axes are taken strictly perpendicular in our simulations which is not exactly the case in real films.

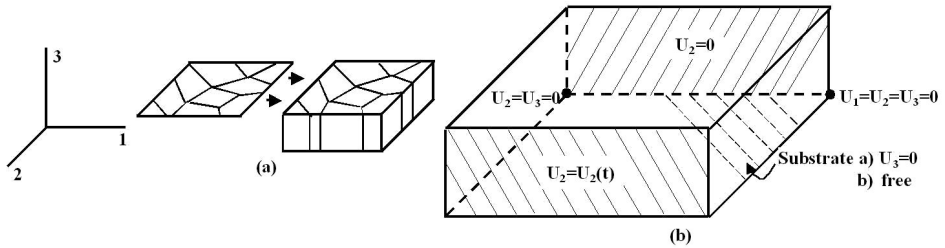


Figure 2.2: Creation of the polycrystalline aggregate (a), boundary conditions (b)

2.2.2 Mesh density

Before starting the simulations, it is necessary to check the parameters of the mesh to produce valid results. Quadratic elements with 15 nodes and 18 integration points are used in the simulations. Four meshes with different mesh densities were created for checking the convergence of the results. The aggregates contain 19 grains with orientation $\{111\}$. A

2.2. DETERMINATION OF SIMULATION PARAMETERS

tensile test in the purely elastic regime was performed on a film. Parameters of the meshes are presented in table 2.1. Tested meshes are shown in figure 2.3.

Mesh	coarse	medium	fine	ultrafine
DoF/grain	1290	2169	3729	6924

Table 2.1: Chosen mesh densities described by average number of degrees of freedom (DoF) per grain

The global and local convergence is checked in the following way. The global convergence is obtained from the comparison of the value of apparent Young's modulus for the different meshes. The global average value of the stress in the direction of the tension is computed when the global average value of imposed deformation is prescribed. Then the apparent Young's modulus is computed as:

$$\Sigma_{22} = \langle \sigma_{22} \rangle = \frac{1}{V} \int \sigma_{22} dV, \quad E_{22} = \langle \varepsilon_{22} \rangle, \quad E_{app} = \frac{\Sigma_{22}}{E_{22}}, \quad (2.15)$$

where E_{22} is the average imposed deformation. The local convergence is obtained from the comparison of the equivalent von Mises stress along a side line of the aggregate. The results for the local and global convergence are shown in figure 2.4. The differences of the results between the individual meshes are small so the computational time becomes the main criterion to choose of the best-suited mesh density. Finally the mesh marked as medium is chosen because it provides sufficient accuracy and reasonable computing time. The density of this mesh is about 240 elements per grain.

2.2.3 Representative volume element

The global properties of the aggregate should correspond to the behaviour which can be measured in experiments and the global properties of the aggregate should not depend on the concrete realizations. This condition is fulfilled when the aggregate contains a sufficient number of the grains. Such aggregate presents the representative volume element. In our case a statistical approach is chosen to obtain the representativity of the results (Kanit

2. FINITE ELEMENT SIMULATIONS OF ELASTIC PROPERTIES OF COPPER THIN FILMS

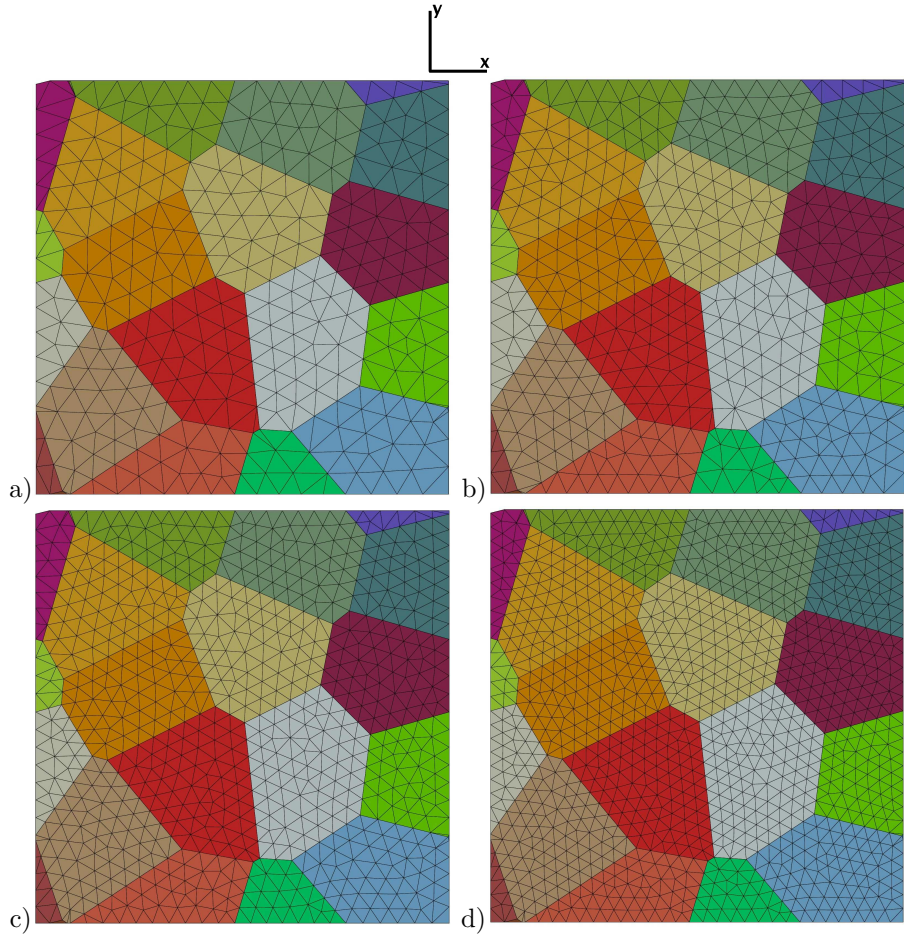


Figure 2.3: Meshes used for estimation of mesh density (a) coarse, (b) medium, (c) fine, (d) ultrafine

et al. [2003], Houdaigui et al. [2007a]) . This approach is based on the comparison of the results from different realizations of the aggregates with the same number of grains in average. The criterion of this approach for the apparent Young's modulus can be written as:

$$\epsilon = \frac{D(E)}{\sqrt{nE}} \leq 1\% \quad (2.16)$$

2.2. DETERMINATION OF SIMULATION PARAMETERS

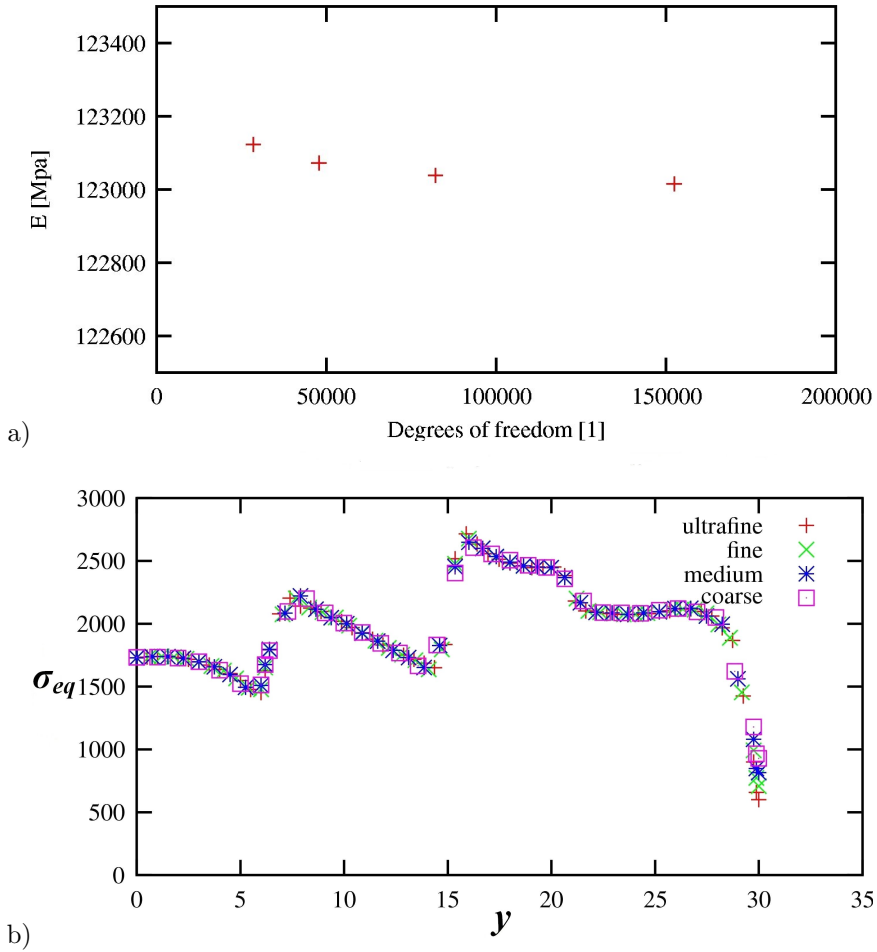


Figure 2.4: Global convergence of meshes (a), local convergence of meshes (b)

where $D(E)$ is the standard deviation of the Young's moduli of realizations, \bar{E} is the mean value with respect to n realizations. The computations of the representative volume element are done for the boundary conditions which correspond to presence of a non deformable substrate. The constraint of the substrate is supposed to cause the higher dispersion in the results. Therefore such an estimate is on a safe side. Two sets of the aggregates are created:

10 realizations of the aggregates with 20 grains and 20 realizations of the aggregates with 47–49 grains. The aggregates are supposed to have only {001} or {111} oriented grains. The results are summarized in the table 2.2.

Number of grains	20	20	47 - 49	47 -49
Orientation	{001}	{111}	{001}	{111}
\bar{E} [MPa]	75 863	125 788	77 550	126 251
ϵ	0.011	0.0019	0.0052	0.0018

Table 2.2: Relative precision of Young’s modulus

The average values of Young’s moduli differ by 2.2 % for the orientation {001} and 0.3 % for the orientation {111} respectively. Such differences are small enough, therefore, the given criterion is fulfilled for both orientations for the case of 20 larger aggregates. So the results obtained with these conditions are valid and sufficiently accurate.

2.3 Tensile test for a single crystal

Tensile test is designed in such a way that tensile axis is contained in one plane {111} or {001}. The tension is applied in x direction of the laboratory coordinates. The orientation is such that the normal of given planes {111} or {001} coincides with z -axis of the laboratory coordinates. This is shown in figure 2.5. The angle ϕ_1 describes the rotation of the crystal coordinates (red) with respect to laboratory ones (black).

The stress tensor in the laboratory coordinates is written as:

$$\sigma = \begin{pmatrix} \sigma & 0 & 0 \\ 0 & 0 & 0 \\ 0 & 0 & 0 \end{pmatrix}. \quad (2.17)$$

2.3. TENSILE TEST FOR A SINGLE CRYSTAL

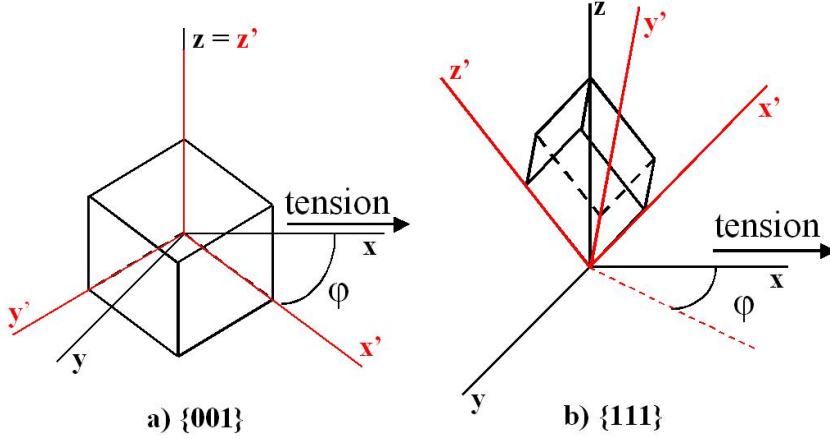


Figure 2.5: Orientation of the crystal coordinates (red) with respect to laboratory coordinates (black).

2.3.1 Orientation {111}

Corresponding Euler angles for this orientation are: $\Phi = 54.74^\circ$, $\phi_2 = 45^\circ$. The angle ϕ_1 is the angle between the x axis of the laboratory coordinates (tensile direction) and projection of the crystal x' axis to the plane $x - y$ of the laboratory coordinates. The transformation matrices are for this case:

$$T = \begin{pmatrix} \frac{\sqrt{2}}{2} \cos \phi_1 - \frac{\sqrt{6}}{6} \sin \phi_1 & \frac{\sqrt{2}}{2} \sin \phi_1 + \frac{\sqrt{6}}{6} \cos \phi_1 & \frac{\sqrt{3}}{3} \\ -(\frac{\sqrt{2}}{2} \cos \phi_1 + \frac{\sqrt{6}}{6} \sin \phi_1) & \frac{\sqrt{6}}{6} \cos \phi_1 - \frac{\sqrt{2}}{2} \sin \phi_1 & \frac{\sqrt{3}}{3} \\ \frac{\sqrt{6}}{3} \sin \phi_1 & -\frac{\sqrt{6}}{3} \cos \phi_1 & \frac{\sqrt{3}}{3} \end{pmatrix}. \quad (2.18)$$

The components of strain tensor in laboratory coordinates can be obtained as follows: The stress tensor (2.17) is transformed into the crystal coordinate frame by the transformation matrix T . Transformed components of the stress tensor are put into the equation (2.12) and the corresponding strain tensor components are derived. The inverse transformation is then applied on the strain tensor to obtain its form in laboratory coordinates. Components of such strain tensor, Young's modulus and Poisson ratio are:

2. FINITE ELEMENT SIMULATIONS OF ELASTIC PROPERTIES OF COPPER THIN FILMS

$$\varepsilon_{11} = \sigma \left(\frac{1}{2} S_{11} + \frac{1}{2} S_{12} + \frac{1}{4} S_{44} \right), \quad (2.19)$$

$$\varepsilon_{22} = \sigma \left(\frac{1}{6} S_{11} + \frac{5}{6} S_{12} - \frac{1}{12} S_{44} \right), \quad (2.20)$$

$$\varepsilon_{33} = \sigma \left(\frac{1}{3} S_{11} + \frac{2}{3} S_{12} - \frac{1}{6} S_{44} \right), \quad (2.21)$$

$$\varepsilon_{12} = 0, \quad (2.22)$$

$$\varepsilon_{23} = \sigma \frac{\sqrt{2} \cos(3\phi_1)}{6} (S_{11} - S_{12} - \frac{1}{2} S_{44}), \quad (2.23)$$

$$\varepsilon_{13} = -\sigma \frac{\sqrt{2} \sin(3\phi_1)}{6} (S_{11} - S_{12} - \frac{1}{2} S_{44}), \quad (2.24)$$

$$E_{111} = \frac{\sigma}{\varepsilon_{11}} = \frac{4}{2S_{11} + 2S_{12} + S_{44}}, \quad (2.25)$$

$$\nu_{2-111} = -\frac{\varepsilon_{22}}{\varepsilon_{11}} = -\frac{2S_{11} + 10S_{12} - S_{44}}{3(2S_{11} + 2S_{12} + S_{44})}, \quad (2.26)$$

$$\nu_{3-111} = -\frac{\varepsilon_{33}}{\varepsilon_{11}} = -\frac{2(2S_{11} + 4S_{12} - S_{44})}{3(2S_{11} + 2S_{12} + S_{44})}. \quad (2.27)$$

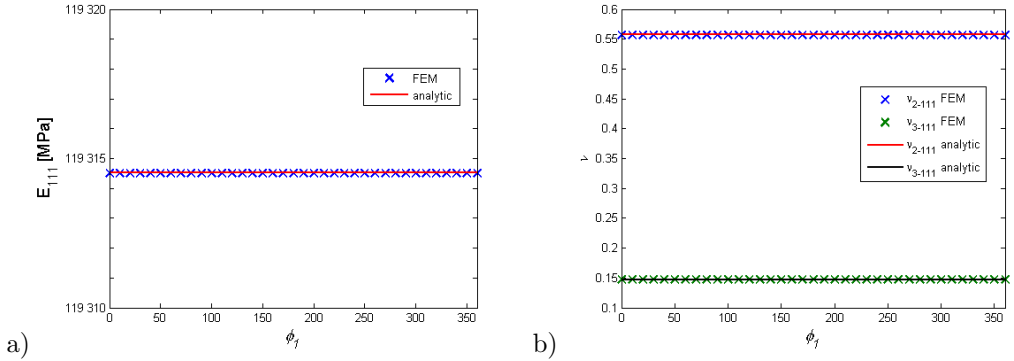


Figure 2.6: Comparison of the results of analytical and finite element computations for the orientation {111}: a) Young's modulus b) Poisson ratios ν_{2-111} , ν_{3-111} .

The diagonal part of the strain tensor is independent of the angle ϕ_1 , therefore, this strain is isotropic. The Young's modulus and the Poisson ratio is also independent of the angle ϕ_1 . This is shown in figure 2.6 with comparison of analytical computations and finite

2.3. TENSILE TEST FOR A SINGLE CRYSTAL

element computations. But there are off diagonal shear components ε_{23} and ε_{31} which depend on the orientation ϕ_1 . This means that during pure tension of $\{111\}$ oriented single crystal, shear strain develops and depends on the orientation of the crystal according to direction of the tension. This is due to the fact that $\{111\}$ planes are not symmetry planes of the crystal. This leads to the development of the stress/strain concentrations in the polycrystalline aggregates as it will be shown later.

2.3.2 Orientation $\{001\}$

Corresponding Euler angles for this orientation are: $\Phi = 0^\circ, \phi_2 = 0^\circ$. The angle ϕ_1 describes the angle between the x' axis of the crystal coordinates and x axis of laboratory ones (tensile direction). The transformation matrix is for this case:

$$T = \begin{pmatrix} \cos \phi_1 & \sin \phi_1 & 0 \\ -\sin \phi_1 & \cos \phi_1 & 0 \\ 0 & 0 & 1 \end{pmatrix}. \quad (2.28)$$

The same procedure of the transformation of the stress and strain tensor into the corresponding coordinates is applied and the final form of the relations for the strain components, Young's modulus and Poisson ratio in the laboratory coordinate system can be expressed as:

$$\varepsilon_{11} = \sigma \left[S_{11} + \frac{\sin^2(2\phi_1)}{4} (2S_{12} - 2S_{11} + S_{44}) \right], \quad (2.29)$$

$$\varepsilon_{22} = \sigma \left[S_{12} + \frac{\sin^2(2\phi_1)}{4} (2S_{11} - 2S_{12} - S_{44}) \right], \quad (2.30)$$

$$\varepsilon_{33} = \sigma S_{12}, \quad (2.31)$$

$$\varepsilon_{12} = \frac{\sigma}{4} (S_{11} - S_{12} - \frac{1}{2} S_{44}) \sin(4\phi_1), \quad (2.32)$$

$$\varepsilon_{23} = \varepsilon_{31} = 0, \quad (2.33)$$

$$E_{001} = \frac{\sigma}{\varepsilon_{11}} = \frac{4}{4S_{11} + \sin^2(2\phi_1)(2S_{12} - 2S_{11} + S_{44})} \quad (2.34)$$

2. FINITE ELEMENT SIMULATIONS OF ELASTIC PROPERTIES OF COPPER THIN FILMS

$$\nu_{2-001} = -\frac{\varepsilon_{22}}{\varepsilon_{11}} = -\frac{4S_{12} + \sin^2(2\phi_1)(2S_{11} - 2S_{12} - S_{44})}{4S_{11} + \sin^2(2\phi_1)(2S_{12} - 2S_{11} + S_{44})}, \quad (2.35)$$

$$\nu_{3-001} = -\frac{\varepsilon_{33}}{\varepsilon_{11}} = -\frac{4S_{12}}{4S_{11} + \sin^2(2\phi_1)(2S_{12} - 2S_{11} + S_{44})}. \quad (2.36)$$

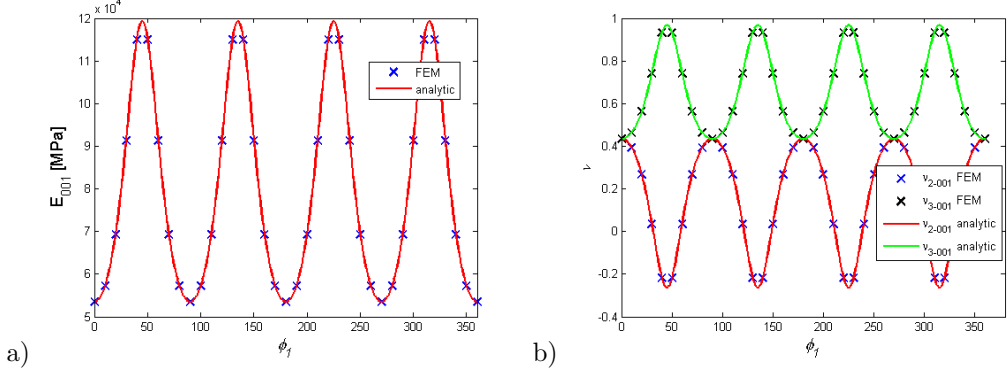


Figure 2.7: Comparison of the results of analytical and finite element computations for the orientation {001}: a) Young's modulus b) Poisson ratios ν_{2-001} , ν_{3-001} .

In this case the diagonal components depend on the orientation of the crystal and only the in-plane shear component is presented. The Young's modulus and Poisson ratio also depend on the crystal orientation ϕ_1 . This is shown in figure 2.7 with comparison of analytical computations and finite element computations. Comparison of the expressions for Young's modulus in equations 2.25 and 2.32 shows that this modulus is higher for the orientation {111}, because for this orientation, the S_{11} is multiplied only by factor of 2. Therefore orientation {111} is stiffer than orientation {001}.

2.4 Tensile test of polycrystalline films

The elastic computations of the tensile test of the polycrystalline aggregates are shown in the following section. The results of these simulations are post-processed to investigate the stress and strain heterogeneities which develop in the grains during the loading. The analysis is realized at several scales. First the mean values of the stresses and the strains for each grain are computed and the dispersion is evaluated according to the crystallographic

orientation of the grains and also to the type of boundary conditions which are applied. The second scale is the dispersion of the stresses inside the grains and dependence of this stress on the position inside the grain.

2.4.1 Texture {001}: mean value per grain

The components of the strain tensor depend on the orientation of the grain with respect to the tensile direction. The stress values are directly related to the strain values through the elastic constants. The highest stresses occur at the points with the largest strain heterogeneities. The highest strain and stress heterogeneities occurs at the grain boundaries. Figure 2.8 shows the distribution of the von Mises stress at the free surface in the aggregates with substrate and the free-standing aggregate. The stress concentration at the grain boundaries is clearly visible. This figure also shows that the distribution of the stresses is quasi-homogeneous through the thickness of the film and the film remains almost plane during the loading. This is because the {001} planes are symmetry planes of the crystal. The deviations from the flat shape of the free surface are caused by the dependence of the Poisson ratio on the crystal orientation ϕ_1 . The grains with different orientations tend to contract differently. The dispersion of the stresses and strains in aggregate is evaluated by the mean von Mises stress and the mean equivalent strain for each grain. The results for the free-standing films and the films with the substrate for 20 realizations are shown in figure 2.9(a)(b). Each point in these plots corresponds to one grain. Value for each grain is normalized by the mean value for whole aggregate. The influence of the substrate on the dispersion of the stresses and the strains is shown on the figure 2.9(a)(b). The relative dispersion ranges between 0.5 – 1.5 for the free-standing films and 0.5 – 2.0 for the films on a substrate. This increase in the dispersion is caused by the influence of the substrate. The boundary conditions force the bottom surface remains flat, but the grains tend to contract in the z direction with respect to the given Poisson ratio $\nu(\phi_1)$. Such a constraint then causes the different increase of strain in grains with different orientations. These differences in strain cause the increasing of dispersion in strain values.

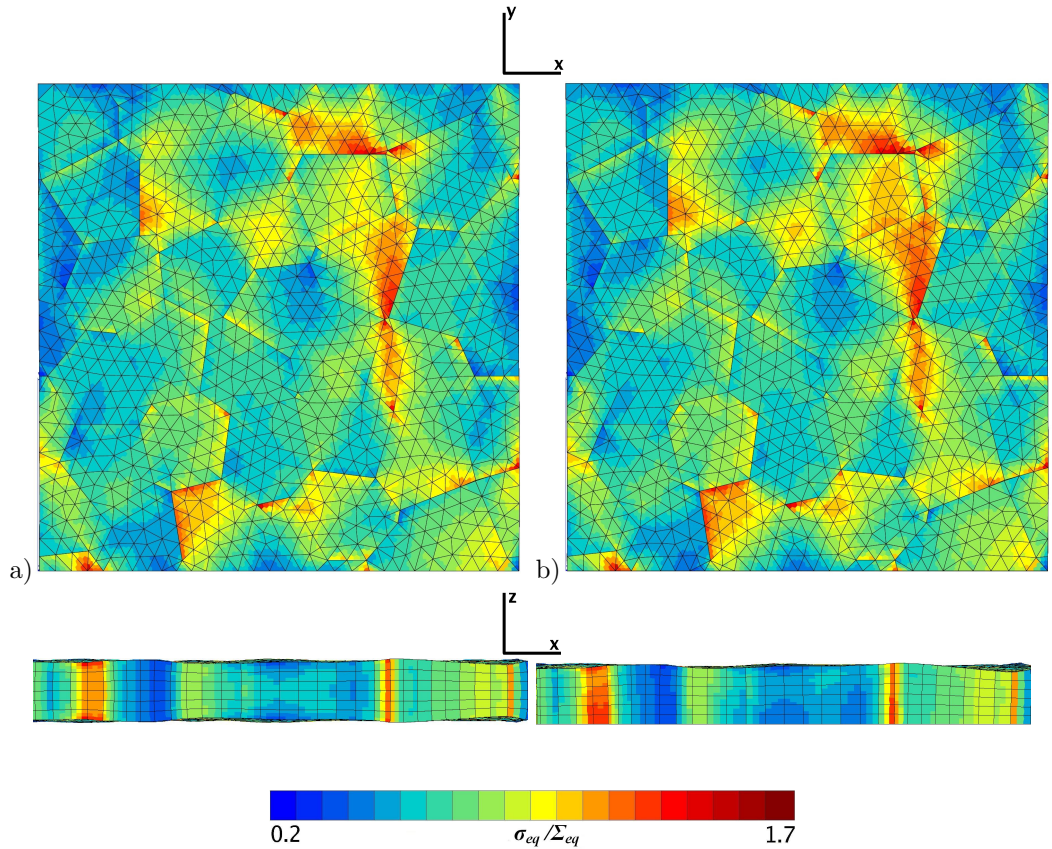


Figure 2.8: Distribution of the von Mises stress at the free surface in the $\{001\}$ oriented grains a) free-standing, b) with substrate.

2.4.2 Texture $\{111\}$: mean values per grain

The diagonal part of the strain tensor is independent of the rotation of the crystal, therefore, the in-plane Young's modulus is isotropic. But the shear components which are presented and which depend on the crystal in-plane orientation cause heterogeneities of stresses and strains. These heterogeneities occur at grain boundaries with maximal differences in shear strain. Presence of this shear causes the stress/strain heterogeneities in the $\{111\}$ oriented films. This is shown in figures 2.10 and 2.11. Figure 2.10(a) shows the aggregate with the

2.4. TENSILE TEST OF POLYCRYSTALLINE FILMS

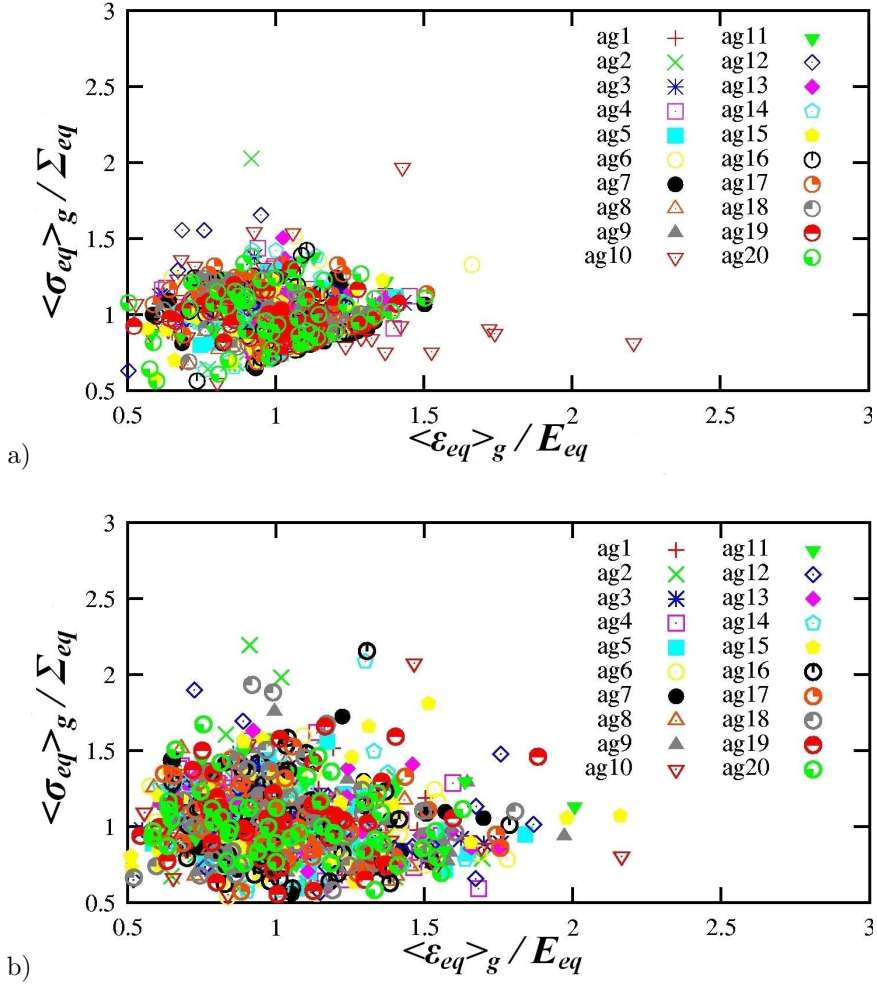


Figure 2.9: Dispersion of the mean von Mises stress per grain and the equivalent strain in the aggregates with {001} oriented grains a) free-standing, b) with substrate.

given grain orientations. Numbers represent the angle ϕ_1 . Figures (b) and (c) then show the distribution of shear strain components ϵ_{23} and ϵ_{31} inside the grains at the free surface. Figures 2.11(a)(b) show the distribution of the von Mises stress at the free surface in the same aggregate for the free-standing conditions and the conditions with substrate. Com-

parison of these figures shows definite correspondence between such stress concentrations and differences of the shear strain components. The stress concentrations are localized in the narrow regions around some grain boundaries and the rest of the grains behave more homogeneously. The planes $\{111\}$ are not symmetry planes of the crystal, therefore, the film have tendency to curve during the loading. The effect of the substrate is much more significant in this case (see fig.2.11). The stress concentrations are much higher for the film on a substrate. Contrary to the $\{001\}$ case the stresses are not constant through the thickness of the film. This is clearly shown in figure 2.12. This figure shows the differences in the von Mises stress distribution at the upper and bottom free surfaces for the free-standing films. The mean value of von Mises stress and equivalent strain are computed for each grain and normalized by the average value for whole aggregate. Dispersion of von Mises stress and equivalent strain is presented in figure 2.13. The influence of the substrate is clearly visible from the comparison of case a) with substrate and b) free-standing. The dispersion in stresses increases approximately by a factor of two. There is a significant difference in the dispersion between the cases $\{001\}$ and $\{111\}$.

2.4.3 Heterogeneities inside the grains

The second level of the heterogeneities is the dispersion of the stresses and the strains inside the grains. The value of the von Mises stress is computed at each integration point and the dependence of this value according to its position is evaluated. Values of von Mises stresses are normalized by the global mean stress in tensile direction. Figure 2.14 shows the dependence of these values on the distance to the geometric centre of the grain. This distance is normalized by the half of the mean grain size. This figure shows the fact that the dispersion of the stresses increases tremendously towards the grain boundaries. Several features can be distinguished from the comparison of the contours of the resulting plots. The dispersion of the stresses in $\{001\}$ grains increases continuously from the center to the grain boundaries while for the $\{111\}$ films there is a significant increase at the value of 1.2 of the average distance to the grain center. This shows the concentration of the stress heterogeneities at the grain boundaries in the $\{111\}$ films as in previous section. Ranges of

2.4. TENSILE TEST OF POLYCRYSTALLINE FILMS

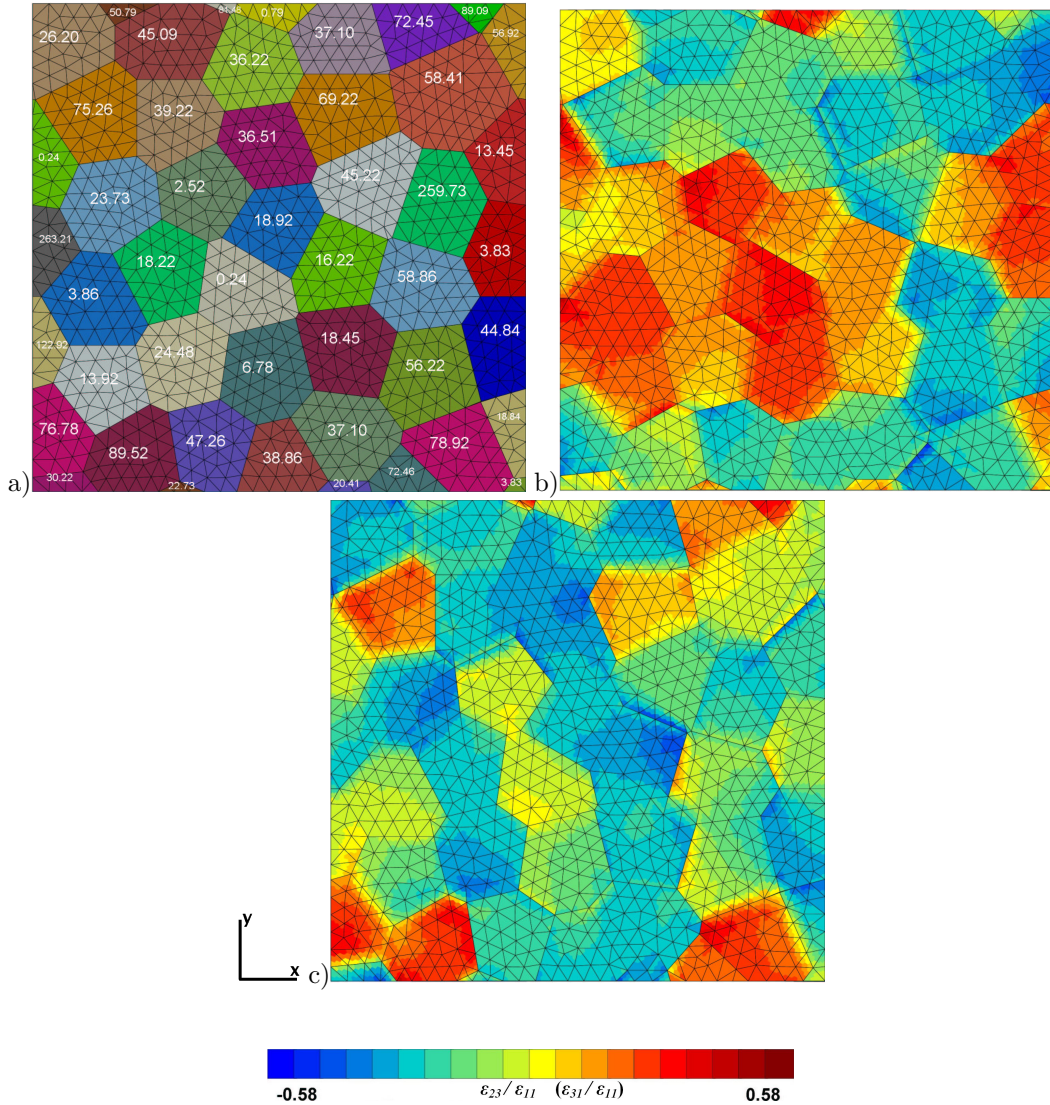


Figure 2.10: Distribution of the shear strain at the free surface in the $\{111\}$ oriented grains a) angle ϕ_1 of orientation of grains, b) ϵ_{23} c) ϵ_{31} components.

the relative values in the $\{001\}$ films are between 0.8 – 1.5 for free-standing and 0.8 – 1.6 for the films on the substrate. This small differences are caused by the smaller influence of the substrate. This is a consequence of the tendency of the film to remain almost flat.

2. FINITE ELEMENT SIMULATIONS OF ELASTIC PROPERTIES OF COPPER THIN FILMS

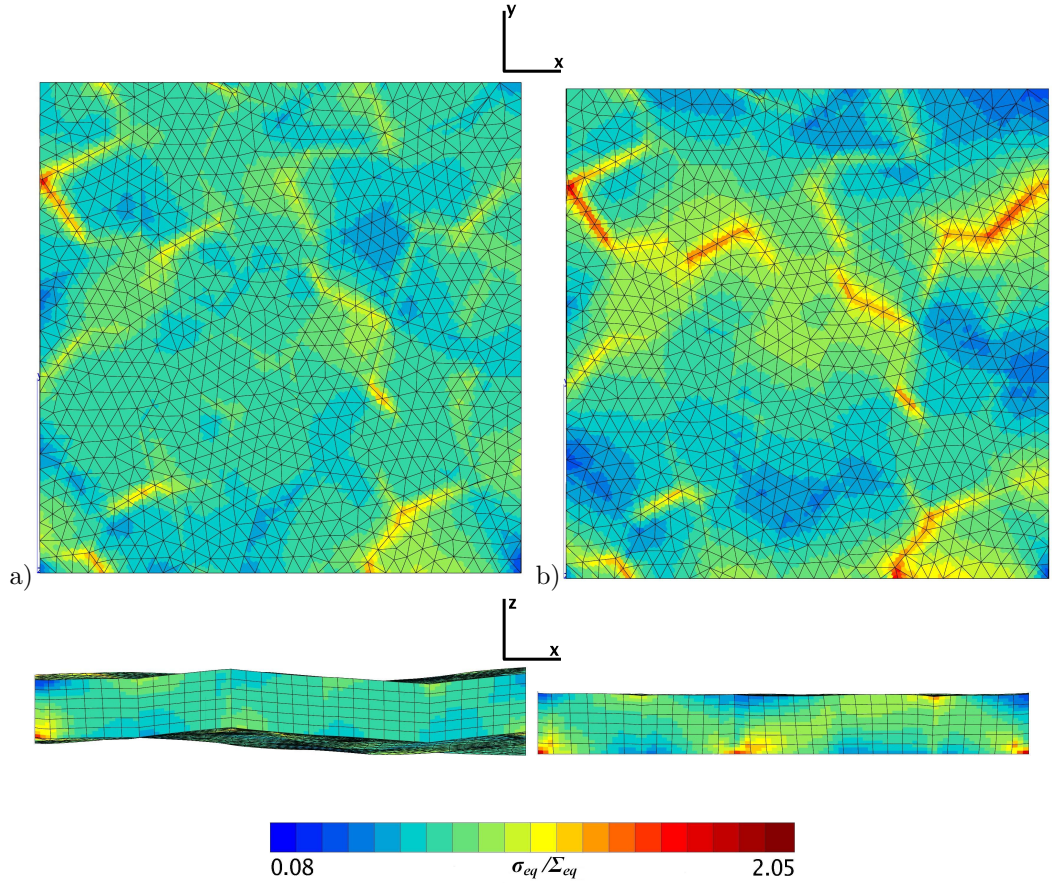


Figure 2.11: Distribution of the von Mises stress at the free surface in the $\{111\}$ oriented grains a) free-standing, b) with substrate.

Higher stress values are in the films with $\{111\}$ oriented grains. Ranges are 0.55 – 1.6 for free-standing and 0.4 – 1.6 for substrate. Absolute values of stresses are higher which is caused by the higher stiffness of the $\{111\}$ orientation. The influence of the substrate is more visible from the wider range of the relative values of the stresses and also from the shift of the points towards higher values in the presence of a substrate. Relative values in the center of grains increase from 1.0 to almost 1.2 which is induced by the constraining due to the presence of a substrate.

2.4. TENSILE TEST OF POLYCRYSTALLINE FILMS

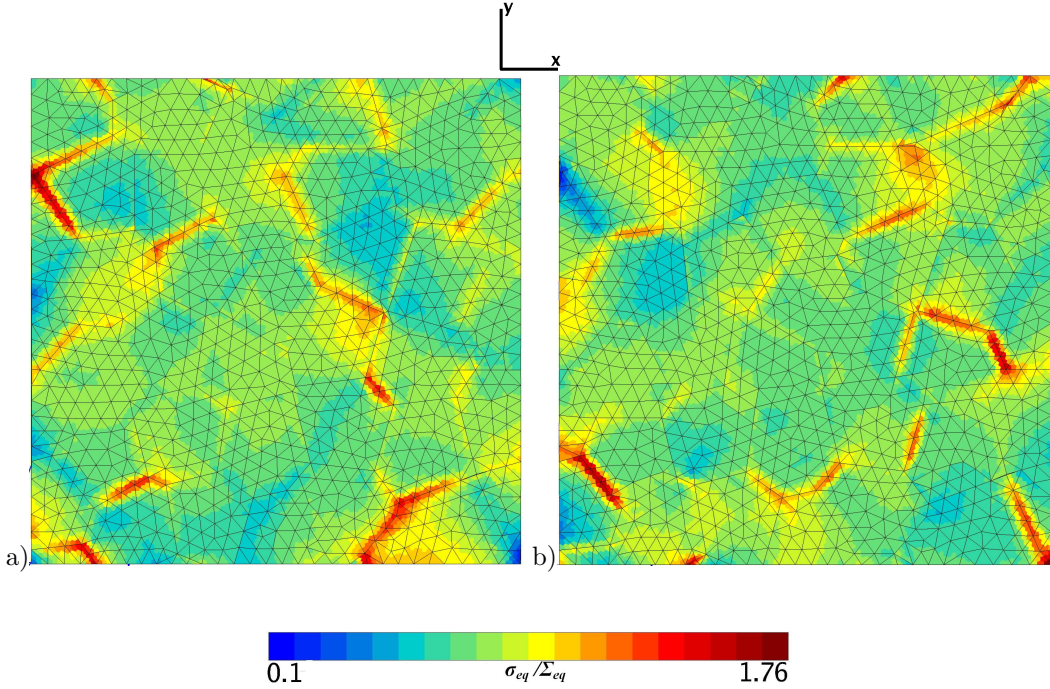


Figure 2.12: Comparison of the von Mises stress distribution at the upper free surface a) and bottom free surface b) for the free-standing film with $\{111\}$ oriented grains.

Similar comparison is shown in figure 2.15. These figures show the values of the von Mises stress at the integration points with respect to the distance from the closest grain boundary. Comparison is done for six different grains. The main features of the films with the $\{001\}$ and $\{111\}$ oriented grains are also clearly recognizable. The values in each of the $\{001\}$ oriented grains are very different. This fact corresponds to the stronger heterogeneities in such films. The values also indicate continuous increase in the dispersion towards the grain boundary. Most of the points for the $\{111\}$ oriented grains are placed in the interval $0.6 - 1.4$ for the free-standing films and $0.7 - 1.3$ for the films with substrate. This is the manifestation of the isotropic behaviour and more homogeneous deformation of these films. The influence of the substrate can be recognized from the increasing of the dispersion and shifting of the average to the higher values. The narrower zones of the stress

2. FINITE ELEMENT SIMULATIONS OF ELASTIC PROPERTIES OF COPPER THIN FILMS

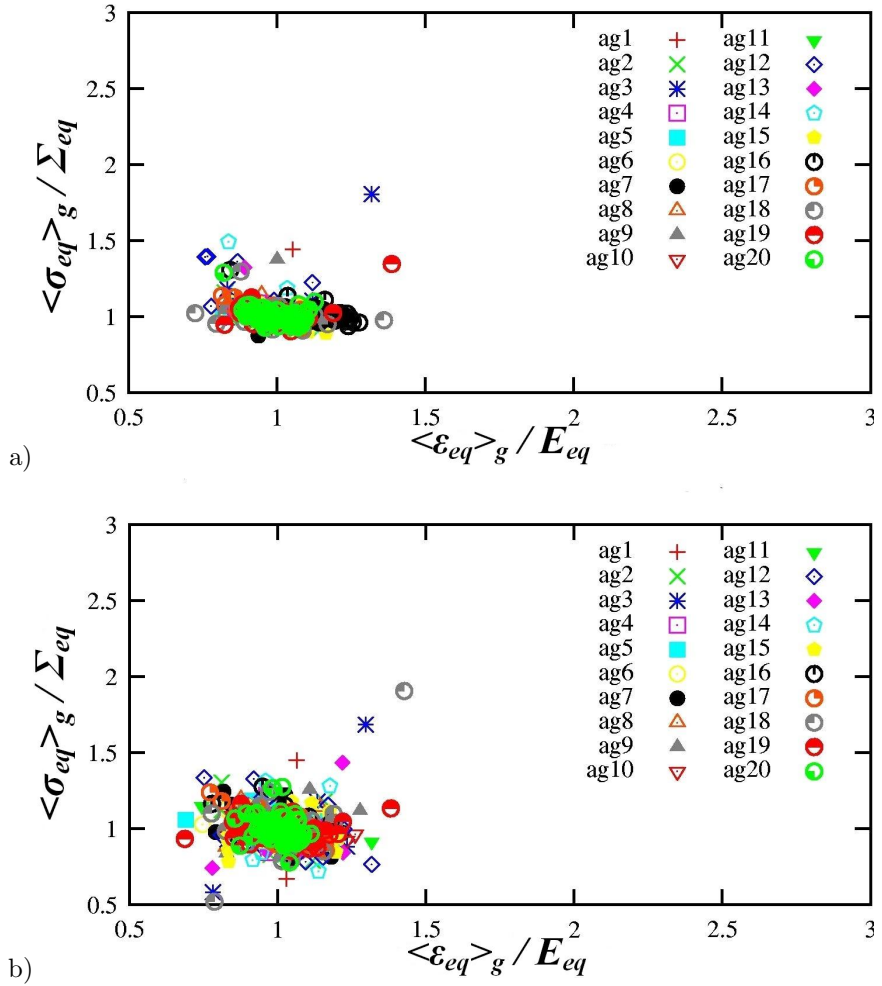


Figure 2.13: Dispersion of the von Mises stress and the equivalent strain in the aggregates with {111} oriented grains a) free-standing, b) with substrate.

concentrations in these films are visible in the black and yellow grains. The values of the stress increase very close to the grain boundary while towards the center of the grain remain the values within the range of the values of other grains.

2.5. CONCLUSIONS

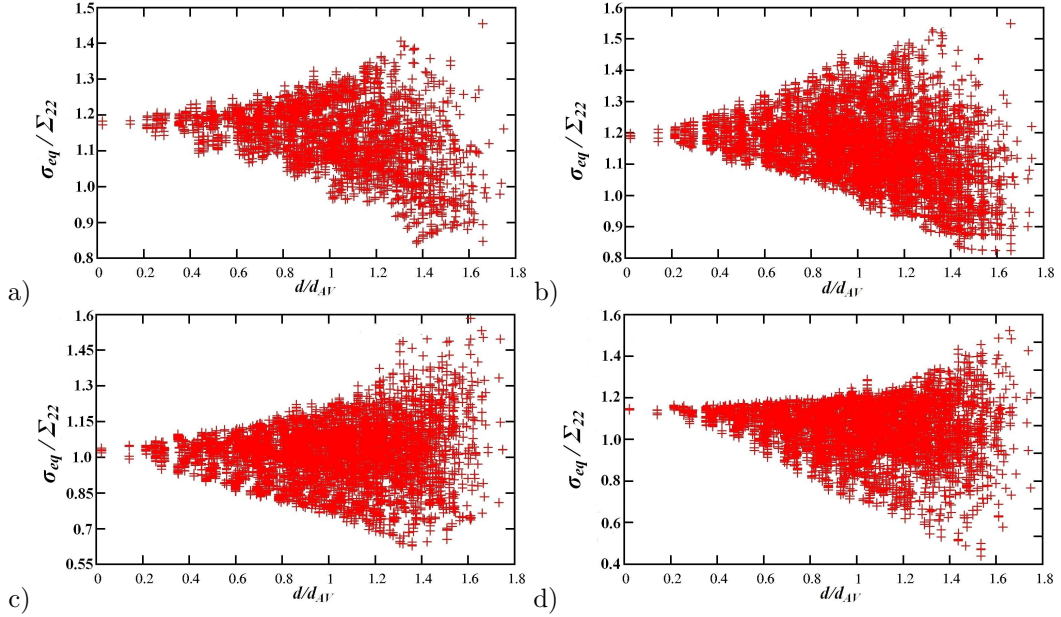


Figure 2.14: Distribution of the von Mises stress related to the distance from the center of grain for a) free-standing $\{001\}$, b) with substrate $\{001\}$, c) free-standing $\{111\}$, d) with substrate $\{111\}$.

2.5 Conclusions

The elastic behaviour of the single crystal and the polycrystalline aggregate with the texture $\{001\}$ and $\{111\}$ was simulated and investigated. The analytical solution for the tensile test of the single crystal was described and the strain/stress heterogeneities were compared. Parameters of the finite element simulations were determined. The main results are:

- A mesh density with 2169 degrees of freedom per grain is sufficient.
- The statistical approach in the determination of RVE provides valid and sufficiently accurate results for 20 different realizations of aggregates with 50 grains.
- The in-plane Young's modulus for the orientation $\{001\}$ depends on the in-plane grain orientation while the in-plane Young's modulus is isotropic for orientation $\{111\}$.

2. FINITE ELEMENT SIMULATIONS OF ELASTIC PROPERTIES OF COPPER THIN FILMS

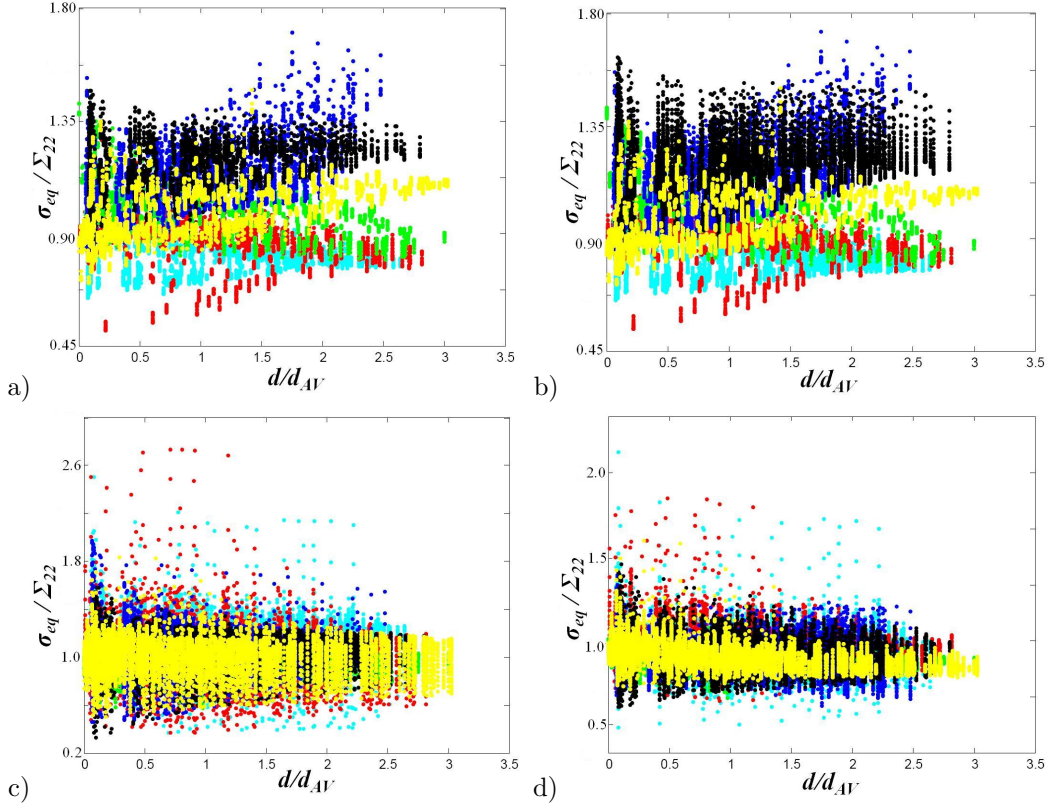


Figure 2.15: Distribution of the von Mises stress related to the distance from the grain boundary for 6 grains in a) free-standing $\{001\}$, b) with substrate $\{001\}$, c) free-standing $\{111\}$, d) with substrate $\{111\}$.

- Deformation is heterogeneous in $\{111\}$ films although $\{111\}$ planes are isotropy planes for Young's modulus.
- The stress and the strain are more heterogeneous in the $\{001\}$ films than in the $\{111\}$ films.
- The stress concentrations are closer to the grain boundaries in the $\{111\}$ films.
- The substrate induces larger dispersions of stress and strain. This effect is more significant in the $\{111\}$ films.

2.5. CONCLUSIONS

Some of these results were published in (Šiška et al. [2007a]).

Chapter 3

Finite element simulations of the plasticity of copper thin films

3.1 Crystal plasticity theory

The elasto–plastic computations are based on the theory of continuum crystal plasticity. The presented theory is based on Mandel and Asaro approaches which use the multiplicative decomposition of deformation gradient into elastic and plastic parts (Mandel [1973], Teodosiu and Sidoroff [1976a], Asaro [1983b], Méric et al. [1991], Cailletaud [1992], Barbe et al. [2001a]). This decomposition can be expressed by the equation:

$$\underline{\mathbf{F}} = \underline{\mathbf{F}}^e \cdot \underline{\mathbf{F}}^p. \quad (3.1)$$

The graphical representation of such a kinematic decomposition is shown in figure 3.1. The change of deformation state is divided into two parts so that there is an intermediate state during deformation at each material point. The intermediate state consists only of the plastic deformation of the crystal lattice. The elastic deformation of the crystal lattice is added during the second step to restore compatibility of the total deformation gradient. The intermediate configuration is such that the lattice orientation is the same as the initial one. Plastic deformation is a consequence of glide processes in N crystal slip systems. These

slip systems are characterized by the normal to the slip plane $\underline{\mathbf{n}}$ and slip direction $\underline{\mathbf{m}}$. The plastic flow is described by the equation:

$$\underline{\dot{\mathbf{F}}}^p \cdot \underline{\mathbf{F}}^{p-1} = \sum_{s=1}^N \dot{\gamma}^s \underline{\mathbf{P}}^s, \quad (3.2)$$

$$\underline{\mathbf{P}}^s = \underline{\mathbf{m}}^s \otimes \underline{\mathbf{n}}^s, \quad (3.3)$$

where γ^s is the amount of slip for each slip system. This slip evolution can be described by the equation:

$$\dot{\gamma}^s = \left\langle \frac{|\tau^s - x^s| - r^s}{k} \right\rangle^n \text{sign}(\tau^s - x^s), \quad (3.4)$$

where τ^s is the resolved shear stress which acts on the given slip plane and slip direction and it is given by:

$$\tau^s = \underline{\mathbf{P}}^s : \underline{\boldsymbol{\sigma}}^s. \quad (3.5)$$

Coefficients k and n come from Norton law according to which the plastic slip is derived. These coefficients describe the amount of viscoplasticity. Parameters r^s and x^s are associated with isotropic and kinematic hardening respectively. These hardening laws are given by the following equations:

$$r^s = r_0 + q \sum_{r=1}^n h^{sr} (1 - \exp(-bv^r)), \quad \dot{v}^s = |\dot{\gamma}^s|, \quad (3.6)$$

$$x^s = c\alpha^s, \quad \dot{\alpha}^s = \dot{\gamma}^s - d\dot{v}^s\alpha^s, \quad (3.7)$$

where r_0 is the initial yield stress and h^{sr} is an interaction matrix. The equations for kinematic hardening contain a dynamic recovery term. The interaction matrix describes the self and latent hardening which is caused by the interactions between the different slip systems. It depends on six coefficients which describe the interactions between the different slip systems. The matrix form is shown in the table 3.1. The matrix is symmetric, therefore, only one half is shown. The coefficient $h1$ describes the self hardening of the given slip systems. The coefficient $h2$ describes the hardening caused by the interaction with slip systems in the same slip plane. The coefficients $h3$, $h4$, $h5$ and $h6$ describe the interaction with the other slip directions in different slip planes.

3.1. CRYSTAL PLASTICITY THEORY

	Bd	Ba	Bc	Db	Dc	Da	Ab	Ad	Ac	Cb	Ca	Cd	slip syst.
Bd	h1	h2	h2	h4	h5	h5	h5	h6	h3	h5	h3	h6	Bd (111)[$\bar{1}01$]
Ba		h1	h2	h5	h3	h6	h4	h5	h5	h5	h6	h3	Ba (111)[$0\bar{1}1$]
Bc			h1	h5	h6	h3	h5	h3	h6	h4	h5	h5	Bc (111)[$\bar{1}10$]
Db				h1	h2	h2	h6	h5	h3	h6	h3	h5	Db ($\bar{1}\bar{1}1$)[$\bar{1}01$]
Dc					h1	h2	h3	h5	h6	h5	h5	h4	Dc ($\bar{1}\bar{1}1$)[011]
Da						h1	h5	h4	h5	h3	h6	h5	Da ($\bar{1}\bar{1}1$)[110]
Ab							h1	h2	h2	h6	h5	h3	Ab ($\bar{1}\bar{1}1$)[$0\bar{1}1$]
Ad								h1	h2	h3	h5	h6	Ad ($\bar{1}\bar{1}1$)[110]
Ac									h1	h5	h4	h5	Ac ($\bar{1}\bar{1}1$)[101]
Cb										h1	h2	h2	Cb ($11\bar{1}$)[$\bar{1}01$]
Ca											h1	h2	Ca ($11\bar{1}$)[101]
Cd												h1	Cd ($11\bar{1}$)[011]

Table 3.1: Interaction matrix h^{sr} . Due to the symmetry only one half of the matrix is shown.

3.1.1 Setting of parameters

The values of the parameters of this model have to be determined. Two sets of parameters have been identified according to the experimental data: one set for the tensile loading and one set for the cyclic loading. Elastic behaviour is described by cubic elasticity. The independent components of the stiffness matrix are C_{11} , C_{12} and C_{44} . Values are summarized in table 3.2.

The parameters for the tensile loading have been set by fitting the experimental curves of the tensile tests of copper single crystals with different crystal orientations (Kawasaki and Takeuchi [1980]). Because these parameters are used only for tensile loading, the kinematic hardening is not included. The computed curves are up to 20 % strain, which is enough, because the total macroscopic deformation of the film does not exceed 2 % in this work. The parameters k and n were chosen to minimize the rate dependence of the behaviour. Graphical comparison of the experimental curves and simulated ones is in figure 3.2(a). This set of parameters is called Copper I. The second set of parameters is used for the simulation of the cyclic loading. Values have been taken from the work of Méric and Cailletaud (Méric et al. [1994]). They studied the simulations of the cyclic loading of a copper bicrystal and the setting of the parameters according to the experimental results were provided in this

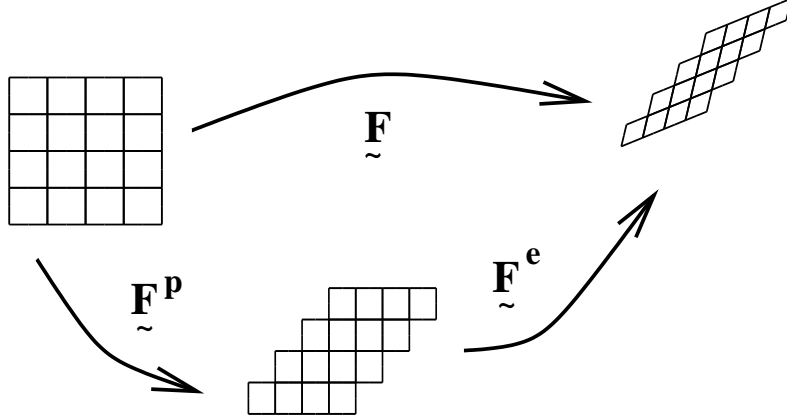


Figure 3.1: Decomposition of the deformation into elastic and plastic part.

work. Graphical results are shown in figure 3.2(b). This parameters set is called Copper II.

This model does not contain any length scale parameter. The influence of the small scale is included by the value of yield stress which is derived from the Hall – Petch relation. The Hall – Petch relation gives the relation between the yield stress and grain size by the following equation:

$$\sigma = \sigma_0 + kd^{-1/2}. \quad (3.8)$$

The experiments show that this Hall – Petch relation is valid for copper with grain size down to $1 \mu\text{m}$ with the value of parameter $k = 0.10 \pm 0.06 \text{ MPam}^{1/2}$ (Kozlov et al. [2004]). The parameter σ_0 is the yield stress for bulk copper and its value is equal 0.817 MPa (Méric et al. [1994]) The comparison of the experiments shows also that the Hall – Petch relation for the bulk copper structures is valid also for thin film copper structures (Spaepen and Yu [2004]). If the effect of the mutual interactions of the grains in the aggregate is taken into account, the final used value of yield stress is according to Taylor model equal to 35 MPa . This value corresponds to the grain size of $1 \mu\text{m}$ and it is used for all grains in aggregates. This means that the differences in sizes of individual grain are not taken into account.

3.1. CRYSTAL PLASTICITY THEORY

Elasticity		
C_{11}	C_{12}	C_{44}
159300 MPa	122000 MPa	81000 MPa
Plasticity		
Par.	Copper I	Copper II
k [MPa s]	2.0	5.0
n	15.0	10.0
q [MPa]	7.96	6.0
b	3.49	15.0
c [MPa]	-	4500.0
d	-	600.0
h1	1.0	1.0
h2	1.4	4.4
h3	1.4	4.75
h4	1.4	4.75
h5	1.4	4.75
h6	1.4	5.0

Table 3.2: Values of the parameters for the tensile and cyclic loading.

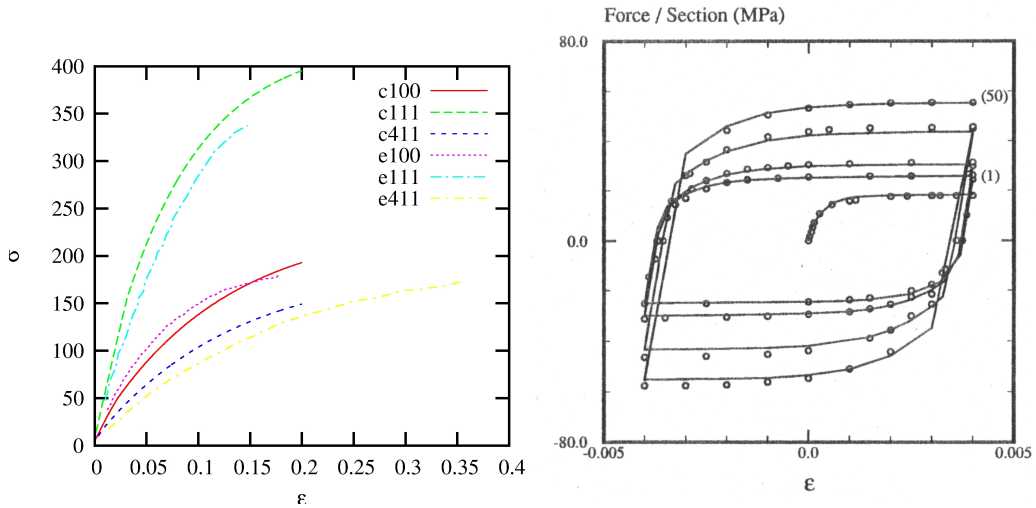


Figure 3.2: Comparison of the experimental and computed results (a) Tensile test e–experimental curves c–computed curves (b) Cyclic loading. (Méric et al. [1994])

3.2 Plastic deformation of single crystal

The studied copper crystal has FCC crystal lattice. The plastic slip occurs in these crystals preferably on twelve octahedral slip systems which belong to $\{111\}$ slip planes family. These slip systems are in this work marked with numbers 1 – 12. The corresponding slip systems are given in table 3.3.

No.	slip plane	slip direction
1	(111)	$[\bar{1}01]$
2	(111)	$[0\bar{1}1]$
3	(111)	$[\bar{1}10]$
4	($\bar{1}\bar{1}1$)	$[\bar{1}01]$
5	($\bar{1}\bar{1}1$)	$[011]$
6	($\bar{1}\bar{1}1$)	$[110]$
7	($\bar{1}1\bar{1}$)	$[0\bar{1}1]$
8	($\bar{1}1\bar{1}$)	$[110]$
9	($\bar{1}1\bar{1}$)	$[101]$
10	($11\bar{1}$)	$[\bar{1}10]$
11	($11\bar{1}$)	$[101]$
12	($11\bar{1}$)	$[011]$

Table 3.3: Overview of the FCC octahedral slip systems.

Each slip system is characterized by its Schmid factor P^s for given type of loading and crystallographic orientation. Increasing value of Schmid factor decreases the value of applied stress necessary for activation of the slip system. A slip system is activated when the critical resolved shear stress value τ^s is reached by applied shear τ^s . The values of Schmid factor and activation of slip systems are described in the following sections.

3.2.1 Tensile loading of the $\{001\}$ oriented single crystal

The normal to the (001) plane of the crystal is oriented in the z direction of the laboratory coordinates. The tension is applied in y direction of the laboratory coordinate system which is contained in the (001) plane – the applied stress is σ_{22} . The angle ϕ_1 describes the angle between direction $[100]$ of the crystal coordinates and the x axis of the laboratory coordinates. The equations for the Schmid factors of given slip systems are:

3.2. PLASTIC DEFORMATION OF SINGLE CRYSTAL

$$P^1 = \frac{\sqrt{3}}{6} \left[\cos\left(2\phi_1 + \frac{\pi}{4}\right) - \frac{\sqrt{2}}{2} \right], \quad (3.9)$$

$$P^2 = -\frac{\sqrt{3}}{6} \left[\cos\left(2\phi_1 - \frac{\pi}{4}\right) + \frac{\sqrt{2}}{2} \right], \quad (3.10)$$

$$P^3 = P^8 = P^{10} = \frac{1}{\sqrt{6}} \cos(2\phi_1), \quad (3.11)$$

$$P^4 = P^9 = \frac{\sqrt{3}}{6} \left[\cos\left(2\phi_1 - \frac{\pi}{4}\right) - \frac{\sqrt{2}}{2} \right], \quad (3.12)$$

$$P^5 = P^7 = -\frac{\sqrt{3}}{6} \left[\cos\left(2\phi_1 + \frac{\pi}{4}\right) + \frac{\sqrt{2}}{2} \right], \quad (3.13)$$

$$P^6 = -\frac{1}{\sqrt{6}} \cos(2\phi_1), \quad (3.14)$$

$$P^{11} = -\frac{\sqrt{3}}{6} \left[\cos\left(2\phi_1 + \frac{\pi}{4}\right) - \frac{\sqrt{2}}{2} \right], \quad (3.15)$$

$$P^{12} = \frac{\sqrt{3}}{6} \left[\cos\left(2\phi_1 - \frac{\pi}{4}\right) + \frac{\sqrt{2}}{2} \right]. \quad (3.16)$$

The graphical representation of these expressions is shown in figure 3.3. The functions which describe Schmid factor values for each slip system have period an equal to 180° . The maximal value of Schmid factor is 0.493. This maximal value occurs for angles $\phi_1=22.5^\circ, 67.5^\circ, 112.5^\circ$ and 157.5° . There are 2 active slip systems for these orientations. The crystal with these orientations has the smallest yield stress values. The second special cases have the maximal value of Schmid factor equal to 0.408. These cases can be further divided into two groups. First one occurs for $\phi_1 = 0^\circ, 90^\circ$ and 180° . These orientations have the smallest Young's modulus and 8 active slips systems while 4 other remains inactive during whole loading. The second case occurs for $\phi_1 = 45^\circ, 135^\circ$. The Young's modulus is the highest for these orientations and there are only 4 active slip systems. The value of the yield stress can be obtained from the equation:

$$\sigma_{min}^s = \frac{r_0}{P_{max}^s}. \quad (3.17)$$

In our case is $r_0 = 35$ MPa so the values of the yield stresses are in range 71 – 86 MPa. Ratio between these values is 1.211.

3. FINITE ELEMENT SIMULATIONS OF THE PLASTICITY OF COPPER THIN FILMS

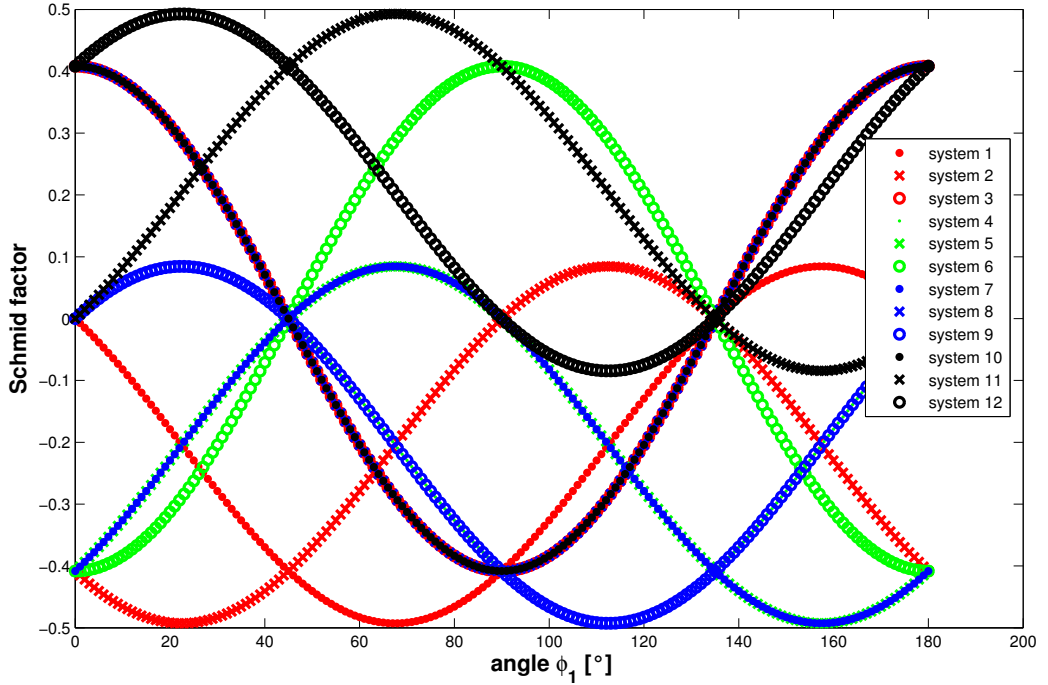


Figure 3.3: The values of the Schmid factors for different slip systems for $\{001\}$ oriented single crystal.

The global stress–strain curves for the monocrystal with the different orientations are shown in figure 3.4(a)(b). Figure (a) contains the curves for the Copper I parameters and figure (b) contains the curves for the Copper II parameters. Three orientations are shown on this figure: one with maximal Schmid factor (22.5°) and two for special cases with Schmid factor value 0.408 (0° , 45°). The direction of the tension is aligned to the crystallographic direction $[010]$ for $\phi = 0^\circ$ and direction $[110]$ for $\phi = 45^\circ$. The values of yield stresses are within the range 73 – 88 MPa. The ratio of these values is 1.205. The slight differences from the theoretical values are caused by the effects of viscoplasticity which take place in FEM computations. The curves clearly show the differences in the Young’s moduli of different orientations. The hardening curves are different for the orientations with Schmid factor value 0.408. This difference is caused by the different number of the active slip

3.2. PLASTIC DEFORMATION OF SINGLE CRYSTAL

systems. The orientations with 8 active slip systems are stiffer because of higher amount of slip system interactions. The curves for the parameters Copper II (b) exhibit the higher hardening rate. This is caused by the higher values of coefficients of the interaction matrix which means the higher amount of slip system interactions.

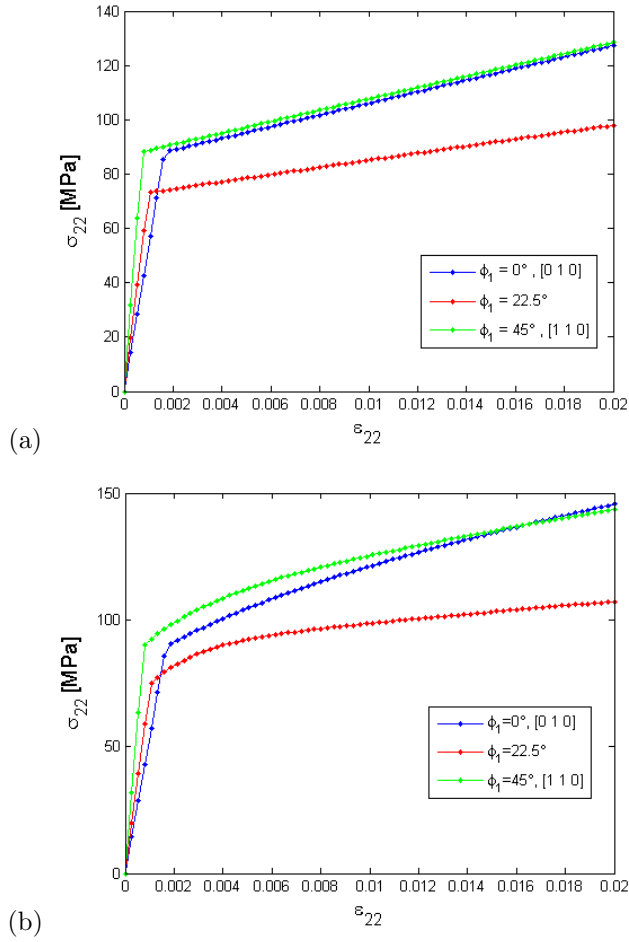


Figure 3.4: Global stress–strain curves for chosen orientations $\{001\}$ with special cases of values of Schmid factor: (a) Copper I, (b) Copper II.

3.2.2 Tensile loading of the $\{111\}$ oriented single crystal

The normal to the (111) plane of the crystal is oriented in the z direction of laboratory coordinates. The tension is applied in y direction of laboratory coordinate system – the applied stress is σ_{22} . The angle ϕ_1 is the angle between axis x and crystallographic direction $[11\bar{2}]$. The equations for the Schmid factors of given slip systems are:

$$P^1 = P^2 = P^3 = 0, \quad (3.18)$$

$$P^4 = -\frac{\sqrt{2}}{3} \sin(2\phi_1 - \frac{\pi}{3}), \quad (3.19)$$

$$P^5 = P^9 = \frac{\sqrt{6}}{9} [\cos(2\phi_1) - \frac{1}{2}], \quad (3.20)$$

$$P^6 = P^{11} = -\frac{\sqrt{6}}{9} [\cos(2\phi_1 + \frac{\pi}{3}) + \frac{1}{2}], \quad (3.21)$$

$$P^7 = -\frac{\sqrt{2}}{3} \sin(2\phi_1 - \frac{2\pi}{3}), \quad (3.22)$$

$$P^8 = P^{12} = -\frac{\sqrt{6}}{9} [\cos(2\phi_1 - \frac{\pi}{3}) + \frac{1}{2}], \quad (3.23)$$

$$P^{10} = -\frac{\sqrt{2}}{3} \sin(2\phi_1). \quad (3.24)$$

The slip systems 1 – 3 are inactive for this orientation. The graphical representation is shown in figure 3.5. The functions of Schmid factors for different slip systems have a period of 180° . Maximal value of the Schmid factor is 0.471. This maximal values occurs for $\phi_1=15^\circ, 45^\circ, 75^\circ, 105^\circ, 135^\circ$ and 165° . Only one slip system is active in these cases. There are also other two special cases with the value of Schmid factor equal to 0.408. This value of Schmid factor occurs with period of 30° . First type occurs for $\phi_1 = 0^\circ, 60^\circ, 120^\circ$ and 180° . There are 2 slip systems active in this case. The second type is found for $\phi_1 = 30^\circ, 90^\circ$ and 150° . In this case 4 slip systems are active. The yield stress levels are within the range 74 – 86 MPa. The ratio of these values is 1.154.

The stress–strain curves for these different cases are shown in figure 3.6. Figure 3.6(a) contains the curves for the Copper I parameters and figure 3.6(b) contains the curves for the Copper II parameters. Orientations $\{111\}$ have isotropic in–plane Young’s modulus so

3.2. PLASTIC DEFORMATION OF SINGLE CRYSTAL

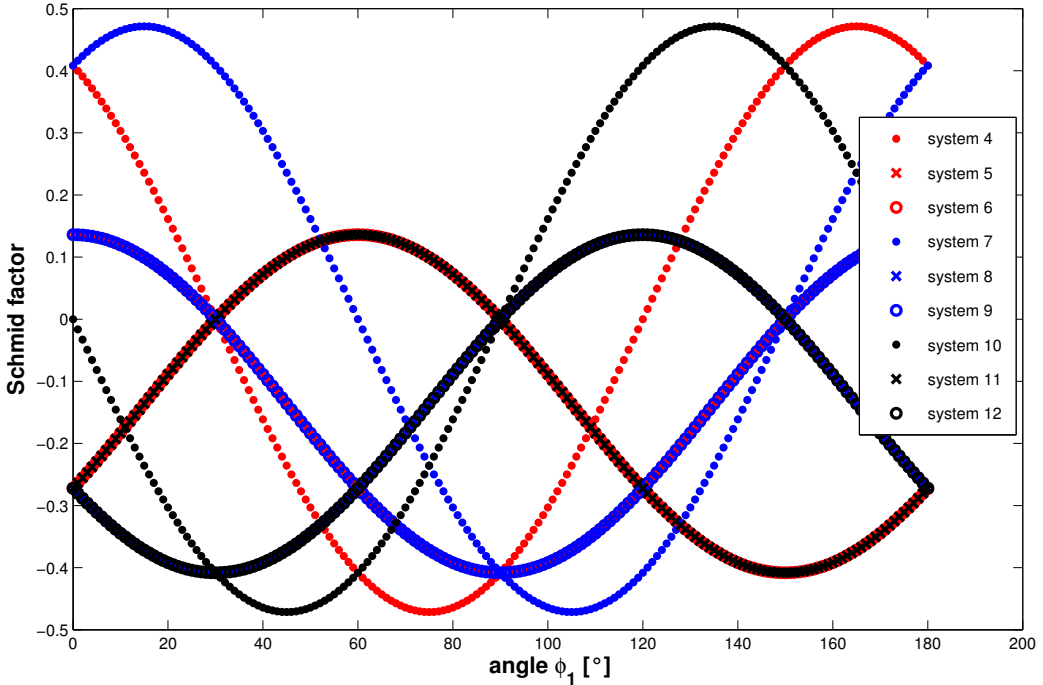


Figure 3.5: The values of the Schmid factors for different slip systems for $\{111\}$ oriented single crystal.

there are no differences in the elastic part between all cases. The cases with maximal value of Schmid factor are represented by the orientations with angle $\phi_1 = 15^\circ$. The special cases with 2 active systems are represented by orientation 0° which corresponds to the tension in the direction $[11\bar{2}]$. The other special cases with 4 active slip systems are represented by the curves for $\phi_1 = 30^\circ, 90^\circ$ which correspond to the tension in the directions $[10\bar{1}]$ and $[\bar{1}10]$ respectively. The yield stress levels are in the interval 77 – 88 MPa. The ratio of these values is 1.143. The differences from the analytical values are again caused by the influence of viscoplasticity. For the case of Copper II set of parameters (b), the hardening curves have larger slope and differences compare to the Copper I set of parameters (a). This is due to the higher interaction between these slip systems because of the higher values of coefficients in the interaction matrix. Two curves corresponding to 4 active slip systems

3. FINITE ELEMENT SIMULATIONS OF THE PLASTICITY OF COPPER THIN FILMS

start to differ at strain about 0.015. This is caused by the activation of the different slip systems in these two different orientations.

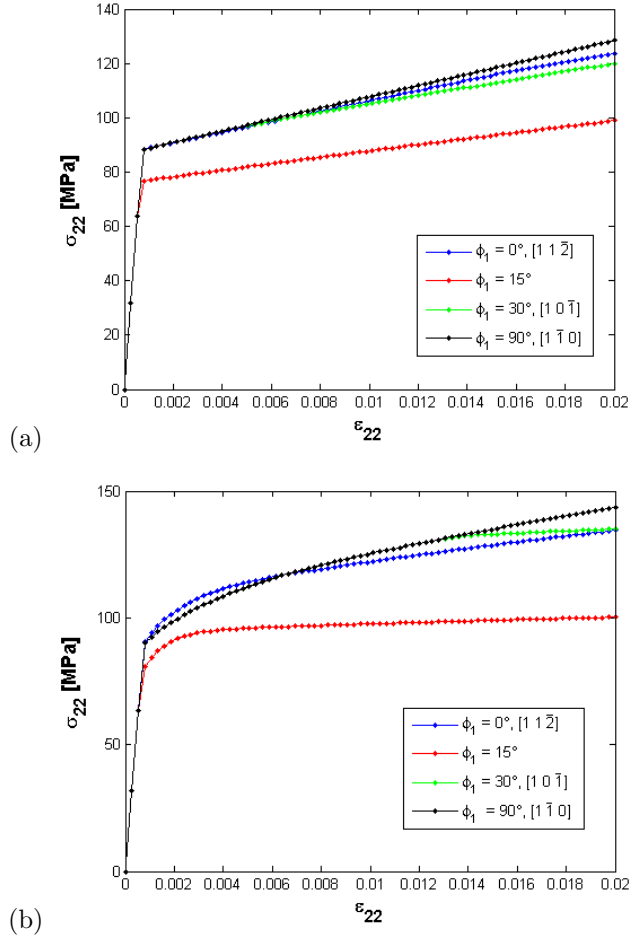


Figure 3.6: Global stress – strain curves for chosen orientations $\{111\}$ with special cases of values of Schmid factor: (a) Copper I, (b) Copper II.

3.2.3 Biaxial loading of the $\{001\}$ oriented single crystal

The biaxial loading corresponds to the application of stresses in the direction x and y . The stress tensor is described by matrix:

3.2. PLASTIC DEFORMATION OF SINGLE CRYSTAL

$$\sigma = \begin{pmatrix} \sigma_{11} & 0 & 0 \\ 0 & \sigma_{22} & 0 \\ 0 & 0 & 0 \end{pmatrix}. \quad (3.25)$$

The plasticity can be described by the yield surface for different combinations of the levels of the σ_{11} and σ_{22} . Figure 3.7 shows the yield surface for the Euler angles $\phi_1, \Phi, \phi_2 = 0^\circ$ which means that direction z coincides with the crystallographic direction $[0\ 0\ 1]$. The stress values are normalized by the yield stress r_0 . The different colours correspond to different slip systems (green (dash-dotted) = slip systems 1, 4, 9; yellow (solid) = slip system 11; red (dashed) = slip system 12; blue (dotted) = slip systems 2, 5, 7).

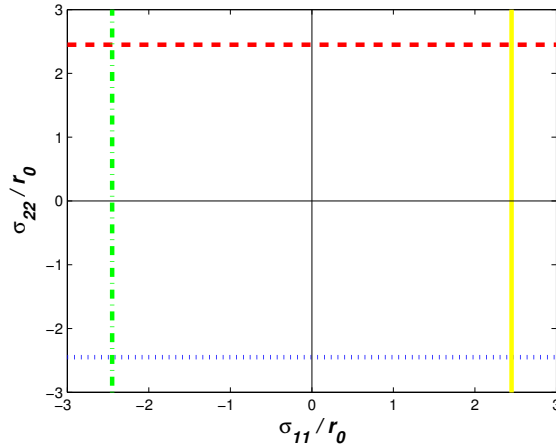


Figure 3.7: Yield surface for $\{001\}$ oriented crystal ($\phi_1, \Phi, \phi_2 = 0^\circ$) under biaxial loading (green (dash-dotted) = slip systems 1, 4, 9; yellow (solid) = slip system 11; red (dashed) = slip system 12; blue (dotted) = slip systems 2, 5, 7).

The special case of the biaxial loading is equibiaxial loading with the same stress levels $\sigma_{11} = \sigma_{22} = \sigma$. The components of the strain tensor can be in this case written by the following equations:

$$\varepsilon_{11} = \sigma(S_{11} + S_{12}), \quad (3.26)$$

$$\varepsilon_{22} = \sigma(S_{11} + S_{12}), \quad (3.27)$$

$$\varepsilon_{33} = 2\sigma S_{12}, \quad (3.28)$$

$$\varepsilon_{12} = \varepsilon_{23} = \varepsilon_{31} = 0. \quad (3.29)$$

These equations show that the strains and the stresses are isotropic and there is no shear strain presented during the loading. The plastic behaviour is also independent of the angle ϕ_1 . The values of Schmid factors for slip systems are:

$$P^1 = P^2 = P^4 = P^5 = P^7 = P^9 = P^{11} = P^{12} = 0.408, \quad (3.30)$$

$$P^3 = P^6 = P^8 = P^{10} = 0. \quad (3.31)$$

There are 8 active slip systems for the orientation $\{001\}$ and the biaxial loading. Such behaviour predicts no stress and strain concentrations for the polycrystalline aggregates.

3.2.4 Biaxial loading of the $\{111\}$ oriented single crystal

Like in the previous case, the yield surface is shown in figure 3.8. The values of Euler angles are $\phi_1 = 0^\circ$, $\Phi = 54.74^\circ$ and $\phi_2 = 45^\circ$ which means that direction z coincides with direction $[111]$ and direction x is aligned with $[\bar{1}10]$ direction. The different colours of lines correspond to different slip systems (blue (solid) = slip systems 5, 9; green (dashed) = slip systems 4, 7; red (dotted) = slip systems 6, 8, 11, 12).

In the case of the equibiaxial loading, the components of the strain are:

$$\varepsilon_{11} = \sigma \left(\frac{2}{3} S_{11} + \frac{4}{3} S_{12} + \frac{5}{12} S_{44} \right), \quad (3.32)$$

$$\varepsilon_{22} = \sigma \left(\frac{2}{3} S_{11} + \frac{4}{3} S_{12} + \frac{5}{12} S_{44} \right), \quad (3.33)$$

$$\varepsilon_{33} = 2\sigma \left(\frac{1}{3} S_{11} + \frac{2}{3} S_{12} - \frac{1}{6} S_{44} \right), \quad (3.34)$$

$$\varepsilon_{12} = \varepsilon_{23} = \varepsilon_{31} = 0. \quad (3.35)$$

The strain tensor components are independent of the angle ϕ_1 . There are no shear strain components during the biaxial loading. The plastic behaviour is also independent of angle

3.3. PLASTIC DEFORMATION OF POLYCRYSTALLINE AGGREGATES

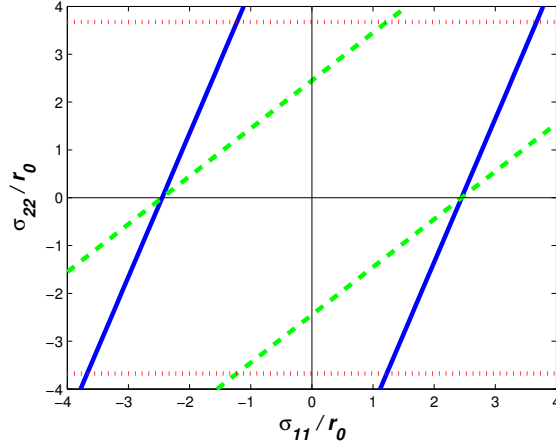


Figure 3.8: Yield surface for $\{111\}$ oriented crystal ($\phi_1 = 0^\circ$, $\Phi = 54.74^\circ$ and $\phi_2 = 45^\circ$) under biaxial loading (blue (solid) = slip systems 5, 9; green (dashed) = slip systems 4, 7; red (dotted) = slip systems 6, 8, 11, 12).

ϕ_1 . The Schmid factors of the slip systems are constants with following values:

$$P^1 = P^2 = P^3 = P^4 = P^7 = P^{10} = 0, \quad (3.36)$$

$$P^5 = P^6 = P^8 = P^9 = P^{11} = P^{12} = 0.272. \quad (3.37)$$

In this case only 6 slips are active and the Schmid factor is lower than for the $\{001\}$ orientation. The $\{111\}$ crystal starts to plastify at higher level of applied stress than the $\{001\}$ oriented crystal.

3.3 Plastic deformation of polycrystalline aggregates

The properties of polycrystalline aggregates are investigated in the spirit of recent experimental work (Hommel and Kraft [2001]). The experiments deal with tensile tests of copper thin films on a polyimide substrate.

3.3.1 Parameters of simulation

The virtual films for the simulations are similar to the real films used in the experiments. The crystallographic texture has the same volume fractions of orientations as in the real films. The $\{111\}$ orientation has a volume fraction of 90 %, $\{001\}$ orientation has a volume fraction of 6 % and the rest 4 % consists of random orientations (Hommel and Kraft [2001]). This is the difference from the films used in the previous chapter which have purely $\{111\}$ or $\{001\}$ textures. The total number of grains in the modelled aggregates is 50 grains. The meshes are created in the same way as was described in the chapter 2.2.1. The substrate was made by further extension of the mesh in the z direction. This is also a difference from the boundary conditions “fixed surface” used in the chapter 2.2.1 where a substrate is simulated only by the boundary conditions ($U_3=0$ at the bottom surface). The thickness of the substrate is 5 times larger than the thickness of the film. The substrate is supposed to have a purely elastic behaviour with elastic constants: Young’s modulus = 2.5 GPa, Poisson ratio = 0.34. The parameters Copper II are taken for the description of the film properties. The interface between the film and the substrate is treated as ideal which means that there is no decohesion nor void creation. Displacement and traction vector are continuous through this interface. Five different realizations of such aggregates were made. One of them is shown in figure 3.9(a).

The whole mesh consists of about 31 100 quadratic prismatic elements and about 85 000 nodes. Because of the size of the mesh, parallel computations were performed. The mesh was divided into 4 domains and each of them was computed by one processor. The division into domains is shown in figure 3.9(b). According to this parallelization the boundary conditions had to be modified compared to the ones used in the previous chapter. The boundary conditions are given in figure 3.9(c) and are called “meshed substrate”. The conditions for displacement U_2 are prescribed for the surfaces perpendicular to the y direction. One surface is fixed in direction U_2 . The displacement U_2 is prescribed at the opposite side. One surface with normal in x direction is fixed and the displacement U_1 is prescribed at the opposite surface. The relation between displacements is $U_1 = -\nu U_2$, where ν is the

3.3. PLASTIC DEFORMATION OF POLYCRYSTALLINE AGGREGATES

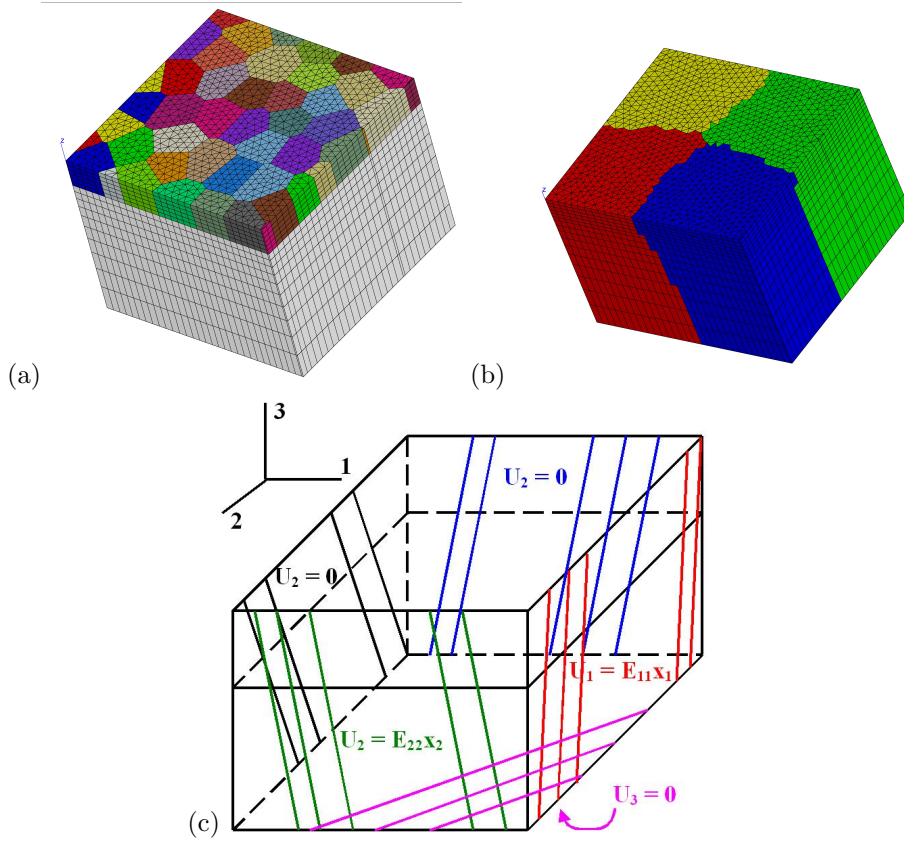


Figure 3.9: a) Mesh of polycrystalline aggregate on polyimide substrate, b) Domains used in parallel computations, c) Boundary conditions.

Poisson ratio of the elastic substrate. The bottom surface of the substrate is fixed in z direction which means $U_3 = 0$.

3.3.2 Global stress–strain curves

The global behaviour of these aggregates was investigated. The global stress–strain curves are plotted individually for the sets of $\{111\}$ and $\{001\}$ oriented grains in each individual aggregate. These results are shown in figure 3.10. The case (a) shows the average curves for all $\{001\}$ oriented grains in the individual aggregates. The average curves for the all $\{111\}$

3. FINITE ELEMENT SIMULATIONS OF THE PLASTICITY OF COPPER THIN FILMS

oriented grains in the individual aggregates are shown in figure (b). The differences of the maximal values of the imposed strain for each aggregate are caused by the different stops of simulations due to the numerical problems. The higher dispersion for the $\{001\}$ oriented grains is caused by their smaller number in the aggregates compared to $\{111\}$ oriented grains. The average yield stress is 81 MPa for $\{001\}$ and 89 MPa for $\{111\}$ oriented grains respectively. The value for the $\{001\}$ oriented grains lies within the interval of stresses for tensile test of single crystals while the value for the $\{111\}$ is above this corresponding interval. The reason for this discrepancy is that all grains in the aggregate are not under uniaxial loading but the stress tensor inside the grains is more complex. But orientation $\{111\}$ is more “sensitive” to the multiaxial loading. This can be clearly recognized from the comparison of the Schmid factors for tensile and biaxial loading. The orientation $\{001\}$ has the same value of Schmid factor for both type of loadings while for the orientation $\{111\}$ the Schmid factor is smaller for biaxial loading (about 2/3 of the lower special case value for tensile loading). The complexity of the stresses in the $\{111\}$ grains is caused by several factors. Out of plane shear strain occurs during the tensile loading of $\{111\}$ oriented grains. This shear depends on the grain orientation (angle ϕ_1). The free surface of such grains does not remain flat during the loading. This undulation concentrates the stresses at the grain boundaries. The substrate limits this undulation which leads to higher stresses.

Comparing the plastic parts of the stress–strain curves for both orientations shows that the hardening curves have very similar slopes. The activation and interaction of slip systems in the model produces almost the same amount of hardening. In contrast, the experimental measurements show significant differences between the hardening curves for the $\{001\}$ and $\{111\}$ oriented grains (Hommel and Kraft [2001]). The hardening of the $\{111\}$ grains is twice higher. Figure 3.11 shows the comparison of the simulations with experimental results of the tensile test of film with 1 μm thickness. The simulation results are found between the experimental ones. The plasticity in the real films starts at lower value of imposed total strain and then the hardening curves have higher slope. These results indicate much stronger interactions between the grains and slip systems than it is supposed in the model. The comparison is also questionable since the measured elastic strain is not the mean

3.3. PLASTIC DEFORMATION OF POLYCRYSTALLINE AGGREGATES

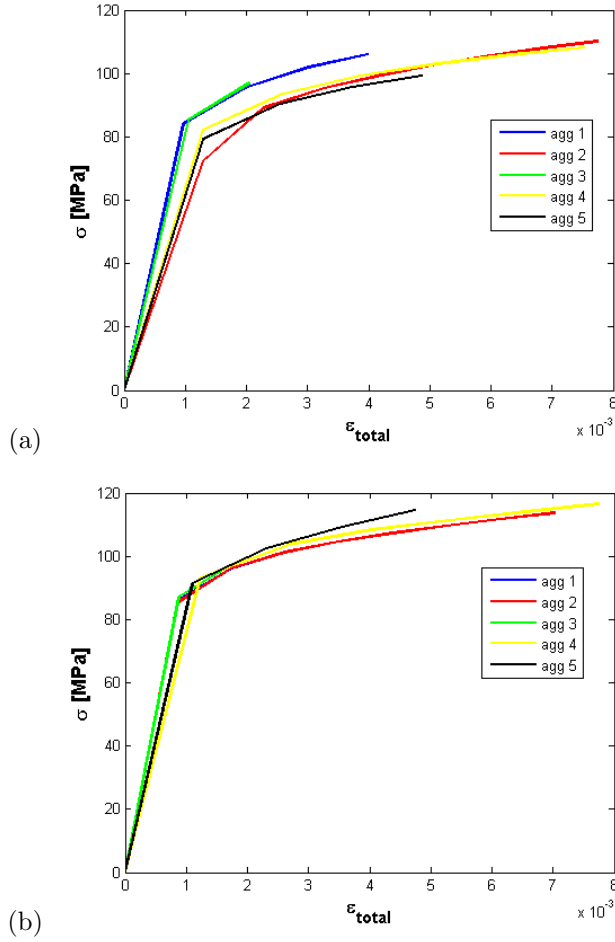


Figure 3.10: Global stress–strain curves for the grains with orientation: a) $\{001\}$, b) $\{111\}$.

value over all the $\{111\}$ grains as in the simulations. This will be discussed in chapter 5 (Comparison of the simulations with experimental data). The other reason for differences is such that parameters of the model were identified for bulk copper bicrystal and the model does not contain any intrinsic length scale for describing the size effects which also play important role in the hardening of thin films.

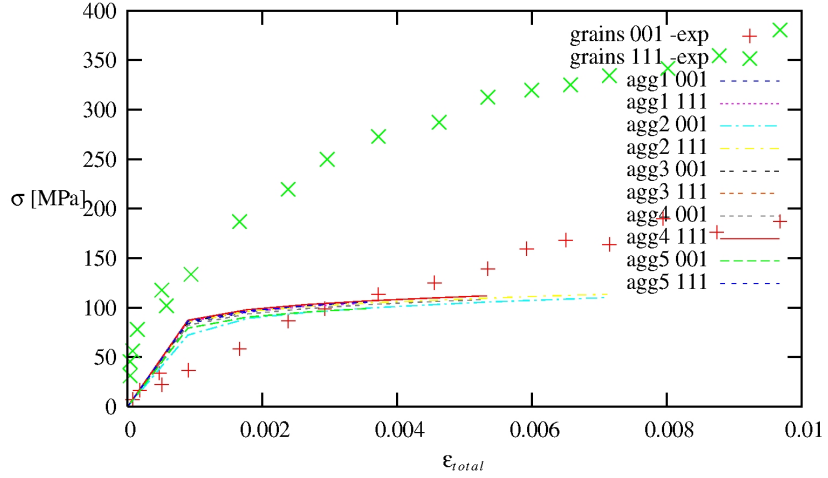


Figure 3.11: Comparison of the stress–strain curves of the tensile test of the copper film on polyimide substrate: experimental results – crosses, simulations – lines. (Hommel and Kraft [2001])

3.3.3 Stress–strain heterogeneities

The distribution of stress and strain in the aggregates is investigated by the comparison of the average values per grains of the von Mises stress and the equivalent strain. Figure 3.12 shows the dispersion of average values for $\{001\}$ oriented grains (a) and for $\{111\}$ oriented grains (b). The values are computed for the imposed total strain 0.2 %. The values are normalized by the average value of each aggregate. The dispersion of the relative equivalent strains lies for the $\{001\}$ oriented grains within the range 0.75 – 1.25 while the values for the $\{111\}$ oriented grains are between 0.5 and 1.5. This difference can be caused by the fact that there are only 15 $\{001\}$ oriented grains. These results are similar to those obtained in the computations of the free–standing aggregates in chapter 2. This comparison indicates small influence of the soft polyimide substrate on the strain dispersion. Such a small influence is illustrated also in figure 3.13 which shows that the film is undulated although it is deposited on this substrate. It is due to the low stiffness of polyimide substrate. The normalized von Mises stress values of most grains are founded in the range 0.85 – 1.1. This range is here

3.3. PLASTIC DEFORMATION OF POLYCRYSTALLINE AGGREGATES

smaller compare to elastic case due the plasticity.

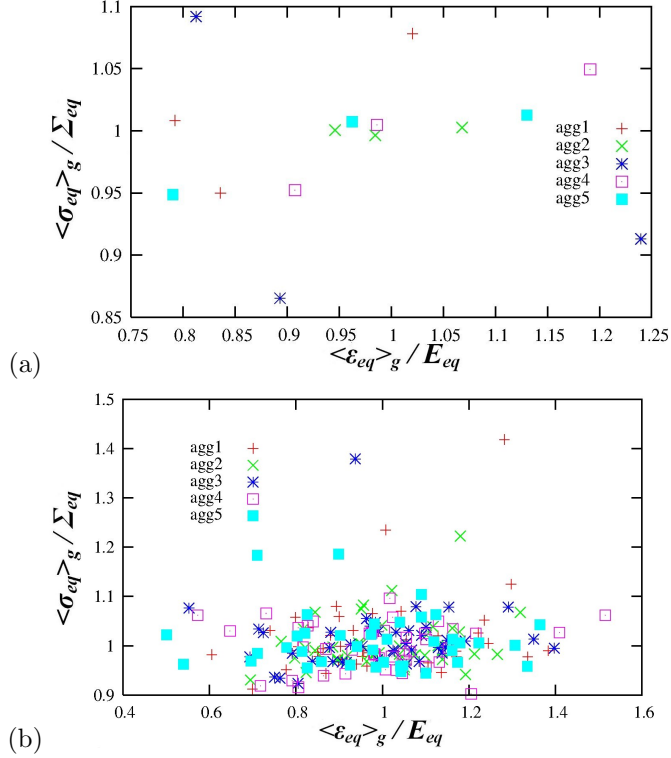


Figure 3.12: Dispersion of the average values per grain for von Mises stress and the equivalent strain: a) $\{001\}$ oriented grains, b) $\{111\}$ oriented grains. Overall strain $E_{22} = 0.005$.

The stress and strain distributions can be compared by the maps of these quantities on the free surface. Figure 3.14 indicates the position of the grains with orientation $\{001\}$ and random in the aggregate (a), the map of the von Mises stress at the free surface (b) and cumulated plastic strain at the free surface (c). The von Mises stress map shows that stress concentrations develop close to grain boundaries in the $\{111\}$ oriented grains while these concentrations are distributed more deeply towards the grain center in the $\{001\}$ and random oriented grains. This map also shows the significant influence of the random and $\{001\}$ oriented grains in the neighbourhood of $\{111\}$ oriented grains. There are higher stress concentrations in these grains and these areas can be favourable for crack initiation. The

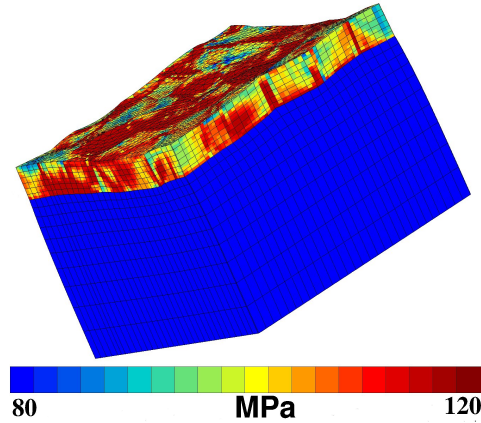


Figure 3.13: The undulation of the copper film deposited on the polyimide substrate. Colours show the levels of von Mises stress. Overall strain $E_{22} = 0.005$. Displacement is magnified by factor of 30.

cumulated plastic strain map shows the amount of plasticity in grains. This map shows the tendency of the plastic strain to form a band structure. The influence of the random and $\{001\}$ oriented grains on the grains in their neighbourhood is also visible in this case. The most deformed $\{111\}$ grains are placed next to $\{001\}$ grains or in their close neighbourhood.

3.4 Conclusions

The elasto–plastic behaviour of single crystals and polycrystalline aggregates were investigated in this chapter. The results for the single crystal can be summarized in the following points:

- The orientations with maximal value of the Schmid factor for $\{001\}$ crystals lead to the same hardening curves and only two slip systems are activated.
- The value of Schmid factor equal to 0.408 for $\{001\}$ oriented crystal to different hardening curves according to the number of active slip systems (4 or 8).
- The orientations with maximal value of the Schmid factor for $\{111\}$ crystal lead to the same hardening curves and only one active slip system.

3.4. CONCLUSIONS

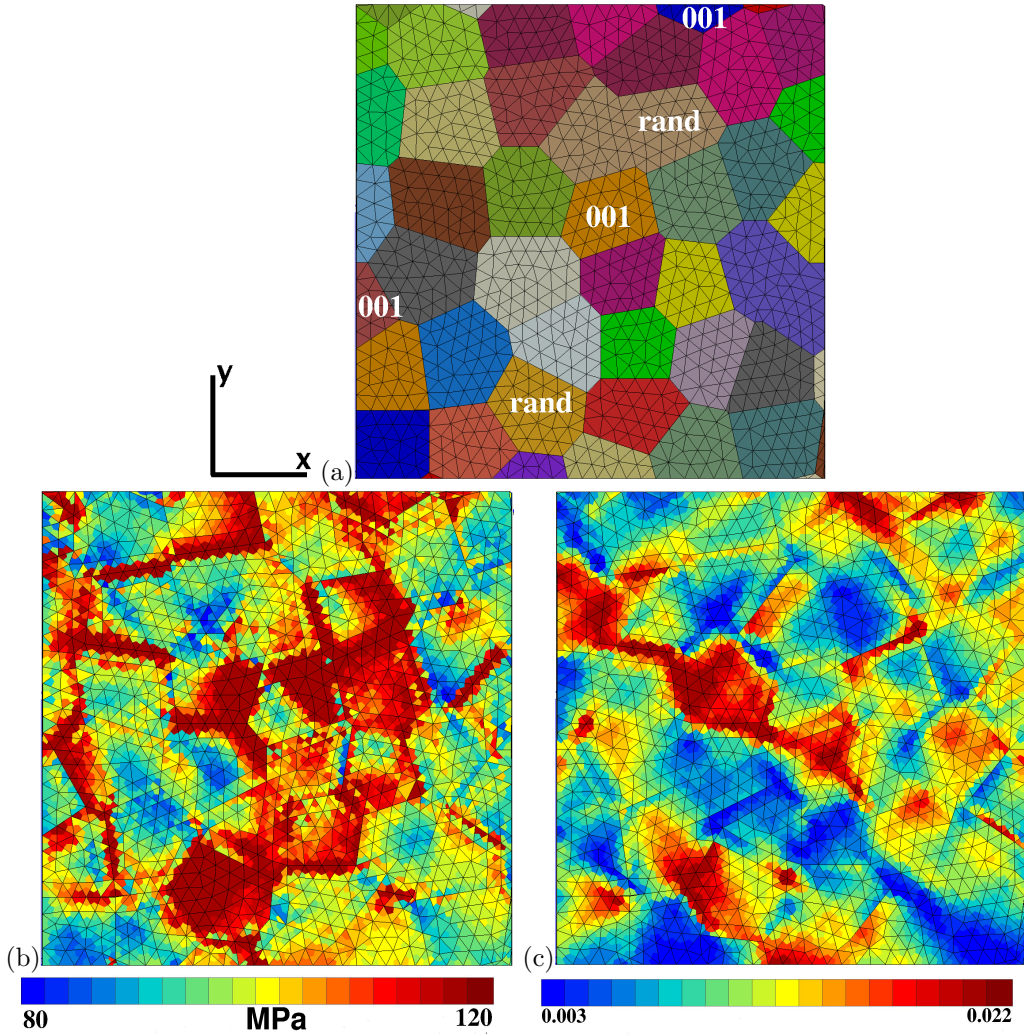


Figure 3.14: a) Positions of the random and $\{001\}$ oriented grains in the aggregate, b) distribution of the von Mises stress at the free surface, c) distribution of the cumulated plastic strain at the free surface. Overall strain $E_{22} = 0.005$.

- The value of Schmid factor equal to 0.408 for $\{111\}$ oriented crystal lead to different hardening curves according to the number of active slip systems (2 or 4).
- The diagonal components of the strain tensor are independent of the angle ϕ_1 in the

3. FINITE ELEMENT SIMULATIONS OF THE PLASTICITY OF COPPER THIN FILMS

case of equibiaxial loading and the off-diagonal components are zero for orientations $\{001\}$ and $\{111\}$.

- The Schmid factors for the slip systems are constant (independent of angle ϕ_1) for orientations $\{001\}$ and $\{111\}$ under equibiaxial loading.
- The maximal values of Schmid factor decrease for equibiaxial loading by factor of 1.208 for $\{001\}$ oriented grains and by factor of 1.732 for $\{111\}$ oriented grains respectively with respect to values for uniaxial loading.

The results for the polycrystalline aggregates can be summarized as follows:

- The yield stress of the $\{111\}$ oriented grains in the aggregates is higher than for the single crystal due to the higher sensitivity of this orientation to the multiaxial loading which occurs inside the grains.
- The soft substrate has small influence on the deformation on the copper film and allows the film to undulate during the loading.
- The presence of $\{001\}$ or random oriented grains causes the increase of stress and strain concentration inside the $\{111\}$ oriented grains in their neighbourhood.

Chapter 4

Mechanical behaviour of copper thin films under cyclic loading

The next step in the elasto–plastic computations is the investigation of the mechanical properties of thin films under cyclic loading. These simulations allow observing the evolution of the stress and strain in the films cycle after cycle. Such simulations can be interesting from the practical point of view because many real thin film structures are subjected to fatigue.

4.1 Parameters of simulations

4.1.1 Representative volume element, mesh size effect and boundary conditions

The films are represented by the polycrystalline aggregates which are created in the same way as mentioned in the chapter 2.2.1. Three types of aggregates are considered for these simulations. The aggregates of the first type have 50 equiaxial grains. This means that ratio between in–plane grain size d and film thickness h is equal to 1. Second type of aggregates has also 50 grains but the ratio $d/h = 0.5$ which means that the grains are columnar. For each type of film 10 different realizations are considered, because the analysis of the results is done in statistical way by averaging over a larger sample. For comparison and validation of this statistical method, one large aggregate with 225 grains and $d/h = 1$ was created.

The influence of the mesh density on the results had to be investigated to check if the mesh density used in previous simulations is suitable for cyclic loading. Four different meshes of the same aggregate were created for this purpose, respectively labelled: coarse (21 555 nodes), standard (34 710), middle (56 973 nodes) and fine (112 163 nodes). These films were subjected to 5 cycles of tension–compression loading with prescribed mean strain $E_{22} = \pm 0.005$. The boundary conditions, described later, correspond to the case of the film on a substrate. Figure 4.1 shows the comparison of the distribution of equivalent plastic strain after 5 cycles for the fine (a) and standard (b) meshes. Quantitative comparison is provided in figure 4.1(c) for the displacement component U_3 along a line made of grain boundaries connecting one lateral side to the other on the free surface. Differences remain small. In particular highly deformed zones are the same in both cases with close plastic strain values (less than 2% differences locally). The “standard” mesh density was confirmed to provide detailed plastic strain maps with limited computation time.

According to the previous results, the meshes used in this chapter are the following:

- The 225 - grain FE mesh of figure 4.2(a) contains 47 000 elements and 136 000 nodes, i.e. 408 000 degrees of freedom (3 displacement components per node);
- The 50 - grain FE mesh with $d/h = 1$ of figure 4.2(b) contains 11 600 elements and 34 400 nodes, i.e. 103 200 degrees of freedom;
- The 50 - grain FE mesh with $d/h = 0.5$ of figure 4.2(c) contains 23 600 elements and 65 400 nodes, i.e. 196 200 degrees of freedom.

Two types of loading conditions are supposed in the simulations:

- Cyclic tension–compression with $E_{22}^{min,max} = \pm 0.005$ where E_{22} is the volume averaged axial deformation in the film.
- Cyclic tension with $E_{22}^{min,max} = 0 - 0.01$.

The strain rate is $2 \times 10^{-6} s^{-1}$.

The simulations mimic the deformation of the thin film on the substrate and free-standing film. Two kinds of boundary conditions are used in the computations. These

4.1. PARAMETERS OF SIMULATIONS

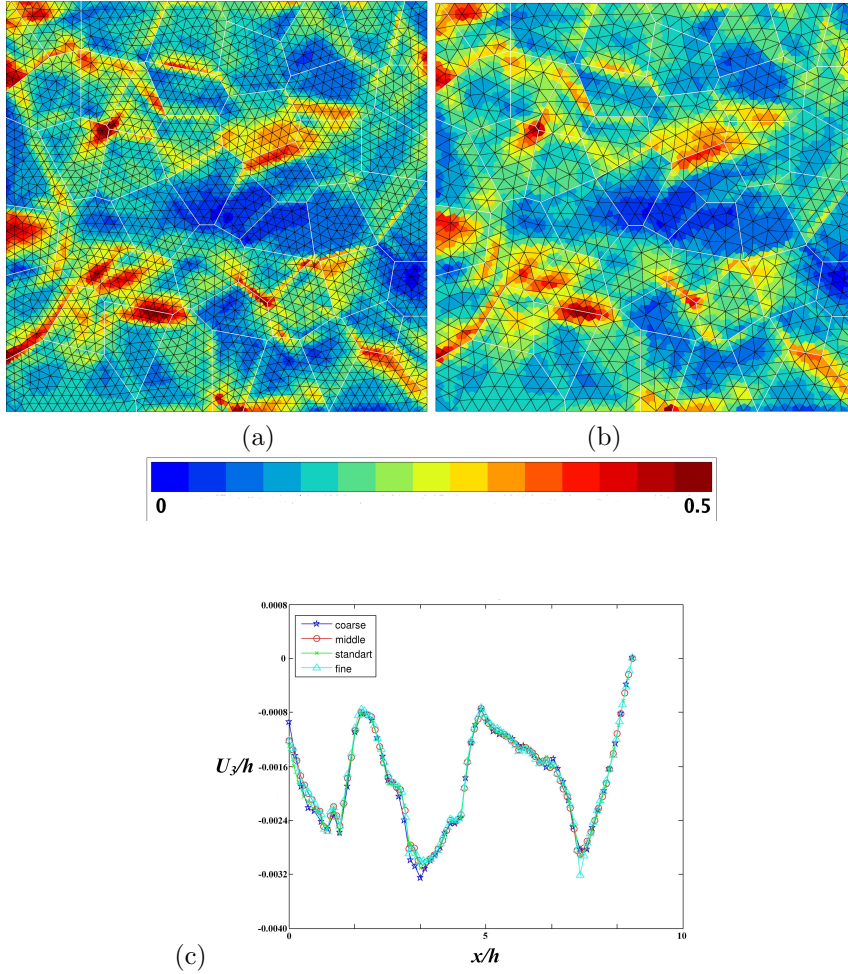


Figure 4.1: Equivalent plastic strain map for different mesh densities ($E_{22} = 0.005$, $N = 5$): (a) fine mesh, (b) standard mesh (used in computations); grains boundaries are in underlined in white; (c) quantitative comparison of displacement U_3 along a line (made of grain boundaries linking the left edge to the right side at the free surface).

boundary conditions are different from those described in chapter 2.2.1 (“free surface”, “fixed surface”) and in chapter 3.3.1 (“meshed substrate”). The boundary conditions are following:

- *Free-standing films*: The faces of the parallelepipedic volume that are perpendicular

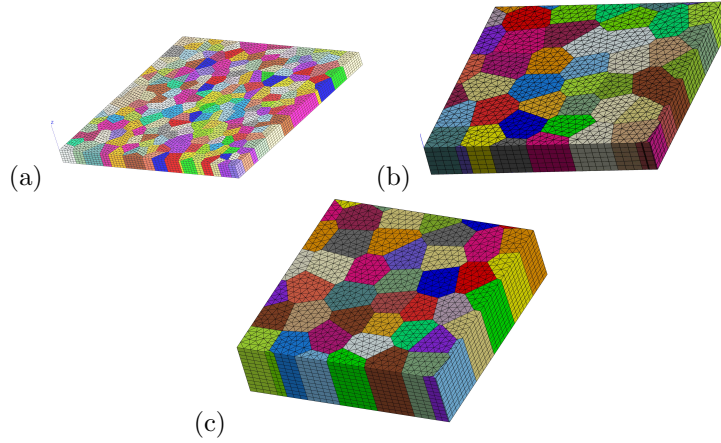


Figure 4.2: Morphology and finite element mesh of multicrystalline films: (a) 225-grain film with $d/h = 1$, (b) 50-grain film with $d/h = 1$, (c) 50-grain film with $d/h = 0.5$.

to the z direction are left free of forces, as shown in figure 4.3 case(a). Tensile loading is prescribed in direction y . For that purpose, the component U_2 of the nodes belonging to the faces perpendicular to y is fixed to 0 at $y = 0$ and increased linearly to a maximal value at $y = L$. The contraction of the film is prescribe in x direction by the same way as in the y direction. The displacement U_1 is prescribed by the equation: $E_1 = -\nu E_2$. This kind of boundary conditions can describe also the thin film on soft substrate (see chapter 3.3.3) and ν is Poisson ratio of such substrate.

- *Film on a stiff substrate*: In addition to the previous boundary conditions, the nodes belonging to the face $z = 0$ are subjected to homogeneous deformation.

$$U_i = E_{ij}^{substrate} x_j, \quad (4.1)$$

where the $E_{ij}^{substrate}$ are the strain components of the substrate subjected to given simple tension, assuming that it deforms homogeneously (see case (b) at figure 4.3). As a result of this simplification, there is no meshing of the substrate. It is assumed that the overall strain of the substrate is homogeneously transmitted to the interface. The displacement component normal to each lateral face of the film is prescribed according to formula (4.1).

4.1. PARAMETERS OF SIMULATIONS

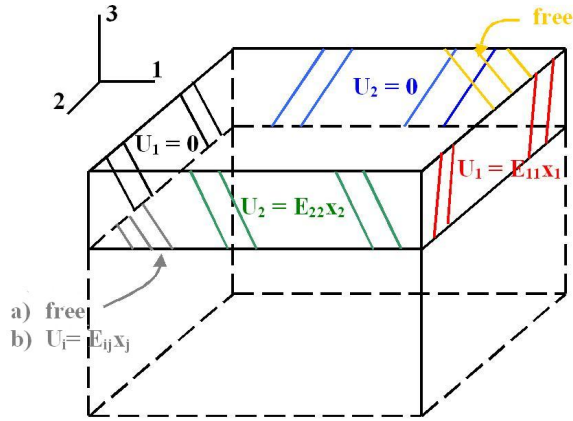


Figure 4.3: Boundary conditions used in the computation of free-standing films (a) and films on substrate (b). The deformation E of the substrate is prescribed at the interface and on the lateral faces of the parallelepipedic volume.

4.1.2 Crystallographic texture and material behaviour

The crystallographic texture of the films is the same as in the previous chapter. The $\{111\}$ orientation has a volume fraction of 90%, $\{001\}$ orientation has a volume fraction of 6% and the rest 4% consists of random orientations (Hommel and Kraft [2001]). The orientations of grains in the 225 grain aggregate are shown in figure 4.4.

The material behaviour of the film is prescribed by the constitutive equations presented in the previous chapter. The Copper II set of parameters is used for the simulations. Some simulations are done with Copper I parameters for comparison. The substrate boundary conditions are described by the parameters of the $\{001\}$ oriented silicon monocrystal – $C_{11} = 165640$ MPa, $C_{12} = 63940$ MPa, $C_{44} = 79510$ MPa (Virginia semiconductor [2006]).

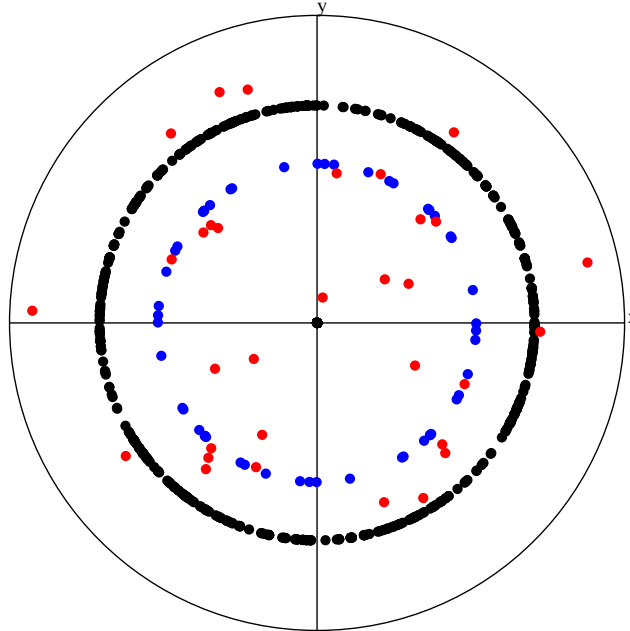


Figure 4.4: Pole figure $\{111\}$ of the grain orientations in the 225-grain multicrystalline film of figure 4.2(a): $\{111\}$ -grains in black, $\{001\}$ -grains in blue, random-grains in red.

4.2 Strain heterogeneities in cyclically deformed thin films

4.2.1 Overall cyclic hardening

The simulations are performed for the aggregates with $d/h = 0.5$ and $d/h = 1$ and “film on a stiff substrate” boundary conditions for both types of loading. First comparison is done for the different sets of parameters (Copper I, Copper II). This comparison for both loading conditions is shown in figure 4.5. The stabilized saturated loops are shown in this figure. The stabilized maximal and minimal stress values are found to be almost identical for both loading conditions. This is due to total relaxation of mean stress during cyclic tension which is a standard feature of low cycle bulk plasticity for nonsymmetric strain loading conditions. No elastic accommodation takes place in the film for the cyclic tension test. The stabilized loops predicted by both models are different. This is due to the fact

4.2. STRAIN HETEROGENEITIES IN CYCLICALLY DEFORMED THIN FILMS

that the two sets of parameters were identified with respect to different experimental data. The simulation based on the Copper I parameters set (isotropic hardening only) shows that the interaction between grains in the film leads to an overall Bauschinger effect, clearly seen in figure 4.5. This is a known feature in bulk polycrystal plasticity (Cailletaud [1992]). The introduction of a back-stress in the single crystal model leads to a slightly stronger Bauschinger effect (blue curve in figure 4.5). The rest of compared simulations are done with Copper II parameters because these were identified with respect to cyclic loading results.

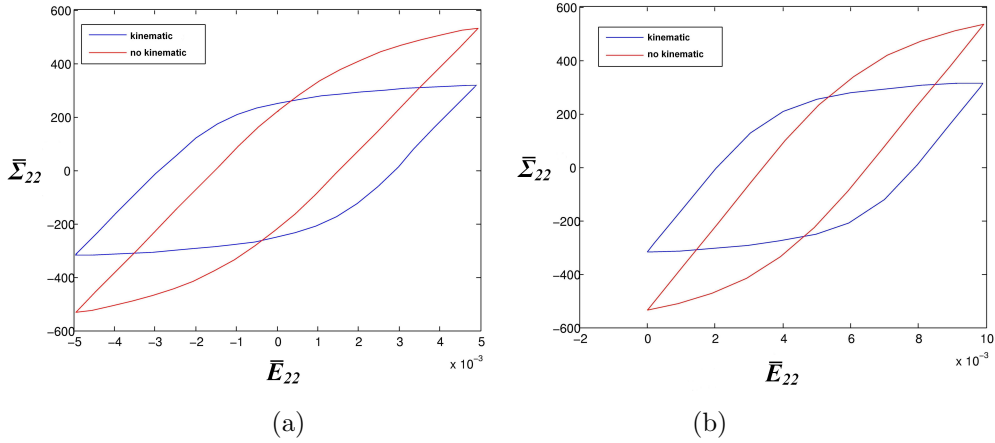


Figure 4.5: Stabilized overall stress–strain loops for models with and without local kinematic hardening:(a) cyclic tension–compression, (b) cyclic tension.

The validity of the statistical approach is checked by the comparison of the stress–strain loop of the 225 grains aggregate and stress–strain loop made as average from the loops of individual small aggregates. This comparison is shown in figure 4.6. The curve for the large aggregate lies within or at the boundary of the error bars of the average values. These small differences show that the statistical approach based on several different realizations of small aggregates provides suitable macroscopical results.

The comparison of stress–strain loops for the different texture components is shown in figure 4.7. For that purpose, the axial stress and strain components are volume averaged over all grains having a given orientation: all $\{111\}$, all $\{001\}$ grains or all random orientations. The first and 100th loops are plotted for 5 realizations of aggregates with 50

4. MECHANICAL BEHAVIOUR OF COPPER THIN FILMS UNDER CYCLIC LOADING

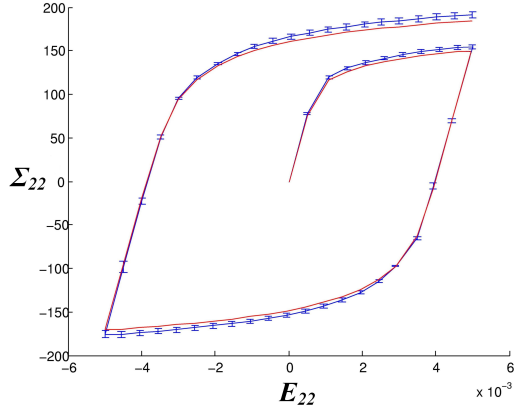


Figure 4.6: Overall stress–strain curve for the deformation of the 225–grain aggregate compared to the average overall curve with respect to 10 aggregates containing 50 grains each. The scatter in the response of the 50–grain aggregates is indicated by error–bars. The films are subjected to cyclic tension–compression.

grains. The grains with $\{001\}$ and random orientations display significantly higher strain and lower stress level than $\{111\}$ ones. A higher dispersion of the loops is observed for $\{001\}$ and random grains than for $\{111\}$ grains, but this is due to the small number of such grains in aggregates: 3 $\{001\}$ and 2 random grains out of 50 for each realization. Complete stress relaxation is observed for all grain orientations in the case of cyclic tension so that the stabilized loops are symmetric in stress. The evolution with the number of cycles of the maximal value of stress averaged over all grains and realizations is shown in figure 4.8 for both loading conditions. The average stress level is stabilized after 70 cycles. The same saturation is observed for the mean stress for each texture component. The rate of saturation does not depend on the orientation group. The highest stress levels develop in $\{111\}$ grains and the softest are $\{001\}$ grains. These cyclic hardening curves results from volume and ensemble averaging over 450 $\{111\}$ grains, 30 $\{001\}$ grains and 20 random grains.

4.2. STRAIN HETEROGENEITIES IN CYCLICALLY DEFORMED THIN FILMS

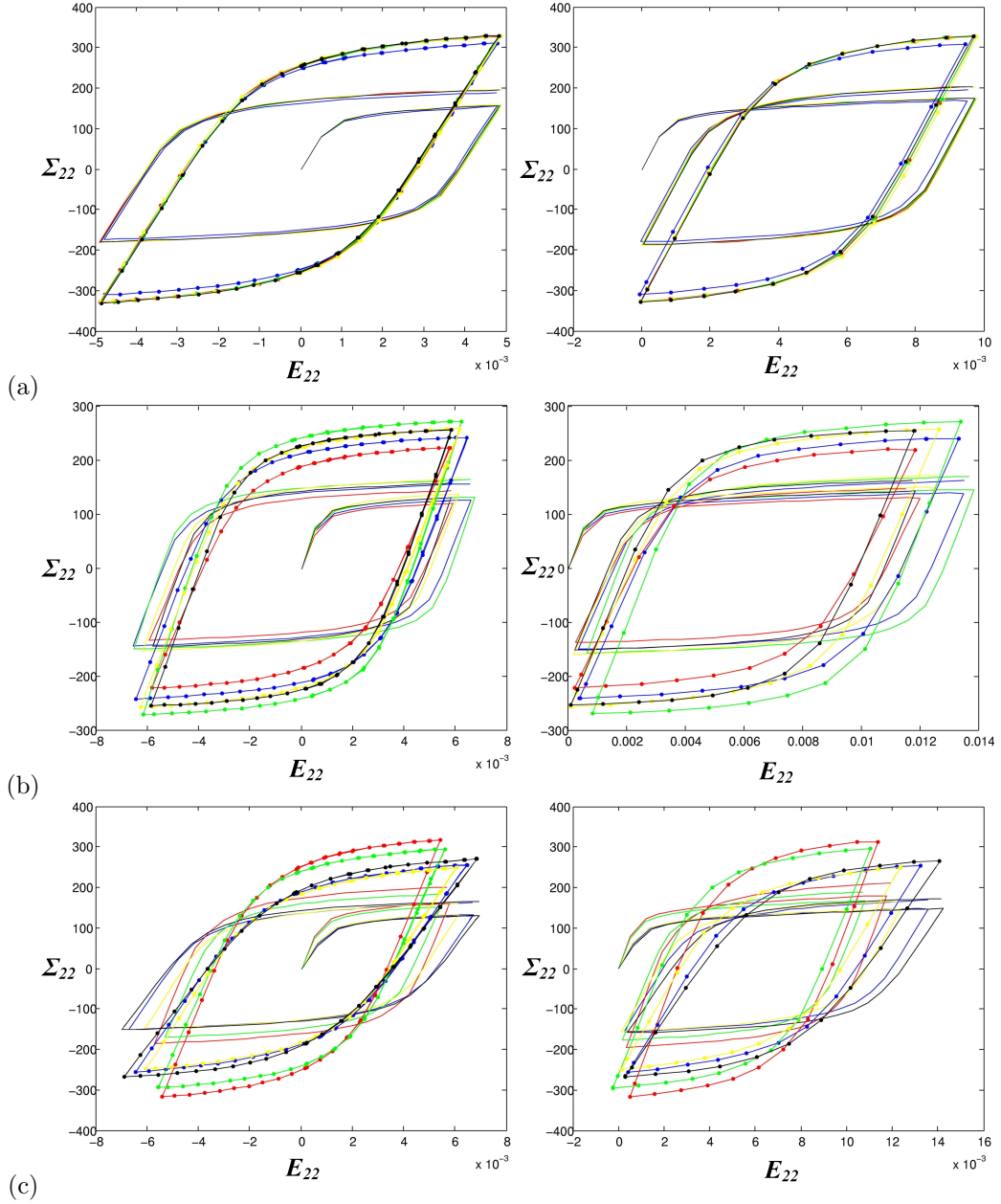


Figure 4.7: Comparison of first and stabilized cycles for different grain orientations in aggregates subjected to cyclic tension-compression (left) and cyclic tension (right): (a) volume average over $\{111\}$ grains, (b) volume average over $\{001\}$ grains, (c) volume average over random grains. In each case, the curves are given for 5 distinct realizations.

4. MECHANICAL BEHAVIOUR OF COPPER THIN FILMS UNDER CYCLIC LOADING

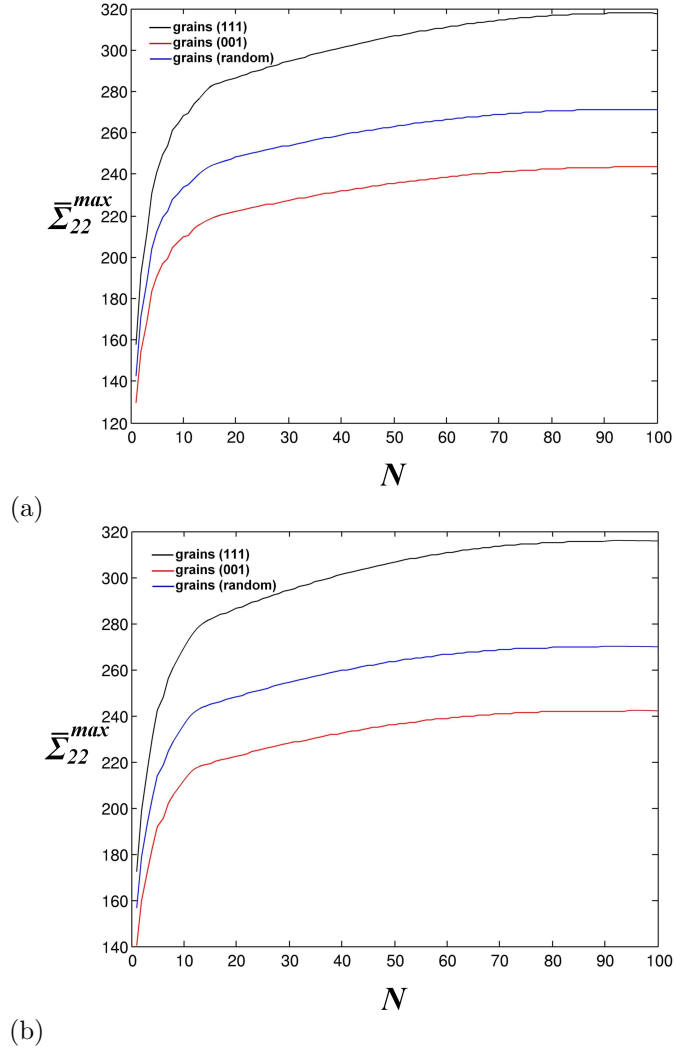


Figure 4.8: Cyclic hardening in multicrystalline aggregates subjected to (a) cyclic tension-compression and (b) cyclic tension. The overall stress curves are averaged over 10 realizations of 50-grain aggregates.

4.2.2 Levels of heterogeneity and statistical analysis

A first dispersion level of stress and strain was analysed in the previous section depending on the grain orientation group. A second dispersion level is given in figure 4.9 which shows the equivalent stress and strain value averaged over each individual grain in all realizations, after 100 cycles tension–compression (with substrate and $d/h = 1$). A stress/strain concentration factor is defined as the ratio of the mean stress/strain in each grain divided by the overall stress/strain value for the corresponding aggregate. Stress concentration factors ranging mainly from 0.8 to 1.2 with extreme values of 0.6 and 1.6. The corresponding strain concentration factor range from 0.4 to 1.6. Low mean stresses are encountered mainly in $\{001\}$ and random grains whereas high strain levels are found in grains belonging to all orientation groups.

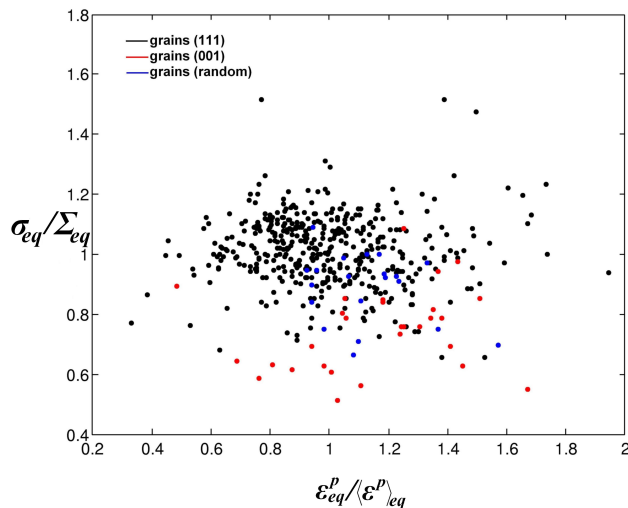


Figure 4.9: Dispersion of equivalent average stress and equivalent plastic strain in the grains of 10 realizations of 50–aggregates subjected to cyclic tension–compression at $N = 100$. The results are given for the films with a substrate with $d/h = 1$. Each point corresponds to the volume averaged stress value over one grain in the 10 aggregates. Black, blue and red dots respectively denote $\{111\}$, $\{001\}$ and random grains. The stress and plastic strain levels are normalized by the volume average values over the corresponding entire aggregate.

The next dispersion level to be investigated is that of local stress and strain values inside

the grains. The fields of equivalent plastic strain are shown in figure 4.10 at the free surface for three film configurations. Case (a) shows the maps for the first and 100th cycles of the films with $d/h = 1$. Case (b) shows the first and 100th cycle for the films with $d/h = 0.5$. The case (c) belongs to free-standing films and the first and 24th cycles. In the simulation shown in figure 4.10, the grain morphology and crystal orientations are the same. Only the film configuration is changed (film thickness and substrate effect). Plastic strain is found to be highly heterogeneous with local values ranging from 0 (elastic response) to more than 0.01, i.e. twice the prescribed mean total strain. The plastic deformation develops into deformation bands inclined with respect to the vertical tensile axis and crossing several grains. Plastic strain is much more localized in these bands in free-standing films (figure 4.10(c)) than in films on a substrate. Plastic strain is more heterogeneous at the free surface in the thick film than in the twice thinner one (see figures 4.10(a) and (b)). Highly deformed grains are observed in figure 4.10(b) which is similar to the case of free-standing films. For each film configuration the comparison of the plastic strain map at first and 100th (24th) cycle shows that the strain heterogeneities are more pronounced after cycling, with, on the one hand, more localized deformation in some grains and close to some grain boundaries (red regions) and, on the other hand, more extended low strained zones (blue regions). A quantitative assessment of the evolution of heterogeneity distribution is possible via the following statistical analysis.

4.2. STRAIN HETEROGENEITIES IN CYCLICALLY DEFORMED THIN FILMS

The plastic strain distribution in all the computed aggregates are represented by the histograms in figures 4.11, 4.12 and 4.13. For each film configuration, the equivalent plastic strain values ε_{eq}^p at each integration point of each realization have been stored, normalized by the global value for the aggregate E_{eq}^p and ranked into classes of size $\Delta\varepsilon_{eq}^p/E_{eq}^p = 0.1$. The procedure was carried out for several cycle numbers: $N = 1, 50, 100$ for films on substrate, $N = 1, 5$ for free-standing films, $N = 1, 15, 30$ for large aggregate. Accordingly, each histogram represents the treatment of 696 000 values (corresponding to 10 realizations \times 11 600 elements \times 6 integration points per element for films with $d/h = 1$). For each cycle number, three histograms are computed, one for each grain orientation group as shown in figures 4.11, 4.12 and 4.13. The evolution of the histograms can be characterized by the position and height of the peak and also by the range of the values. For all film configurations, texture component and loading conditions, the relative plastic strain values range from 0 to 5. The height, position and width at half of maximum are shown in table 4.1 for $\{111\}$ grains which create the largest part of the aggregates. Comparison of these values shows the following features: The position of the peak remains unchanged for the 50-grains aggregates on the substrate. The height of the peak and value of FWHM increases with cycling. These features show the broadening of the distribution and this means that the dispersion of the plastic strain increases during the cycling. The aggregates loaded by the tension-compression show very significant decrease and broadening of the distribution (about 50%) between the first and the 50th cycle while between the 50th and 100th cycle the differences are much smaller. Contrary to this, the histograms for films loaded by cyclic tension show the decrease and broadening within the range of 10% between the first and the 50th cycle. This difference is caused by the twice higher value of imposed strain (1% for cyclic tension) which causes earlier accommodation, and redistribution of plastic strain. The histograms for the tensile loaded $d/h = 1$ films show the small peak at ratio of 0.25. Such a peak does not exist for the films with $d/h = 0.5$. This small peak is caused by the accommodation to the loading conditions. In the case of the films with $d/h = 0.5$ such an accommodation cannot be possible due to higher constraints of the grains. In this case the grains have larger area of grain boundaries, therefore, they are more influenced by the

neighbouring grains. The effect of boundary conditions is also much more important in these films due to their larger area of the side faces which are restricted by these conditions. The histograms for the large aggregate under tension–compression are more asymmetric compared to ones for small aggregates, and the position of maxima moves from 0.35 to 0.45 (see fig. 4.12(b)). The maximum is shifted towards the smaller values of plastic strain compared to the histograms of the small aggregates. This is caused by the boundary effect in the small aggregates where the grains behaviour is more influenced by the boundary conditions. Similar results are obtained for the free–standing films where the distribution is also asymmetric and does not spread with cycling. This is due to a stronger tendency to strain localization so that strain develops in the same grains and cannot extend to neighbouring harder grains, as shown in figure 4.10(c).

4.2. STRAIN HETEROGENEITIES IN CYCLICALLY DEFORMED THIN FILMS

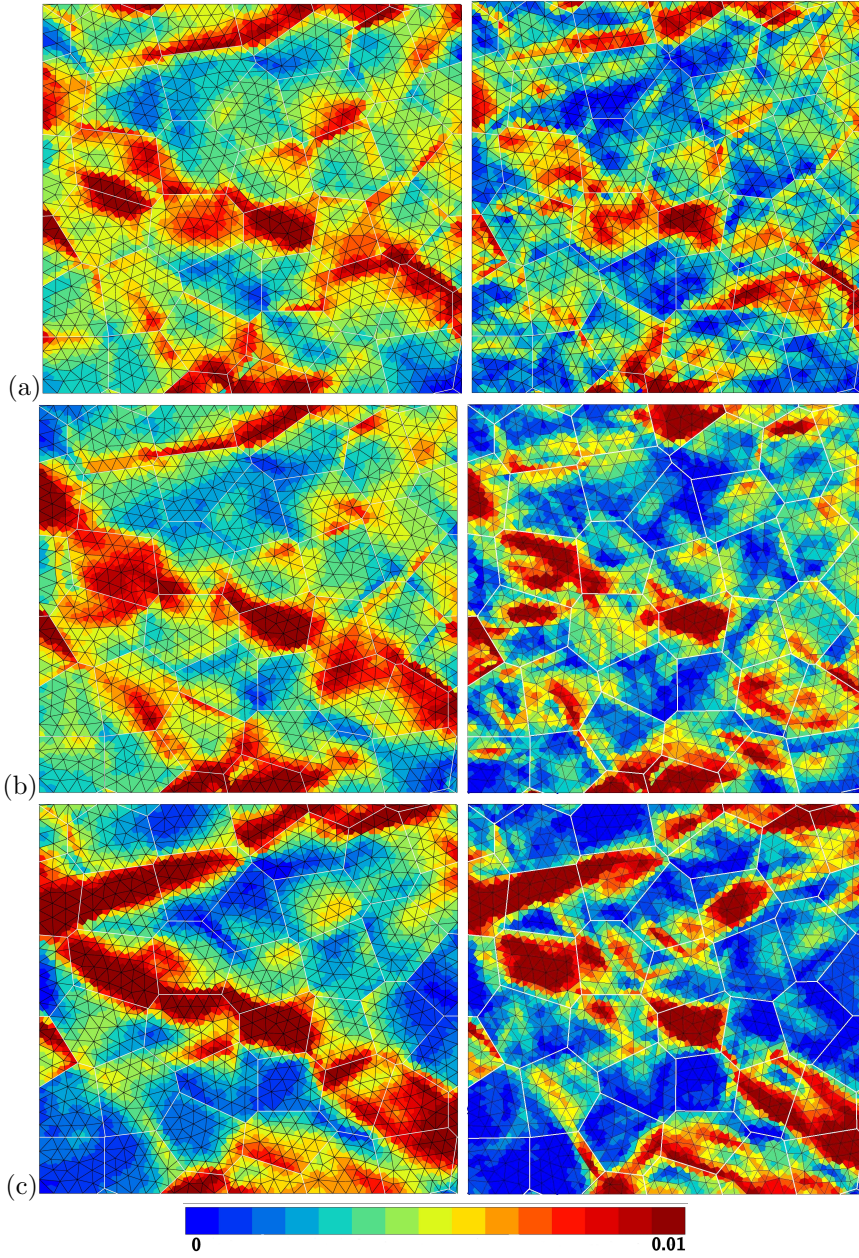


Figure 4.10: Distribution of equivalent plastic strain after $N = 1$ cycle (left) and $N = 100$ cycles (a)(b) and $N = 24$ cycles (c) (right): (a) multocrystalline film on a substrate with $d/h = 1$, (b) multocrystalline film on a substrate $d/h = 0.5$, (c) free-standing film.

4. MECHANICAL BEHAVIOUR OF COPPER THIN FILMS UNDER CYCLIC LOADING

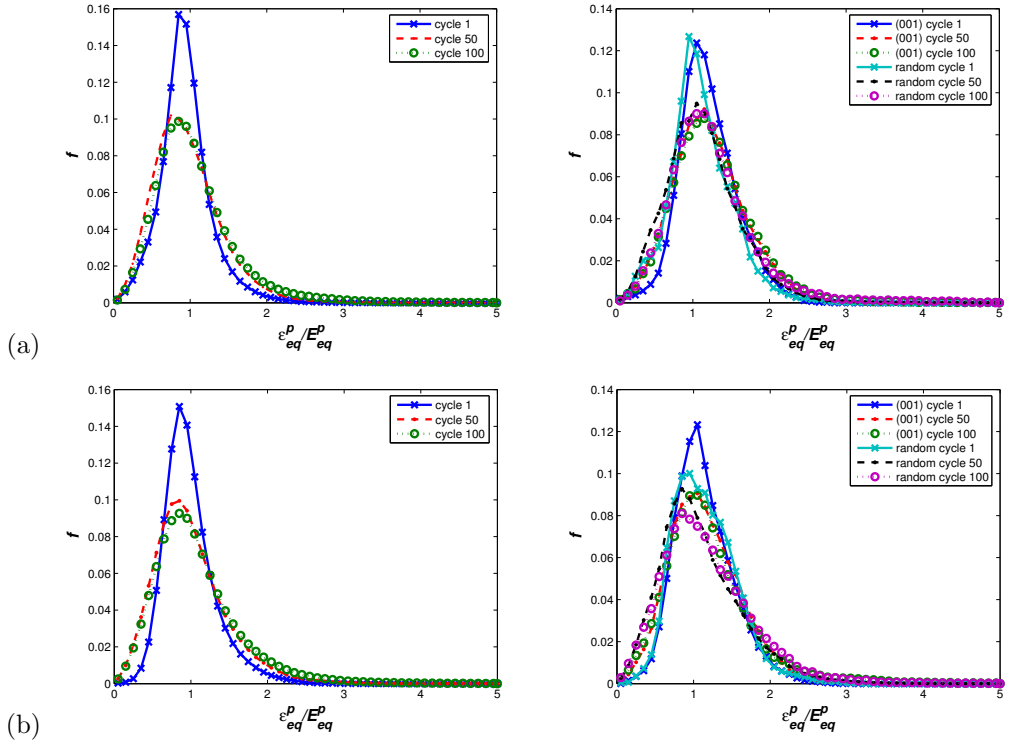


Figure 4.11: Histograms of equivalent plastic strain distribution in $\{111\}$ grains (left) and $\{001\}$ and random grains (right): (a) multocrystalline aggregate on a substrate with $d/h = 1$, (b) multocrystalline aggregate on a substrate with $d/h = 0.5$. The loading conditions are cyclic tension–compression.

4.2. STRAIN HETEROGENEITIES IN CYCLICALLY DEFORMED THIN FILMS

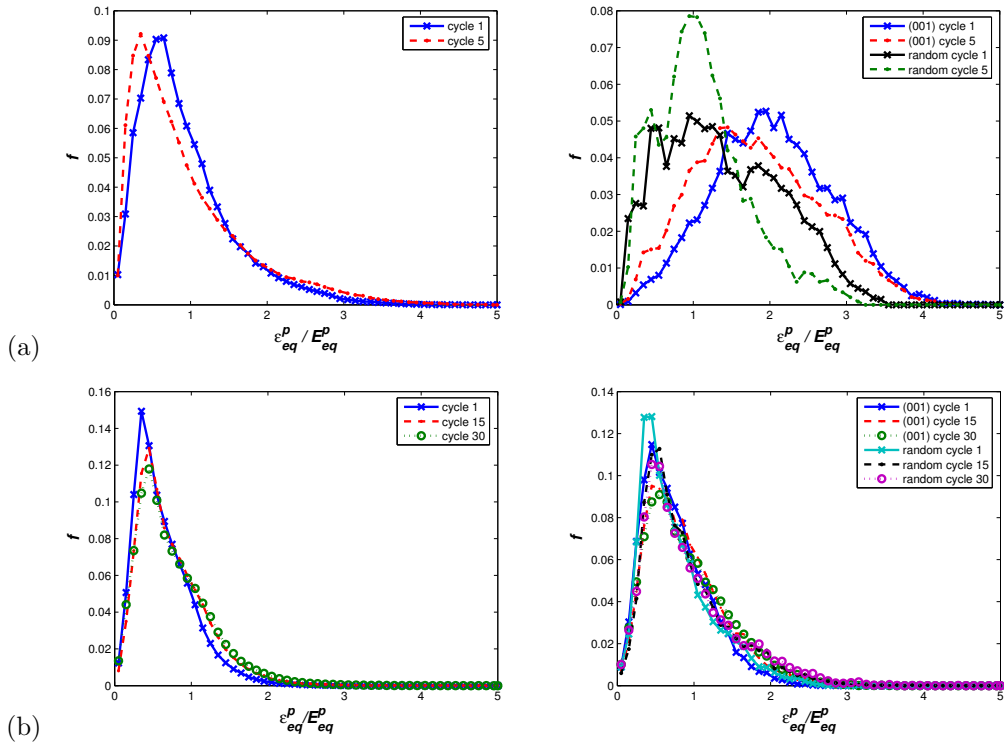


Figure 4.12: Histograms of equivalent plastic strain distribution in $\{111\}$ grains (left) and $\{001\}$ and random grains (right): (a) free-standing films, (b) large aggregate (225 grains). The loading conditions are cyclic tension-compression.

4. MECHANICAL BEHAVIOUR OF COPPER THIN FILMS UNDER CYCLIC LOADING

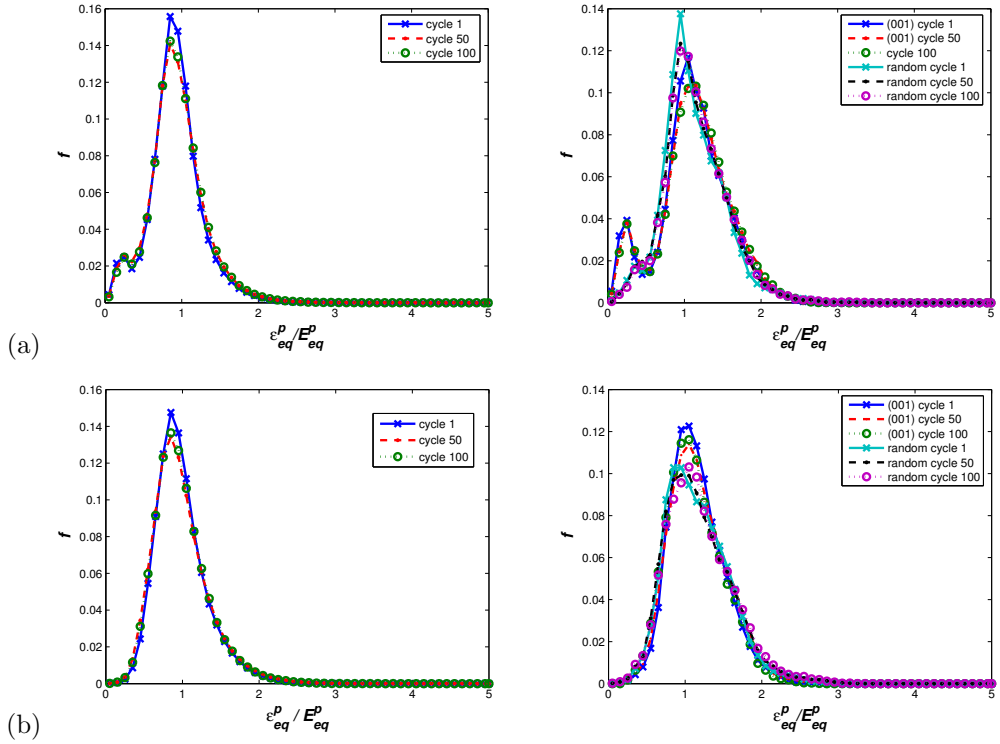


Figure 4.13: Histograms of equivalent plastic strain distribution in $\{111\}$ grains (left) and $\{001\}$ and random grains (right): (a) multicrystalline aggregate on a substrate with $d/h = 1$, (b) multicrystalline aggregate on a substrate with $d/h = 0.5$. The loading conditions are cyclic tension.

4.2. STRAIN HETEROGENEITIES IN CYCLICALLY DEFORMED THIN FILMS

cycle	peak value	peak strain	FWHM
film with substrate (d/h=1) - tension-compression			
cycle 1	0.157	0.85	0.505
cycle 50	0.102	0.75	0.915
cycle 100	0.099	0.85	0.880
film with substrate (d/h=0.5) - tension-compression			
cycle 1	0.151	0.85	0.565
cycle 50	0.099	0.85	0.890
cycle 100	0.093	0.85	0.940
freestanding film - tension-compression			
cycle 1	0.091	0.65	1.000
cycle 5	0.092	0.35	0.900
225 grains aggregate - tension-compression			
cycle 1	0.149	0.35	0.570
cycle 15	0.129	0.45	0.670
cycle 30	0.118	0.45	0.740
film with substrate (d/h=1) - cyclic tension			
cycle 1	0.156	0.85	0.505
cycle 50	0.141	0.85	0.520
cycle 100	0.142	0.85	0.525
film with substrate (d/h=0.5) - cyclic tension			
cycle 1	0.147	0.85	0.590
cycle 50	0.134	0.85	0.655
cycle 100	0.137	0.85	0.660

Table 4.1: Peak value, peak strain and width at half maximum in the relative equivalent plastic strain distribution in the $\{111\}$ grains in different film configurations and loading conditions.

The histograms for the {001} grains display higher dispersion of the values of plastic strain. This is due to the fact that the {001} grains are the softest grains in the aggregates (see. fig 4.8) and the most deformed grains. Note also the completely different shape of histogram for {001} grains in free-standing films compared to the histograms for the films on substrate. This is again caused by the lower level of grain constraining.

The other way of comparing of the histograms is done by the fitting of an analytical statistical distribution. The chosen distributions are: Normal, Log-normal, Weibull and Gamma distributions. These distributions are described by the following equations:

- Normal:

$$f(x) = \frac{1}{x\sigma\sqrt{2\pi}} \exp\left(-\frac{(x + \mu)^2}{2\sigma^2}\right) \quad (4.2)$$

- Log-normal

$$f(x) = \frac{1}{x\sigma\sqrt{2\pi}} \exp\left(-\frac{(\ln(x) + \mu)^2}{2\sigma^2}\right) \quad (4.3)$$

- Weibull

$$f(x) = \left(\frac{k}{\lambda}\right) \left(\frac{x}{\lambda}\right)^{k-1} \exp\left(-\left(\frac{x}{\lambda}\right)^k\right) \quad (4.4)$$

- Gamma

$$f(x) = \frac{\beta^\alpha}{\Gamma(\alpha)} x^{\alpha-1} \exp(-\beta x). \quad (4.5)$$

The parameters of the distributions for given films and number of cycle are given in the tables 4.2, 4.3, 4.4 and 4.5. Except the normal one, all distributions lead to asymmetric histogram which is able to fit the measured ones. The normal distribution is used for comparison and it fits also the {001} grain histogram for free-standing films. The quality of the fitting is given by the equation:

$$M = \sum (A - Q)^2, \quad (4.6)$$

where A are the analytical frequencies and Q are the measured frequencies. The results show that the best suitable analytical distribution is the Log-normal one followed by the Gamma distribution. The broadening of the histograms, i.e. increasing of the dispersion of plastic deformation, shows also the increasing of the dispersion of the Log-normal distribution.

4.2. STRAIN HETEROGENEITIES IN CYCLICALLY DEFORMED THIN FILMS

These results are in contrast with results for the infinitely long columnar grains where the plastic strain distribution follows the quasi-Gaussian distribution (Sai et al. [2006]).

cycle	Normal	Log-normal	Weibull	Gamma
film with substrate (d/h=1) - cyclic tension				
cycle 1	$\mu = 0.91$	$\mu = -0.06$	$k = 3.83$	$\alpha = 12.09$
	$\sigma = 0.27$	$\sigma = 0.29$	$\lambda = 0.99$	$\beta = 12.66$
	$M = 0.0024$	$M = 0.0029$	$M = 0.0030$	$M = 0.0027$
cycle 50	$\mu = 0.91$	$\mu = -0.05$	$k = 3.44$	$\alpha = 9.85$
	$\sigma = 0.30$	$\sigma = 0.32$	$\lambda = 1.01$	$\beta = 10.16$
	$M = 0.0017$	$M = 0.0024$	$M = 0.0023$	$M = 0.0021$
cycle 100	$\mu = 0.92$	$\mu = -0.05$	$k = 3.50$	$\alpha = 10.24$
	$\sigma = 0.30$	$\sigma = 0.32$	$\lambda = 1.01$	$\beta = 10.53$
	$M = 0.0017$	$M = 0.0021$	$M = 0.0023$	$M = 0.0020$
film with substrate (d/h=0.5) - cyclic tension				
cycle 1	$\mu = 0.91$	$\mu = -0.06$	$k = 3.61$	$\alpha = 10.53$
	$\sigma = 0.28$	$\sigma = 0.32$	$\lambda = 1.00$	$\beta = 10.99$
	$M = 0.0016$	$M = 0.0003$	$M = 0.0022$	$M = 0.0005$
cycle 50	$\mu = 0.90$	$\mu = -0.07$	$k = 3.29$	$\alpha = 8.72$
	$\sigma = 0.31$	$\sigma = 0.35$	$\lambda = 1.01$	$\beta = 9.08$
	$M = 0.0016$	$M = 0.0003$	$M = 0.0018$	$M = 0.0003$
cycle 100	$\mu = 0.91$	$\mu = -0.06$	$k = 3.38$	$\alpha = 9.20$
	$\sigma = 0.30$	$\sigma = 0.34$	$\lambda = 1.01$	$\beta = 9.54$
	$M = 0.0014$	$M = 0.0002$	$M = 0.0017$	$M = 0.0003$

Table 4.2: Identification of statistical distribution functions for the relative equivalent plastic strain in $\{111\}$ grains for different film configurations.

4. MECHANICAL BEHAVIOUR OF COPPER THIN FILMS UNDER CYCLIC LOADING

cycle	Normal	Log-normal	Weibull	Gamma
film with substrate (d/h=1) - tension-compression				
cycle 1	$\mu = 0.91$ $\sigma = 0.27$ $M = 0.0015$	$\mu = -0.06$ $\sigma = 0.29$ $M = 0.0023$	$k = 3.85$ $\lambda = 0.99$ $M = 0.0020$	$\alpha = 11.97$ $\beta = 12.53$ $M = 0.0020$
cycle 50	$\mu = 0.87$ $\sigma = 0.39$ $M = 0.0007$	$\mu = -0.07$ $\sigma = 0.46$ $M = 0.0008$	$k = 2.54$ $\lambda = 1.03$ $M = 0.0003$	$\alpha = 5.12$ $\beta = 5.24$ $M = 0.0002$
cycle 100	$\mu = 0.92$ $\sigma = 0.41$ $M = 0.001$	$\mu = -0.02$ $\sigma = 0.46$ $M = 0.0005$	$k = 2.57$ $\lambda = 1.08$ $M = 0.0007$	$\alpha = 5.28$ $\beta = 5.14$ $M = 0.0003$
film with substrate (d/h=0.5) - tension-compression				
cycle 1	$\mu = 0.91$ $\sigma = 0.27$ $M = 0.0018$	$\mu = -0.06$ $\sigma = 0.31$ $M = 0.0004$	$k = 3.71$ $\lambda = 0.99$ $M = 0.0025$	$\alpha = 11.13$ $\beta = 11.65$ $M = 0.0006$
cycle 50	$\mu = 0.88$ $\sigma = 0.41$ $M = 0.0009$	$\mu = -0.05$ $\sigma = 0.47$ $M = 0.0006$	$k = 2.48$ $\lambda = 1.05$ $M = 0.0005$	$\alpha = 4.92$ $\beta = 4.94$ $M = 0.0002$
cycle 100	$\mu = 0.92$ $\sigma = 0.44$ $M = 0.0011$	$\mu = -0.01$ $\sigma = 0.49$ $M = 0.0005$	$k = 2.38$ $\lambda = 1.10$ $M = 0.0007$	$\alpha = 4.57$ $\beta = 4.38$ $M = 0.0002$
freestanding film - tension-compression				
cycle 1	$\mu = 0.69$ $\sigma = 0.49$ $M = 0.0022$	$\mu = -0.21$ $\sigma = 0.69$ $M = 0.0005$	$k = 1.77$ $\lambda = 0.95$ $M = 0.0008$	$\alpha = 2.58$ $\beta = 2.87$ $M = 0.0002$
cycle 5	$\mu = 0.54$ $\sigma = 0.54$ $M = 0.0042$	$\mu = -0.30$ $\sigma = 0.88$ $M = 0.0001$	$k = 1.47$ $\lambda = 0.92$ $M = 0.0018$	$\alpha = 1.87$ $\beta = 2.16$ $M = 0.0008$
225 grains aggregate - tension-compression				
cycle 1	$\mu = 0.50$ $\sigma = 0.33$ $M = 0.0054$	$\mu = -0.58$ $\sigma = 0.63$ $M = 0.0007$	$k = 1.87$ $\lambda = 0.66$ $M = 0.0025$	$\alpha = 2.92$ $\beta = 4.70$ $M = 0.0011$
cycle 15	$\mu = 0.58$ $\sigma = 0.38$ $M = 0.0049$	$\mu = -0.43$ $\sigma = 0.64$ $M = 0.0006$	$k = 2.48$ $\lambda = 0.77$ $M = 0.0023$	$\alpha = 2.93$ $\beta = 4.08$ $M = 0.0011$
cycle 30	$\mu = 0.59$ $\sigma = 0.42$ $M = 0.0037$	$\mu = -0.39$ $\sigma = 0.69$ $M = 0.0007$	$k = 1.76$ $\lambda = 0.81$ $M = 0.0014$	$\alpha = 2.58$ $\beta = 3.43$ $M = 0.0006$

Table 4.3: Identification of statistical distribution functions for the relative equivalent plastic strain in $\{111\}$ grains for different film configurations.

4.2. STRAIN HETEROGENEITIES IN CYCLICALLY DEFORMED THIN FILMS

cycle	Normal	Log-normal	Weibull	Gamma
film with substrate (d/h=1) - tension-compression				
cycle 1	$\mu = 1.15$ $\sigma = 0.34$ $M = 0.0013$	$\mu = 0.16$ $\sigma = 0.29$ $M = 0.0003$	$k = 3.78$ $\lambda = 1.26$ $M = 0.0019$	$\alpha = 11.87$ $\beta = 9.88$ $M = 0.0004$
cycle 50	$\mu = 1.16$ $\sigma = 0.45$ $M = 0.0004$	$\mu = 0.19$ $\sigma = 0.39$ $M = 0.0007$	$k = 2.92$ $\lambda = 1.32$ $M = 0.0004$	$\alpha = 6.83$ $\beta = 5.44$ $M = 0.0003$
cycle 100	$\mu = 1.17$ $\sigma = 0.47$ $M = 0.0004$	$\mu = 0.02$ $\sigma = 0.40$ $M = 0.0006$	$k = 2.87$ $\lambda = 1.34$ $M = 0.0004$	$\alpha = 6.59$ $\beta = 5.18$ $M = 0.0002$
film with substrate (d/h=0.5) - tension-compression				
cycle 1	$\mu = 1.07$ $\sigma = 0.35$ $M = 0.0013$	$\mu = 0.09$ $\sigma = 0.33$ $M = 0.0002$	$k = 3.44$ $\lambda = 1.19$ $M = 0.0016$	$\alpha = 9.71$ $\beta = 8.59$ $M = 0.0003$
cycle 50	$\mu = 1.08$ $\sigma = 0.45$ $M = 0.0006$	$\mu = 0.12$ $\sigma = 0.42$ $M = 0.0005$	$k = 2.75$ $\lambda = 1.24$ $M = 0.0004$	$\alpha = 6.09$ $\beta = 5.17$ $M = 0.0001$
cycle 100	$\mu = 1.09$ $\sigma = 0.47$ $M = 0.0006$	$\mu = 0.15$ $\sigma = 0.43$ $M = 0.0005$	$k = 2.70$ $\lambda = 1.28$ $M = 0.0005$	$\alpha = 5.86$ $\beta = 4.83$ $M = 0.0002$
freestanding film - tension-compression				
cycle 1	$\mu = 1.99$ $\sigma = 0.79$ $M = 0.0002$	$\mu = 0.74$ $\sigma = 0.40$ $M = 0.0009$	$k = 2.88$ $\lambda = 2.29$ $M = 0.0002$	$\alpha = 6.57$ $\beta = 3.04$ $M = 0.0005$
cycle 5	$\mu = 1.72$ $\sigma = 0.87$ $M = 0.0004$	$\mu = 0.61$ $\sigma = 0.52$ $M = 0.0009$	$k = 2.31$ $\lambda = 2.07$ $M = 0.0002$	$\alpha = 4.22$ $\beta = 2.17$ $M = 0.0004$
225 grains aggregate - tension-compression				
cycle 1	$\mu = 0.63$ $\sigma = 0.40$ $M = 0.0031$	$\mu = -0.36$ $\sigma = 0.63$ $M = 0.0005$	$k = 1.91$ $\lambda = 0.82$ $M = 0.0011$	$\alpha = 2.99$ $\beta = 3.90$ $M = 0.0003$
cycle 15	$\mu = 0.73$ $\sigma = 0.46$ $M = 0.0026$	$\mu = -0.22$ $\sigma = 0.63$ $M = 0.0004$	$k = 1.91$ $\lambda = 0.94$ $M = 0.0009$	$\alpha = 3.03$ $\beta = 3.42$ $M = 0.0003$
cycle 30	$\mu = 0.73$ $\sigma = 0.50$ $M = 0.0025$	$\mu = -0.18$ $\sigma = 0.67$ $M = 0.0006$	$k = 1.80$ $\lambda = 0.99$ $M = 0.0007$	$\alpha = 2.68$ $\beta = 2.90$ $M = 0.0003$

Table 4.4: Identification of statistical distribution functions for the relative equivalent plastic strain in $\{001\}$ grains for different film configurations.

4. MECHANICAL BEHAVIOUR OF COPPER THIN FILMS UNDER CYCLIC LOADING

cycle	Normal	Log-normal	Weibull	Gamma
film with substrate (d/h=1) - cyclic tension				
cycle 1	$\mu = 1.13$	$\mu = 0.17$	$k = 3.34$	$\alpha = 10.00$
	$\sigma = 0.39$	$\sigma = 0.32$	$\lambda = 1.27$	$\beta = 8.27$
	$M = 0.0042$	$M = 0.0042$	$M = 0.0050$	$M = 0.0044$
cycle 50	$\mu = 1.16$	$\mu = 0.20$	$k = 3.24$	$\alpha = 9.32$
	$\sigma = 0.41$	$\sigma = 0.33$	$\lambda = 1.30$	$\beta = 7.48$
	$M = 0.0030$	$M = 0.0036$	$M = 0.0036$	$M = 0.0035$
cycle 100	$\mu = 1.17$	$\mu = 0.20$	$k = 3.29$	$\alpha = 9.50$
	$\sigma = 0.41$	$\sigma = 0.33$	$\lambda = 1.31$	$\beta = 7.58$
	$M = 0.0028$	$M = 0.0034$	$M = 0.0034$	$M = 0.0033$
film with substrate (d/h=0.5) - cyclic tension				
cycle 1	$\mu = 1.10$	$\mu = 0.12$	$k = 3.69$	$\alpha = 11.24$
	$\sigma = 0.33$	$\sigma = 0.30$	$\lambda = 1.21$	$\beta = 9.79$
	$M = 0.0014$	$M = 0.0001$	$M = 0.0020$	$M = 0.0003$
cycle 50	$\mu = 1.11$	$\mu = 0.13$	$k = 3.43$	$\alpha = 9.67$
	$\sigma = 0.36$	$\sigma = 0.33$	$\lambda = 1.24$	$\beta = 8.23$
	$M = 0.0013$	$M = 0.0002$	$M = 0.0015$	$M = 0.0002$
cycle 100	$\mu = 1.07$	$\mu = 0.02$	$k = 3.39$	$\alpha = 9.45$
	$\sigma = 0.35$	$\sigma = 0.33$	$\lambda = 1.20$	$\beta = 8.34$
	$M = 0.0012$	$M = 0.0003$	$M = 0.0014$	$M = 0.0002$

Table 4.5: Identification of statistical distribution functions for the relative equivalent plastic strain in $\{001\}$ grains for different film configurations.

4.3 Plasticity induced roughness

Heterogeneous plastic deformation is known to induce roughness at the free surface in films and coating (Parisot et al. [2001], Raabe et al. [2003], Sachtleber et al. [2004]). Starting from an initially ideal plane surface in the simulation, the crystal plasticity model provides estimates of plasticity induced roughness. The purpose of this section is to quantify the obtained roughness and its evolution during cyclic loading.

4.3.1 Definition of roughness parameters

Plasticity induced roughness is developed due to the 3D character of glide processes and the grain to grain strain incompatibility which produces non-homogeneous out of plane displacement. Figure 4.14 shows the map of out of plane displacement U_3 for the same aggregate placed in all three film configurations. Displacements are shown after 100 and 30 (free-standing) cycles with a magnification of 50 for the illustration. The constraining effect of the flat interface can be clearly seen in figures 4.14(a) and (b) compared with free-standing film (c). In figure, blue grains correspond to a sink on the surface and red zones to a rise. Several thin and acute mountains can be seen, that coincide with grain boundaries, especially in the films on substrate.

The absolute roughness R_{RMS} or root mean square roughness and the relative roughness R of the free surface are defined as:

$$R_{RMS} = \sqrt{\frac{1}{n} \sum_{i=1}^n (U_3(x^i, y^i) - \overline{U_3}(x^i, y^i))^2}, \quad (4.7)$$

$$R = \frac{R_{RMS}}{|\langle \overline{U_3} \rangle|}, \quad (4.8)$$

where $U_3(x^i, y^i)$ is the displacement component of the given surface node (x^i, y^i) with respect to its initial position, $\overline{U_3}(x^i, y^i)$ is the displacement of the average plane at the given position. The average plane is obtained by linear regression of the values of displacement using the least square method. Example of such plane is shown in figure 4.15. The relative roughness R is obtained by normalizing R_{RMS} by the average displacement value of the

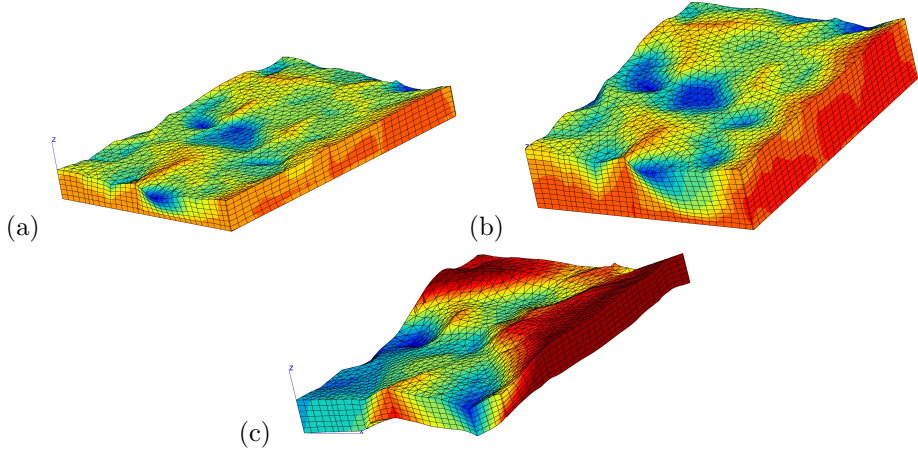


Figure 4.14: Deformed state of a multicrystalline aggregate: (a) film on a substrate with $d/h = 1$, (b) film on a substrate with $d/h = 0.5$, (c) free-standing film. The grain morphology and orientation are the same in the three simulations. The considered field variable is the displacement component U_3 . For the illustration, displacements have been magnified by a factor of 50.

average plane $\langle \overline{U_3} \rangle$. The previous definitions are valid for a sufficiently high number n of uniformly distributed points on the surface. Here the chosen points ($n = 4000$ in average) are the finite elements nodes at the free surface, the distribution of which is almost uniform.

A local relative roughness parameter can be defined at each point (x^i, y^i) of the free surface by:

$$R_{loc}(x^i, y^i) = \frac{U_3(x^i, y^i) - \overline{U_3}(x^i, y^i)}{|\langle \overline{U_3} \rangle|} \quad (4.9)$$

4.3.2 Results

The evolution of local relative roughness for the different film configurations at different cycles is shown in figure 4.16. The relative roughness is found to vary between -120% and +120% in films with a substrate and between -200% and 200% in a free-standing film. The comparison of the maps shows that the value of R_{loc} increases during cycling: sinking grains have the tendency to sink even more, rising grain boundaries rise even more after cycling. The grain boundaries are superimposed on the mesh to confirm that rising regions

4.3. PLASTICITY INDUCED ROUGHNESS

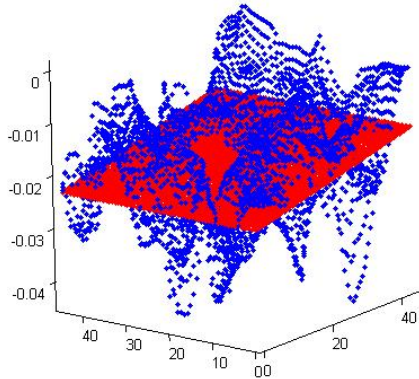


Figure 4.15: Example of the average plane computed by the least square method from the displacement U_3 . The surface nodes are blue points and the average plane is made of red points. Displacement is magnified by factor of 500.

are mainly located at grain boundaries in the case of films on a substrate.

The analysis of plastic strain in differently oriented grains has shown that the $\{001\}$ and random grains on a substrate are significantly more deformed than $\{111\}$ grains. This plastic deformation induces also higher roughness in these grains compared with the $\{111\}$ ones. To show that, the $\{001\}$ and random grains are indicated in figure 4.16(a) on the left. The same is shown in figure 4.17 for the large aggregates. These figures show that local roughness is higher in these grains. For comparison, in the experimental works (Schwaiger et al. [2003], Schwaiger and Kraft [2003]), higher amounts of extrusions were observed in the grains $\{001\}$ which cause higher roughening of the surface.

The evolution of global roughness R is given in figure 4.18 as a function of cycle number, for three film configurations and both loading conditions and for all computed realizations. Roughness is computed at the maximal prescribed strain level. The global roughness for films on a substrate is found to saturate after about 10 cycles which is early compared with the saturation of cyclic hardening shown in figure 4.8. The dispersion in the asymptotic roughness associated with the different realizations is about 25% of the mean. The relative

roughness for tension–compression loading is higher than for the cyclic tension even though the prescribed maximal deformation is smaller. The highest roughness and its dispersion is found for the free–standing films and no saturation is indicated up to 55 cycles for tension–compression. The evolution of relative global roughness during the cyclic tension is different. The relative global roughness is smaller compare to the tension–compression case. This is in constrast with the behaviour of aggregates on a substrate. The relative roughness values during cyclic tension increase slower than in the case of tension–compression. Figure 4.19 shows the evolution of the surface roughness in large aggregate. The values correspond to ones obtained in small aggregates.

The roughness amplitude, defined as $|U_3^{max} - U_3^{min}|$ at a given time, is of the order of magnitude 1/100 of the film thickness in our simulations. This value is ten times smaller than the values measured in experiments (Schwaiger et al. [2003], Schwaiger and Kraft [2003]). Two reasons can be put forward to explain this feature. First the experimental results were obtained after 10 000 cycles in contrast to 100 cycles simulated in the present work. Secondly, roughness measured in the experiments is related to the height of the extrusions. These extrusions are related to the movement of dislocations. In the thin film with thickness of about 1 μm these extrusions are created by dislocation events such as reactions of individual dislocations and multiple sources activation (Schwaiger et al. [2003]). In the thicker films (100 μm) these extrusions are associated with the formation of persistent slip bands (Schwaiger and Kraft [2003]). The used continuum crystal plasticity framework is not able to predict transition in the damage mechanism, leading to extrusions and intrusions, without or with PSB formation. This model is able to provide rough comparison of the areas of strain accumulation with extrusion areas. This will be discussed in the chapter 5. Precise simulations of these effects may be necessary at a lower scale than that accounted for by the model. The simulations based on dislocation dynamics in a single grain plead for such a discrete modelling of dislocation reactions (Weygand and Gumbsch [2005]) and PSB formation (Déprés et al. [2004]). These simulations will be presented in the chapters 6.

4.3. PLASTICITY INDUCED ROUGHNESS

An important result of the computations is the fact that roughness is mainly observed at grain boundaries that sink or rise. This is due the high strain incompatibilities between neighbouring grains. This feature can be compared with the experimental observations and simplified model presented in (Wilson and Lee [2001]). The authors indicate that grain boundary rising or sinking is the predominant mechanism responsible for roughness development in some aluminium alloys during metal forming. In their observations, the emergence of slip lines, not accounted for in our simulations, played a smaller role in the roughening process. The proposed continuum crystal plasticity framework is indeed best suited for the interpretation of such experimental evidence.

Saturation of global roughness does not mean that the local roughness does not evolve any longer. The evidence of ratcheting phenomena was found at certain locations on the free surface in the aggregates. Such a situation is illustrated in figure 4.20 where the local roughness is plotted along the grain boundary overlined in white in figure 4.16(a) for $N = 1, 100, 500$ and 1000 . An increase in the local roughness at several points of the grain boundary is observed from $N = 100$ to $N = 1000$ although both the overall stress-strain loop and the global roughness are already saturated. The simulation of higher number of cycles up to 1000 cycles shows that ratchetting phenomena tend to saturate, except at some nodes. A continuing ratcheting effect may be the precursor of fatigue strain accumulation and possible damage initiation.

4. MECHANICAL BEHAVIOUR OF COPPER THIN FILMS UNDER CYCLIC LOADING

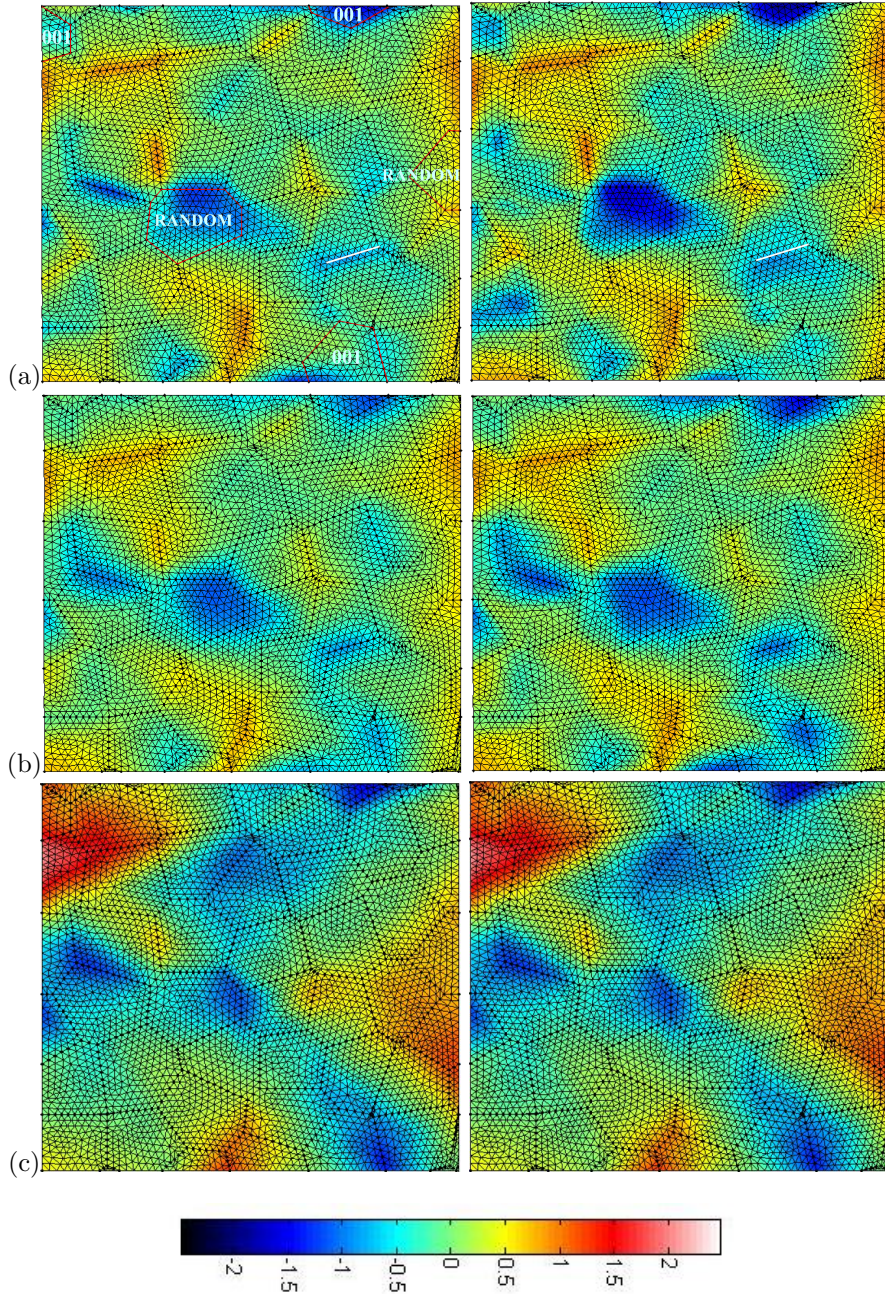


Figure 4.16: Roughness maps R_{loc} after $N = 1$ (left) and $N = 100$ (right) at maximal overall strain: (a) film on a substrate with $d/h = 1$, (b) film on a substrate with $d/h = 0.5$, (c) free-standing film.

4.3. PLASTICITY INDUCED ROUGHNESS

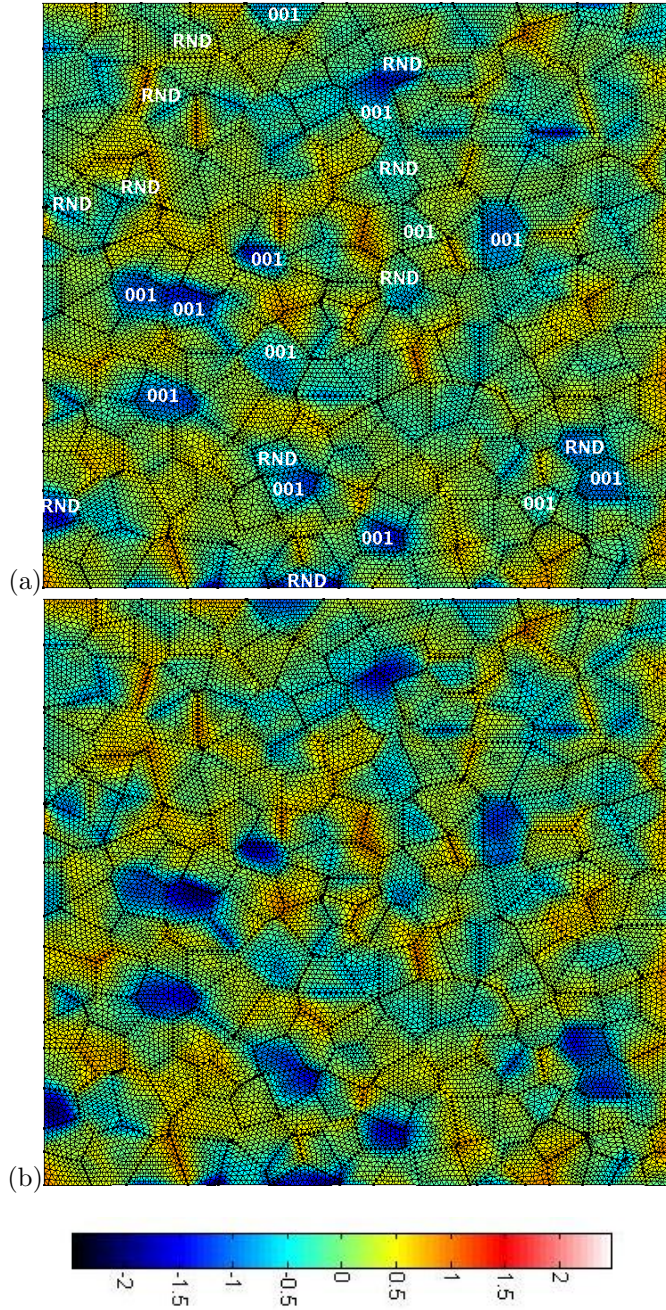


Figure 4.17: Roughness maps R_{loc} after $N = 1$ (a) and $N = 29$ (b) at maximal overall strain for large aggregate (225 grains).

4. MECHANICAL BEHAVIOUR OF COPPER THIN FILMS UNDER CYCLIC LOADING

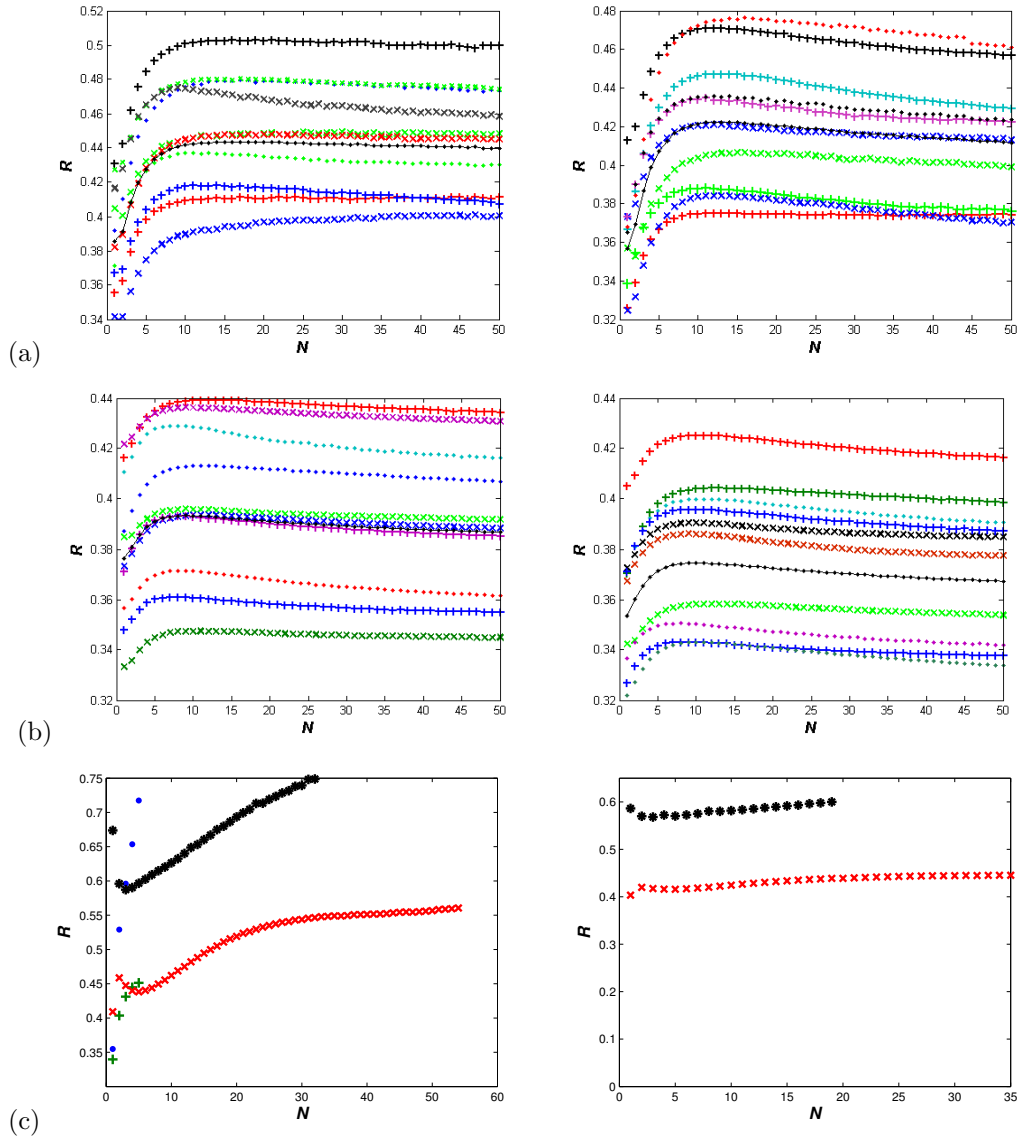


Figure 4.18: Evolution of global roughness with the number of cycles during cyclic tension–compression (left) and cyclic tension (right): (a) film on a substrate with $d/h = 1$, (b) film on a substrate with $d/h = 0.5$, (c) free–standing film with $d/h = 0.5$. The results are plotted for all considered realizations, the black curve in cases (a) and (b) corresponds to the mean value.

4.3. PLASTICITY INDUCED ROUGHNESS

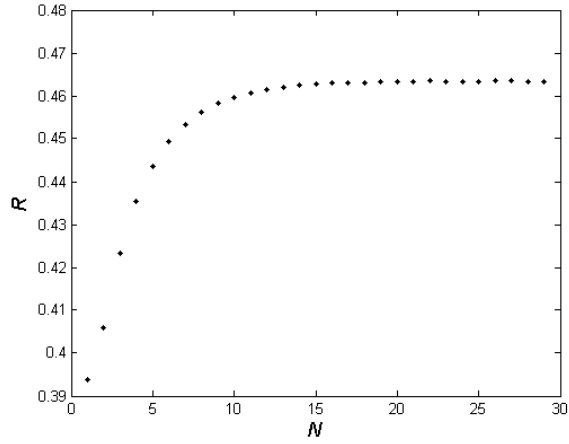


Figure 4.19: Evolution of global roughness with the number of cycles during cyclic tension–compression of the large aggregate (225 grains).

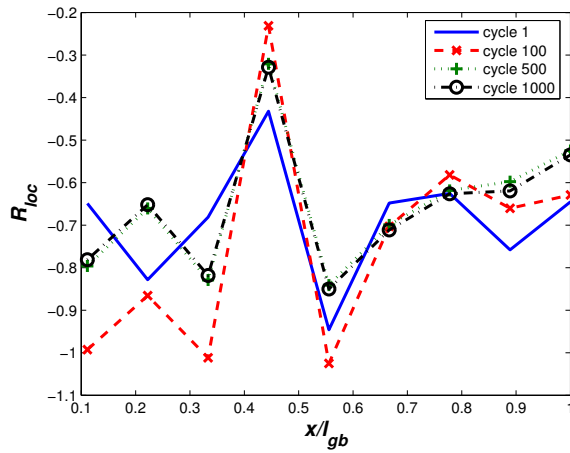


Figure 4.20: Evolution of local roughness along a selected grain boundary at the free surface. This grain boundary is marked by a white line in figure 4.16(a) on the left. Its total length is l_{gb} .

4.4 Conclusion

A large-scale computational and statistical strategy has been undertaken to investigate the development of strain heterogeneities and free surface roughness in multicrystalline films on a substrate subjected to cyclic loading conditions, based on continuum crystal plasticity. For comparison, the case of free-standing films was also tackled. The main results are the following:

- Saturation of overall stress-strain loops towards the same limit cycle is observed in cyclic tension-compression and cyclic tension after about 70 cycles for films on a substrate. Significant overall kinematic hardening of the films is obtained which is due to both intergranular interaction and local back-stress component introduced in the crystal plasticity model.
- A large dispersion in plastic strain distribution is observed in all film configurations with plastic strain concentration factors ranging from 0 to 5. This dispersion is shown to increase significantly during cycling in films on substrates but not in free-standing films.
- Higher deformation levels and dispersion are found in the $\{001\}$ and random grains than in $\{111\}$ grains which is in accordance with experimental results provided in (Schwaiger et al. [2003], Schwaiger and Kraft [2003]).
- The plastic strain distributions are found to be asymmetric in all films with peak decreasing and distribution broadening in films on a substrate during cycling. Comparison of the plastic strain distributions shows also higher constraint of the grains in $d/h=0.5$ films and small 50 grains aggregates compared to large 225 grain aggregate.
- Plasticity induced roughness is shown to develop due to strain incompatibilities from grain to grain. The global relative roughness is found to saturate within 10 cycles at values in the range 40–50% in films on a substrate and towards higher values in free-standing films.

4.4. CONCLUSION

- Higher roughness levels are found to develop during cyclic tension–compression than during pure cyclic tension for the same strain amplitude and same limit cycle.
- The rising and sinking of grain boundaries in films on a substrate is observed at many places. This is the preferential location where local ratcheting phenomena can be observed.

Some of these results were published in (Šiška et al. [2007b]).

Chapter 5

Comparison of the simulations with experimental data

The objectives of this chapter are comparing the results of simulations with the experimental results available in the literature. Such a comparison tests the suitability of the crystal plasticity framework in the case of thin film structures.

5.1 Introduction – experiments on thin films

The used experimental results are taken from the papers (Kraft et al. [2000], Hommel and Kraft [2001], Schwaiger et al. [2003]). These experiments contain tensile and cyclic tensile tests of copper thin films on a soft polyimide substrate.

The experiments were realized with samples consist of the copper film the polyimide substrate (Capton, DuPont) with thickness 125 μm . The copper film was sputtered on this substrate. The thickness of the sputtered films is within the range 0.4 to 3.2 μm . The effect of grains size was investigated with the films of thickness 1 μm and different grain sizes. The film textures were investigated by the Focus Ion Beam (FIB) microscopy. The results are presented in (Hommel and Kraft [2001]).

The tensile tests were performed with the electro-mechanical tensile machine. The substrate was subjected to displacement controlled tensile loading which was divided into steps of about 10 μm . After each step the elastic strain in the film was measured by X-ray

5. COMPARISON OF THE SIMULATIONS WITH EXPERIMENTAL DATA

diffraction. Each measurement took about 30 min, therefore, the effective strain rate was 10^{-7} s^{-1} . The imposed global strain was measured as the displacement of the markers on the substrate by the laser extensometer.

The elastic strain in the films was measured by X-ray diffraction. This method measured the lattice spacing which determines the elastic strain state of the film. The method called $\sin^2 \psi$ - method was used to determine the elastic strain state. In this method the interplanar spacing of a particular set of crystallographic planes is measured as function of the inclination angle ψ which is the angle between the normal of the film surface and the normal of diffracting planes. The chosen diffracting planes are $\{311\}$ for (111) oriented grains and $\{420\}$ for (001) oriented grains. The layout of the measuring devices allows measuring the diffraction of the X-rays which come off only under certain angles. These possible incident angles which allow the measurement of the lattice spacing in the chosen planes are 19.7° and 46.3° for $\{331\}$ planes in (111) oriented grains and 8.9° and 45.8° for $\{420\}$ planes in (001) oriented grains. These conditions (incident angles for chosen diffracting planes) cause that the measurements include only grains having direction $[211]$ in (111) grains and direction $[001]$ in (001) grains aligned to the tensile direction (Hommel and Kraft [2001]). The results of lattice spacing for these two incident angles were then extrapolated for the values of angles which give $\sin^2 \psi = 1$ and $\sin^2 \psi = 0$. These values correspond to lattice spacing in the tensile direction (d_2) and direction perpendicular to the film plane (d_3) respectively. The elastic strain in given direction can be calculated as:

$$\varepsilon_{22}^{el} = \frac{d_2 - d_0}{d_0}, \quad \varepsilon_{33}^{el} = \frac{d_3 - d_0}{d_0}, \quad (5.1)$$

where d_0 is lattice unstrained spacing. The corresponding stresses can be then calculated by the following equations:

$$\sigma_{11} = C'_{11}\varepsilon_{11}^{el} + C'_{12}\varepsilon_{22}^{el} + C'_{13}\varepsilon_{33}^{el}, \quad (5.2)$$

$$\sigma_{22} = C'_{12}\varepsilon_{11}^{el} + C'_{11}\varepsilon_{22}^{el} + C'_{13}\varepsilon_{33}^{el}, \quad (5.3)$$

$$\sigma_{33} = C'_{13}\varepsilon_{11}^{el} + C'_{13}\varepsilon_{22}^{el} + C'_{33}\varepsilon_{33}^{el}, \quad (5.4)$$

where the elasticity coefficients C'_{11} , C'_{12} , C'_{13} and C'_{33} in the laboratory coordinates are function of C_{11} , C_{12} and C_{44} defined in the crystal coordinates. Using the thin film assumption $\sigma_{33} = 0$ and excluding shear components we have a system of three equations for three unknowns (σ_{11} , σ_{22} and ε_{22}). The value of unstrained lattice spacing d_0 is crucial for the determination of the elastic strain state. For the thin films with (111) texture exists a certain angle ψ_0 for which the lattice spacing is independent of the stresses in the film and the temperature (Kraft et al. [2000]). This angle is given by:

$$\sin^2 \psi_0 = \frac{2C'_{13}}{2C'_{13} + C'_{33}}. \quad (5.5)$$

The lattice spacing belonging to this angle ψ_0 fulfills the conditions for the unstrained lattices spacing. The strain in the direction of tension in the film is determined as follows: The initial value of the elastic strain in the film prior testing which is measured by X-ray diffraction is noted as $\varepsilon_{el,0}$. The applied strain ε_{app} is measured by the extensometer and is zero at the beginning. The total film strain is $\varepsilon_{total} = \varepsilon_{el,0} + \varepsilon_{app}$. The plastic strain is then given as difference of the total strain and elastic strain measured by X-ray: $\varepsilon_{pl} = \varepsilon_{total} - \varepsilon_{el}$ (Hommel and Kraft [2001]).

The X-ray diffraction also allows to estimate the micro stresses and dislocation densities which are related to the width of the measured peaks of X-rays. This peak width is determined as classic FWHM (full width at half maximum). During the tensile loading the peak width increases and this broadening (β_s) is related to the increase of the internal micro strains which can be described by the dislocation density (Hommel and Kraft [2001]). The dislocation density can be estimated as:

$$\rho = \frac{3}{4} \frac{\pi(1+\nu)}{b^2 \ln(r/r_0)} \beta_s^2 (\cot \theta)^2, \quad (5.6)$$

where ν is Poisson's ratio, b is Burgers vector, θ is Bragg angle and r/r_0 the ratio between an outer and inner cut-off radius of the dislocation strain field. This equation describes the increase of the dislocation density due to the deformation of the film.

5.2 Simulations of aggregates with suitable grain orientations

A comparison of the simulations with experimental results has been already presented in chapter 3. This comparison has shown that used model is not able to predict different amount of hardening in (111) and (001) oriented grains. However all the grains of the aggregates were considered for the comparison. In contrast only some grains are taken into account during the measurement. These are grains with directions [211] for (111) grains and [001] for (001) grains aligned to the tensile direction. In this section we investigate aggregates which contain different numbers of the correctly oriented (111) grains. The (001) oriented grains are not investigated due to their small number (3 per aggregate).

Five different aggregates were created with 5, 7, 10, 12 and 15 [211](111) grains in total of 50 grains. The ratio $d/h=1$ and the boundary conditions correspond to those in the section 4.1.1 of the previous chapter noted as “film on a stiff substrate”. The typical global stress–strain curves which are representative for all aggregates are shown in figure 5.1(a),(b). These figures show the resulting stress–strain curves for different sets of grains in one aggregate. The blue curve is the stress–strain curve of all grains in aggregate. The red one describes the behaviour of all (111) oriented grains and the green one is the result for the grains with orientation [211] (111). These results show very small differences between these curves. The [211] (111) grains are the hardest grains from the compared grains groups but the differences from the results for all (111) grains are about 2 % and differences from the overall curve is about 5 %. Figure (b) also shows that the [211](111) grains are less deformed than the grains from other two groups. Figure 5.2 then shows the comparison of the overall stress strain curves for the aggregates with different number of the [211] (111) oriented grains (5, 7, 10, 12 and 15). These curves show that the amount of hardening does not increase with increasing number of these grains in aggregate. So, it can be stated that the [211] (111) grains are generally harder than other (111) oriented grains but the difference remains very small. The discrepancy between the experimental results and simulations in chapter 3 is not caused by the fact that all (111) grains are used.

5.3. COMPARISON OF MACROSCOPIC BEHAVIOUR

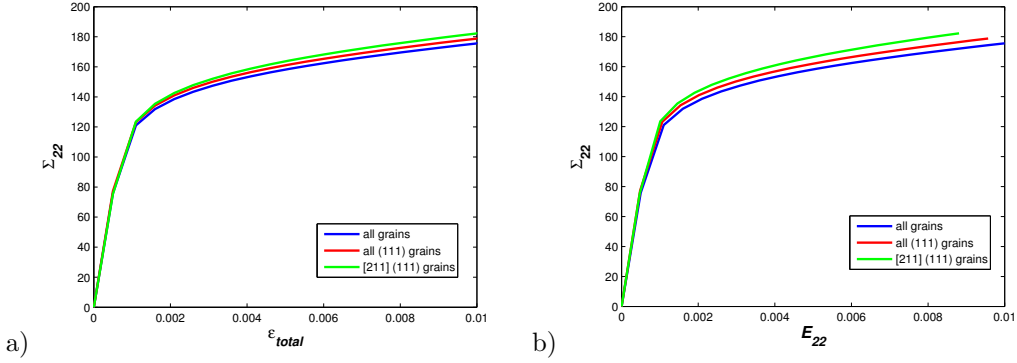


Figure 5.1: Stress–strain curves for different grains in aggregate on a stiff substrate: blue – all grains, red – all (111) grains, green – [211](111) grains.

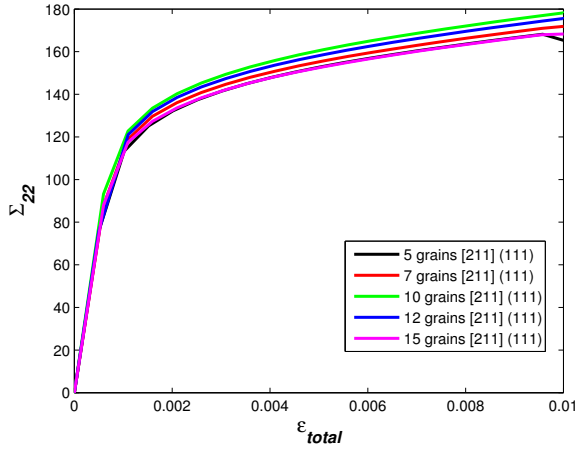


Figure 5.2: Stress–strain curves for aggregates with a different number of [211] (111) grains.

5.3 Comparison of macroscopic behaviour

The comparison of the macroscopic behaviour is realized by the comparison of the evolution of the elastic strain in the tensile direction, in-plane elastic strain perpendicular to the tensile direction and stress in the tensile direction. The comparison is performed for the simulations with aggregates that contain [211] (111) oriented grains (see previous section

5.2), free-standing films from chapter 4 and films on a polyimide substrate from chapter 3.

The first comparison is performed for the aggregates with [211](111) oriented grains. The boundary conditions simulate the tensile test of the film on a stiff substrate (chapter 4.1.1). The substrate is not formed by a mesh but its influence is describe only by these boundary conditions. This assumption of stiff substrate is different from the experiments, but the comparison can show if there can be founded some common features in behaviour. The experimental results are taken from (Kraft et al. [2000]). The results are obtained from the tensile test of the 1 μm thick copper thin films. They show the evolution of the elastic strain in film with respect to total imposed strain by the substrate. The stress in the direction of tension is then computed according to equations (5.4). The experimental results show whether or not is the strain fully transferred from the substrate to the film and at which value of imposed strain the film starts to yield. The first comparison is presented in figure 5.3. This plot shows the elastic strain in the tensile direction E_{22}^{el} which is computed for all grains in aggregate. The experimental results (points) show the clear deviation from the elastic behaviour (dashed line) during which all imposed strain is transferred to the film. The simulation results (lines - each lines = one realization of aggregate) show larger declination from this elastic behaviour which corresponds to the fact that there is higher amount of plasticity in the simulations. The deviation from the ideal behaviour (dashed line) starts in simulations earlier at about 0.05% of total imposed deformation while the declination in experiments starts at 0.1% of total imposed deformation.

Figure 5.4 shows the evolution of the in-plane elastic strain perpendicular to the tensile direction E_{11}^{el} . The experimental results (points) show several features: The strain does not start at zero which means that there is some initial strain before testing or this offset could be also some measuring errors. The experimentally measured strain increases until the 0.001 of applied strain. Then the film starts to yield and the substrate constrains the deformation of the film in this direction, therefore, the magnitude of the strain decreases (Kraft et al. [2000]). The results of simulations show that the elastic strain E_{11}^{el} starts at 0 and increases up to 0.05% of total imposed strain and then the film starts yielding and the elastic strain starts to decreases. The slope of the curves and the experimental results are

5.3. COMPARISON OF MACROSCOPIC BEHAVIOUR

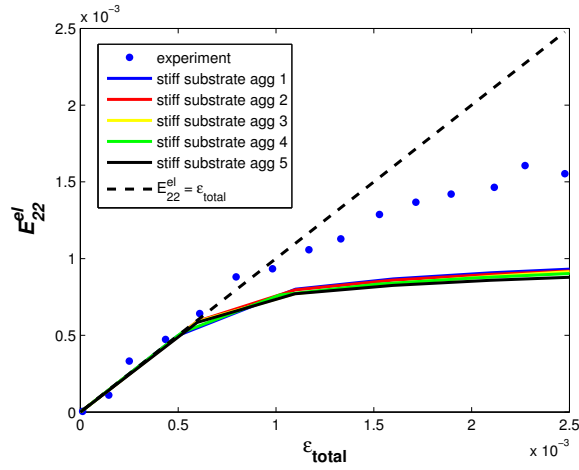


Figure 5.3: Evolution of strain in the tensile direction in aggregates on a stiff substrate.

similar within the range $0 - 0.0005$ of total imposed strain. This could be caused by the similar Poisson ratios of the Capton ($\nu = 0.34$) and silicon ($\nu = 0.2785$). The slope of the decrease of the elastic strain is then higher in the experimental results.

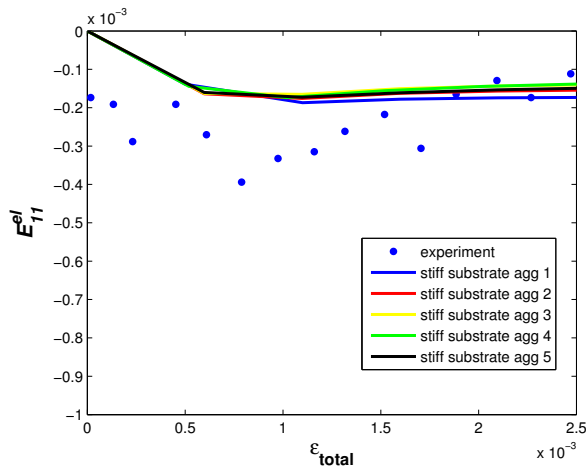


Figure 5.4: Evolution of strain in the direction perpendicular to tensile direction (in-plane of the film) in aggregates on a stiff substrate.

5. COMPARISON OF THE SIMULATIONS WITH EXPERIMENTAL DATA

The comparison of the stress in the tensile direction (Σ_{22}) is shown in figure 5.5. The experimental results (points) show the high amount of hardening in the real film. The stress values are about 2.5 – 3 times higher in experiment than in simulations. This discrepancy shows that the interactions between the slip systems and individual grains are much higher in real thin films. The average value of Σ_{33} , component perpendicular to the film plane is in the simulations approximately $10^5 - 10^6$ times smaller than the other components (Σ_{11}, Σ_{22}). The shear components are also $10^3 - 10^4$ times smaller than components Σ_{11} and Σ_{22} . This proves the validity of thin film assumption: $\sigma_{33}=0$.

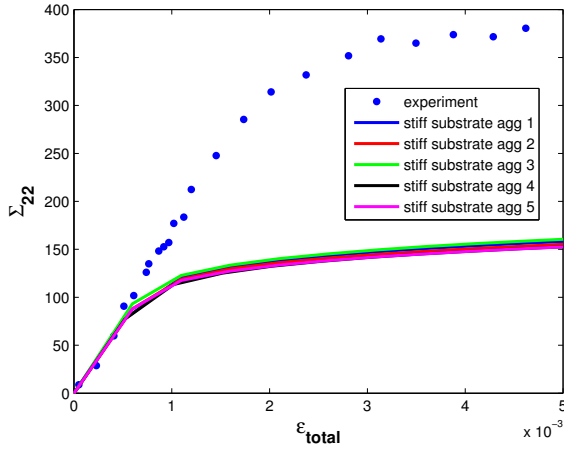


Figure 5.5: Evolution of stress in the tensile direction (in-plane of the film) in aggregates on a stiff substrate.

The second case of comparison is performed for the aggregates subjected to the boundary conditions noted as “free-standing” (see section 4.1.1). This kind of boundary conditions can be also used for simulation of the film on a soft substrate. The results for elastic strain evolution are shown in figure 5.6(a),(b). The case (a) shows the evolution of elastic strain in tensile direction (E_{22}^{el}) and case (b) shows the in-plane elastic strain perpendicular to tensile direction (E_{11}^{el}). The simulations results show the features similar to the previous case. The deviation from the elastic behaviour is larger than in the experimental data. The films have the pure elastic behaviour up to about 0.6×10^{-3} of the total imposed strain which is more

5.3. COMPARISON OF MACROSCOPIC BEHAVIOUR

than in previous case. This is caused by the smaller constraining of the bottom surface compare to previous case. The elastic strain E_{11}^{el} increases with the similar slope in range $0 - 0.6 \times 10^{-3}$. The decrease after yielding is comparable with the previous case of the film on a stiff substrate. The comparison of the stress in the tensile direction is shown in figure 5.7. The differences between the experiment and simulations are even higher in this case because the aggregates are less constrained, therefore, the stress does not increase as much as in previous case. The thin film assumption ($\sigma_{33} = 0$) is also valid in this case.

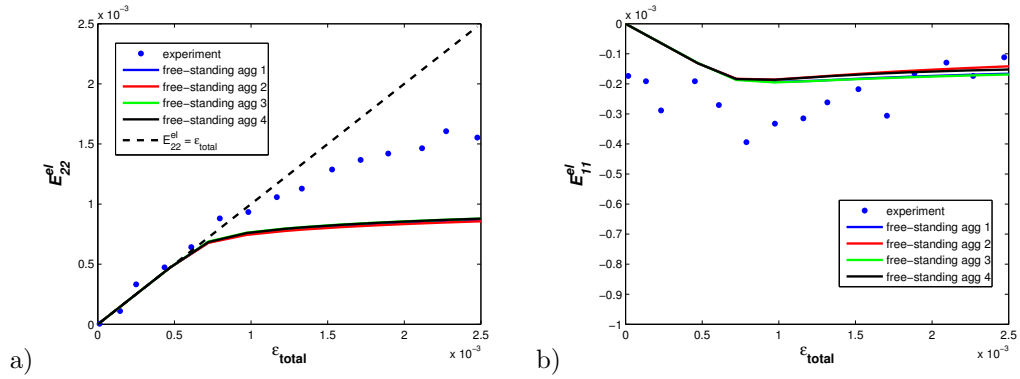


Figure 5.6: Evolution of strain in the free-standing aggregates a) strain in tensile direction, b) strain in direction perpendicular to the tensile direction (in-plane of the film).

The last comparison is made for the aggregates with the meshed polyimide substrate. These simulations set up is the closest to the experimental conditions because of the physical presence of the substrate. The comparison of the elastic strains is shown in figure 5.8(a) and (b). The case (a) shows that the curves are much more deviated from the dashed line than the experimental results. The curves start to deviate from the elastic behaviour a bit earlier than in previous case. This corresponds to the fact that the soft polyimide substrate constrains the bottom surface more than the free-standing conditions. The comparison of the data for the perpendicular elastic strain (b) shows that this elastic strain increases with lower slope than in previous case. This is due to the lower value of ν of polyimide substrate. The decrease of the curves starts at about 0.75×10^{-3} total applied strain. This decrease occurs earlier compare to the experimental data. The slope of the decreasing

5. COMPARISON OF THE SIMULATIONS WITH EXPERIMENTAL DATA

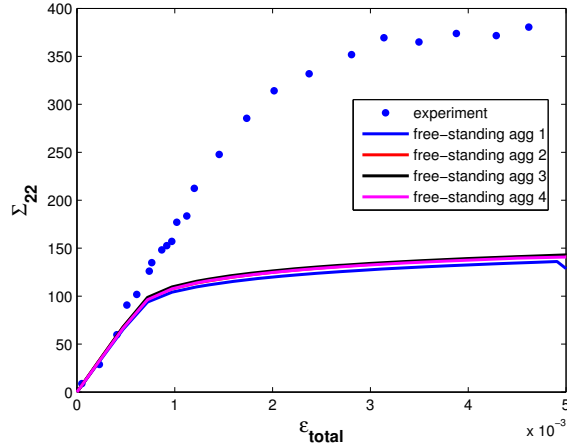


Figure 5.7: Evolution of stress in the tensile direction in the free-standing aggregates.

part of experimental data is again higher than in the simulations results. The difference between the simulations and experiments can be caused by the fact that in experiments is the substrate 125 times thicker than the film while in the simulations is the substrate only 5 times thicker. Therefore the film is not constrained enough. The comparison of the tensile stress is presented in figure 5.9. The simulated stress levels are comparable with the previous case of free-standing films. The thin film assumption is also valid in this case. These results show larger amount of plasticity in the simulations. This fact together with the large differences of hardenings show that the used continuum model is not able to account all possible interactions which occurs in the real films (slip system interactions, grain to grain interactions, film – substrate interactions, dislocations interactions).

5.4 Comparison of local strain and displacement evolution

As mentioned in the first section of this chapter, the X-ray method allows investigation of the development of microstrains in the films by the measuring of the broadening of the peak of diffracted X-rays. This broadening is related to the increase of dislocation density by

5.4. COMPARISON OF LOCAL STRAIN AND DISPLACEMENT EVOLUTION

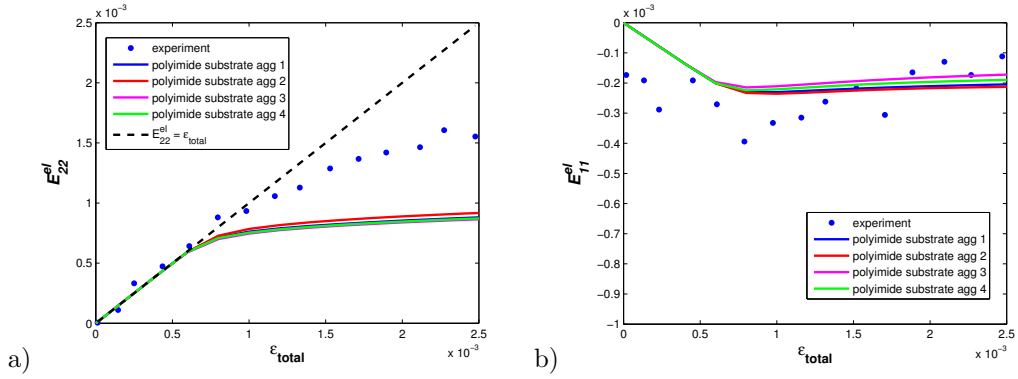


Figure 5.8: Evolution of strain in the aggregates on polyimide substrate a) strain in tensile direction, b) strain in direction perpendicular to the tensile direction (in-plane of the film).

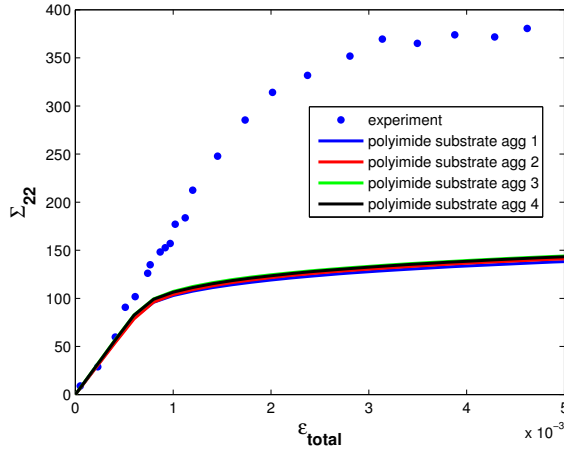


Figure 5.9: Evolution of stress in the tensile direction in the aggregates on polyimide substrate.

the equation (5.6). The peak broadening increases with square root of dislocation density.

Dislocation density can be related to plastic strain by Orowan equation:

$$\Delta\epsilon_p = \rho b \Delta x, \quad (5.7)$$

5. COMPARISON OF THE SIMULATIONS WITH EXPERIMENTAL DATA

where $\Delta\varepsilon$ is the increase of the plastic strain, ρ is the dislocation density, b is the Burgers vector and Δx is the increase of the lattice displacement. The plastic strain can also increase due to the increasing of the dislocation density. Let us assume for simplicity that the dislocation density grows linearly with respect to equivalent plastic strain. We call $\tilde{\rho}$ this density estimated from FE simulations. A more accurate estimation of dislocation densities can be gained from the crystal plasticity model but a rude estimate is sufficient in this section due to the precision of experimental evaluation of ρ by the peak broadening method. As a result, the peak broadening is proportional to the square root of this dislocation density ($\beta_s \propto \sqrt{\tilde{\rho}}$). The dislocation density for each aggregate can be computed as:

$$\tilde{\rho} = \int_V \tilde{\rho}(x) dx \propto \int_V \varepsilon_{eq}^p(x) dx, \quad (5.8)$$

where $(\varepsilon_{eq}^p)(x)$ is the equivalent plastic strain at point x in aggregate. Figure 5.10(a) shows the experimental results (points) of peak broadening with respect to total imposed strain (Hommel and Kraft [2001]). The case (b) shows the evolution of $\tilde{\rho}$ with respect to the total imposed strain for different realizations of aggregates and different boundary conditions (points, crosses, circles). Experimental and simulated data were fitted by the function $y = k\sqrt{\varepsilon_{total}} + q$. This fitting shows that both data are proportional to $\sqrt{\varepsilon_{total}}$ and this means that the evolution of the plastic microstrains in simulations is similar to that in the real films in experiment. The best fitting occurs for the aggregates with polyimide substrate and the worst one is for the case of free-standing films. Such a comparison is only qualitative and very crude because the relation between the peak broadening mechanism and the evolution of dislocation density remains qualitative.

The other phenomena which can be compared with the experiments is the creation of extrusions at the film surface during the cyclic loading. As already mentioned in the section 4.3.2, the used model is not able to predict the formation of extrusion and intrusions in the film, because their formation is caused by the localized discrete slip processes. Formation of such structures in the real films is connected with coalescence of voids and decohesion between the film and the substrate. In such a case, the film is no longer connected to the substrate and the deformation from the substrate is not transferred directly to the film

5.4. COMPARISON OF LOCAL STRAIN AND DISPLACEMENT EVOLUTION

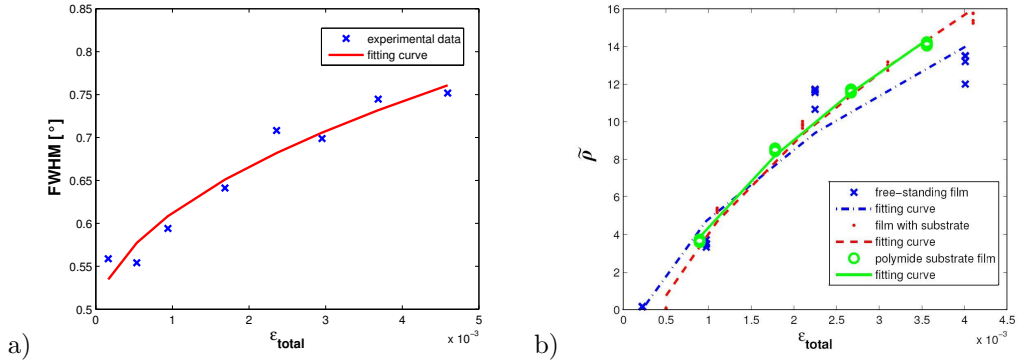


Figure 5.10: a) Evolution of the peak broadening of diffracted X-ray during tensile loading. b) Evolution of the total plastic microstrain during tensile loading.

(Schwaiger et al. [2003]) and the free surface is created. Such places are mostly found in the $\{001\}$ oriented grains and between the twins. Extrusions and intrusions grow and cracks initiate preferably at these locations. However related effects can be found in our simulations of free-standing films. In real films these places are very localized while in the simulations the whole aggregate is supposed to be disconnected from the substrate. But at least a qualitative comparison can be drawn to see if there is a tendency of the films in the simulations to produce some localized deformation zones which can be related to extrusion formation. Two such regions in different aggregates are presented in figure 5.11(a),(b). This figure shows the evolution of the out of plane displacement U_3 during cycling for different type of loading. This displacement is shown when the applied deformation is 0 (residual deformation). It evolves and grows during cycling. Strain localization zones are at the grain boundary between two differently oriented $\{111\}$ grains and between $\{001\}$ and $\{111\}$ grains which is similar to what occurs in real films.

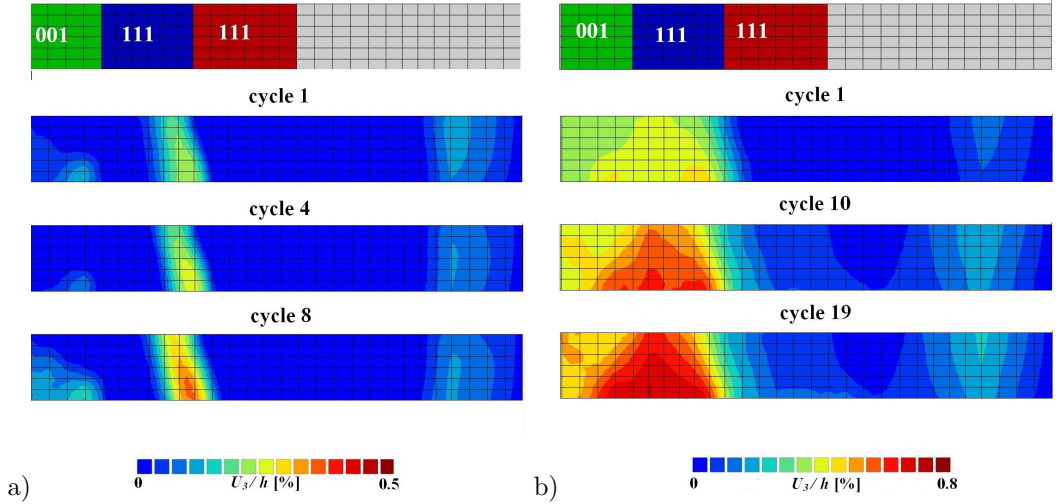


Figure 5.11: Evolution of the residual deformation in the free-standing aggregates during cycling a) cyclic tension, b) tension-compression.

5.5 Comparison of the influence of the different grain morphology

The grain structure of the aggregates used in the simulations is produced by the Voronoï tessellation. This method produces grain shapes which are crude representations of the real grain shapes. The grains have 5 to 7 edges which correspond approximately to real columnar grain structures (Weygand et al. [1998]) but the grain size distribution does not corresponds to the real log-normal one. Therefore simulations with aggregates with more realistic grain shapes are performed to check the differences in results obtained with Voronoï aggregates. The grain shapes are obtained by 2D simulations of grain growth (Weygand et al. [1998]). The resulting 2D image of the grains is then meshed and simple extension into 3D is performed. The grain size thickness ratio (d/h) is approximately equal to 1. The resulting aggregate is again a simplification of reality because the grain boundaries are still regarded as perpendicular to the plane of the film. Also the real copper films contain twins in grains which are not accounted here. The image of the aggregate is shown in figure 5.12 where (001) and RND indicate the position of the {001} and random oriented grains respectively.

5.5. COMPARISON OF THE INFLUENCE OF THE DIFFERENT GRAIN MORPHOLOGY

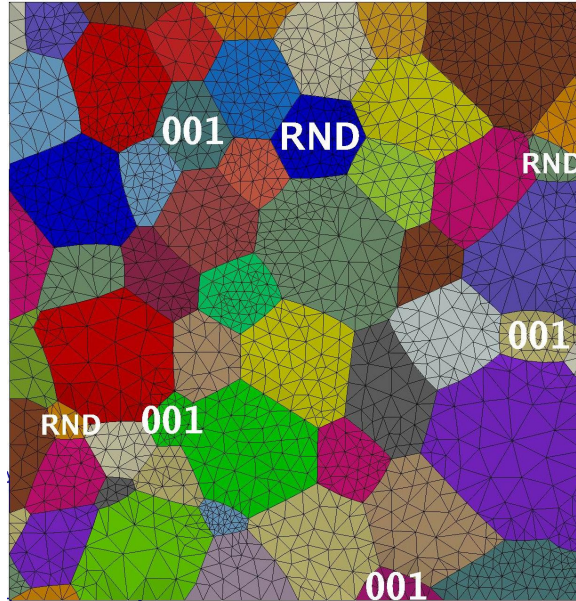


Figure 5.12: The surface of the aggregate with the real shape grains. $\{001\}$ and RND indicates the $\{001\}$ and random oriented grains respectively.

The simulations are performed in the same way as in the chapter 4. Five cycles of tension–compression ($\pm 0.5\%$) and cyclic tension (0–1%) are applied. The boundary conditions correspond to “film on a stiff substrate” from section 4.1.1. The results are post–processed as in the chapter 4. The macroscopic behaviour is presented in figure 5.13(a)(b). These plots show the evolution of the stress–strain loops during the five cycles under tension–compression (a) and cyclic tension (b). The evolution of the average values is shown for all grains and for each grain orientation. The comparison with the results for the Voronoï aggregates indicates that there are almost no differences in the macroscopic behaviour. The values of stress and strain for different orientations are almost identical for Voronoï and log–normal grain aggregates.

The next level comparison is done for the distribution of the plastic strain in the aggregate and its evolution during cycling. The histograms of the equivalent plastic strain for different orientations and different loading conditions are shown in figure 5.14(a),(b). These

5. COMPARISON OF THE SIMULATIONS WITH EXPERIMENTAL DATA

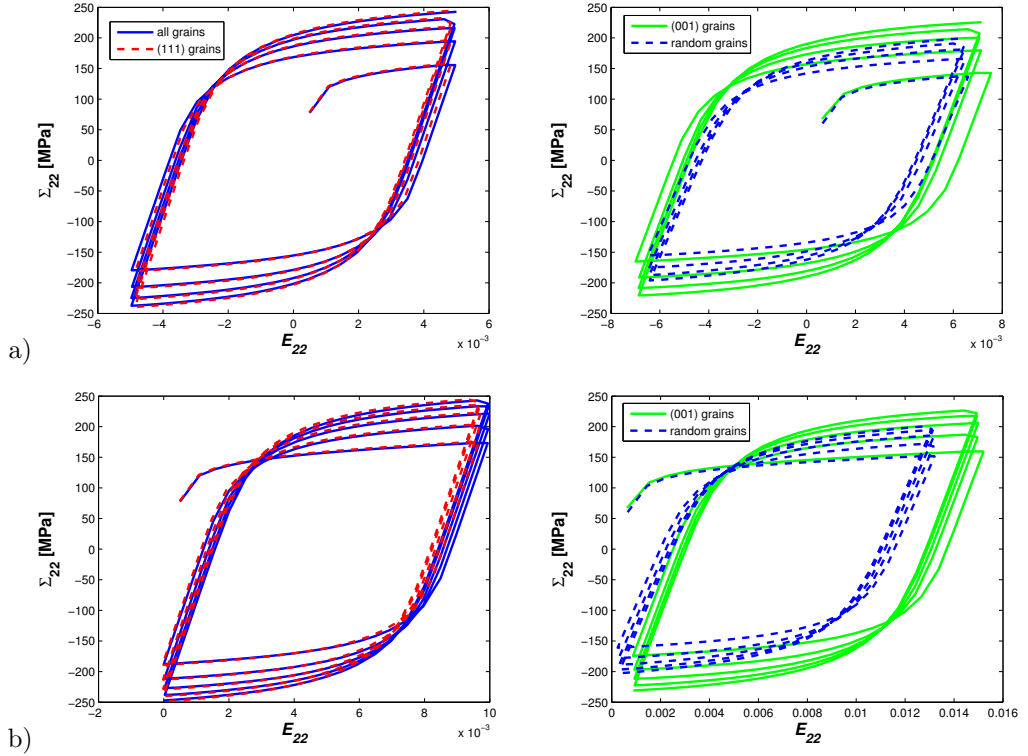


Figure 5.13: Evolution of the stress–strain loops during the five cycles for different orientations and loading conditions: a) tension–compression, b) cyclic tension.

histograms are again fitted by the same statistical distributions as in the chapter 4.2.2. The values of the parameters of distributions are in the tables 5.1 and 5.2. Comparison of these parameters shows that the histograms for $\{111\}$ oriented grains are very similar and the dispersions for different number of cycles differ within the range of 5–7 %. The histograms for $\{001\}$ oriented grains have no sharp peak but there are the significant numbers of the integration points with the relative plastic strain values within the interval 2.5 – 3.5 for both type of loading conditions. The direct comparison of the histograms of equivalent plastic strain for both type of grain shape is shown in figure 5.15(a),(b). The maxima of the histograms for $\{111\}$ oriented grains are shifted about 10% towards the higher values

5.5. COMPARISON OF THE INFLUENCE OF THE DIFFERENT GRAIN MORPHOLOGY

of plastic strain for both types of loading conditions. The dispersions of the values (width of the peak) are almost identical. The histograms for $\{001\}$ and random oriented grains are shifted towards higher values for real grain shapes. The dispersion of the values is also about 10% higher compare to the Voronoï grains. This means that the $\{001\}$ and random oriented grains are more deformed than in the Voronoï aggregates. But these results are also influenced by the fact that the histograms are made from one representation while the histograms of Voronoï aggregates are made for 10 realizations.

The differences in the results are relatively small especially for the $\{111\}$ oriented grains which make the main part of the aggregates. According to these results we can state that even if the simulations with Voronoï grain shape represent sort of simplification, they can provide suitable results in the simulations of mechanical behaviour of thin films.

cycle	Normal	Log-normal	Weibull	Gamma
$\{111\}$ grains - tension-compression				
cycle 1	$\mu = 1.05$	$\mu = 0.08$	$k = 4.49$	$\alpha = 16.02$
	$\sigma = 0.26$	$\sigma = 0.26$	$\lambda = 1.13$	$\beta = 14.64$
	$M = 0.0021$	$M = 0.0013$	$M = 0.0032$	$M = 0.0014$
cycle 5	$\mu = 1.13$	$\mu = 0.15$	$k = 4.06$	$\alpha = 13.27$
	$\sigma = 0.31$	$\sigma = 0.28$	$\lambda = 1.23$	$\beta = 11.22$
	$M = 0.0013$	$M = 0.0005$	$M = 0.0020$	$M = 0.0006$
$\{111\}$ grains - cyclic tension				
cycle 1	$\mu = 0.98$	$\mu = 0.006$	$k = 4.04$	$\alpha = 12.87$
	$\sigma = 0.27$	$\sigma = 0.29$	$\lambda = 1.07$	$\beta = 12.56$
	$M = 0.0017$	$M = 0.0009$	$M = 0.0025$	$M = 0.0009$
cycle 5	$\mu = 1.01$	$\mu = 0.04$	$k = 3.92$	$\alpha = 12.11$
	$\sigma = 0.29$	$\sigma = 0.29$	$\lambda = 1.10$	$\beta = 11.47$
	$M = 0.0014$	$M = 0.0008$	$M = 0.0020$	$M = 0.0008$

Table 5.1: Identification of statistical distribution functions for the relative equivalent plastic strain in $\{111\}$ grains for different loading conditions.

5. COMPARISON OF THE SIMULATIONS WITH EXPERIMENTAL DATA

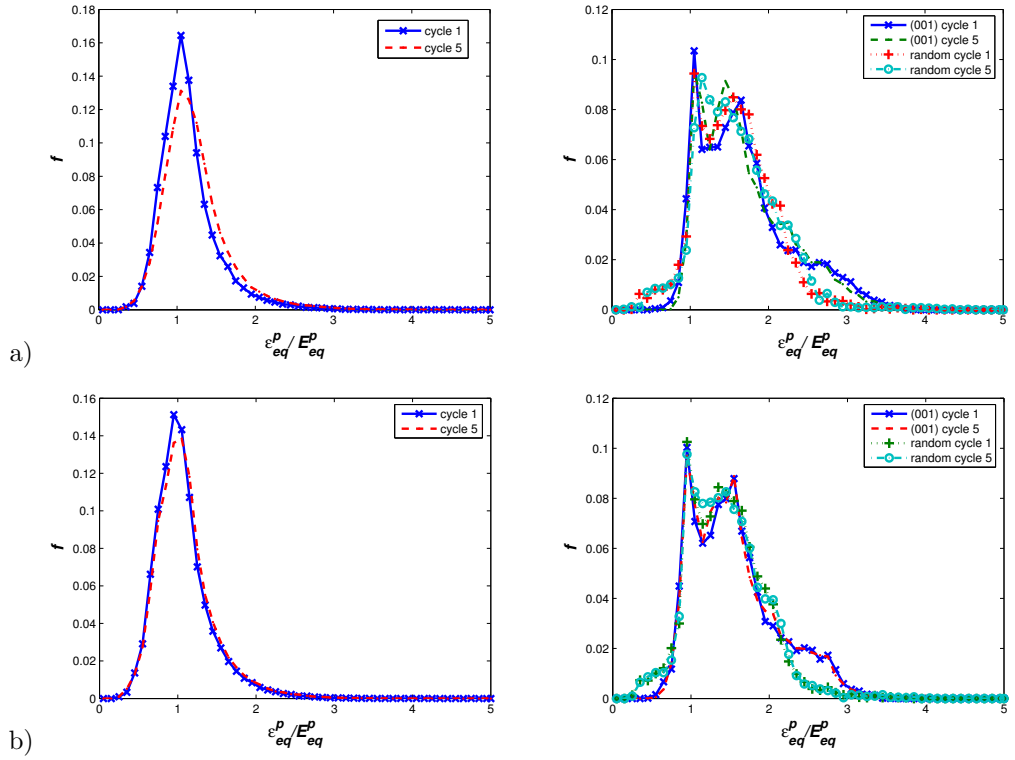


Figure 5.14: Evolution of the equivalent plastic strain histograms for aggregates with real grains shapes for different orientations and loading conditions: a) tension-compression, b) cyclic tension.

5.5. COMPARISON OF THE INFLUENCE OF THE DIFFERENT GRAIN MORPHOLOGY

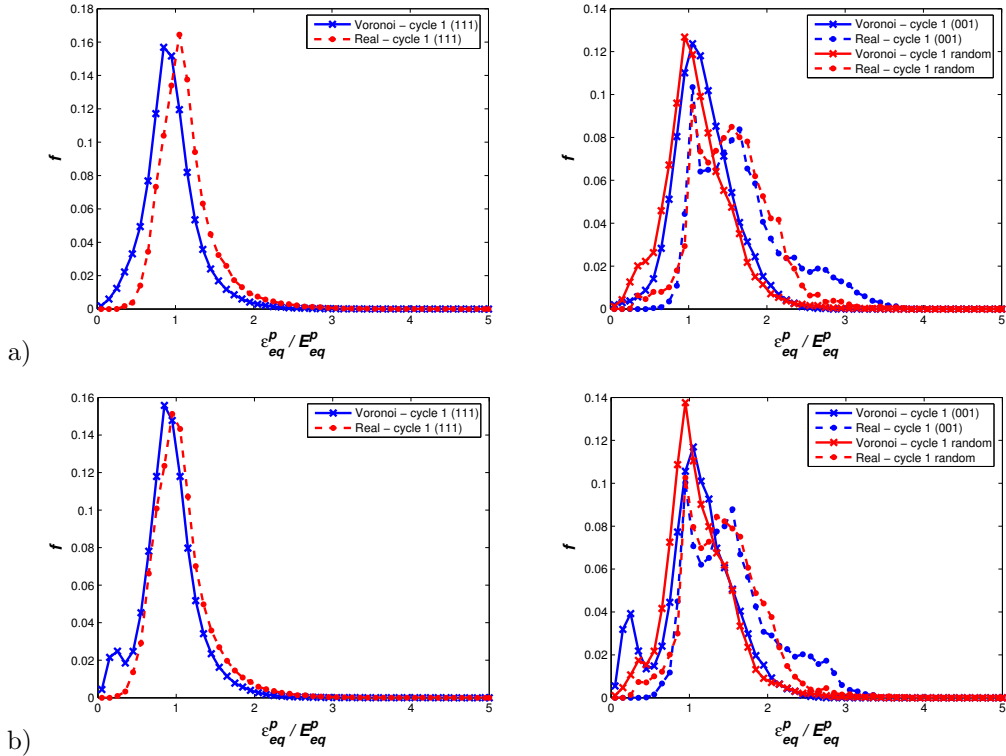


Figure 5.15: Comparison of the equivalent plastic strain histograms for aggregates with different grain shapes for different orientations and loading conditions: a) tension-compression, b) cyclic tension.

5. COMPARISON OF THE SIMULATIONS WITH EXPERIMENTAL DATA

cycle	Normal	Log-normal	Weibull	Gamma
{001} grains - tension-compression				
cycle 1	$\mu = 1.5$ $\sigma = 0.49$ $M = 0.0059$	$\mu = 0.44$ $\sigma = 0.34$ $M = 0.0037$	$k = 3.39$ $\lambda = 1.68$ $M = 0.0061$	$\alpha = 9.14$ $\beta = 5.73$ $M = 0.0033$
cycle 5	$\mu = 1.5,$ $\sigma = 0.47$ $M = 0.0064$	$\mu = 0.43$ $\sigma = 0.32$ $M = 0.0034$	$k = 3.46$ $\lambda = 1.68$ $M = 0.0070$	$\alpha = 10.17$ $\beta = 6.43$ $M = 0.0042$
{001} grains - cyclic tension				
cycle 1	$\mu = 1.40$ $\sigma = 0.49$ $M = 0.0053$	$\mu = 0.37$ $\sigma = 0.36$ $M = 0.0033$	$k = 3.22$ $\lambda = 1.57$ $M = 0.0054$	$\alpha = 8.23$ $\beta = 5.52$ $M = 0.0037$
cycle 5	$\mu = 1.39$ $\sigma = 0.48$ $M = 0.0052$	$\mu = 0.36$ $\sigma = 0.35$ $M = 0.0028$	$k = 3.25$ $\lambda = 1.57$ $M = 0.0053$	$\alpha = 8.53$ $\beta = 5.76$ $M = 0.0034$

Table 5.2: Identification of statistical distribution functions for the relative equivalent plastic strain in {111} grains for different film configurations.

5.6 Conclusion

The comparison of the different simulations with experimental results was made in this chapter. The following conclusions can be stated:

- The stress–strain curves show that the hardening in $[211](111)$ grains which are used in experimental measurements is larger than the average hardening in (111) grains or average hardening in all grains. However these differences are about 5%, therefore, they cannot explain the difference in the hardening of real films and simulated aggregates.
- The comparison of the stress–strain curves shows that the used continuum model is not able to describe the amount of hardening in the real films and the level of the stresses. The hardening depends mostly on the individual dislocation mechanism and interactions. All these processes are not included in this continuum model or in the simulations.
- The comparison of the evolution of the elastic strain in the tensile direction shows the higher amount of plasticity in simulations than in the real films. The plasticity starts in the simulations at smaller value of total imposed strain than in the experiments. The results of simulations with different boundary conditions are very similar with respect to experimental data.
- The evolution of the in–plane strain perpendicular to the tensile direction shows the decreasing of its values in the experimental data due to the constraining of the film by the substrate. This decrease is observed in the simulations but with smaller slope. This decrease starts in simulations at the smaller value of the total imposed strain than in experiments.
- Areas of strain accumulation can be found in the simulations of the cyclic loading of free–standing films. They are located at the grain boundaries and close to the $\{001\}$ oriented grains. These phenomena can be related to the areas of creation of extrusions in the real films.

5. COMPARISON OF THE SIMULATIONS WITH EXPERIMENTAL DATA

- The comparison of the simulations results with more realistic grain shape aggregate and results with Voronoï grains aggregates shows only small differences, therefore, the simulations with Voronoï grains can give the suitable results.

A better description of thin film behaviour seems to require the introducing of discrete dislocation processes which cannot be included in this continuum model. Description and modelling of these processes will be described in the following chapter.

Chapter 6

Discrete dislocation dynamics simulations of multicrystalline aggregates

6.1 Introduction

The question of the mechanical behaviour of thin film was treated in the previous chapters within the framework of continuum theory. However the experimental observations show that many phenomena are based on the individual dislocation behaviour and interactions which are discrete objects. Such behaviour cannot be described by the classical continuum crystal plasticity as was shown in the chapters 4 and 5. Therefore the simulation with discrete dislocation dynamics (DDD) will be presented in this chapter.

6.1.1 DDD theory

The used DDD model belongs to nodal codes (Weygand et al. [2001], Weygand et al. [2002]) in which the dislocation line is interpolated between nodes. The dislocation is allowed to move on certain glide planes. A minimal distance between glide plane is imposed, as no annihilation processes between dislocations in parallel glide planes are included. The example of a discretized dislocation loop on its glide plane is shown in figure 6.1. The vector $\underline{\mathbf{b}}$ is the Burgers vector of this loop, $\underline{\mathbf{n}}$ is the normal to the glide plane, $\underline{\mathbf{r}}_A = \underline{\mathbf{r}}(l_A)$ is the

coordinate of the node A , where l_A is its curvilinear coordinate. The DDD simulations are based on the computation of the velocity of dislocation at l_A according to the force which acts on the dislocation line. An interpolation relation between local and nodal velocities is used:

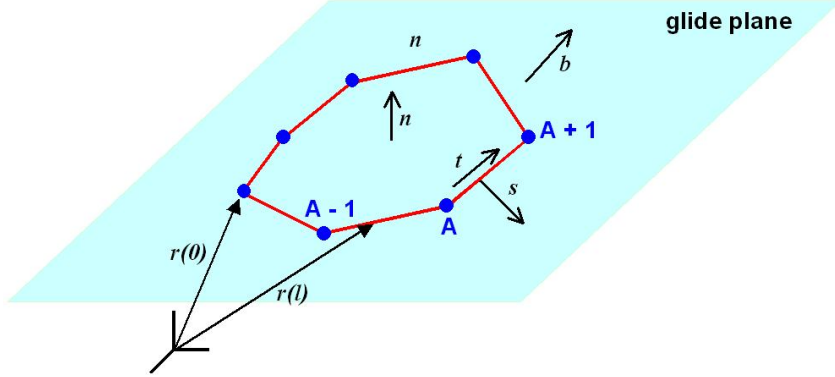


Figure 6.1: Discretized dislocation loop in the glide plane.

$$v_i(l) = \sum_{A=1}^N N_A(l) V_{Ai} \quad i = 1, 2, 3, \quad (6.1)$$

where V_{Ai} is the i -th component of the nodal velocity V_A and N_A is the linear shape function of node A . The driving force of the dislocation is the Peach–Koehler force. The force component in the glide plane is relevant for the pure glide. This force is noted as f^s . Its direction can be written as $\underline{s} = \underline{t} \times \underline{n}$. The relation between the Peach–Koehler force and dislocation velocity is established on the base of the atomistic processes. This relation is described by the following constitutive rule:

$$v_i(l) = V_T \left(\frac{f^s(l)}{\mu b} \right)^m \frac{f_i^s(l)}{f^s(l)}. \quad (6.2)$$

The f_i^s is the Peach–Koehler force computed according to the approach which will be described later. The power law exponent m is equal to 1 for FCC materials and V_T is the drag coefficient. Therefore this law can be for FCC crystals rewritten as:

6.1. INTRODUCTION

$$f_i^s(l) = Dv_i(l), \quad D = \mu b/V_T. \quad (6.3)$$

The coefficient V_T is temperature dependent and also depends weakly on the character of dislocation (edge, screw, mixed) for fcc materials. But this latter dependence is neglected. According to the principle of the virtual work, the equation (6.3) can be rewritten for the energy dissipation due to the dislocation motion as:

$$\oint_L f_i^s(l) \delta v_i(l) dl = D \oint_L v_i(l) \delta v_i(l) dl, \quad (6.4)$$

where $\delta v_i(l)$ is the virtual velocity of the dislocation at position l . This velocity is interpolated from the nodal values δV_{Ai} by using the interpolation according to the equation (6.1):

$$\delta v_i(l) = \sum_{A=1}^N N_A(l) \delta V_{Ai}. \quad (6.5)$$

There are some constraints of the motion of nodes which are located on free surfaces or which belongs to dislocations junctions. These nodes can move only along a given direction. Therefore these possible restrictions must be taken into account in evaluation of the nodal velocity. For safe of clarity, the derivation of the equations of motion is done for unconstrained nodes only. Using the previous definitions the virtual work expression can be written as:

$$\sum_{A=1}^N \left[\oint_L f_i^s(l) N_A(l) dl - D \sum_{B=1}^N V_{Bj} \oint_L N_A(l) N_B(l) dl \right] \delta V_{Ai} = 0. \quad (6.6)$$

To fulfill this equation for the arbitrary virtual velocities δV_{Ai} , the following expressions must be valid:

$$F_{Ai} - \sum_{B=1}^N K_{ABij} V_{Bj} = 0, \quad i = 1, 2, 3; \quad A = 1, \dots, N, \quad (6.7)$$

for the N common nodes. The nodal force F_{Ai} and the “stiffness” matrix K_{AB} are defined as:

$$F_{Ai} = \oint_L f_i^s(l) N_A(l) dl, \quad (6.8)$$

$$K_{AB} = D \oint_L N_A(l) N_B(l) dl. \quad (6.9)$$

The resulting nodal force at node A can be then written as:

$$\underline{\mathbf{F}}_A = \underline{\mathbf{s}}_{A-1,A} \int_{A-1}^A f^s(l) N_A(l) dl + \underline{\mathbf{s}}_{A,A+1} \int_A^{A+1} f^s(l) N_A(l) dl, \quad (6.10)$$

where $\underline{\mathbf{s}}_{A-1,A}$ is the in-plane unit normal vector to the segment with endpoints $(A-1)$ and (A) .

The next task is the computation of the Peach–Koehler force on the dislocation line. The resulting force is taken as a superposition of the forces caused by the stress field of other dislocations including the self stress and the externally applied forces. The dislocation stress field is evaluated for each straight segment of dislocation. The solution by superposition proposed by (Van der Giessen and Needleman [1995]) is shown in figure 6.2. The force from dislocation is computed as a problem of dislocation singularity in the infinite space. The correction for the boundary conditions is done solving a linear elastic problem. The boundary conditions for solving of this problem can be written as:

$$\hat{u}_i = u_i^0 - \tilde{u}_i \quad \hat{T}_i = T_i^0 - \tilde{\sigma}_{ij} n_j, \quad (6.11)$$

where u_i^0 and T_i^0 are prescribed values of displacement and tractions on the different parts of the boundary. The variables with (\sim) are the displacement resp. stresses for dislocations in the infinite space. The final solution is then obtained from equations:

$$\sigma_{ij} = \tilde{\sigma}_{ij} + \hat{\sigma}_{ij}, \quad \varepsilon_{ij} = \tilde{\varepsilon}_{ij} + \hat{\varepsilon}_{ij}, \quad u_i = \tilde{u}_i + \hat{u}_i. \quad (6.12)$$

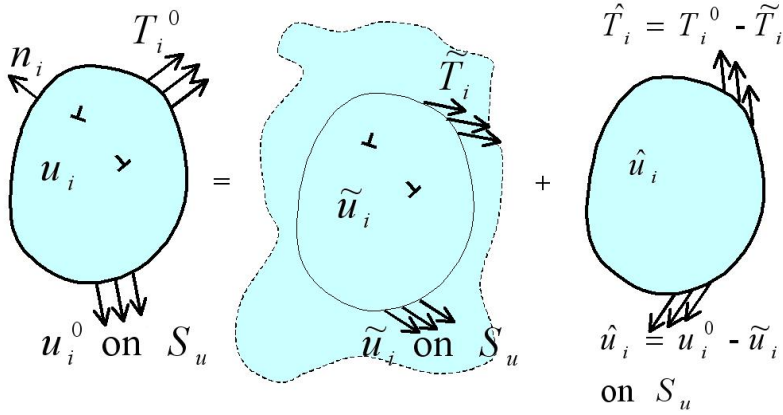


Figure 6.2: Superposition of the analytical solution of dislocation singularities in infinite space ($\tilde{\cdot}$) with image field ($\hat{\cdot}$) corrected by boundary conditions (u_i^0, T_i^0) (Van der Giessen and Needleman [1995]).

6.1.2 Presentation of the polycrystalline simulations

The simulations were performed for polycrystalline aggregates which consist of 9 cuboidal grains. The grain boundaries are impenetrable to dislocations, however the dislocations influence each other across the boundaries by the stress fields, they induce. These conditions mean some simplification, but this is the current state of the given DDD code. The boundary conditions are shown in figure 6.3. The aggregate has a fixed face perpendicular to the y direction and the displacement of the opposite face is prescribed in the y direction. The other surfaces of the aggregates are traction free. These boundary conditions correspond to a free-standing film.

The code allows setting the properties of the initial dislocation sources in each grain. These properties are: number of sources in given slip plane family, length of the sources and minimal number of glide planes between these sources. The sources are placed randomly inside the grains. The typical representation of the aggregate (FE mesh + initial dislocation sources) is shown in figure 6.4.

The boundary conditions are treated by using a FE mesh and a homogeneous elastic material with Young's modulus $E = 72\,738$ MPa and Poisson ratio $\nu = 0.347$. These values

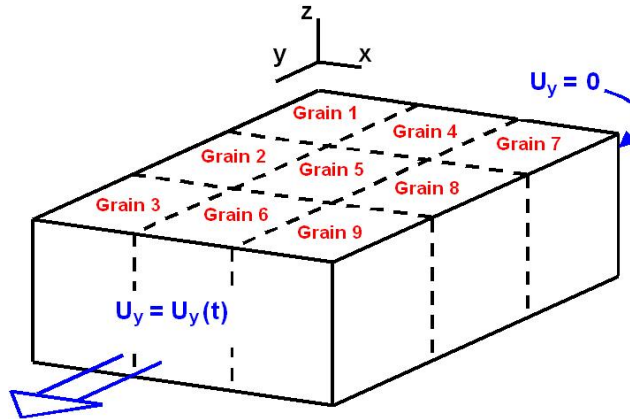


Figure 6.3: Boundary conditions of the DDD simulations of the polycrystalline aggregate. The grain numbers corresponds to those used in table 6.1.

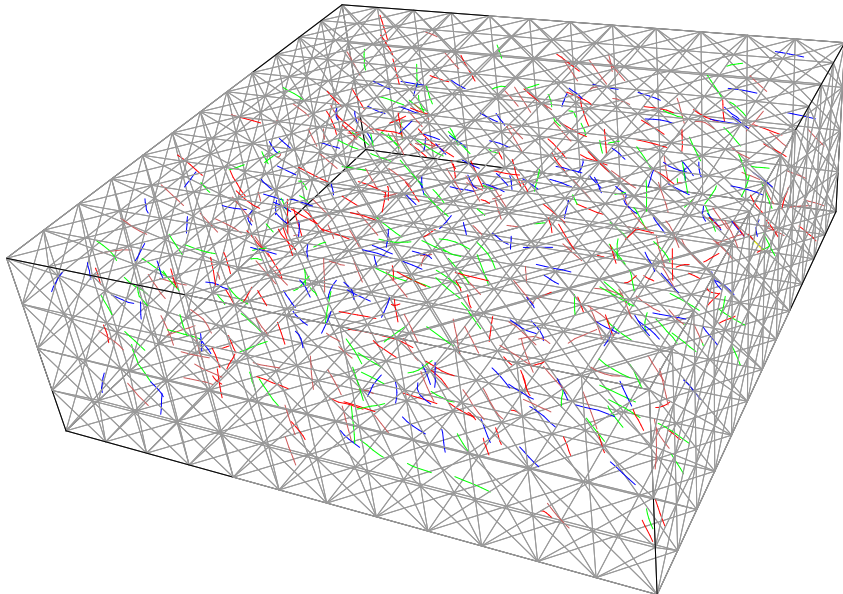


Figure 6.4: Aggregate for DDD simulations: FE mesh – grey lines, Dislocation sources at different glide systems – red, green, blue, brown lines.

6.1. INTRODUCTION

correspond to properties of aluminum. Two families of crystallographic orientations were chosen: random, and (001) central grain surrounded by (111) grains. The Euler angles for crystallographic orientations of the grains are described in the table 6.1. The values of angles are written in notation used in the simulations. This notation is inverse with respect to one presented in the chapter 2. Instead of matrix T is used its transpose. The central grain is grain 5 (see fig. 6.3). The textures are also represented by their pole figures in figure 6.5(a),(b).

Grain	ϕ_1	Φ	ϕ_2
Random aggregates			
Grain 1	18.45	54.7356	45.00
Grain 2	89.52	54.7356	45.00
Grain 3	38.86	54.7356	45.00
Grain 4	263.21	54.7356	45.00
Grain 5	72.46	0.00000	0.00
Grain 6	78.92	54.7356	45.00
Grain 7	20.41	54.7356	45.00
Grain 8	0.79	54.7356	45.00
Grain 9	259.73	54.7356	45.00
(111)(001) aggregates			
Grain 1	135.0	54.7356	161.5523
Grain 2	135.0	54.7356	90.4823
Grain 3	135.0	54.7356	141.1392
Grain 4	135.0	54.7356	-83.208
Grain 5	180.0	0.00000	107.5440
Grain 6	135.0	54.7356	101.0791
Grain 7	135.0	54.7356	159.5888
Grain 8	135.0	54.7356	179.2124
Grain 9	135.0	54.7356	-79.7329

Table 6.1: Values of Euler angles of the grains orientations for different types of aggregates.

The main parameters which are used for classification of simulations are: crystallographic texture, grain size (in-plane, film thickness), initial dislocation density, glide plane distance and initial source length. The values of grain size, glide plane distance and source length are taken as multiples of the lattice constant ($a=4.04496 \times 10^{-10}$ m). The simulations are classified according to their parameters into the following groups:

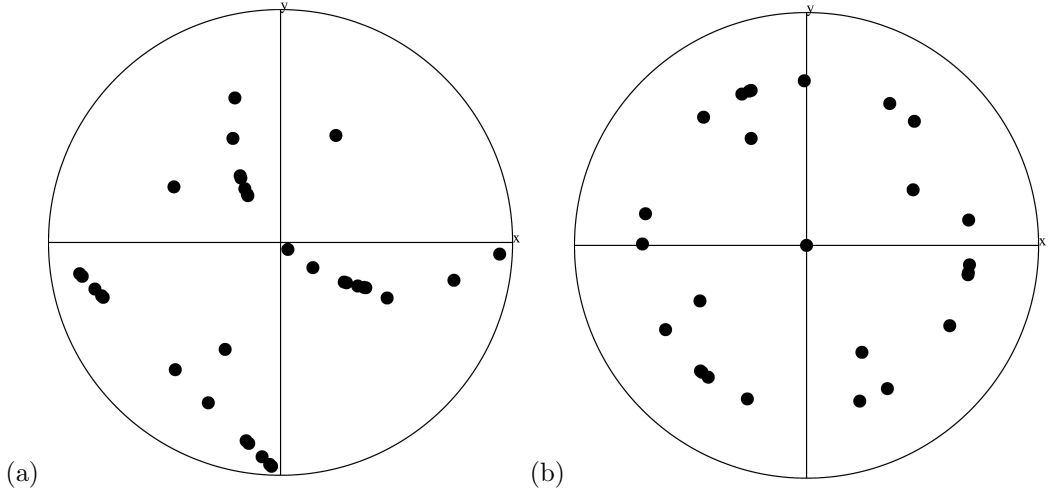


Figure 6.5: Pole figures for (a) random texture, (b) (111)(001) texture.

1. Group 1

This group consists of the aggregates with the same grain size and the same initial dislocation density. These aggregates have the largest grain size ($2500 a$) and the lowest initial dislocation density ($0.3 \times 10^{13} [m^{-2}]$). The aggregates have random texture. The differences are in the glide plane distance and initial source length. Two simulations have the random source length within a given range and one has a constant initial source length. These simulations are used for the determination of the influence of the source length for large grains and low initial dislocation density. The parameters of these simulations are presented in table 6.2.

2. Group 2

This group includes three simulations. The grain orientations are random. The initial dislocation density is identical $10^{13} [m^{-2}]$ which is in the middle of the range of used initial dislocation densities. These aggregates have different grain sizes (two have columnar grains and one have cubic grains). The in-plane grain sizes of these aggregates are small ($1300 a$ and $1500 a$) comparing to other simulations. Two simulations have the random source length within a given range and one has constant

6.1. INTRODUCTION

simulation	grain orientation	grain size (in-plane - d, film thickness - h) [a]	glide planes distance [a]	source length [a]	dislocation density 10^{13} [m^{-2}]
G1-1	Random	$d = 2500$ $h = 2500$	100	50-500	0.2
G1-2	Random	$d = 2500$ $h = 2500$	25	50-500	0.2
G1-3	Random	$d = 2500$ $h = 2500$	25	300	0.2

Table 6.2: Basic properties of the Group 1 simulations. Lengths are given as multiples of the lattice constant ($a=4.04496 \times 10^{-10}m$).

initial source length. The influence of the grain size and source length can be estimated for small grains and higher dislocation density from this group of simulations. The parameters of these simulations are presented in table 6.3.

simulation	grain orientation	grain size (in-plane - d, film thickness - h) [a]	glide planes distance [a]	source length [a]	dislocation density 10^{13} [m^{-2}]
G2-1	Random	$d = 1300$ $h = 2500$	25	50-500	1.0
G2-2	Random	$d = 1500$ $h = 1500$	25	50-500	1.0
G2-3	Random	$d = 1300$ $h = 2500$	25	300	1.0

Table 6.3: Basic properties of the Group 2 simulations. Lengths are given as multiples of the lattice constant ($a=4.04496 \times 10^{-10}m$).

3. Group 3

This group consists of only two simulations. These simulations have different dislocation density from the previous groups (0.5 and 2.1×10^{13} [m^{-2}]). The in-plane grain size is very different in these simulations ($1300 a$ and $2500 a$). They have the same texture and long initial dislocation sources ($600 a$). The influence of the in-plane grain size and initial dislocation density can be estimated from this group of simulations. The parameters of these simulations are presented in table 6.4.

4. Group 4

6. DISCRETE DISLOCATION DYNAMICS SIMULATIONS OF MULTICRYSTALLINE AGGREGATES

simulation	grain orientation	grain size (in-plane - d, film thickness - h) [a]	glide planes distance [a]	source length [a]	dislocation density 10^{13} [m^{-2}]
G3-1	Random	$d = 2500$ $h = 2500$	25	600	0.5
G3-2	Random	$d = 1300$ $h = 2500$	25	600	2.1

Table 6.4: Basic properties of the Group 3 simulations. Lengths are given as multiples of the lattice constant ($a=4.04496 \times 10^{-10}m$).

This group covers 5 simulations with the same low initial dislocation density (0.3×10^{13} [m^{-2}]) and random texture. Two aggregates have columnar grains of the same small in-plane size (1300 a) and large thickness (2500 a) but with different initial source lengths (300 a and 600 a). Another two simulations have the cubic grains of the same middle size (1600 a) but again different initial source length (300 a and 600 a). In this group the significance of the grain size or source length can be estimated for the low initial dislocation density and small and middle in-plane grain size. The parameters of these simulations are presented in table 6.5.

simulation	grain orientation	grain size (in-plane - d, film thickness - h) [a]	glide planes distance [a]	source length [a]	dislocation density 10^{13} [m^{-2}]
G4-1	Random	$d = 2500$ $h = 2500$	25	600	0.3
G4-2	Random	$d = 1300$ $h = 2500$	25	300	0.3
G4-3	Random	$d = 1300$ $h = 2500$	25	600	0.3
G4-4	Random	$d = 1600$ $h = 1600$	25	300	0.3
G4-5	Random	$d = 1600$ $h = 1600$	25	600	0.3

Table 6.5: Basic properties of the Group 4 simulations. Lengths are given as multiples of the lattice constant ($a=4.04496 \times 10^{-10}m$).

5. Group 5

This group includes three simulations. The only difference between them is the film

6.1. INTRODUCTION

thickness. Due to the film thickness, the grain shape changes from the cubic to the columnar grains. Other parameters are the same for all simulations. These simulations are characteristic by the short initial dislocation sources ($200 a$), middle value of initial dislocation density ($10^{13} [\text{m}^{-2}]$) and the small in-plane grain size ($1250 a$). These simulations can show the influence of the film thickness on the resulting behaviour. The parameters of these simulations are presented in table 6.6.

simulation	grain orientation	grain size (in-plane d, film thickness h) $[a]$	glide planes distance $[a]$	source length $[a]$	dislocation density $10^{13} [\text{m}^{-2}]$
G5-1	Random	$d = 1250$ $h = 1250$	25	200	1.0
G5-2	Random	$d = 1250$ $h = 1875$	25	200	1.0
G5-3	Random	$d = 1250$ $h = 2500$	25	200	1.0

Table 6.6: Basic properties of the Group 5 simulations. Lengths are given as multiples of the lattice constant ($a=4.04496 \times 10^{-10}\text{m}$).

6. Group 6

This group covers 5 simulations of the aggregates which are characteristic by the texture consisting of the (001) central grain and (111) surrounding grains, the short initial dislocation sources ($200 a$ and $266 a$), middle value of initial dislocation density ($10^{13} [\text{m}^{-2}]$) and the small in-plane grain size ($1250 a$). Four simulations have the same initial source length ($200 a$). The film thickness in these four simulations increases from the half of the in-plane grain size to twice the in-plane grain size. These simulations can also show the influence of the film thickness but also the influence of the initial source length. The parameters of these simulations are presented in table 6.7.

7. Group 7

Three simulations are included in this group. All simulations have the (111) texture with the (001) central grain and the cubic grains of the same small size ($1250 a$). Two of them have the same high initial dislocation density ($2 \times 10^{13} \text{ m}^{-2}$), but different

6. DISCRETE DISLOCATION DYNAMICS SIMULATIONS OF MULTICRYSTALLINE AGGREGATES

simulation	grain orientation	grain size (in-plane - d, film thickness - h) [a]	glide planes distance [a]	source length [a]	dislocation density 10^{13} [m^{-2}]
G6-1	(111)(001)	$d = 1250$ $h = 1250$	25	200	1.0
G6-2	(111)(001)	$d = 1250$ $h = 1875$	25	200	1.0
G6-3	(111)(001)	$d = 1250$ $h = 2500$	25	200	1.0
G6-4	(111)(001)	$d = 1250$ $h = 625$	25	200	1.0
G6-5	(111)(001)	$d = 1250$ $h = 1250$	25	266	1.0

Table 6.7: Basic properties of the Group 6 simulations. Lengths are given as multiples of the lattice constant ($a=4.04496 \times 10^{-10}\text{m}$).

initial source length. One simulation has a twice larger dislocation density ($4 \times 10^{13} \text{m}^{-2}$). These simulations are used for investigation of the influence of the initial dislocation density. The parameters of these simulations are presented in table 6.8.

simulation	grain orientation	grain size (in-plane - d, film thickness - h) [a]	glide planes distance [a]	source length [a]	dislocation density 10^{13} [m^{-2}]
G7-1	(111)(001)	$d = 1250$ $h = 1250$	25	200	2.0
G7-2	(111)(001)	$d = 1250$ $h = 1250$	25	500	1.9
G7-3	(111)(001)	$d = 1250$ $h = 1250$	25	200	4.0

Table 6.8: Basic properties of the Group 7 simulations. Lengths are given as multiples of the lattice constant ($a=4.04496 \times 10^{-10}\text{m}$).

6.2 Results

6.2.1 Macroscopic behaviour of aggregates

Global comparison is done for the overall stress-strain curves and for the evolution of dislocation density with applied strain. The results and discussion are divided according to the categories presented previously.

1. Group 1

The evolution of the dislocation density and stress-strain curves are shown in figure 6.6(a),(b). These aggregates have the same grain size and initial dislocation density. The difference is in the initial source length. The influence of this initial source length on the yield stress value is clearly visible in figure. The yield stress and strain is about 27% higher in the case of the constant source length. This difference is caused by the presence of the longer sources in the G1-1 and G1-2 simulations. The slope of the dislocation density curves and hardening rates are very similar in all cases. The differences are about 5%.

2. Group 2

The results for this group of simulations are shown in figure 6.7(a),(b). The following features can be observed: The influence of the initial source length is visible from the comparison of the curves for G2-1 and G2-3 simulations. The source length is the only difference between them. The yield stress is about 13% higher for the case of constant sources length. The influence of the in-plane grain size can be shown on the comparison of the simulations G2-1 and G2-2. The simulation G2-2 has cubic grains with about 15% larger in-plane grain size. But the yield stress is only about 2% higher for the G2-1 with smaller in-plane grain size. The hardening rate is about 16% higher for the G2-1 with smaller in-plane grain size. Comparison of these three simulations shows the higher influence of the initial source length on the stress-strain behaviour than the in-plane grain size. The significant dependence of the yield stress on the source length is also described in (von Blanckenhagen et al. [2004]).

6. DISCRETE DISLOCATION DYNAMICS SIMULATIONS OF MULTICRYSTALLINE AGGREGATES

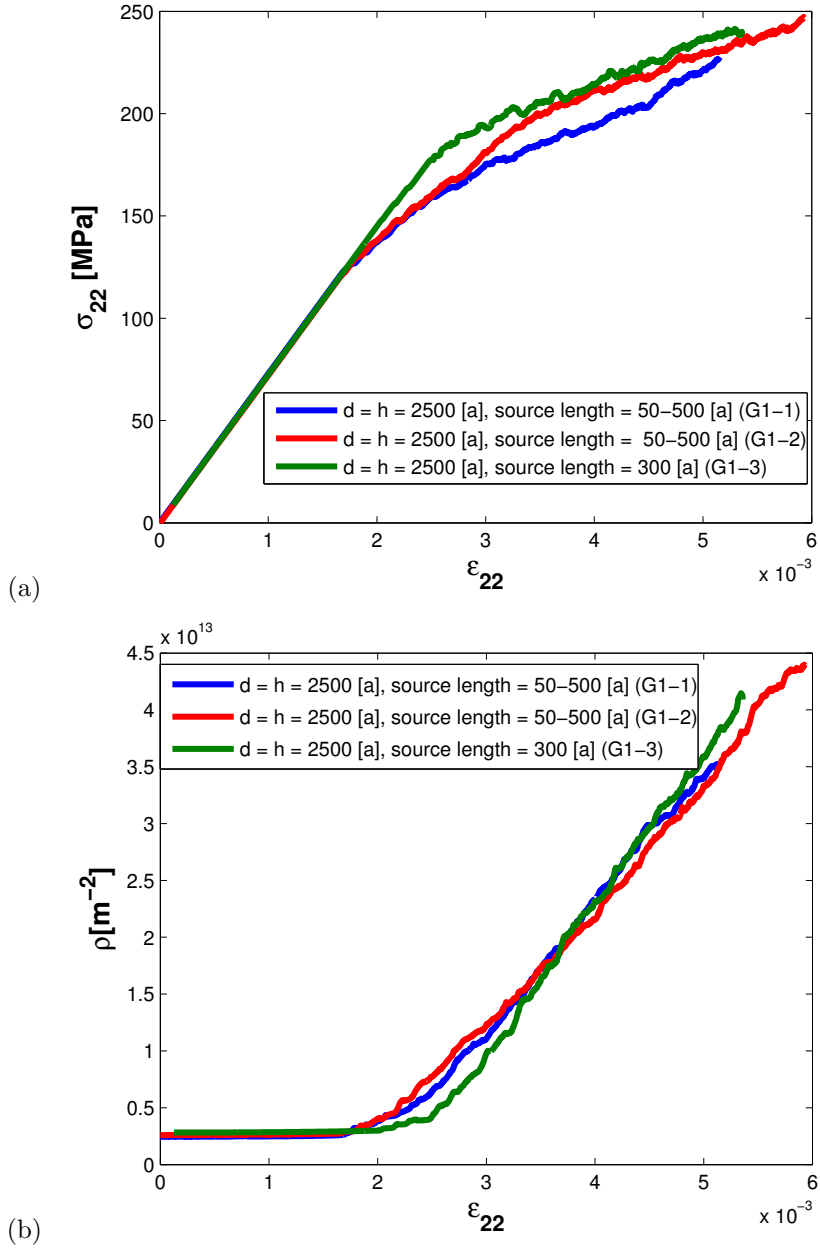


Figure 6.6: Stress–strain curves (a) and evolution of dislocation density (b) in the aggregates from Group 1.

6.2. RESULTS

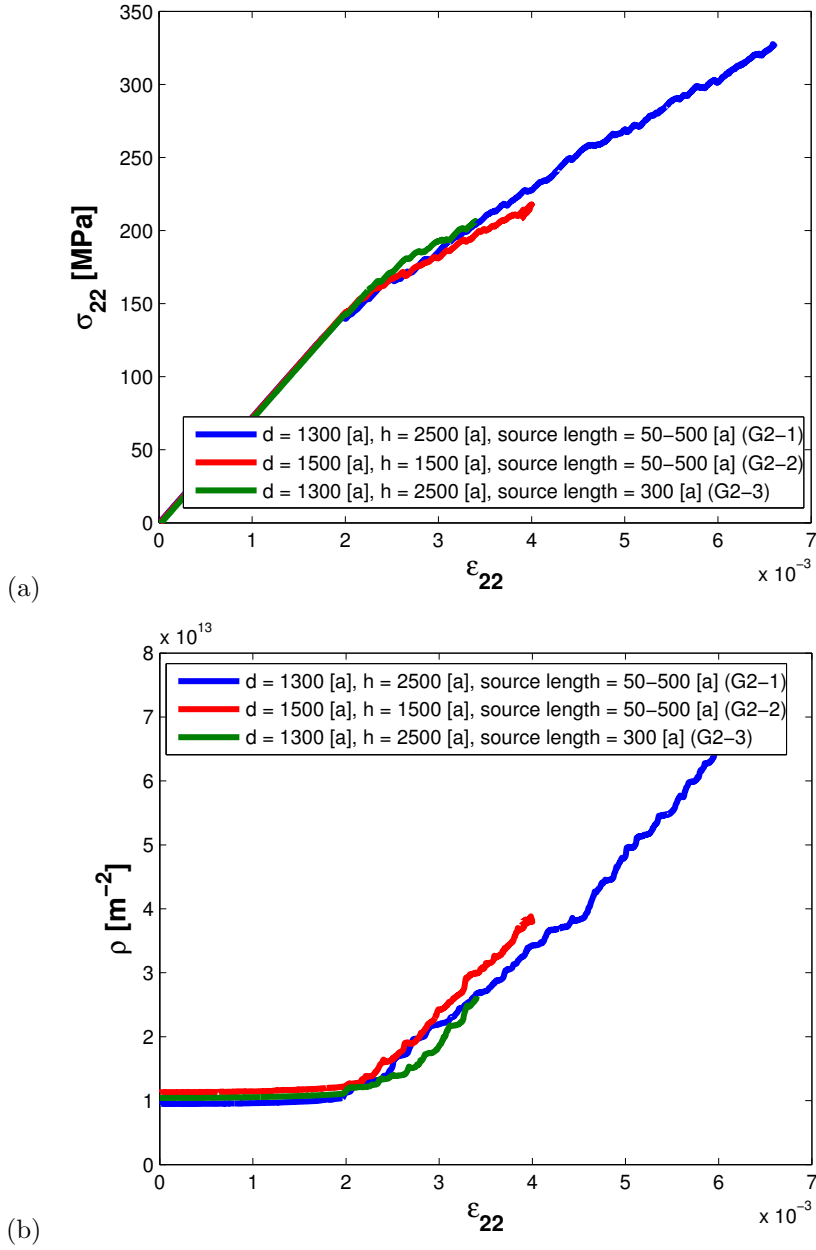


Figure 6.7: Stress–strain curves (a) and evolution of dislocation density (b) in the aggregates from Group 2.

3. Group 3

The curves for the two simulations from this group are shown in figure 6.8(a),(b). These simulations have only the same initial source length and the film thickness. The simulations G3-1 has 4 times smaller initial dislocation density and 1.9 larger in-plane grain size. The curves are very similar for both cases. The main differences are in the hardening rate which is higher for the G3-2 with smaller in-plane grain size and higher dislocation density. The similarity of the stress-strain curves shows the large influence of the initial source lengths compared to other parameters.

4. Group 4

This category consists of aggregates with different grain size and source length but with the same initial dislocation density. The stress-strain curves and evolution of dislocation density are shown in figure 6.9(a),(b). The influence of the different source length can be observed by the comparison of the results for G4-2 and G4-3 or G4-4 and G4-5 respectively. Both cases show the increase of yield stress and strain for the shorter sources, but the aggregates with longer sources have higher hardening rate which corresponds to the smaller number of sources and lower possibility of gliding. The differences are more significant for the aggregates which have smaller in-plane grain size (G4-2, G4-3 – 1300 a). The influence of the in-plane grain size can be identified by comparison of the simulations with the same source length (G4-2 and G4-4 or G4-1, G4-3 and G4-5). Such an influence is again small. This small effect is most likely due to the fact that the source strength and back stresses are controlling the plasticity. When the difference between the in-plane grain size is 23%, the difference in the yield stress is about 1% for shorter source length (300 a) simulations and about 5% for longer source length (600 a) simulations. When the in-plane grain size is 1.92 times larger (G4-1 compare to G4-3), the difference in the yield stress about 27%. The hardening rate depends on the number of initial sources, therefore, the aggregates with smaller number of sources have higher hardening rate. This corresponds again with results presented in (von Blanckenhagen et al. [2004], Nicola et al. [2005]). The aggregates with smaller grains have less sources and higher hardening rates. The

6.2. RESULTS

difference is 15% for aggregates G4-2 (1300 a) and G4-4 (1600 a) and about 40% between G4-1 (2500 a) and G4-3 (1300 a).

5. Group 5

In this category there are aggregates with the same source length and in-plane grain size but with different thickness of grains. The thickness increases from the one to two times of the in-plane grain size. The stress-strain curves and evolution of dislocation density is shown in figure 6.10(a),(b). The stress-strain curves are very similar and the results show very small effect of different film thickness. The yield stresses and strains are almost the same (differences about 2%). The differences in hardening rate are also very small (about 3-5 %). These are caused by the different number of initial sources. These results show that the main influence of grain size is provided by the in-plane grain size which the smallest grain dimension. This dependence of the smallest dimension was observed also in (von Blanckenhagen et al. [2001]).

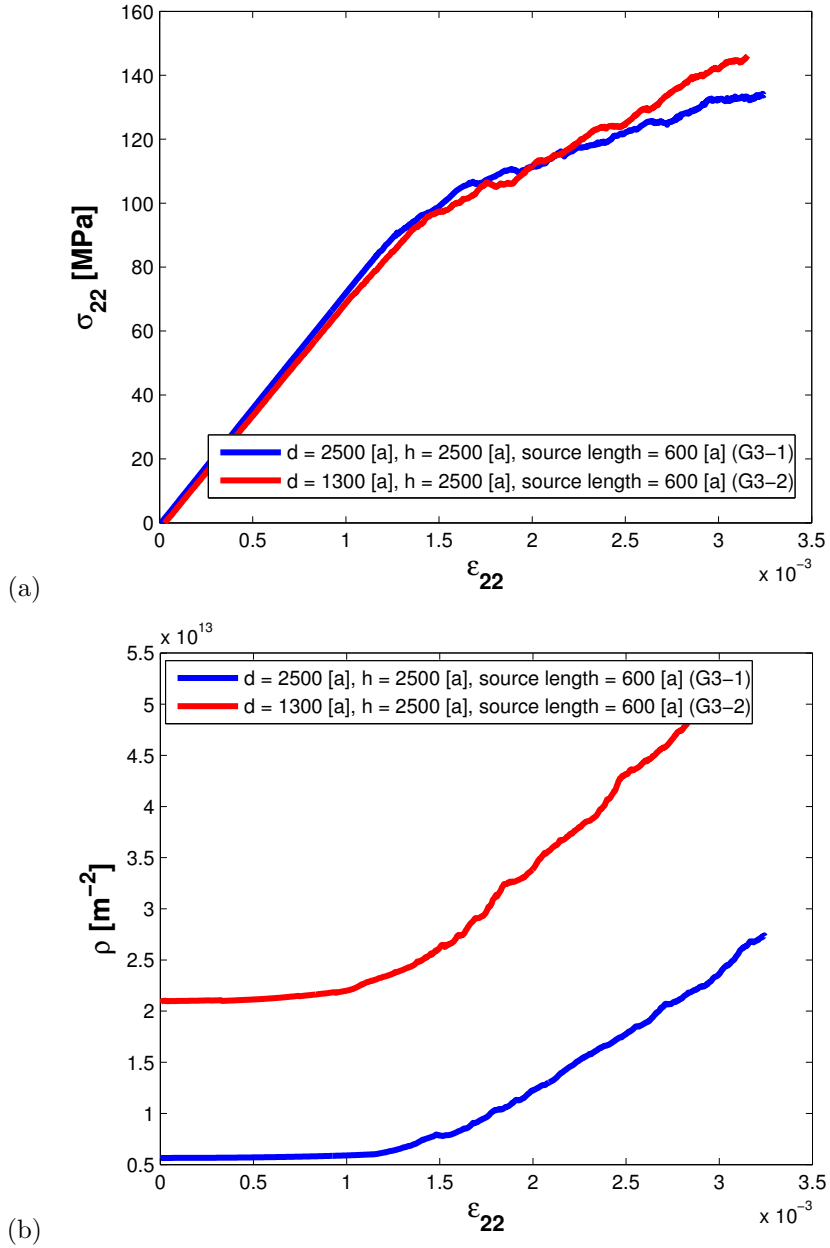


Figure 6.8: Stress–strain curves (a) and evolution of dislocation density (b) in the aggregates from Group 3.

6.2. RESULTS

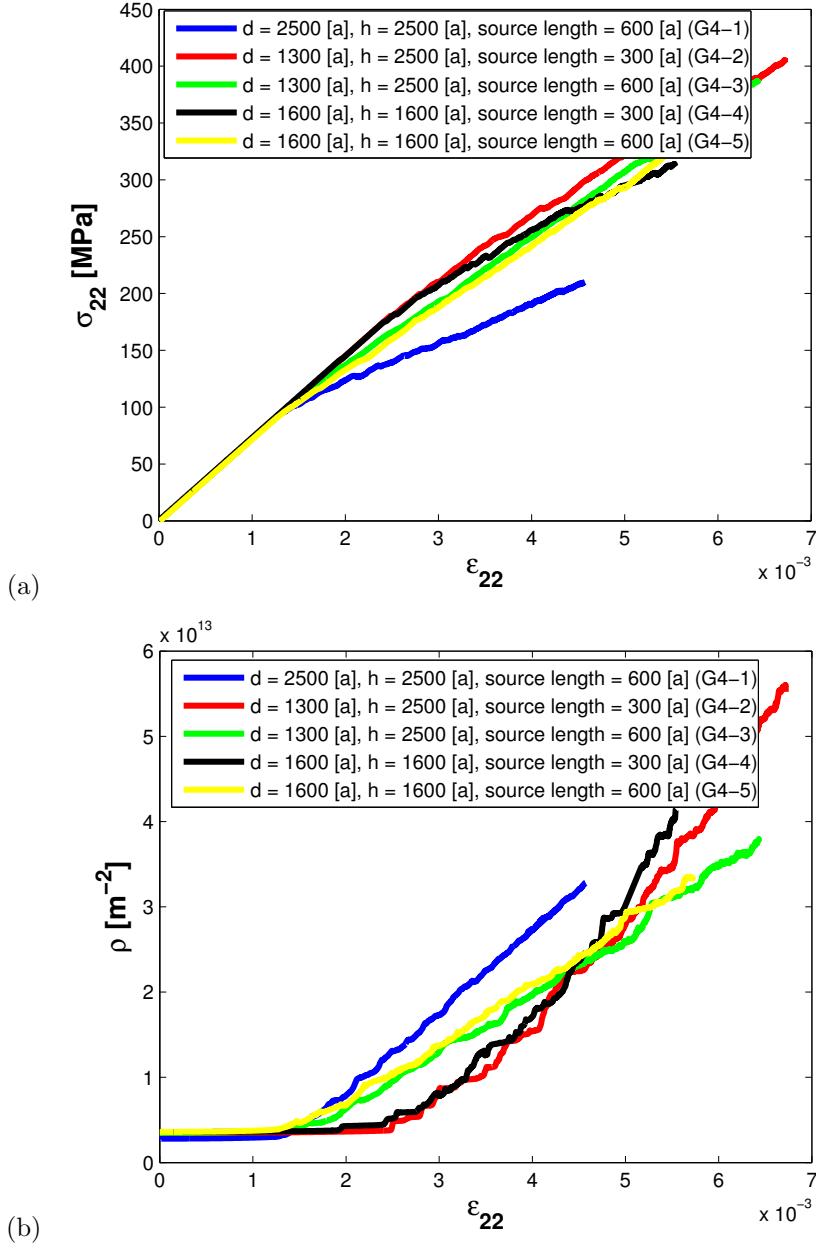


Figure 6.9: Stress–strain curves (a) and evolution of dislocation density (b) in the aggregates from Group 4.

6. DISCRETE DISLOCATION DYNAMICS SIMULATIONS OF MULTICRYSTALLINE AGGREGATES

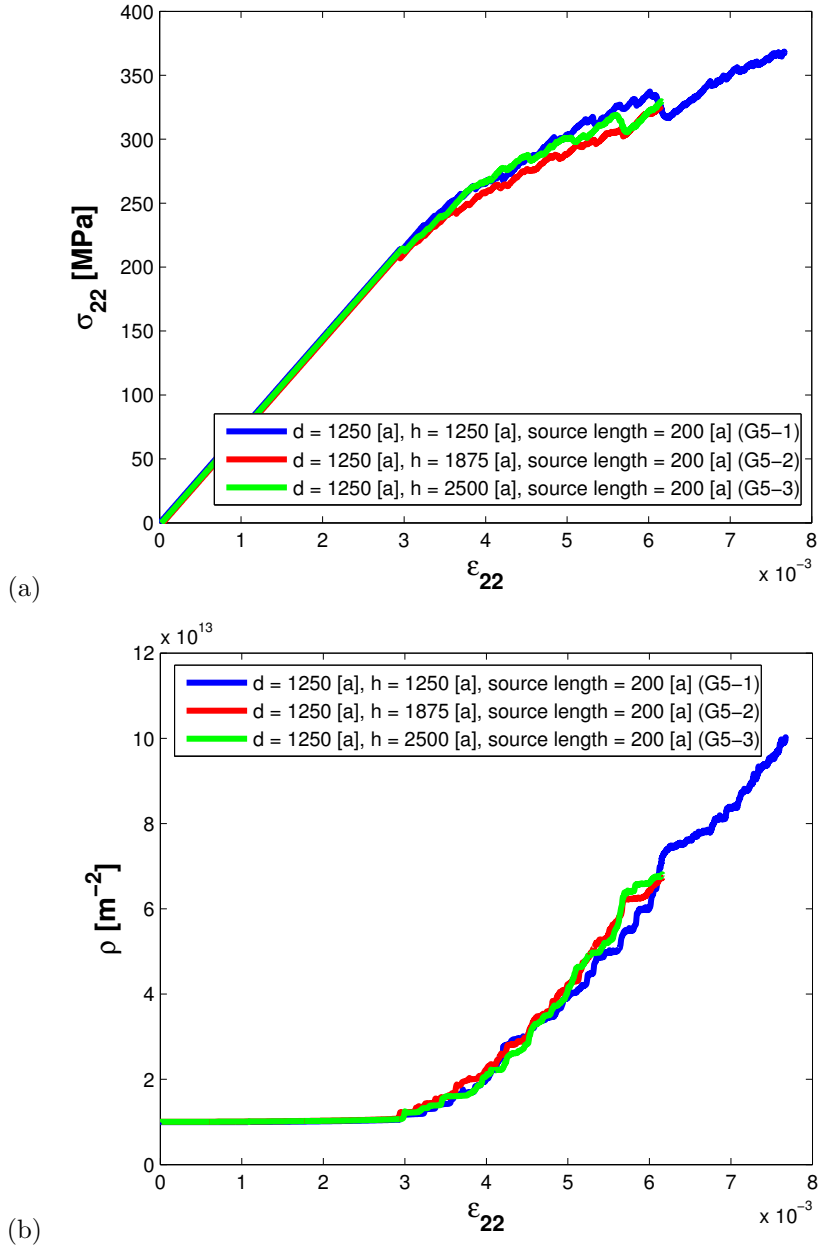


Figure 6.10: Stress–strain curves (a) and evolution of dislocation density (b) in the aggregates from Group 5.

6.2. RESULTS

6. Group 6

This group consists of aggregates which have (001) oriented grain surrounded by (111) oriented grains. The results are shown in figure 6.11(a),(b). First comparison shows the influence of the film thickness. This thickness is from 1/2 of the in-plane grain size to twice the in-plane grain size. The results again show the small influence of the thickness on the yield stresses and strain which differs in the order of 3 – 5% (Nicola et al. [2005]). The hardening rate is also very similar. The only large difference is for the aggregate G6-4 with the smallest film thickness. The hardening rate in this case is about 12% higher and it is due to the very low number of initial sources (von Blanckenhagen et al. [2001], von Blanckenhagen et al. [2004]). The influence of the initial source length is clearly visible from the comparison of the curves for the aggregates G6-1 and G6-5. The sources are 1.33 times longer in G6-5 and yield stress is about 18% lower. Slightly higher hardening rate for longer sources is again caused by the smaller amount of these initial sources. This comparison again shows the large influence of the source length on the global behaviour. Comparison of the curves for the random oriented grains (Group 5) and curves from this group does not show significant differences in the results for these two textures.

7. Group 7

This group consists of the simulations with the highest initial dislocation densities compared to the previous simulations. The results are shown in figure 6.12. The influence of the source length can be observed on curves of aggregates G7-1 and G7-2. The yield stress value is twice higher for the aggregate with the 2.5 times longer initial source length. The hardening rate is about 28% higher for the longer sources which is again the effect of the smaller number of these initial sources.

The comparison of the influence of the initial dislocation density can be done with the aggregates G6-1, G7-1 and G7-3. The yield stress decreases towards the higher initial dislocation density. When the density increases from 1 to $2 \times 10^{13} \text{ m}^{-2}$, the yield stress decreases about 8% and when the density increases from 2 to $4 \times 10^{13} \text{ m}^{-2}$, the yield stress decreases about 22%. The hardening rate decreases toward

the higher dislocation density but the differences are of order 5%. This means that with such values of dislocation densities there are not many dislocation interactions and junctions which could significantly increase the hardening rate (Weygand et al. [2007]).

6.2.2 Summary of macroscopic behaviour

The results of macroscopic behaviour of the aggregates show that the main influence on the yield stress has the length of the initial sources of dislocations. The grain size within the investigated range has only the minor influence. Especially the film thickness which was mostly larger or equal to the in-plane grain size, seems to have almost no influence on the stress-strain behaviour of the aggregates. The hardening rate increases with the decreasing grain size and increasing initial source length. This is due to the fact that in the aggregates with the smaller grains or longer sources there are few of these sources and smaller possibility of creation of dislocations and an extensive function of pile-ups. Dislocations also more influence each other in smaller grains. The small number of initial sources also causes small number of junctions which could increase also the hardening rate.

6.2. RESULTS

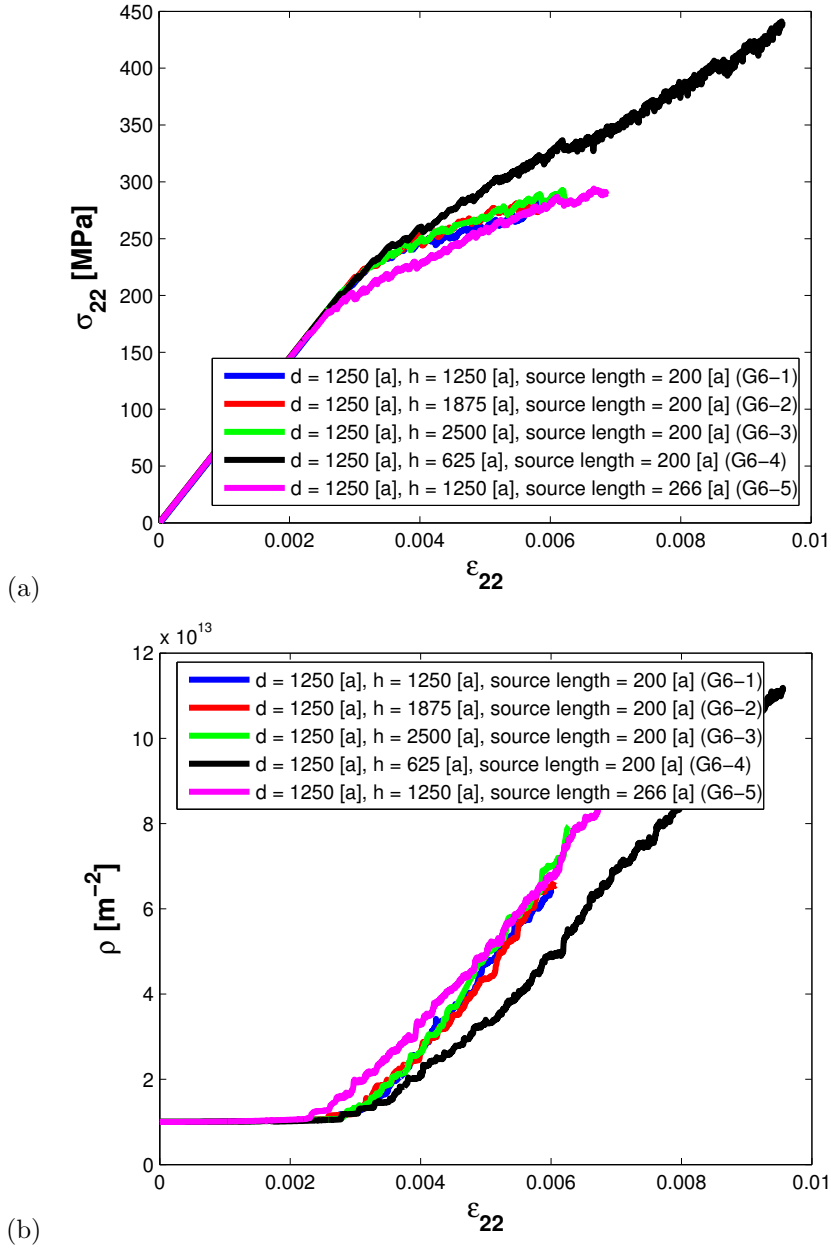


Figure 6.11: Stress–strain curves (a) and evolution of dislocation density (b) in the aggregates from Group 6.

6. DISCRETE DISLOCATION DYNAMICS SIMULATIONS OF MULTICRYSTALLINE AGGREGATES

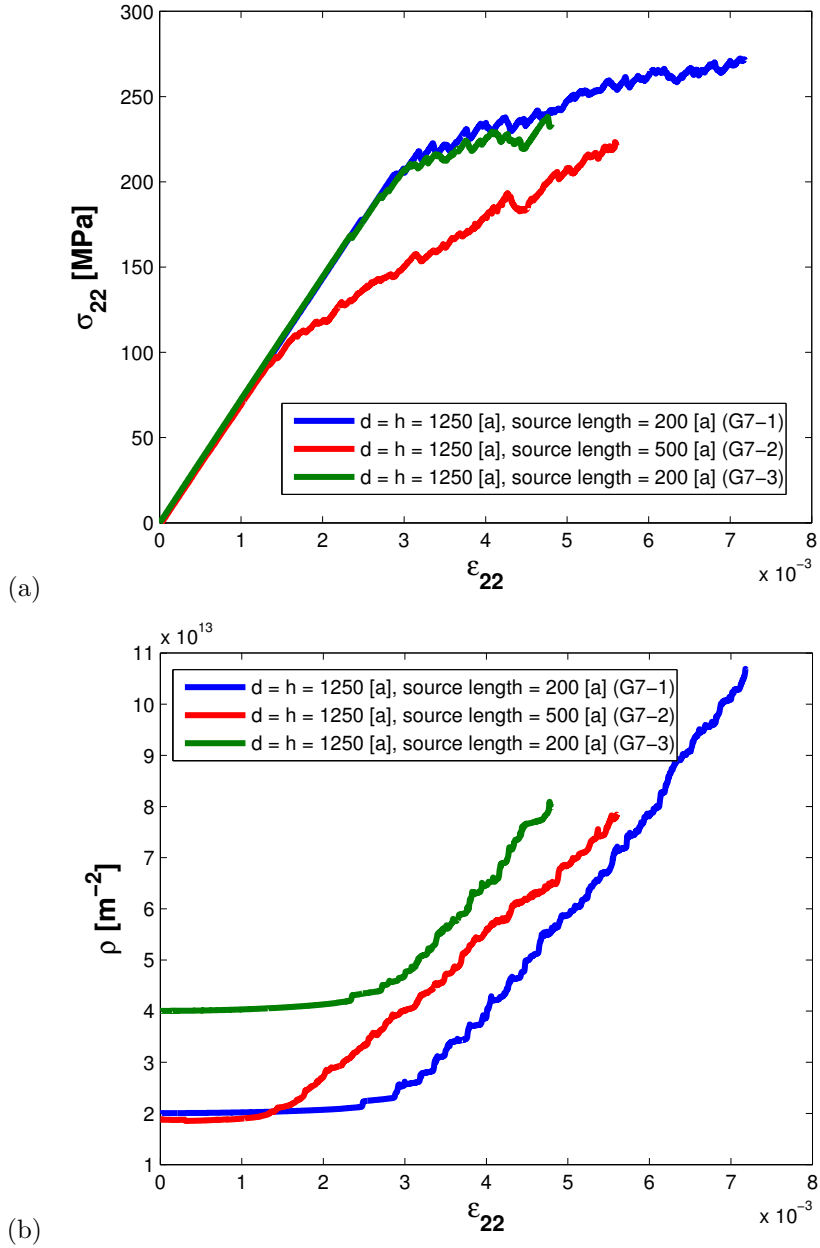


Figure 6.12: Stress–strain curves (a) and evolution of dislocation density (b) in the aggregates from Group 7.

6.2.3 Stress/strain heterogeneities - evolution of plasticity

This section is focused on the local properties of the aggregates. The observations of the dislocation structure evolution show that the first activated sources are found in the central (001) grain. But the activation of sources in the surrounding grains (random and (111)) depends on the particular configuration of the sources in these grains. The activation of each source causes the relaxation of stress which can be observed on the stress–strain curves as jumps (see previous section). Because of the small number of initial sources, there are very small amount of dislocations junctions and the main dislocation interaction is pile-up against the grain boundary which is the main mechanism causing the hardening of the aggregates (von Blanckenhagen et al. [2004]).

The local distributions of stress (σ_{yy}) and rotation (ω) are shown in this section. The rotation ω is the norm of the vector of rotation which is defined as:

$$\omega = \sqrt{rot_{xy}^2 + rot_{yz}^2 + rot_{xz}^2}, \quad (6.13)$$

where rot_{ij} are the components of the small rotation tensor and these are defined as:

$$rot_{ij} = \frac{1}{2} \left(\frac{\partial u_i}{\partial x_j} - \frac{\partial u_j}{\partial x_i} \right). \quad (6.14)$$

Distributions of these quantities depend on the initial positions of the sources and their activity. These quantities are compared for the 0.5 % of imposed total strain. Figures of the map of the σ_{yy} show the distribution of this stress component on the upper free surface of the aggregate and the curves inside the grains are the projections of the dislocations which are inside the grains, on this surface. This shown stress is the sum of dislocation induced stress and image field stress. The maps of the rotation then show the distribution of ω on the three sides and in middle plane of the aggregates. The comparison is done for the chosen aggregates from the groups presented in the previous section.

1. Group 1

This group consist of aggregates with the same grain size (2500 a). The comparison of the stresses in direction of tension is in figure 6.13. This figure shows that the

distribution of stresses is similar in the aggregates. The dislocation structure is similar for all aggregates. The rotations are shown in figure 6.14. These plots show the high rotation about 0.01° in the grains 1, 4 and 7. This corresponds to higher dislocation activity and density in these grains.

2. Group 4

This group consists of four aggregates. Two of them have columnar grains (G4-2, G4-3) and other two (G4-4, G4-5) have equiaxial grains. They have different source lengths ($300 a$ and $600 a$). The dispersion of stresses is shown in figure 6.15. The dispersion of stresses contains some similar features for all aggregates. The number of dislocations is smaller in this case because of the lower initial density. The main difference is in the central grain which is (001) oriented. The aggregates a) and c) have source length $300 a$ and there is activation of this source in this grain. In contrast, there is no activity in the other two cases with source length $600 a$. This is because of the small amount of initial sources which are badly orientated for slip according to direction of tension. Rotation is shown in figure 6.16. The amount of rotation is smaller than in previous case which is caused by the smaller amount of dislocations. The rotation is concentrated to the corner grains and the distribution of rotations is similar for both thicknesses and source lengths. The activation of sources in the central grain in the case a) is clearly visible since the rotation is increasing here.

6.2. RESULTS

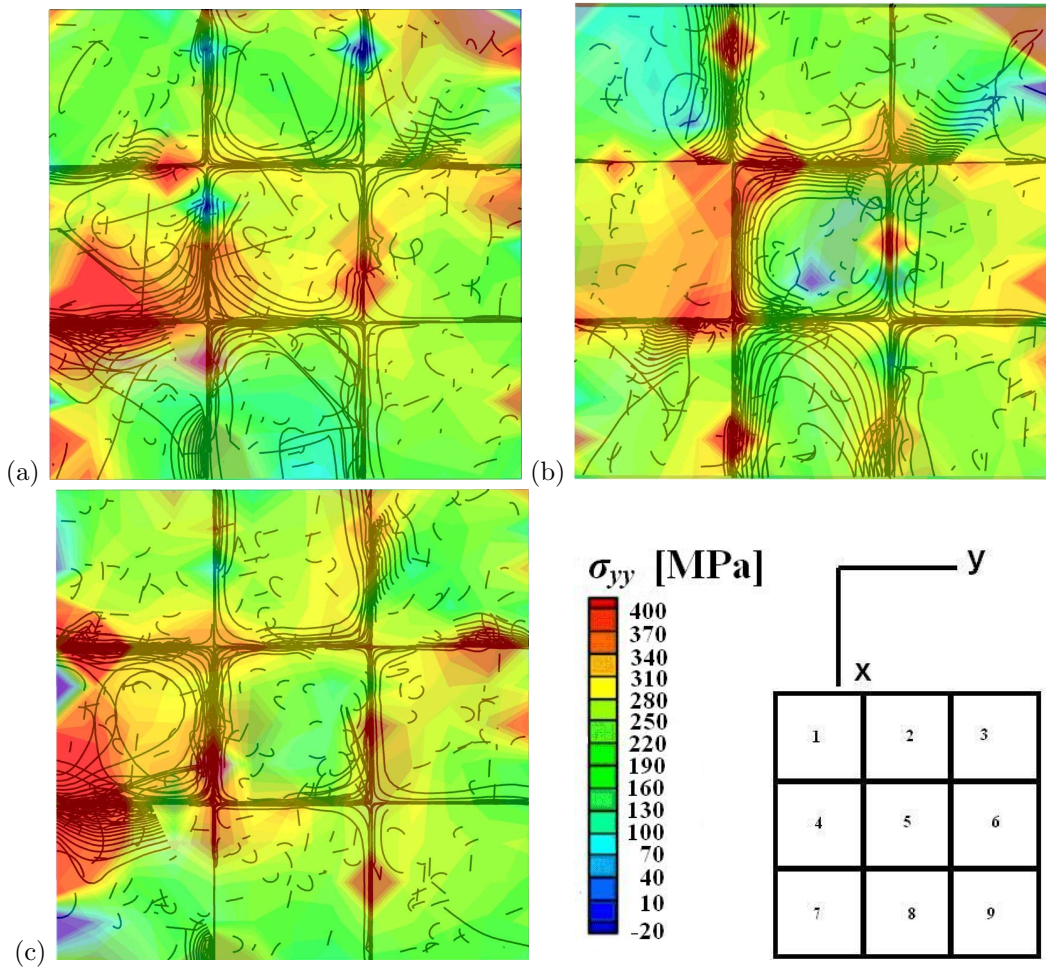


Figure 6.13: Distribution of the σ_{yy} on the free surface in the aggregates: a) G1-1, b) G1-2, c) G1-3.

6. DISCRETE DISLOCATION DYNAMICS SIMULATIONS OF MULTICRYSTALLINE AGGREGATES

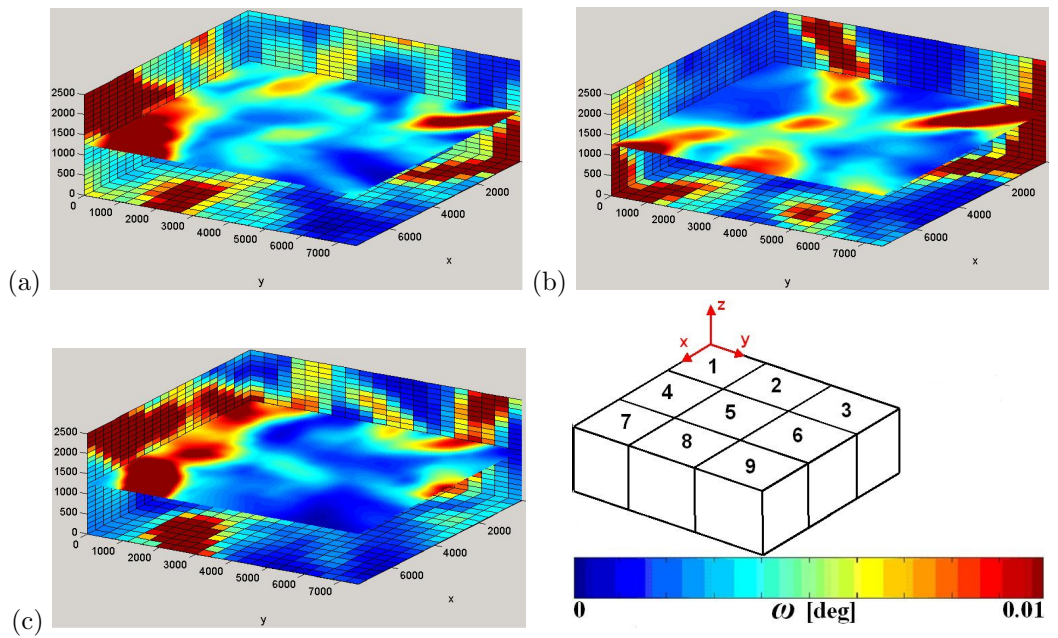


Figure 6.14: Distribution of the ω in the aggregates: a) G1-1, b) G1-2, c) G1-3.

6.2. RESULTS

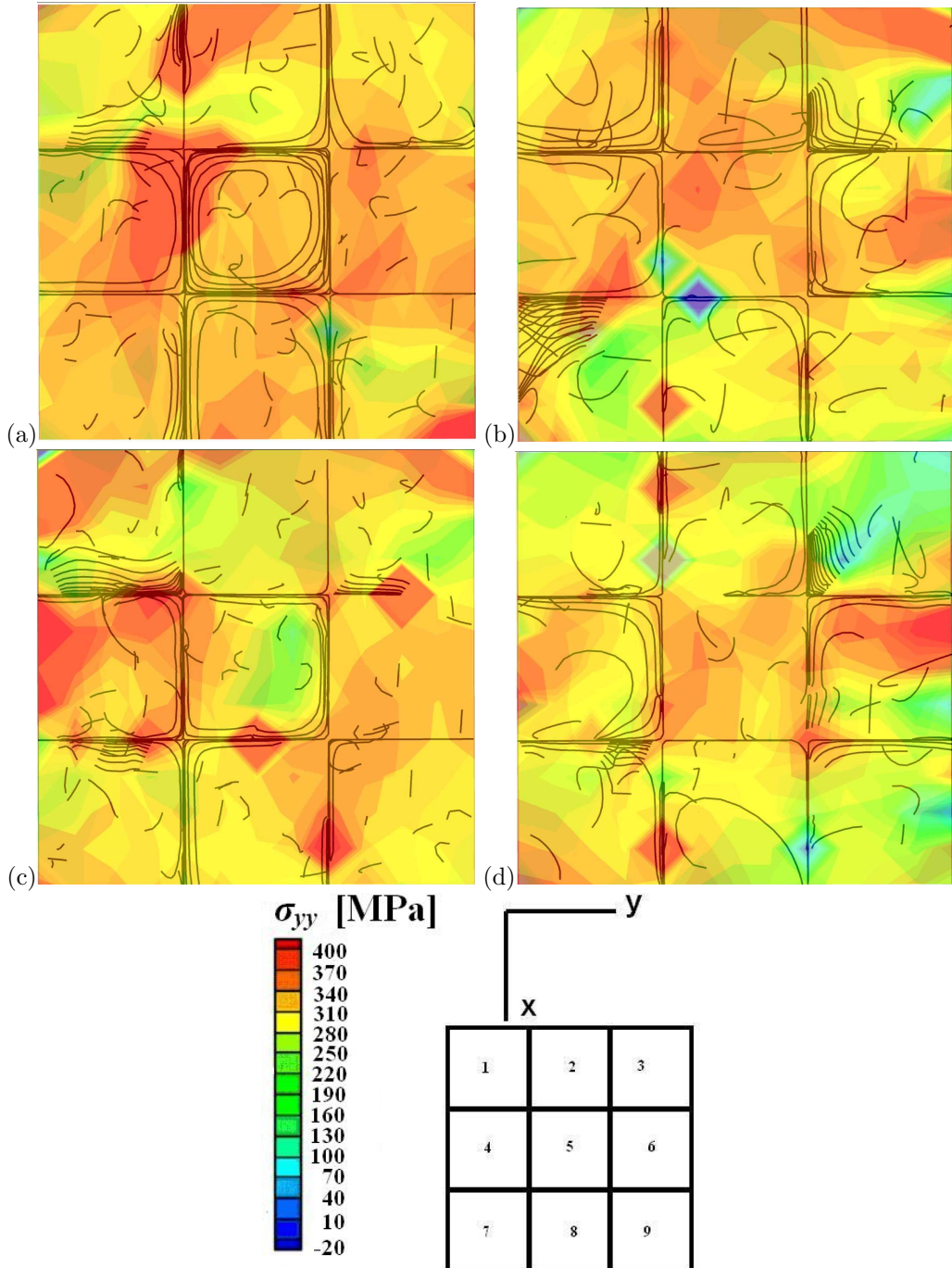


Figure 6.15: Distribution of the σ_{yy} on the free surface in the aggregates: a) G4-2, b) G4-3, c) G4-4, d) G4-5.

6. DISCRETE DISLOCATION DYNAMICS SIMULATIONS OF MULTICRYSTALLINE AGGREGATES

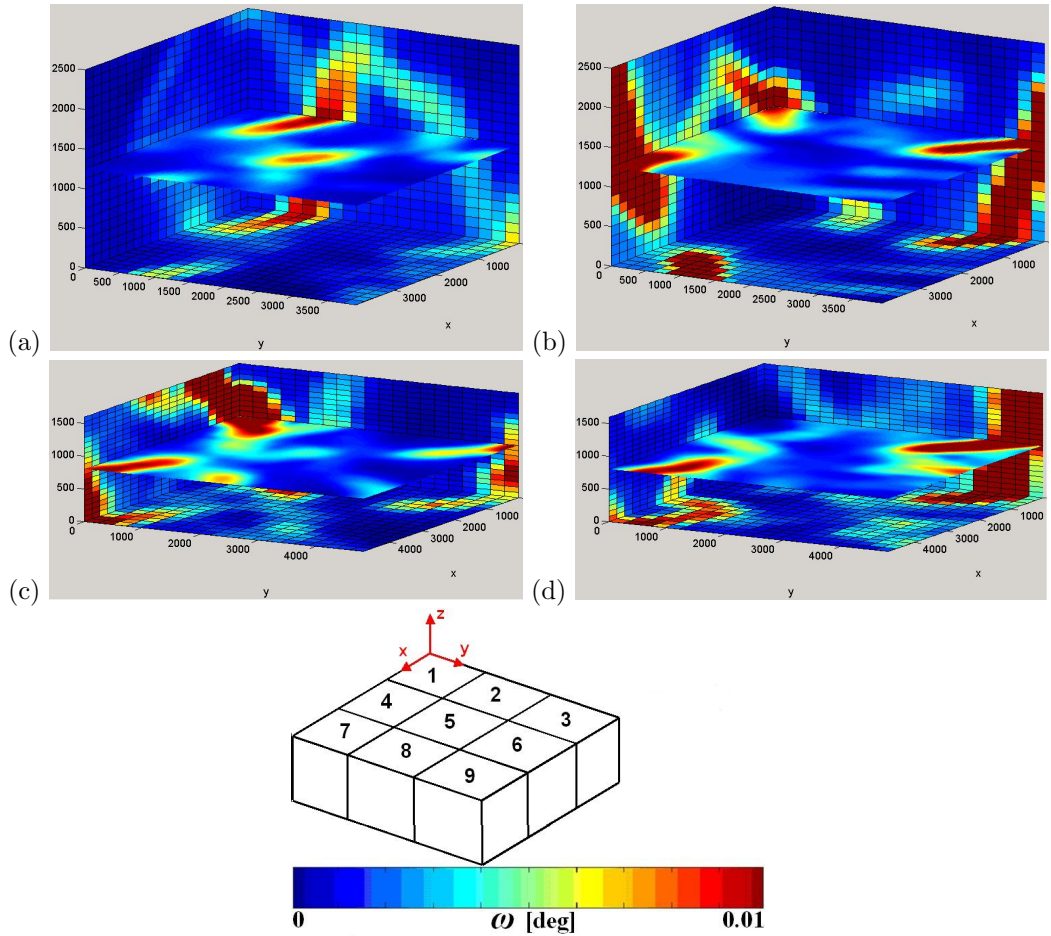


Figure 6.16: Distribution of the ω in the aggregates: a) G4-2, b) G4-3, c) G4-4, d) G4-5.

3. Group 5

These aggregates have the same initial dislocation density 10^{13} m^{-2} . The same source length ($200 a$) and in-plane grain size. They differ in the thickness of the aggregate. The distribution of stresses is shown in figure 6.17. The overall stress values are smaller than in the previous case. The higher density of dislocations allows better relaxation of stresses during plasticity. The dislocation activity is also very similar in all cases. The most active grain is the central (001) oriented grain. This similarity is also clear in the global stress-strain curves (see fig 6.10). The distribution of rotation is shown in figure 6.18. The most activity occurs in grains 2,3 and 7. The activity of sources in central grain can also be clearly recognized in this figure where rotation is increasing up to 0.01° in the central part of aggregate.

4. Group 6

This group consists of aggregates with a (001) oriented central grain and border grains with orientation (111). The only difference between the aggregates is their thickness. The dispersion of stresses is in figure 6.19. Due to the (111) orientation, the stresses are more homogeneous in these cases. The lowest value of stresses occurs in the central (001) oriented grain. The activity of sources is relatively small compared to activity in random oriented grains. This is caused by the fact that only few sources have the proper orientation according to the loading conditions that's why only few sources can be activated. These small differences can be also observed in the global stress-strain curves. The rotations are shown in figure 6.20. The distribution of rotation is similar in all aggregates but the values are much higher in the aggregate with equiaxial grains especially grain 2 and 3 and central (001) grain. These values decreases with increasing film thickness.

6. DISCRETE DISLOCATION DYNAMICS SIMULATIONS OF MULTICRYSTALLINE AGGREGATES

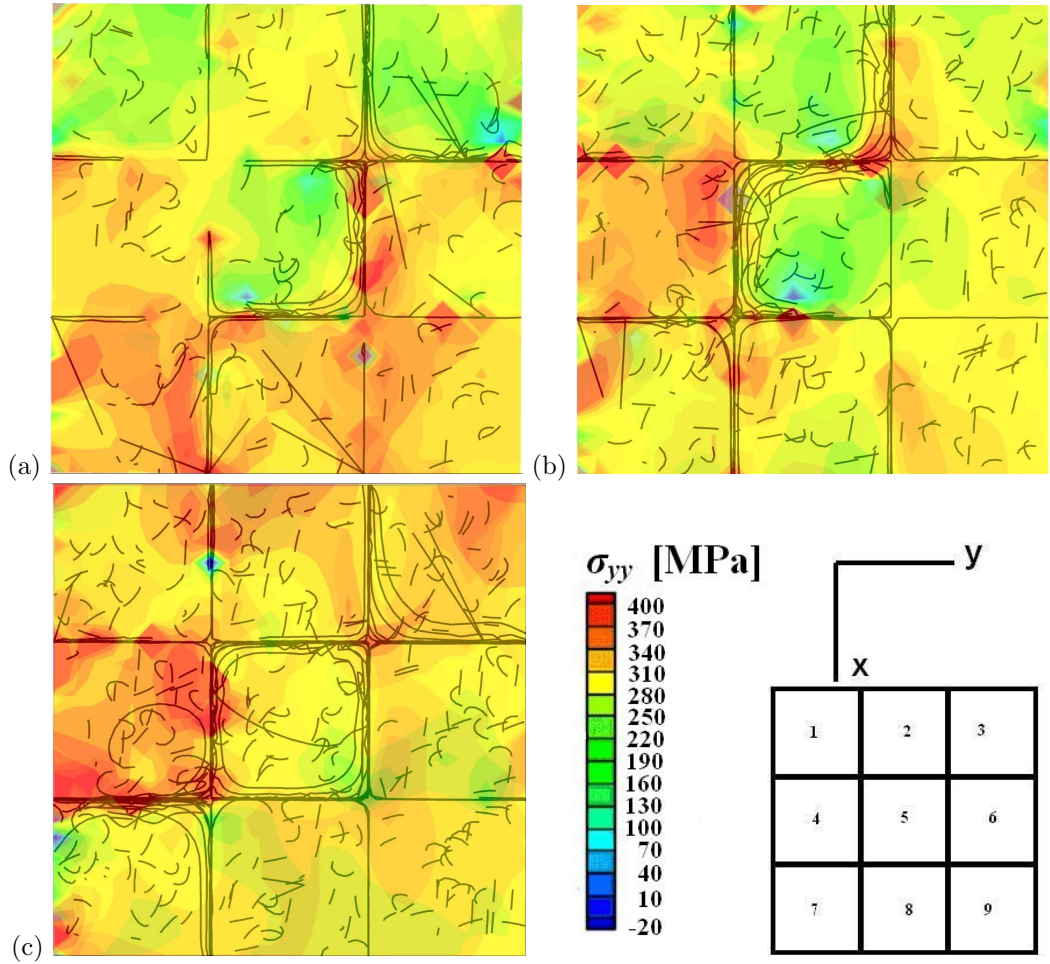


Figure 6.17: Distribution of the σ_{yy} on the free surface in the aggregates: a) G5-1, b) G5-2, c) G5-3.

6.2. RESULTS

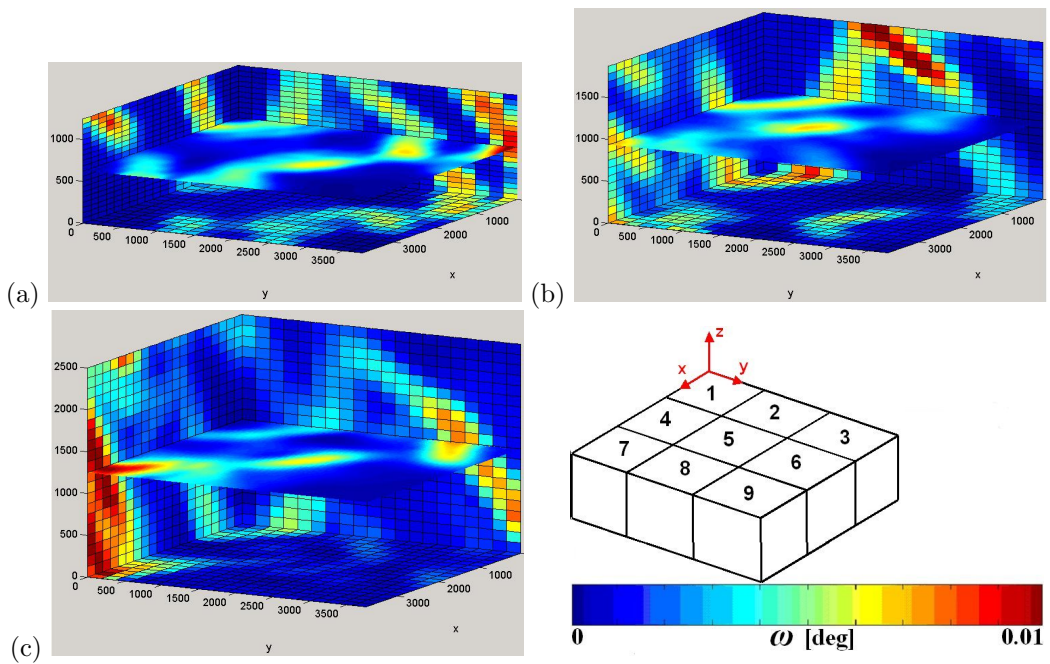


Figure 6.18: Distribution of the ω in the aggregates: a) G5-1, b) G5-2, c) G5-3.

6. DISCRETE DISLOCATION DYNAMICS SIMULATIONS OF MULTICRYSTALLINE AGGREGATES

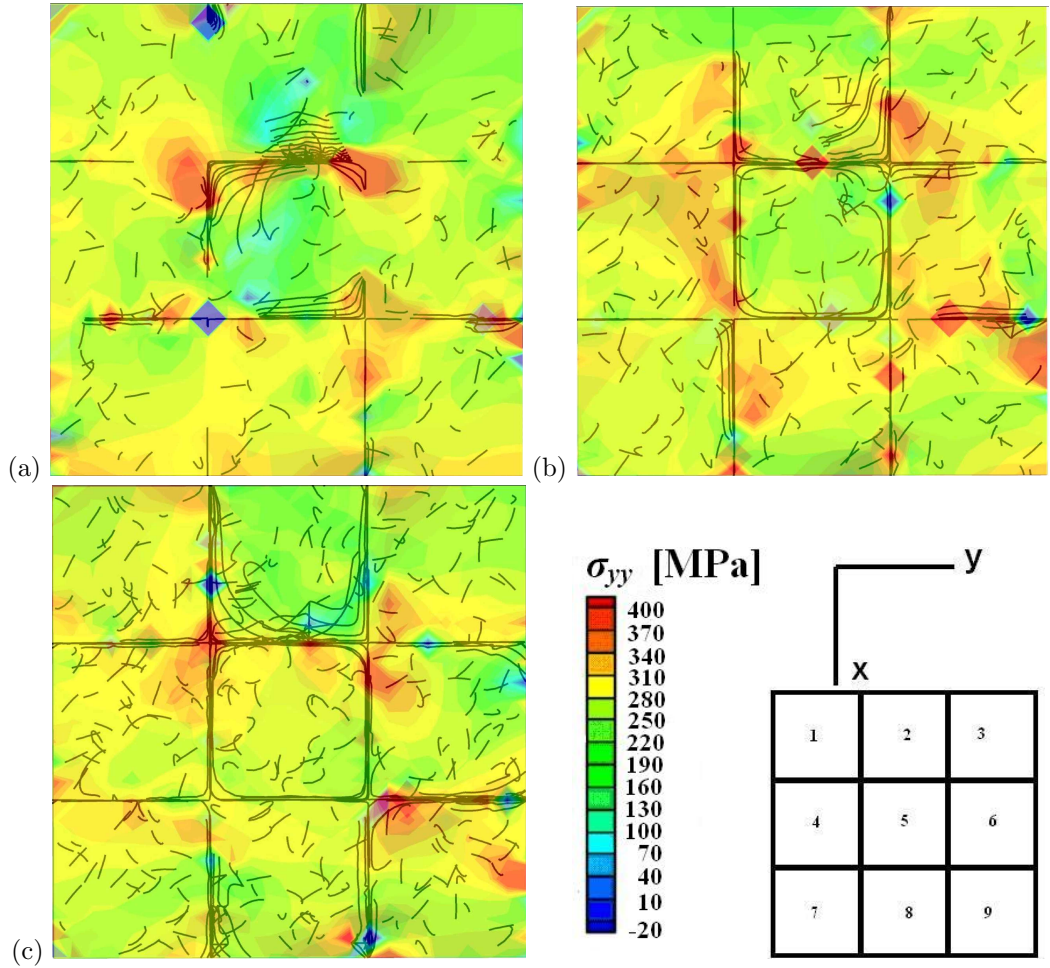


Figure 6.19: Distribution of the σ_{yy} on the free surface in the aggregates: a) G6-1, b) G6-2, c) G6-3.

6.2. RESULTS

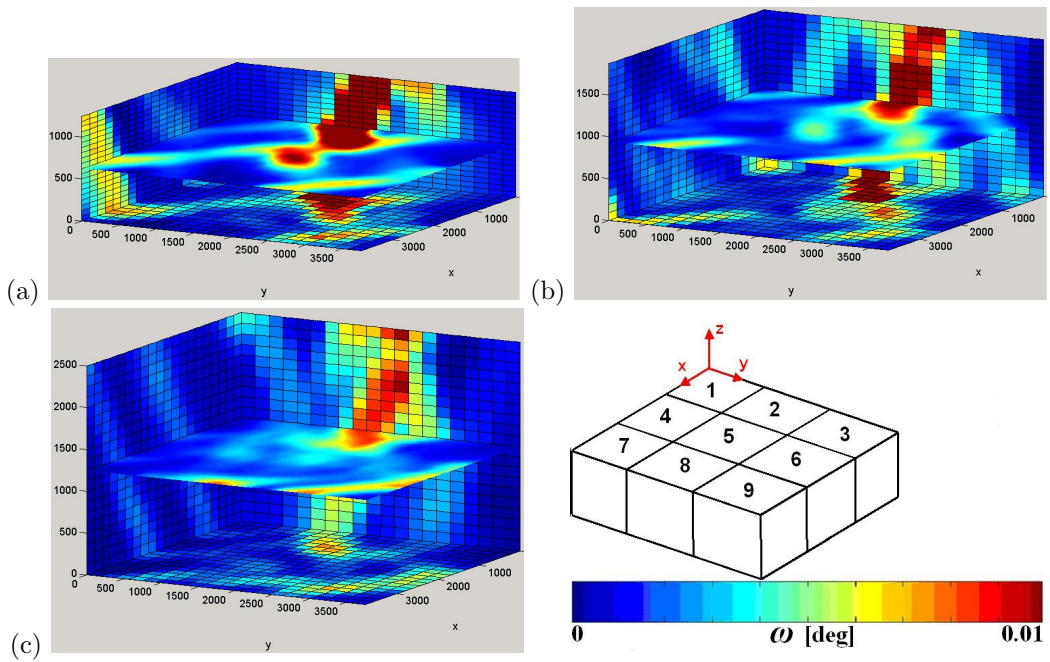


Figure 6.20: Distribution of the ω in the aggregates: a) G6-1, b) G6-2, c) G6-3.

6.3 Conclusions

The simulations of the polycrystalline aggregates within the framework of discrete dislocation dynamics were presented in this section. The global stress–strain behaviour as well as the local stress distribution and dislocation structure were investigated. The results can be summarized in the following points.

- The global behaviour like values of yield stress, strain and hardening rate are much more influenced by the length and number of the initial sources than the grain size in the range of grain sizes considered in this work.
- The stress–strain curves show that the most important dimension is the in–plane grain size while the film thickness does not influenced the global behaviour in the range of grain sizes considered in this work and when the thickness is equal or larger than the in–plane grain size.
- The initial number of the dislocation sources is small and the activation of each source can be observed on the global stress–strain curve.
- The main hardening mechanism is the dislocation pile–up due to the small number of sources.
- The first activated grain is central (001) oriented one which corresponds to the fact that this orientation is the softest.
- The dislocation activity in the (111) oriented grains is small which corresponds to the fact that this orientation is the hardest.

Chapter 7

Comparison of the crystal plasticity and DDD simulations

It is difficult to compare the previous discrete and continuum simulations, since the DDD results deal with rather small numbers of dislocations, whereas the continuum model assumes a sufficient number of dislocations at each integration point. However a statistical treatment of the DDD results will reveal some features of the transition from discrete to continuum behaviour. A comparison of the simulations performed by crystal plasticity and DDD is presented in this chapter. This comparison is done for the polycrystalline aggregates made of 9 grains which are the same as those presented in chapter 6.

7.1 Continuum crystal plasticity simulations

The first step is the estimation of the model parameters. The isotropic elasticity is used as in the previous DDD simulations. The elastic constants are also the same (see table 7.1). The parameters of the continuum crystal plasticity model are estimated from the stress-strain behaviour of single crystals with different crystallographic orientations with respect to the tensile direction obtained from DDD simulations. Tensile tests on single crystals with crystallographic direction $[010]$, $[011]$ and $[111]$ respectively aligned with the tensile direction are performed. The parameters of the DDD simulations are shown in table

7. COMPARISON OF THE CRYSTAL PLASTICITY AND DDD SIMULATIONS

7.1. These parameters are the same as in the DDD multicrystalline aggregates considered in chapter 6.

Orientation	grain size – in plane (d) film thickness (h) [a]	glide planes distance [a]	source length [a]	dislocation density 10^{13} [m ⁻²]
[010]	$d = 1250$ $h = 1250$	25	200	2.0
[011]	$d = 1250$ $h = 1250$	25	200	2.0
[111]	$d = 1250$ $h = 1250$	25	200	2.0

Table 7.1: Basic properties of the simulations of tensile test of single crystal. Lengths are written as the multiple of the lattice constant ($a=4.04496 \times 10^{-10}$ m).

The stress–strain curves produced by DDD simulations have very jagged shape due to the particular activations of the dislocation sources. Therefore these curves are smoothed by the straight line fitting. The estimation of the parameters is done by the optimization procedure in Zebulon code. This represents the same procedure used for the estimation of parameters in chapter 3. The resulting values of the parameters are shown in table 7.1. The graphical comparison of the DDD tensile curves and estimated ones is shown in figure 7.3. The results of several DDD simulation show that there is no hardening for orientations [111] and [011] and linear hardening for orientation [010]. This case is not possible to reproduce by the continuum model, therefore, there are differences between the resulting curves for DDD and continuum model simulations.

The 3D mesh of the multicrystalline aggregate is designed to have the same shape as mesh used in DDD simulations. The comparison is performed for the aggregates with grains which have the same in–plane grain size and film thickness. Each grain of the aggregate is a cube consisting of $5 \times 5 \times 5$ quadratic elements with 15 integration points. The crystallographic orientations of the grains represent the aggregate with central (001) oriented grain surrounded by (111) oriented grains. The crystallographic orientations are shown in table 7.3. They represent the same orientations as (111),(001) ones introduced in chapter 6 like simulation G7–1. The boundary conditions are also the same as in the DDD

7.1. CONTINUUM CRYSTAL PLASTICITY SIMULATIONS

Elasticity	
E	ν
72738 MPa	0.347

Plasticity	
Par.	Value
k [MPa s]	2.0
n	15.0
q [MPa]	0.091
b	0.089
r_0 [MPa]	75.0
h1	1.0
h2	1.4
h3	1.4
h4	1.4
h5	1.4
h6	1.4

Table 7.2: Values of the parameters from the fitting of DDD simulations of tensile test of singlecrystal.

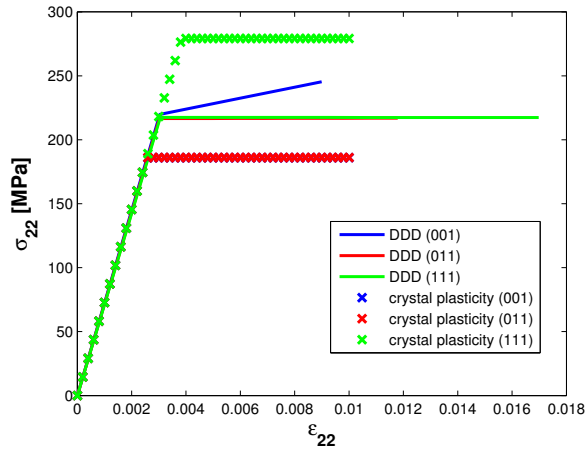


Figure 7.1: Comparison of the DDD simulations curves and curves obtained by crystal plasticity computations.

simulations (chapter 6). The boundary conditions and the aggregate mesh are shown in

figure 7.2(a),(b).

Grain	ϕ_1	Φ	ϕ_2
Random aggregates			
Grain 1	18.45	54.7356	45.00
Grain 2	89.52	54.7356	45.00
Grain 3	38.86	54.7356	45.00
Grain 4	263.21	54.7356	45.00
Grain 5	72.46	0.00000	0.00
Grain 6	78.92	54.7356	45.00
Grain 7	20.41	54.7356	45.00
Grain 8	0.79	54.7356	45.00
Grain 9	259.73	54.7356	45.00

Table 7.3: Values of Euler angles of the grains orientations for aggregate used in crystal plasticity simulation.

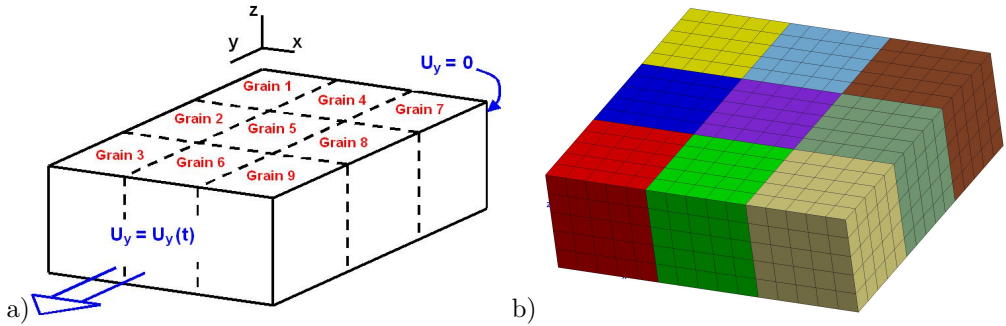


Figure 7.2: Boundary conditions of crystal plasticity simulations a), representation of 9 grain aggregate b).

7.2 DDD simulations

These simulations are performed for the aggregates with equiaxial grains and properties mentioned in table 7.4. These properties are the same as for the simulation G7-1 in chapter 6. The discrete nature of the plasticity processes together with the small number of dislocation sources cause that the stress-strain behaviour of the aggregate is strongly in-

7.3. RESULTS

fluenced by the particular distribution of these dislocation sources in the grains. Therefore a statistical approach is used to average this effect. Ten different realizations of the same aggregate are produced. They differ only by the positions of the dislocation sources inside the grains. The ensemble averaging is then applied. The resulting value at the node or integration point \underline{x} is computed as an ensemble average of values at the same geometrical node/point \underline{x} in the different simulations. The reader is referred to (Zeghadi et al. [2007a], Zeghadi et al. [2007b]) for the description of an ensemble averaging strategy. This can be expressed for stress as:

$$\sigma_{ij}^a(\underline{x}) = \frac{1}{N} \sum_{k=1}^N \sigma_{ij}^k(\underline{x}). \quad (7.1)$$

The average value per grain is then:

$$\langle \sigma_{ij}^a \rangle = \frac{1}{V_g} \int_{V_g} \left(\frac{1}{N} \sum_{k=1}^N \sigma_{ij}^k \right) dV_g \quad (7.2)$$

where $N = 10$ is the number of simulations, σ_{ij}^k the stress component at given node/integration point of the k -th simulation and V_g is the volume of given grain.

simulation	grain orientation	grain size – in plane (d) film thickness (h) [a]	glide planes distance [a]	source length [a]	dislocation density 10^{13} [m ⁻²]
G7-1	(111)(001)	$d = 1250$ $h = 1250$	25	200	2.0

Table 7.4: Basic properties of the DDD simulations. Lengths are written as the multiple of the lattice constant ($a=4.04496 \times 10^{-10}$ m).

7.3 Results

The comparison of simulations is performed on three different levels: macroscopic stress–strain curves, averages per grains and local distribution of stresses and plastic strain at a free surface. The global stress–strain curves are shown in figure 7.3. This plot shows the curves of individual DDD simulations and the corresponding ones for the continuum crystal

7. COMPARISON OF THE CRYSTAL PLASTICITY AND DDD SIMULATIONS

plasticity simulations. This comparison shows the higher overall stress level in the DDD simulations. This is caused by the stresses produced by discrete dislocations and also by the constrained plasticity due to the small number of initial dislocation sources. The scatter of the DDD simulations curves also shows the influence of the different aggregate realizations on the macroscopic results.

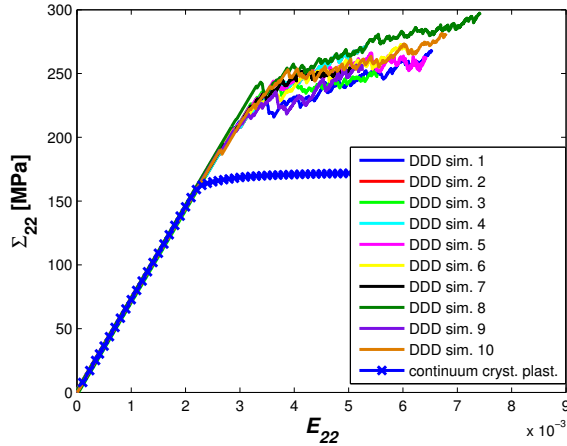


Figure 7.3: Global stress strain curves for 10 realizations of DDD simulations (lines) and one realization of crystal plasticity simulation (crosses).

The average values per grain are compared in figure 7.4(a),(b). The case (a) shows the absolute values of average stresses in DDD and crystal plasticity simulations and case (b) shows the relative values normalized by the average stress value for the whole aggregate. The numbers on x axis is the label of each grain in the aggregate. The grain 5 has orientation (001) while the others are (111) oriented. The comparison is done for 0.5 % total applied strain. These plots again show the higher stress level in the DDD simulations. The relative values show the distribution of stress values in the aggregate. The relative stress values are in relatively good agreement for grains 1,2,3,4 and 8. The larger discrepancy occurs for grains 5, 6, 7 and 9, but the values for grains 5 and 6 are at least at the same side from the average. These results show that the mutual stress levels in aggregates can be comparable for the different approaches. The discrepancies are caused by the influence of

7.3. RESULTS

the dislocation sources activation. Also the existence of pile-ups at grain boundaries is not accounted for by the continuum crystal plasticity model. Closer results could be obtained with higher numbers of DDD simulations which contain higher amount of initial dislocation sources.

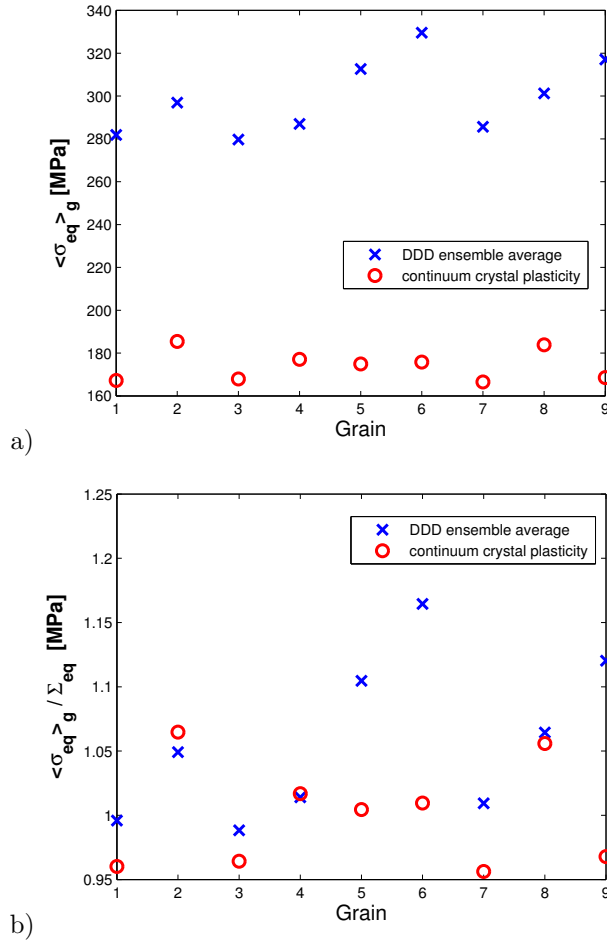


Figure 7.4: a) Comparison of the average von Mises stress values per grain in simulations. b) Comparison of relative von Mises stress values per grain in simulations.

The third level of analysis is the comparison of the von Mises stress and plastic strain

7. COMPARISON OF THE CRYSTAL PLASTICITY AND DDD SIMULATIONS

maps in aggregates. This comparison is only qualitative due to the different stress and strain levels in different simulations. The stress and strain distributions in DDD simulations are still strongly influenced by the initial positions of the dislocation sources but some general similarities can be recognized in both simulations. The first comparison is shown in figure 7.5(a – d). The figures (a) and (b) show the distribution of von Mises stress in crystal plasticity simulation at free surfaces $z=0$ (a) and $z=h$ (b). The figures (c) and (d) then show the distribution of von Mises stress in DDD simulation. The DDD simulations produce higher stress concentrations and higher localization of these extremal values. This is caused by the presence of dislocations which induce high stress concentrations. But some similarities can be pointed out. The following features can be found at the bottom surface $z = 0$. The band of the higher stress through the grains 6, 8 and 9 is clearly visible in both simulations. The stress concentrations at grain boundaries of grains 6 and 5, 2 and 5 are also remarkable. The grains 1 and 3 have smaller level of stress in both type of simulations. The upper surface ($z = h$) shows the similarities mostly by the stress concentrations at the grain boundaries. This is clearly visible at the boundaries between grains 5 and 8, 6 and 9, 2 and 3 or 1 and 2. Lower stress level in grain 3 is also comparable in both simulations. There are also many differences presented in the simulations. The large stress concentration areas can be found in DDD simulations at upper surface like those at grain boundaries of grains 4 and 7, 3 and 6, 6 and 9 or 2 and 5. These stress concentration are absent in continuum crystal plasticity simulations.

A similar comparison is made for the plastic strain maps. This comparison is shown in figure 7.6(a–d). Higher plastic deformations are generally found in the continuum crystal plasticity simulations. The scale of the deformation values is different for different simulations in order to provide a better resolution in color maps. As in the previous case, the bottom ($z = 0$) and upper ($z = h$) surfaces are compared. The bottom surfaces show the following features. The similarities can be observed in grains 6 and 9, where higher plastic deformation develops. Such an increase can be also observed in grain 3 and also in (001) oriented grain 5. But there are also large discrepancies like those in grain 2 and grain 1. They are again caused by the discrete nature of plasticity and its dependence on

7.3. RESULTS

dislocations positions in the DDD simulations. The increased level of plasticity in grains 6 and 9 is observed also at the upper surface. The increasing plasticity in grain 5 also occurs in both type of simulations. But again the discrepancies can be observed in grains 1, 7, 8. There is significant strain band in the grain 3 in DDD simulations. Such a band is also visible in crystal plasticity simulation but in this case this band is much less significant.

7. COMPARISON OF THE CRYSTAL PLASTICITY AND DDD SIMULATIONS

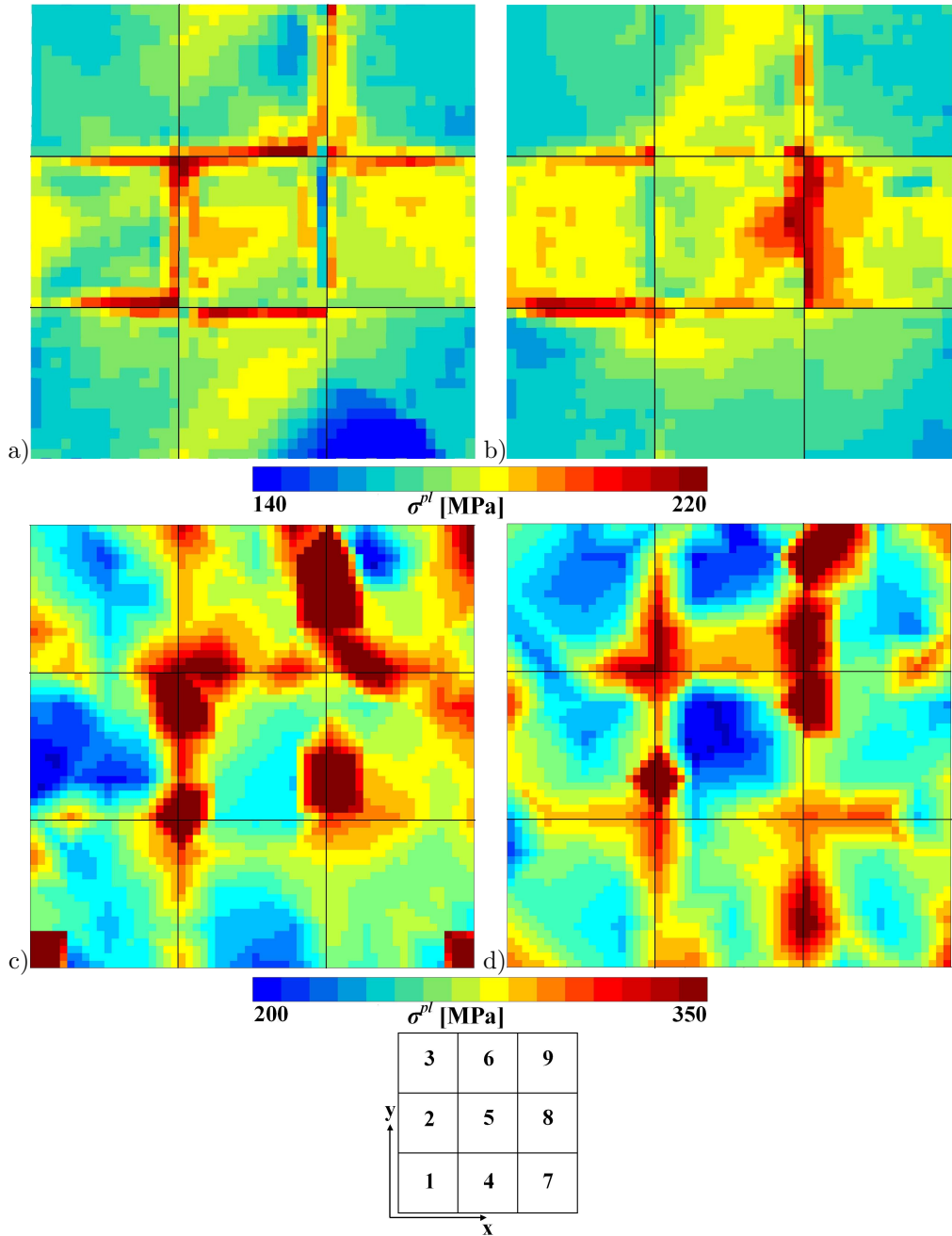


Figure 7.5: Von Mises stress maps at free surfaces a) continuum crystal plasticity simulation $z=0$, b) continuum crystal plasticity simulation $z=h$, c) DDD simulations $z=0$, d) DDD simulations $z=h$ (ensemble averaged fields).

7.3. RESULTS

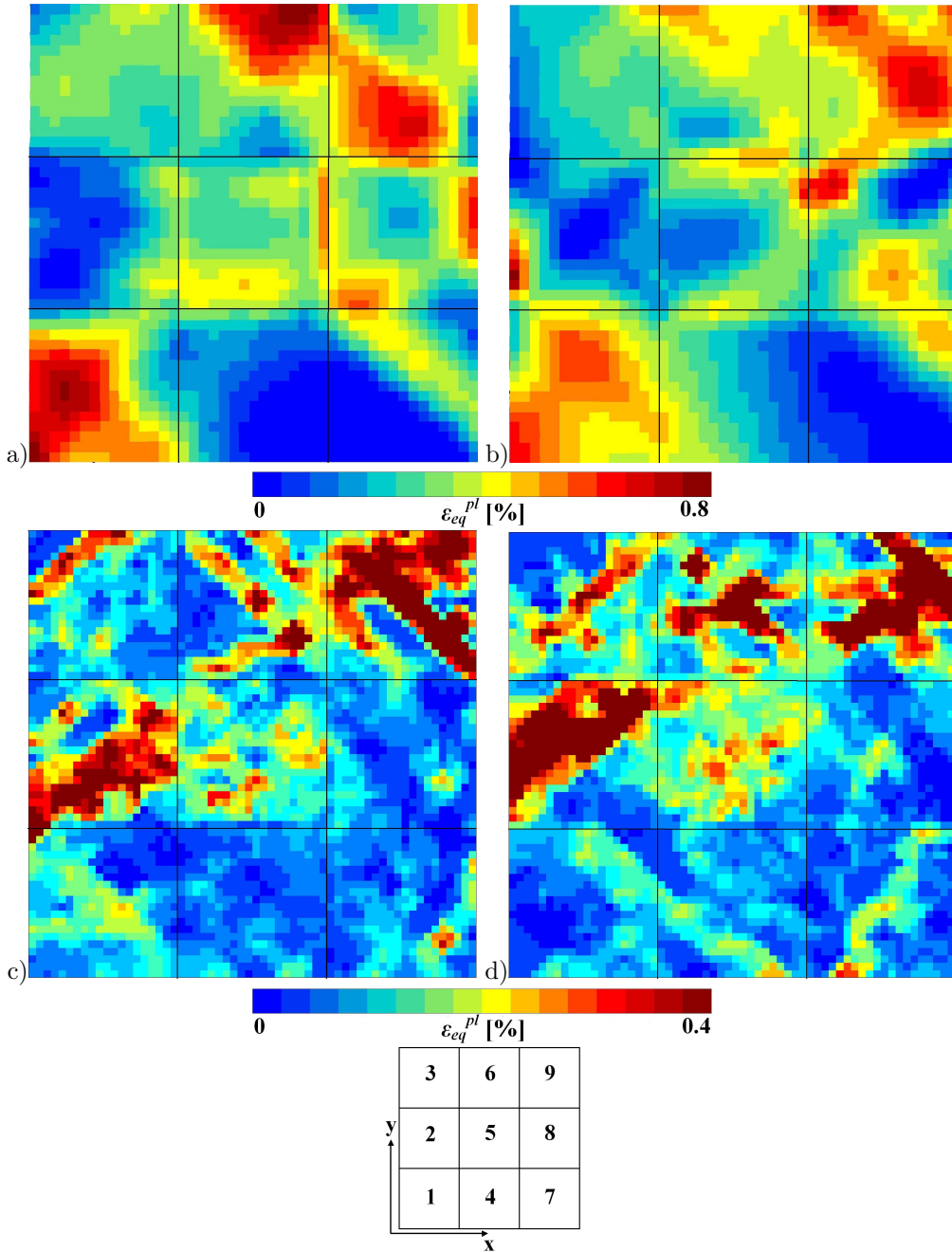


Figure 7.6: Equivalent plastic strain maps at free surfaces a) continuum crystal plasticity simulation $z=0$, b) continuum crystal plasticity simulation $z=h$, c) DDD simulations $z=0$, d) DDD simulations $z=h$ (ensemble averaged fields).

7.4 Conclusions

The comparison of the DDD and crystal plasticity simulations of 9 grains multicrystalline aggregate was performed in this chapter. The obtained results can be summarized into following points:

- The statistical ensemble averaging approach is useful for minimizing of the effect of positions of initial dislocation sources on the behaviour of aggregate. But the number of 10 realizations as well as the small number of dislocation sources (32 per grain) are not sufficient to reach the continuum behaviour.
- The comparison of macroscopic stress–strain curves shows the higher level of stress in the DDD simulations which is caused by the stress concentrations due to restricted plasticity caused by the small number of dislocation sources and pile–up structures. Pile–ups induce high internal stresses not accounted for in the continuum model.
- The comparison of the average stresses in grains shows that the stresses are distributed in similar way in both type of simulations. The discrepancies are caused again by the discrete nature of plasticity process in DDD simulations.
- The qualitative comparison of the von Mises stress and plastic strain maps show that areas of stress and strain concentrations can be localized at the same positions in both types of simulations.

This comparison shows that there is a transition from discrete behaviour to continuum crystal plasticity taking place at the micron scale. The closer results should be obtained when these models will go closer toward to each other. This means more realization of DDD aggregates with higher numbers of initial dislocation sources. And from the continuum point of view, scale dependent internal stresses should be introduced. The comparison should now be drawn with higher order continuum models like second gradient crystal plasticity (Shu and Fleck [1999]), Cosserat crystal plasticity (Forest et al. [2000]) and statistical theory of dislocations (Groma et al. [2003], Yefimov and Van der Giessen [2005]).

Chapter 8

Conclusions and prospects

The summary of the obtained results is given in this chapter as well as the outline of the possible perspectives of the investigation in the simulations of the mechanical behaviour of thin films.

8.1 Conclusions

The main task of this thesis is the application of the different numerical approaches in the investigation of the mechanical properties of thin films. The continuum approach is represented by classical continuum crystal plasticity. This approach was applied to the modelling of the copper thin films. The discrete dislocation dynamics represents the discrete approach. This theory was used in simulations of behaviour of thin polycrystalline aggregates. The starting point of a systematic comparison of both approaches was performed in the final chapter. All the simulations were based on the finite element method.

The finite element method together with a statistical approach used in the thesis, can provide reliable results and the statistical methods allows to reduce the requirements on the computational effort.

The main results of the mechanical behaviour of the copper thin films within the framework of the classical continuum crystal plasticity obtained in this work can be summarized as follows:

8. CONCLUSIONS AND PROSPECTS

- The out of plane shear develops during the tensile loading of $\{111\}$ oriented grains. This shear is responsible for the local stress concentrations at the grain boundaries, which can be potentially initiators of damage. This local shear concentration contrasts with the average shear stress values per aggregates which are close to zero as shown in the simulations and also as it is supposed during experiments.
- The $\{001\}$ and random oriented grains also act as a kind of stress concentrators since the simulations show the increasing of the stresses in the $\{111\}$ grains, which are located in the neighborhood of $\{001\}$ and random grains.
- The copper film which mostly consists of $\{111\}$ oriented grains has also strong tendency to become wavy during the uniaxial tension, because the $\{111\}$ planes are not symmetry planes. This undulation could play an important role in the processes of decohesion between the film and the substrate.
- The model predicts the saturation of hardening in the films on stiff substrate after 70 cycles of uniaxial loading. The dispersion of the plastic strain values increases during cycling and also this plastic strain becomes more localized during cycling. This plastic strain localization is more pronounced in the free-standing films due to their smaller constraints. These more and more localized areas of increased plastic strain are created especially in the $\{001\}$ and random oriented grains. These microstrain concentrations may lead to creation of extrusions in the real films which are the primary attributes of fatigue damage.
- The global plasticity induced surface roughness of the film on stiff substrate saturates after 10 cycles of uniaxial loading, but locally, there are some areas, especially grain boundaries, where the roughness evolve continuously (up to 1000 cycles). These places are again potentially dangerous from the point of view of damage of thin films. In contrast, the global roughness does not saturate up to 55 cycles (reached in simulations) for free-standing films and its value strongly depends on the particular realization of the polycrystalline aggregate and the mutual grain orientations.

8.1. CONCLUSIONS

- The comparison with experimental data of tensile tests of copper thin films on a polyimide substrate shows the level of ability of the model to predict the behaviour of the thin copper films. The stress level and hardening rate in experiments are significantly higher than those predicted by the model. The model also predicts higher amount of plastic deformation than in the experimental measurements. But at least the model is able to predict the trends in evolution of plastic strain at global and also local level. The quantitative discrepancies are caused by the fact that this model is derived for bulk structures and does not take into account the effects belonging to single dislocations motion and interactions, which become more important at the micron scale of thin films. Therefore this model is not able to predict the size-effects in thin films, because these phenomena are based on the dislocation motion and interactions in a confined volume.

The discrete dislocation dynamics was found to be well suited for predictions of the mechanical behaviour of thin films. Therefore the simulations of the tensile test of free-standing multicrystalline aggregates were performed using this approach. The main results are the following:

- The most important influence on the value of yield stress and hardening rate is that of the length of the initial dislocation sources. It is more important than the grain size at least in the range of the grain sizes considered in this work.
- Comparison of the influence of the particular grain dimensions shows that the behaviour is more influenced by the in-plane grain size than the film thickness when the thickness is equal or larger than the in-plane size.
- These simulations show that with such a small number of initial dislocation sources, the dislocation piling-up at grain boundaries is the main hardening mechanism. The dislocation activity is the smallest in $\{111\}$ oriented grains and highest in $\{001\}$ oriented grains, which can be linked with continuum crystal plasticity simulations where the $\{111\}$ oriented grains are indeed less deformed than the $\{001\}$ ones.

- The main limitation of the presented DDD code is in the representation of the grains and their boundaries. The grains are realized by simple cubic shape and the grain boundaries are set to be impenetrable for the dislocations. These conditions limits the dislocation motion and as a consequence they influence the estimation of the stress and strain levels in the aggregates. Another limitation is represented by the limited number of dislocation sources in grains. This limitation is caused by the numerical stability of the given code and computational effort of used computers.

The comparison of both approaches is performed to check how "close" are the predictions obtained by these different approaches. The results of this comparison can be summarized into the following points:

- The discrete dislocation simulations predict higher stress levels than the continuum theory. This is due to the fact that DDD theory takes into account the back stress of dislocation pile-ups which acts on the dislocation sources. The number of these sources is also small, which further constrains the evolution of plasticity compare to the continuum theory, which assumes a high number of sources at every integration point.
- Taking into account the qualitative distribution of average stress per grain and local stress and strain values, both models predict close results for some locations inside the aggregate. But there are also still large discrepancies at some locations, because this comparison remains still rough due to the different nature of the models. These discrepancies also indicate the transition from continuum to discrete behaviour at the micron scale.

8.2 Prospects

The present work shows the limits of both theories and therefore some suggestions for the future studies can be given:

8.2. PROSPECTS

- The future study of thin films within the framework of the continuum theory should be focused on the application of the higher order crystal plasticity theories like second-gradient crystal plasticity (Shu and Fleck [1999]) or Cosserat crystal plasticity (Forest et al. [2000]). These models introduce some intrinsic length-scales and they could be able to predict the size-effects and effects caused by the collective dislocation motion and interactions. These continuum models should be also compared with statistical theory of dislocations, which lies in-between the continuum and discrete approach (Groma et al. [2003], Yefimov and Van der Giessen [2005]).
- The discrete dislocation dynamics approach investigation of the thin film should be aimed on the performing more realistic 3D simulations. This include namely the more realistic grain shape, penetrable grain boundaries or possibility of application of anisotropic elasticity. The other task is to realize the simulations with much higher amount of initial dislocation sources, but this is the problem of available computational capacity and numerical stability of computations.
- Once stress and strain fields are correctly estimated in polycrystalline thin films, theoretical fatigue damage initiation models can be applied to estimate the lifetime of coated or layered components.

Bibliography

- ARZT E., DEHM P., GUMBSCH P., KRAFT O., AND WEISS D. (2001). *Interface controlled plasticity in metals: dispersion hardening and thin film deformation*. Progress in Material Science, vol. 46, pp 283–307. 1.3, 1.7
- ASARO R.J. (1983a). *Crystal Plasticity*. Journal of Applied Mechanics, vol. 50, pp 921–934. 1.1
- ASARO R.J. (1983b). *Micromechanics of crystals and polycrystals*. Advances in Appl. Mech., vol. 23, pp 1–115. 1.1, 3.1
- BACHU V. AND KALIDINDI S. (1998). *On the accuracy of the predictions of texture evolution by the finite element technique for fcc polycrystals*. Material Science and Engineering A, vol. A257, pp 108–117. 1.1
- BAKER S. P., KELLER-FLAIG R. M., AND SHU J. B. (2003). *Bauschinger effect and anomalous thermomechanical deformation by oxygen in passivated thin Cu films on substrates*. Acta Materialia, vol. 51, pp 3019–3036. 1.2.1, 1.2.3
- BAKER S. P., KRETSCHMANN A., AND ARZT E. (2001). *Thermomechanical behavior of different texture components in Cu thin films*. Acta materialia, vol. 49, pp 2145–2160. 1.2.1, 1.2.2, 1.2.3
- BARBE F., DECKER L., JEULIN D., AND CAILLETAUD G. (2001a). *Intergranular and intragranular behavior of polycrystalline aggregates. Part 1: FE model*. International Journal of Plasticity, vol. 17, pp 513–536. 1.1, 2.2.1, 3.1

BIBLIOGRAPHY

- BARBE F., DECKER L., JEULIN D., AND CAILLETAUD G. (2001b). *Intergranular and intragranular behavior of polycrystalline aggregates. Part 2: Results*. International Journal of Plasticity, vol. 17, pp 537–563. 1.1
- BEAUDOIN A., DAWSON P. R., MATHUR K. K., AND KOCKS U. F. (1995). *A hybrid finite element formulation for polycrystal plasticity with consideration of macrostructural and microstructural linking*. International Journal of Plasticity, vol. 11, pp 501–521. 1.1
- BEAUDOIN A., MATHUR K. K., DAWSON P. R., AND JOHNSON G. C. (1993). *Three-dimensional deformation process simulation with explicit use of polycrystal plasticity models*. International Journal of Plasticity, vol. 9, pp 833–860. 1.1
- BECKER R. (1991). *Analysis of texture evolution in channel die compression—effects of grain interaction*. Acta Metallurgica et Materialia, vol. 39, pp 1211–1230. 1.1
- BECKER R. (1998). *Effects of strain localization on surface roughening during sheet forming*. Acta Materialia, vol. 46, pp 1385–1401. 1.1
- BERVEILLER M. AND ZAOUÏ A. (1978). *An extension of the self-consistent scheme to plastically flowing polycrystals*. Journal of the Mechanics and Physics of Solids, vol. 26, pp 325. 1.1
- BHATTACHARYYA A., EL-DANAF E., KALIDINDI S.R., AND DOHERTY R.D. (2001). *Evolution of grain-scale microstructure during large strain simple compression of polycrystalline aluminium with quasi columnar grains : OIM measurements and numerical simulations*. Acta Materialia, vol. 17, pp 861–883. 2.2.1
- BORG U. (2007). *Strain gradient crystal plasticity effects on flow localization*. International Journal of Plasticity, vol. 23, pp 1400–1416. 1.2.3
- BUCHHEIT T. E., WELLMAN G. W., AND BATTLE C. C. (2005). *Investigating the limits of polycrystal plasticity modeling*. International Journal of Plasticity, vol. 21, pp 221–249. 1.1

BIBLIOGRAPHY

- CAILLETAUD G. (1992). *A Micromechanical Approach to Inelastic Behaviour of Metals*. Int. J. Plasticity, vol. 8, pp 55–73. 3.1, 4.2.1
- CHEONG K.-S. AND BUSSO E. P. (2004). *Discrete dislocation density modelling of single phase FCC polycrystalline aggregates*. Acta Materialia, vol. 52, pp 5665–5675. 1.2.3
- CHO N. I. AND PARK D. I. (1997). *Microstructures of copper thin films prepared by chemical vapor deposition*. Thin Solid Films, vol. 308, pp 465–469. 1.2.1
- CHOI Y. AND SURESH S. (2002). *Size effects on the mechanical properties of thin polycrystalline metal films on substrates*. Acta Materialia, vol. 50, pp 1881–1893. 1.3
- DÉPRÉS C., ROBERTSON C.F., AND FIVEL M.C. (2004). *Crack initiation in fatigue: experiments and three-dimensional dislocation simulations*. Materials Science and Engineering, vol. A387–389, pp 288–291. 4.3.2
- DEVINCRE B., KUBIN L., AND HOC T. (2006). *Physical analyses of crystal plasticity by DD simulations*. Scripta Materialia, vol. 54, pp 741–746. 1.2.3
- DIARD O., LECLERCQ S., ROUSSELIER G., AND CAILLETAUD G. (2005). *Evaluation of finite element based analysis of 3D multicrystalline aggregates plasticity. Application to crystal plasticity model identification and the study of stress and strain fields near grain boundaries*. International Journal of Plasticity, vol. 21, pp 691–722. 1.1
- DUCHENE L. AND HABRAKEN A. M. (2005). *Analysis of the sensitivity of FEM predictions to numerical parameters in deep drawing simulations*. European Journal of Mechanics – A/Solids, vol. 55, pp 614–629. 1.1
- FOREST S., BARBE F., AND CAILLETAUD G. (2000). *Cosserat Modelling of Size Effects in the Mechanical Behaviour of Polycrystals and Multiphase Materials*. International Journal of Solids and Structures, vol. 37, pp 7105–7126. 1.2.3, 7.4, 8.2
- FREUND L. B. (1987). *The stability of a dislocation threading a strained layer on a substrate*. Journal of Applied Mechanics–Transactions of the ASME, vol. 54, pp 553. 1.3

BIBLIOGRAPHY

- GONDA V., JANSEN K. M. B., ERNST L. J., DEN TOONDER J., AND ZHANG G. Q. (2007). *Micro-mechanical testing of SiLK by nanoindentation and substrate curvature techniques*. *Microelectronics Reliability*, vol. 47, pp 248–251. 1.2.3
- GROMA I., CSIKOR F.F., AND ZAISER M. (2003). *Spatial correlations and higher-order gradient terms in a continuum description of dislocation dynamics*. *Acta Materialia*, vol. 51, pp 1271–1281. 7.4, 8.2
- HAN CH.-S., MA A., ROTERS F., AND RAABE D. (2007). *A Finite Element approach with patch projection for strain gradient plasticity formulations*. *International Journal of Plasticity*, vol. 23, pp 690–710. 1.2.3
- HARREN S. AND ASARO R. (1989). *Nonuniform deformation in polycrystals and aspects of the validity of the Taylor model*. *Journal of the Mechanics and Physics of Solids*, vol. 37, pp 191. 1.1
- HARREN S., DÉVE H., AND ASARO R. (1988). *Shear band formation in plane strain compression*. *Acta Metallurgica*, vol. 36, pp 2435–2480. 1.1
- HOMMEL M. AND KRAFT O. (2001). *Deformation behaviour of thin copper films on deformable substrates*. *Acta Materialia*, vol. 49, pp 3935–3947. 1.2.1, 1.2.3, 1.3, 2.2.1, 3.3, 3.3.1, 3.3.2, 3.11, 4.1.2, 5.1, 5.1, 5.4
- HOUDAUGUI F. EL, FOREST S., GOURGUES A.-F., AND JEULIN D. (2007a). *On the size of the Representative Volume Element for isotropic elastic polycrystalline copper*. In : IUTAM Symposium on Mechanical Behavior and Micro-Mechanics of Nanostructured Materials, Beijing, China, June 27-30, 2005, pp 171–180. 1.2.3, 2.2.3
- HOUDAUGUI F. EL, FOREST S., GOURGUES A.-F., AND JEULIN D. (2007b). *Representative Volume Element sizes for copper bulk polycrystals and thin layers*. In : Colloque 3M – Interfaces de l'atome au polycrystal, Paris, June 14-15, 2006, pp 141–153. 1.2.3
- HUANG H. AND SPAEPEN F. (2000). *Tensile testing of free-standing Cu, Ag and Al thin films and Ag/Cu multilayers*. *Acta Materialia*, vol. 48, pp 3261–3269. 1.2.1

BIBLIOGRAPHY

- JANSSEN G. C. A. M. (2007). *Stress and strain in polycrystalline thin films*. Thin Solid Films, vol. 515, pp 6654–6664. 1.2.3
- KALIDINDI S.R., BRONKHORST C. A., AND ANAND L. (1992). *Crystallographic texture evolution during bulk deformation processing of fcc metals*. Journal of the Mechanics and Physics of Solids, vol. 40, pp 537–569. 1.1
- KANIT T., FOREST S., GALLIET L., MOUNOURY V., AND JEULIN D. (2003). *Determination of the size of the Representative Volume Element for random composites : statistical and numerical approach*. International Journal of Solids and Structures, vol. 40, pp 3647–3679. 1.5, 2.2.3
- KAWASAKI Y. AND TAKEUCHI T. (1980). *Cell structures in copper single crystals deformed in the [001] and [111] axes*. Scripta Metallurgica, vol. 14, pp 183–188. 3.1.1
- KELLER R.-M, BAKER S. P., AND ARZT E. (1999). *Stress–Temperature behavior of unpassivated thin copper films*. Acta Materialia, vol. 47, pp 415–426. 1.2.1, 1.2.3
- KIM S.H., NA S. W., LEE N.-E., AND NAM, Y. W. AD KIM Y.-H. (2005). *Effect of surface roughness on the adhesion properties of Cu/Cr films on polyimide substrate treated by inductively coupled oxygen plasma*. Surface and Coating Technology, vol. 200, pp 2072–2079. 1.1
- KNORR D. B. AND TRACY D. P. (1995). *A review of microstructure in vapor deposited copper thin films*. Materials Chemistry and Physics, vol. 41, pp 206–216. 1.2.2
- KOBRINSKY M. J., DEHM G., THOMPSON C. V., AND ARZT E. (2001). *Effect of thickness on the characteristic length scale of dislocation plasticity in Ag thin films*. Acta Materialia, vol. 49, pp 3597–3607. 1.2.1
- KOCKS U. F. AND H. CHANDRA (1982). *Slip geometry in partially constrained deformation*. Acta Metallurgica, vol. 30, pp 695. 1.1

BIBLIOGRAPHY

- KOZLOV E. V., ZHDANOV A. N., POPOVA N. A., PEKARSKAYA E. E., AND KONEVA N. A. (2004). *Subgrain structure and internal stress fields in UFG materials: problem of Hall–Petch relation*. Material Science and Engineering A, vol. 397–389, pp 789–794. 3.1.1
- KRAFT O., HOMMEL M., AND E. ARZT (2000). *X – ray diffraction as a tool to study the mechanical behaviour of thin films*. Materials Science and Engineering A, vol. A288, pp 209–216. 1.2.3, 5.1, 5.1, 5.3, 5.3
- KURODA M. AND TVERGAARD V. (2007). *On the formulations of higher–order strain gradient crystal plasticity models*. Journal of the Mechanics and Physics of Solids, vol. in press. 1.2.3
- LAZIK S., ESLING C., AND WEGRIA J. (1995). *Cracking in zinc layers on continuous galvanized steel sheets*. Textures and Microstructures, vol. 23, pp 131–147. 1.1
- LEBENSOHN R., LIU Y., AND CASTANEDA P. (2004). *On the accuracy of the self–consistent approximation for polycrystals: comparison with full–field numerical simulations*. Acta Materialia, vol. 52, pp 5347–5361. 1.1
- MA A., ROTERS F., AND RAABE D. (2006). *Studying the effect of grain boundaries in dislocation density based crystal–plasticity finite element simulations*. International Journal of Solids and Structures, vol. 43, pp 7287–7303. 1.2.3
- MAEDA S., SHIMOMURA H., FUJISAWA A., AND KONISHI M. (1996). *The structure and deformation behavior of hot–dip galvanized coatings*. Scripta Metallurgica, vol. 35, pp 333–338. 1.1
- MAHMUDI R. AND MEHDIZADEH M. (1998). *Surface roughening during uniaxial and equi–biaxial stretching of 70–30 brass sheets*. Journal of Materials Processing Technology, vol. 80–81, pp 707–712. 1.1

BIBLIOGRAPHY

- MANDEL J. (1973). *Equations constitutives et directeurs dans les milieux plastiques et viscoplastiques*. International Journal of Solids and Structures, vol. 9, pp 725–740. 1.1, 3.1
- MANE A. U. AND SHIVASHANKAR S. A. (2005). *Growth of (111)-textured copper thin films by atomic layer deposition*. Journal of Crystal Growth, vol. 275, pp 1253–1257. 1.2.2
- MAO W. (1998). *Modeling of rolling texture in aluminum*. Material Science and Engineering, vol. A257, pp 171. 1.1
- MÉRIC L., CAILLETAUD G., AND GASPERINI M. (1994). *F.E. calculations of copper bicrystal specimens submitted to tension-compression tests*. Acta Metall. Mater., vol. 42, pp 921–935. 3.1.1, 3.1.1, 3.2
- MÉRIC L., POUBANNE P., AND CAILLETAUD G. (1991). *Single Crystal Modeling for Structural Calculations. Part 1: Model Presentation*. J. Engng. Mat. Technol., vol. 113, pp 162–170. 3.1
- MIKA D. AND DAWSON P.R. (1998). *Effects of grain interaction on deformation in polycrystals*. Material Science and Engineering, vol. A257, pp 62–76. 1.1
- MIKA D. AND DAWSON P.R. (1999). *Polycrystal plasticity modelling of intracrystalline boundary textures*. Acta Materialia, vol. 47, pp 1355–1369. 1.1
- MINDSLAB (2007). <http://mems.utdallas.edu/>. 1.2, 1.1
- MOLINARI A. AND CANOVA G.R. (1987). *A self-consistent approach of the large deformation polycrystal viscoplasticity*. Acta Metallurgica, vol. 35, pp 2983–2994. 1.1
- MUSIENKO A., TATSCHL A., SCHMIDEGG K., KOLEDNIK O., PIPPAN R., AND CAILLETAUD G. (2007). *Three-dimensional finite element simulation of a polycrystalline copper specimen*. Acta Materialia, vol. 55, pp 4121–4136. 1.1
- NICOLA L., VAN DER GIESSEN E., AND NEEDLEMAN A. (2005). *Size effects in polycrystalline thin films analyzed by discrete dislocation plasticity*. Thin Solid Films, vol. 479, pp 329–338. 1.2.3, 4, 6

BIBLIOGRAPHY

- NIX W. D. (1989). *Mechanical properties of thin films*. Metallurgical transactions A—Physical Metallurgy and Materials Science, vol. 20, pp 2217. 1.3
- OH J., LEE J., AND LEE CH. (2002). *Plasma pretreatment of the Cu seed layer surface in Cu electroplating*. Materials Chemistry and Physics, vol. 73, pp 227–234. 1.1
- OKOLO B., LAMPARTER P., WELZEL U., WAGNER T., AND MITTEMEIJER E.J. (2005). *The effect of deposition parameters and substrate surface condition on texture, morphology and stress in magnetron-sputter-deposited Cu thin films*. Thin Solid Films, vol. 474, pp 50–63. 1.2.2, 1.5, 2.2.1
- PALUMBO G. AND TRICARICO L. (2007). *Numerical and experimental investigations on the Warm Deep Drawing process of circular aluminum alloy specimens*. Journal of Materials Processing Technology, vol. 184, pp 115–123. 1.1
- PARISOT R., FOREST S., GOURGUES A.-F., PINEAU A., AND MAREUSE D. (2001). *Modeling the mechanical behavior of a multicrystalline zinc coating on a hot-dip galvanized steel sheet*. Computational Materials Science, vol. 19, pp 189–204. 1.1, 1.2.3, 2.2.1, 4.3
- PARISOT R., FOREST S., PINEAU A., NGUYEN F., X. DEMONET, AND MATAIGNE J.-M. (2004). *Deformation and Damage Mechanisms of Zinc Coatings on Galvanized Steel Sheets, Part I: Deformation Modes*. Metallurgical and Materials Transactions, vol. 35A, pp 797–811. 1.1
- PEREZ-PRADO M. T. AND VLASSAK J. J. (2002). *Microstructural evolution in electroplated Cu thin films*. Scripta Materialia, vol. 47, pp 817–823. 1.2.2, 2.2.1
- RAABE D. AND ROTERS F. (2004). *Using texture components in crystal plasticity finite element simulations*. International Journal of Plasticity, vol. 20, pp 339–361. 1.1
- RAABE D., SACHTLEBER M., WEILAND H., SCHEELE G., AND ZHAO Z. (2003). *Grain-scale micromechanics of polycrystal surfaces during plastic straining*. Acta Materialia, vol. 51, pp 1539–1560. 1.1, 4.3

BIBLIOGRAPHY

- RAABE D., WANG Y., AND ROTERS F. (2005). *Crystal plasticity simulation study on the influence of texture on earing in steel*. Computational Material Science, vol. 34, pp 221–234. 1.1
- RAABE D., ZHAO Z., AND MAO W. (2002). *On the dependence of in-grain subdivision and deformation texture of aluminum on grain interaction*. Acta Materialia, vol. 50, pp 4379–4394. 1.1
- RAPHANEL J. L. AND VAN HOUTTE P. (1985). *Simulation of rolling textures of bcc metals by means of the relaxed Taylor theory*. Acta Metallurgica, vol. 33, pp 1481–1488. 1.1
- SACHS G. (1928). *Zur ableitung einer fleissbedingun*. Z Ver Dtsch Ing, vol. 72, pp 734. 1.1
- SACHTLEBER M., RAABE D., AND WEILAND H. (2004). *Surface roughening and color changes of coated aluminium sheets during plastic straining*. Journal of Materials Processing Technology, vol. 148, pp 68–76. 1.1, 4.3
- SAI K., CAILLETAUD G., AND FOREST S. (2006). *Micro-mechanical modeling of the inelastic behavior of directionally solidified materials*. Mechanics of Materials, vol. 38, pp 203–217. 1.2.3, 4.2.2
- SARMA G. B. AND DAWSON P. R. (1996). *Effects of interactions among crystals on the inhomogeneous deformations of polycrystals*. Acta Materialia, vol. 44, pp 1937–1953. 1.1
- SCHWAIGER R., DEHM G., AND KRAFT O. (2003). *Cyclic deformation of polycrystalline Cu films*. Philosophical Magazine, vol. 83, pp 693–710. 1.2.1, 4.3.2, 4.3.2, 4.4, 5.1, 5.4
- SCHWAIGER R. AND KRAFT O. (2003). *Size effects in the fatigue behavior of thin Ag films*. Acta Materialia, vol. 51, pp 195–206. 1.2.1, 4.3.2, 4.3.2, 4.4
- SHU J. Y. AND FLECK N. A. (1999). *Strain gradient crystal plasticity: size-dependent deformation of bicrystals*. Journal of the Mechanics and Physics of Solids, vol. 47, pp 297–324. 1.2.3, 7.4, 8.2

BIBLIOGRAPHY

- ŠIŠKA F., FOREST S., AND GUMBSCH P. (2007a). *Simulation of stress–strain heterogeneities in copper thin films: Texture and substrate effects*. Computational Materials Science, vol. 39, pp S137–S141. 2.5
- ŠIŠKA F., FOREST S., GUMBSCH P., AND WEYGAND D. (2007b). *Finite element simulations of cyclic elastoplastic behavior of copper thin films*. Modelling and Simulation in Material Science and Engineering, vol. 15, pp S217–S238. 4.4
- SPAEPEN F. AND YU D. Y. W. (2004). *A comparison of the strength of multilayers, thin films and nanocrystalline compacts*. Scripta Materialia, vol. 50, pp 729–732. 1.3, 3.1.1
- TAYLOR G.I. (1938). *Plastic strain in metals*. J Inst Metals, vol. 62, pp 307–324. 1.1
- TEODOSIU C. AND SIDOROFF F. (1976a). *A theory of finite elastoviscoplasticity of single crystals*. International Journal of Engineering Science, vol. 14, pp 165–176. 1.1, 3.1
- TEODOSIU C. AND SIDOROFF P. (1976b). *A finite theory of the elastoviscoplasticity of single crystals*. International Journal of Engineering Science, vol. 14, pp 713–723. 1.1
- THOMPSON C. V. (1993). *The yield stress of polycrystalline thin–films*. Journal of Materials Research, vol. 8, pp 237. 1.3
- TIKHOVSKIY I., RAABE D., AND ROTERS F. (2007). *Simulation of earing during deep drawing of an Al-3% Mg alloy (AA 5754) using a texture component crystal plasticity FEM*. Journal of Materials Processing Technology, vol. 183, pp 169–175. 1.1
- VAN DER GIESSEN E. AND NEEDLEMAN A. (1995). *Discrete dislocation plasticity: a simple planar model*. Modelling and Simulation in Material Science and Engineering, vol. 3, pp 689–735. 1.2.3, 6.1.1, 6.2
- VINCI R. P., ZIELINSKY E. M., AND BRAVMAN J. C. (1995). *Thermal strain and stress in copper thin films*. Thin Solid Films, vol. 262, pp 142–153. 1.2.1, 1.2.2, 1.2.3
- VIRGINIA SEMICONDUCTOR INC. (2006). *Basic mechanical and thermal properties of silicon*. www.virginasemi.com. 4.1.2

BIBLIOGRAPHY

- VON BLANCKENHAGEN B., ARTZ E., AND GUMBSCH P. (2004). *Discrete dislocation simulation of plastic deformation in metal thin films*. Acta Materialia, vol. 52, pp 773–784. 1.2.3, 1.3, 2, 4, 6, 6.2.3
- VON BLANCKENHAGEN B., GUMBSCH P., AND ARTZ E. (2001). *Dislocation sources in discrete dislocation simulations of thin-film plasticity and the Hall–Petch relation*. Modelling and Simulation in Materials Science and Engineering, vol. 9, pp 157–169. 1.2.3, 1.3, 5, 6
- WALDE T. AND RIEDEL H. (2007). *Simulation of earing during deep drawing of magnesium alloy AZ31*. Acta Materialia, vol. 55, pp 867–874. 1.1
- WEIHNACHT V. AND BRUCKNER W. (2002). *Abnormal grain growth in {111} textured Cu thin films*. Thin Solid Films, vol. 418, pp 136–144. 1.2.2, 2.2.1
- WEISS D., GAO H., AND ARTZ E. (2001). *Constrained diffusional creep in UHV-produced copper thin films*. Acta Materialia, vol. 49, pp 2395–2403. 1.2.1, 1.2.3
- WENDROCK H., BRÜCKNER W., HECKER M., KOETTER T. G., AND SCHLOREB H. (2000). *Room temperature grain growth in electroplated copper thin films*. Microelectronics Reliability, vol. 40, pp 1301–1304. 1.2.2
- WEYGAND D., BRECHET Y., AND LEPINOUX J. (1998). *A vertex dynamics simulation of Grain Growth in two dimensions*. Phil. Mag. B, vol. 78, pp 329–352. 2.2.1, 5.5
- WEYGAND D., FRIEDMAN L.H., VAN DER GIESSEN E., AND NEEDLEMANN A. (2001). *Discrete dislocation modeling in three-dimensional confined volumes*. Materials Science and Engineering A, vol. 309–310, pp 420–424. 1.2.3, 6.1.1
- WEYGAND D., FRIEDMAN L.H., VAN DER GIESSEN E., AND NEEDLEMANN A. (2002). *Aspect of boundary-value problem solutions with three-dimensional dislocation dynamics*. Modelling and Simulation in Materials Science and Engineering, vol. 10, pp 437–468. 1.2.3, 6.1.1

BIBLIOGRAPHY

- WEYGAND D. AND GUMBSCH P. (2005). *Study of dislocation reactions and rearrangements under different loading conditions*. Materials Science and Engineering, vol. A 400–401, pp 158–161. 4.3.2
- WEYGAND D., POIGNANT M., GUMBSCH P., AND KRAFT O. (2007). *Three-dimensional dislocation dynamics simulation of the influence of sample size on the stress-strain behavior of fcc single-crystalline pillars*. Materials Science and Engineering: A, vol. In Press, Corrected Proof. 7
- WIKSTRÖM A. AND NYGÅRDS M. (2002). *Anisotropy and texture in thin copper films—an elastoplastic analysis*. Acta Materialia, vol. 50, pp 857–870. 1.2.3
- WILSON W. R. D. AND LEE W. (2001). *Mechanics of surface roughening in metal forming processes*. Journal of Manufacturing Science and Engineering, vol. 123, pp 279–283. 1.1, 4.3.2
- WITTRIDGE N.J AND KNUTSEN R.D (1999). *A microtexture based analysis of the surface roughening behaviour of an aluminium alloy during tensile deformation*. Materials Science and Engineering: A, vol. 269, pp 205–216. 1.1
- YEFIMOV S. AND VAN DER GIESSEN E. (2005). *Size effects in single crystal thin films: nonlocal crystal plasticity simulations*. European Journal of Mechanics A/Solids, vol. 24, pp 183–193. 1.2.3, 7.4, 8.2
- ZEGHADI A., NGUYEN, F. AND FOREST S., GOURGUES A.F., AND BOUAZIZ O. (2007a). *Ensemble averaging stress-strain fields in polycrystalline aggregates with a constrained surface microstructure—Part 1: Anisotropic elastic behaviour*. Philosophical Magazine, vol. 87, pp 1401–1424. 7.2
- ZEGHADI A., NGUYEN, F. AND FOREST S., GOURGUES A.F., AND BOUAZIZ O. (2007b). *Ensemble averaging stress-strain fields in polycrystalline aggregates with a constrained surface microstructure—Part 2: Crystal plasticity*. Philosophical Magazine, vol. 87, pp 1425–1446. 7.2

BIBLIOGRAPHY

ZHAO Z., KUHNICKI S., RADOVITZKY R., AND CUITINO A. (2007). *Influence of in-grain mesh resolution on the prediction of deformation textures in fcc polycrystals by crystal plasticity FEM*. Acta Materialia, vol. 55, pp 2361–2373. 1.1